

Numerical Studies of the Jet Interaction Flowfield with a Main Jet and an Array of Smaller Jets

Valerio Viti

*Dissertation Submitted to the Faculty of the
Virginia Polytechnic Institute and State University
in partial fulfillment of the requirements for the degree of*

**DOCTOR OF PHILOSOPHY
in Aerospace Engineering**

Dr. Joseph Schetz, Chair _____

Dr. Bernard Grossman _____

Dr. William Devenport _____

Dr. Reece Neel _____

Dr. William McGrory _____

*September 16th, 2002
Blacksburg, VA*

*Keywords: Jet Interaction, Normal Injection, Numerical Simulation, CFD.
Copyright ©2002, Valerio Viti*

Numerical Studies of the Jet Interaction Flowfield with a Main Jet and an Array of Smaller Jets

Valerio Viti

Abstract

A numerical study of a proposed innovative jet interaction configuration is presented. This work aimed at improving present-day jet interaction configurations in their applications as control thrusters on hypersonic vehicles. Jet thrusters are a useful control system for fast-moving vehicles flying in the upper layers of the atmosphere because of their effectiveness and responsiveness. They produce a strong and responsive lateral force on the vehicle through the interaction of two main mechanisms. The first mechanism comes from the momentum of the injectant itself, basically the thrust of the jet. The second and subtler contribution comes from the jet interaction flowfield, the interaction of the expanding injectant with the crossflow. This interaction produces areas of high pressure ahead of the injector and areas of low pressure in the region aft of the jet. The combination of the high-pressure regions in front of and low-pressure regions aft of the injector produces an undesirable nose-down pitching moment on the vehicle. In order to counterbalance the nose-down attitude, modern-day thruster designs include a large secondary injector far aft of the center of gravity of the vehicle. The thrust of this second injector acting far aft of the primary injector neutralizes the nose-down pitching moment. This is not an efficient method to obviate the problem since it requires the vehicle to be designed to carry two large thrusters and double the quantity of fuel necessary for one thruster. In light of these considerations, this study aimed at developing a jet interaction configuration that can dispense from the need of a large secondary injector to compensate for the nose-down pitching moment. The cases studied here were first a primary jet alone and then a primary jet with pairs of smaller jets. This configuration was based on the notion that the interaction of the secondary jets, conveniently located immediately aft of the thruster, with the barrel shock and the wake of the primary jet can drastically reduce the nose-down pitching moment. Because of the complexity of the jet interaction flowfield the investigation of the feasibility and the assessment of the efficiency of the new jet interaction configurations combined the present numerical effort with experimental studies of jet interaction flowfields performed in the supersonic wind tunnel at Virginia Tech.

During the present numerical study the jet interaction flowfield associated with the sonic injection of a gas into a high-speed crossflow was simulated by numerically solving the Reynolds Averaged Navier Stokes (RANS) equations. Turbulence was modeled through a first-order model, the Wilcox's 1988 $k-\omega$ turbulence model. The computations made use of the finite volume code General Aerodynamic Simulation Program (GASP) Version 4. For simplicity and to keep the study general, the jet interaction flowfield was studied on a flat plate instead of a body of revolution as on a vehicle. Calculations were run for a

number of jet interaction configurations consisting of a primary jet alone, a primary jet and one pair of secondary jets, and a primary jet and two pairs of secondary jets. The flow conditions of the simulations ranged from a Mach number of 2.1 up to a Mach number of 4.5 and jet total pressure to freestream static pressure ratios of 14 to 680. A large effort was dedicated to the development of an efficient computational grid that could capture most of the flow-physics with a minimum number of cells. To this end, Chimera or overset grids were employed in the simulation of the secondary injectors. Grid convergence was shown to be achieved for the case of single injection by conducting a thorough convergence study. The discretization error was calculated through a modified Richardson extrapolation to be low. The numerical solutions were compared to the experimental results in order to assess the capability of RANS equations and of first-order turbulence models to properly simulate the complex flowfield. The $k-\omega$ turbulence model proved to be reliable and robust and the results it provided for this type of flowfield were accurate enough from an engineering standpoint to make informed decisions about the configuration layout. In spite of the overall good performance, the $k-\omega$ turbulence model failed to correctly predict the flow in the regions of strong adverse pressure gradients. Comparisons with experimental results showed that the separation region was often under-predicted thus highlighting the need to employ better turbulence models for more accurate results. The RANS equations were found accurate enough to provide physical mean-flow solutions. Further, the numerical simulations provided information about the detailed physics of the flowfield that is impossible to obtain through experimental work. The analysis of the numerical solutions highlighted the existence of a complex system of counter-rotating trailing vortices that are responsible for the mixing of the injectant with the freestream. The typical features of the flowfield created by an under-expanded jet exhausting in a quiescent medium were visible in the jet interaction flowfield with the difference of the existence of a crossflow and a non-uniform back-pressure. The region of low pressure aft of the injector was shown to be generated by the detachment of the barrel shock from the surface of the flat plate that leaves a large volume to be filled by the surrounding fluid.

The simulations showed that the innovative configuration with one primary jet and an array of smaller secondary jets can effectively decrease the nose-down pitching moment by as much as 101%. In some cases, it also increased the total normal force acting on the flat plate (namely the thrust) by as much as 5%. This effect was found to be caused by the reduction in size and intensity of the low-pressure region aft of the primary injector.

Dedication

*In memory,
Zio Renato*

and

To my family.

Acknowledgments

As usual, the author of this work is one but many are the people who, in different ways and at different degrees, contributed to the finalization of the project. I would like to thank some of the many people who made this work possible.

First of all I would like to thank Dr. Schetz, for giving me the opportunity to work with him on this project. His guidance and enthusiasm have been essential in overcoming the obstacles that sometimes I found myself to face. A special acknowledgement goes to Dr. Neel for his everlasting support, willingness to share his knowledge with me and, above all, patience in teaching me the basics of the job. Without him I would still be running my laminar calculations. Thank you Reece! Dr. McGrory for being there when I needed him and for making available to me, without any reserve, the resources of AeroSoft Inc. Dr. Devenport and Dr. Grossman for their advice and for serving on my committee. I would also like to thank the people at AeroSoft, Andy, Angel, Mark and Mike, who, during my three years at AeroSoft, have always been extremely helpful and friendly. Finally I would like to acknowledge the support of the Air Force Research lab through contract AFR-2T-3014-AOS.

On a more personal note there are many more people that, most likely unknowingly, have helped me finish my studies, grow as a person, and enjoy my life in Blacksburg. In same way I finished my doctorate for them!

For dad, mum and Silvia who have always supported me even when they disagreed with my decisions. You are my point of reference.

For Ive who taught me some of the most important lessons in my life.
For Lucas, who is the greatest of these lessons.

For Luca and his always-shining inspiration

For Dot and her everlasting support and for all the funny, loving, sad and mad moments we shared together. I have so much “cariño” for you.

For Diego and his patience in sharing the Lantern Ridge Apartment with me and for his friendship that grew up since the very first moment we started school at Tech together.

For Chittiappa and Tone and their infinite friendliness and kindness.

For Dimitris and his Mediterranean temper!

For Borja and his infectious determination.

For Regis and his motivational drive.

For Andrea and our talks about the flow of life.

For “La Directiva”, Carlos, Mauricio, Pedro and the laughs we had together.

For “Los Ponchaos”.

For “Los Pajeros”.

For the people of the Latin American and Iberian Graduate Student Association who adopted me as one of them and especially Raul, Aida, Virgilio, Tatiana, Alejandro, Alejandra, Leonardo, Sebastian, Bernardo, Jose, Sergio Iglesias, Sergio Busques.

For friends and colleagues in the Aerospace Department, especially Patrick, Serhat, Philippe, Lance, Samantha, Michelle.

Also for Lionel, Christelle, Burak, Dwight, Elene, Marianne, Stilian, Hristo, Alex, Linda. Paulo, Evelyn and the usuals of “The Cellar”.

And for Blacksburg and the special people who live here.

TABLE OF CONTENTS

LIST OF FIGURES.....	IX
LIST OF TABLES.....	XVI
NOMENCLATURE	XIX
CHAPTER 1 INTRODUCTION.....	1
1.1 BACKGROUND	1
1.2 FLOWFIELD DESCRIPTION.....	2
1.3 MOTIVATION	6
1.4 APPROACH TO THE PROBLEM.....	8
1.5 OBJECTIVES.....	10
1.6 OVERVIEW OF THE DOCUMENT	11
CHAPTER 2 LITERATURE REVIEW.....	13
2.1 EXPERIMENTAL WORK	13
2.2 NUMERICAL WORK	19
CHAPTER 3 GOVERNING EQUATIONS AND NUMERICAL SOLVERS	25
3.1 GASP	25
3.2 GOVERNING EQUATIONS	26
3.3 NON-DIMENSIONAL FORM OF THE GOVERNING EQUATIONS.....	32
3.4 THE REYNOLDS AVERAGED AND FAVRE AVERAGED FORM OF THE GOVERNING EQUATIONS.....	36
3.5 TURBULENCE MODELING	38
5.5.1 $k-\omega$	39
CHAPTER 4 BOUNDARY CONDITIONS AND COMPUTATIONAL GRIDS.....	40
4.1 BOUNDARY CONDITIONS	41
4.2 COMPUTATIONAL GRIDS.....	45
CHAPTER 5 RESULTS	51
5.1 OVERVIEW OF CONSIDERED CASES	51
5.2 DEFINITION OF PARAMETERS.	54
5.3 SOURCES OF ERROR IN THE NUMERICAL SIMULATIONS.....	59
5.3.1 <i>Iterative convergence of the numerical solutions</i>	60
5.3.2 <i>Grid-convergence error</i>	65
General Richardson extrapolation	65
Mixed 1 st +2 nd order Richardson extrapolation	67
5.3.3 <i>Discretization error and round-off error</i>	70
5.3.4 <i>Perfect gas assumption</i>	71
5.3.5 <i>Accuracy of boundary conditions</i>	74
5.4 SOURCES OF ERROR OF THE EXPERIMENTAL DATA USED FOR COMPARISON WITH THE NUMERICAL SOLUTIONS.	76
5.4.1 <i>Experimental Uncertainty</i>	76
5.4.2 <i>Pressure Mapping Uncertainty</i>	76
5.4.3 <i>Discharge Coefficient Uncertainty</i>	78
5.5 LAMINAR CASES.....	79
5.5.1 <i>Schetz Laminar Case (PR62, Mach 2.10)</i>	79
5.5.2 <i>Cubbison Laminar Case (PR677, Mach 2.92)</i>	87
5.5.3 <i>Letko turbulent case (Mach 4.50, PR680)</i>	97

Grid-Convergence Study with a discharge coefficient of 1.00.....	99
Calculation of Discharge Coefficient for the Injector	108
Comparison of CFD calculations with a jet discharge coefficient of 0.78 to Experiment	111
Letko Turbulent case with Simulated Secondary Jets	116
5.6 VIRGINIA TECH MACH 2.4, TURBULENT (PR 14)	122
5.6.1 <i>Description of the experiment</i>	122
5.6.2 <i>Numerical results</i>	126
5.6.3 <i>Comparison of numerical results with experiment</i>	138
5.7 VIRGINIA TECH MACH 4.00, TURBULENT (PR 532)	147
Comparison of experimental and numerical results	161
CHAPTER 6 ANALYSIS OF THE JET INTERACTION FLOWFIELD USING THE NUMERICAL RESULTS.....	174
CHAPTER 7 SUMMARY AND CONCLUSIONS.....	196
7.1 SUMMARY OF THE RELEVANT ACCOMPLISHMENTS	196
7.2 CONCLUSIONS	200
7.3 RECOMMENDATIONS FOR FUTURE WORK.....	201
CHAPTER 8 BIBLIOGRAPHY	203
APPENDIX A. GENERAL FORM OF CONSERVATION LAWS	210
APPENDIX B. FULL SET OF NUMERICAL RESULTS ON ALL THE GRID SEQUENCES FOR THE VIRGINIA TECH CASES.	213
APPENDIX C. REYNOLDS STRESS TURBULENCE MODEL.	215
REYNOLDS STRESS TURBULENCE MODEL	215

List of Figures

Figure 1.1. Schematic cut along the tunnel centerline. The definition of the jet pressure ratio (PR) as given by Cubbison [22] is consistently used as the primary injection parameter all through the present work.	3
Figure 1.2. Typical pressure distribution along the plate centerline for a three-dimensional jet interaction flowfield created by the normal injection of a gas into a supersonic crossflow. From the experimental work of Spaid, et al. [70].	3
Figure 1.3. Detail of the separation-jet plume region along the tunnel centerline.....	5
Figure 1.4. Schematic view of the flowfield at section AA (Figure 1.3).....	5
Figure 1.5. Three-dimensional schematic view of the jet interaction problem with a single circular jet normally injecting into a supersonic cross flow.	6
Figure 1.6. (a) Model of the effect of a jet thruster on a hypersonic vehicle. (b) The effect of the nose-down moment. (d) Modern control system configuration. (e) Innovative configuration.	7
Figure 2.1. The three-dimensional schematic view of the jet interaction problem with a single circular jet normally injecting into a supersonic cross flow as proposed by Glagolev, et al. [30].	16
Figure 2.2. Three-dimensional schematic view of the jet interaction problem with a single circular jet normally injecting into a supersonic cross flow as proposed by Santiago and Dutton [63].	18
Figure 2.3. Mach contours at 4 diameters downstream of the injection location In this case the injection is inclined to the surface of the flat plat and the jet conditions are supersonic. [15].....	23
Figure 4.1. Computational domain for the flat plate with normal injection. The surface of the flat plate is highlighted in gray. The arrangement of the computational domain is the same for all the calculations even though the dimensions of the plate and of the injector changed from case to case.	42
Figure 4.2. Overview of the adaptation of the computational grid.	47
Figure 4.3. Comparison of the grids wrapping around the injector for the three grid topologies. See also the previous figure for comparison.	48
Figure 5.1. Reference coordinate system and pitching moment sign convention for the jet interaction problem. Note also the pressure ratio definition used in this work. The definition comes from Cubbison '61 [22].....	56
Figure 5.2. Reference coordinate system and pitching moment sign convention for the jet interaction problem. Note also the pressure ratio definition used in this work. The definition comes from Cubbison '61 [22].....	58
Figure 5.3. Residual history for the medium grid sequence of the Virginia Tech Mach 4.0 case with only the primary jet activated.	62
Figure 5.4. History of the convergence of the numerical solution. The three main parameters used to check for convergence were (a) the normal force, (b) the pitching moment and (c) the axial force. This history is for the Virginia Tech Mach 4.0 case with only the primary jet activated.	63

Figure 5.5. Residual history for the Virginia Tech Mach 4.0 case with only the primary jet activated.	64
Figure 5.6. Temperature contours and streamlines inside the barrel shock. The white thick diagonal line represents the line along which the velocity magnitude is plotted in Figure 5.7. This calculation is representative of all the other jet interaction cases and uses flowfield data of the Virginia Tech case with only the primary jet activated... ..	72
Figure 5.7. Velocity magnitude and static temperature distribution along the particle path AB (see Figure 5.6).....	73
Figure 5.8. Plan-view of the flat plate used by Cubbison [22] in his jet interaction experiments. The pressure orifices used to draw the pressure contours of Figure 5.22 are shown as circles. The drawing on the left is a detailed drawing of the locations of the pressure orifices in the area around the injector. All dimensions in inches. From Ref. [22].	77
Figure 5.9. Experimental set up of the Schetz experiment (from Ref. [65]).	80
Figure 5.10. (a) Perspective and (b) side view of the 4-zone computational grid. The grid dimensions (nodes) of the four zones are (73x65x57) for zone 1 and 3 and (73x57x57) for zone 2 and 4 for a total of 967,680 cells.....	82
Figure 5.11. (a) Perspective and (b) top view of the of the surface mesh around the injector.	83
Figure 5.12. Schlieren picture with superimposed major flow features obtained with the CFD calculations.....	84
Figure 5.13. Mach number contour lines as predicted by the CFD calculations. The solid black lines represent the shock waves, jet plume and boundary layer thickness that can be observed in the Schlieren picture of Figure 5.12.....	85
Figure 5.14. (a) Plume height comparison for the Schetz experiment (from Ref. [65]). The arrow indicates where the data point corresponding to the experiment simulated in this work. The star is the data point corresponding to the numerical simulation. As expected from looking at Figure 5.13 the height of the plume for the numerical calculation and the experiment are exactly the same. (b) Definition of plume height.	86
Figure 5.15. Experimental flat plate configuration for the Cubbison test case as shown in Ref. [22].	87
Figure 5.16. Perspective view of the computational domain for the Cubbison case (not all gridlines are shown). The flat plate surface (no-slip adiabatic) is in red, the injector (fixed jet conditions) is in black, the back-plane (extrapolation) is in purple and the far cross-plane (extrapolation) is in blue.	88
Figure 5.17. Detail of the grid laying on the flat plate surface and around the injector. Note how the C-type grid (in red) wraps around the injector (in black) and how it allows a much more efficient clustering than the H-type grid since it “fans-out” the finely spaced cells near the injector to a larger area.	89
Figure 5.18. Comparison of the experimental and CFD force for the three grid sequences.	91
Figure 5.19. Comparison of the experimental moment and the CFD moment for the three grid sequences.	91

Figure 5.20. Comparison of the experimental and the CFD (for the three sequences) C_p distribution along the centerline. Mach 2.92, PR=1247.	92
Figure 5.21. Mach number contour lines on the plane of symmetry. Mach 2.92, PR=677, sequence 1(709,161 cells).....	93
Figure 5.22. C_p contour lines on the flat plate surface. Mach 2.92, PR=677.....	93
Figure 5.23. Comparison of the experimental and the C_p distribution along the centerline. Cubbison case, Mach 2.92, PR=677.....	94
Figure 5.24. (a) Perspective view of the new grid topology used for the Letko case.(b) Detailed view of the grid around the injector. Letko case, Mach 4.50, PR=680.....	96
Figure 5.25. Experimental flat plate configuration for the Letko test case as presented in Ref. [42]......	98
Figure 5.26. Comparison of the normal force coefficient on the four grid sequences for the Letko case.	102
Figure 5.27. Comparison of the pitching moment coefficient on the four grid sequences for the Letko case.....	102
Figure 5.28. Comparison of the pressure coefficient just ahead of the injector for the four grid sequences.....	103
Figure 5.29 Comparison of the skin friction coefficient just ahead of the injector for the four grid sequences.	103
Figure 5.30 Comparison of the (a) dimensional plot of the boundary layer velocity profiles and of (b) the wall law plot just ahead of the separation ($x/d=-8.5$) on the symmetry plane for the four grid sequences.	104
Figure 5.31. Comparison of the Mach number contour lines on the plane of symmetry for the four grid sequences. Some of the main flow parameters, such as the penetration height and the plume angle were measured and compared.....	106
Figure 5.32. Comparison of the C_p contour lines on the flat plate for the four grid sequences. The angle formed by the zero- C_p line and the flow direction was measured and compared (β). Other parameters used for comparison are the normal force on the flat plate (F_y) and the moment about the z-axis (M_z).....	107
Figure 5.33. (a) The nozzle drawing from the original Letko paper [42] (all dimensions in inches). (b) The different inflow conditions that were used to calculate the nozzle flow. Drawings not to scale.	109
Figure 5.34. Discharge coefficient (C_d) results of the GASP calculations with the different flow conditions.....	110
Figure 5.35. Comparison of the force on the flat plate obtained from the solution on the three sequences of Grid 5 for the Letko case with a discharge coefficient of 1.00 and 0.78.....	112
Figure 5.36. Comparison of the moment obtained from the solution on the three sequences of Grid 5 for the Letko case with a discharge coefficient of 1.00 and 0.78.	112
Figure 5.37. Comparison of the C_p mapping on the surface of the flat plate for the Letko experiment (top) and the numerical simulation (bottom) with a discharge coefficient of 0.78.	113
Figure 5.38. Comparison of the experimental and the C_p distribution along the centerline. Letko case, Mach 4.50, PR=680.	113

Figure 5.39. Comparison of the Mach contours on the plane of symmetry on the three grid sequences of the Letko calculation with a discharge coefficient of 0.78. Letko case, Mach 4.50, PR=680.	115
Figure 5.40. Plan view of the location of the secondary injectors with superimposed the C_p mapping of the Cubbison case [22].	119
Figure 5.41. Plan view of the grid on the surface of the flat plate in the region behind the main injector. The secondary injectors were created by specifying a flow-rate for some cells on the surface of the flat plate. Not all gridlines shown.	119
Figure 5.42. Mach number contours for the Letko case with simulated secondary injector. Top view is on the plane of symmetry ($z/d = 0.00$) and the one at the bottom is on the longitudinal plane intersecting the secondary jet axis ($x/d = -1.31$).	120
Figure 5.43. Comparison of the C_p for the Letko case with only the primary jet on and the Letko case with both the primary and the secondary jet on (medium grid sequence, 127,976 cells).	121
Figure 5.44. Top view of the flat plate used in the Virginia Tech jet interaction experiments. The primary and secondary injectors are highlighted. All dimensions in centimeter [84].	123
Figure 5.45. Cross-section of the primary (main) and secondary injectors as drilled in the flat plate. All dimensions in centimeter [84].	124
Figure 5.46. Perspective view of the computational grid employed for the Virginia Tech Mach 2.4 cases. It is composed of 12-zone some of which are H-type and others are C-type grid topology. The C-type grids wrap around the primary injector to optimize the.	127
Figure 5.47. Plan view of the grid on the surface of the flat plate.	128
Figure 5.48. Comparison of the normal force coefficient acting on the flat plate for the three Virginia Tech, Mach 2.4, Pr=14 test cases.	132
Figure 5.49. Comparison of the pitching moment coefficient acting on the flat plate for the three Virginia Tech, Mach 2.4, Pr=14 test cases.	132
Figure 5.50. Comparison of the CFD Mach contours on the plane of symmetry for the primary jet only case (top), the primary jet plus the secondary jets of Group 1(center) and the primary jet plus the secondary jets of Group 1 and Group 2 case (bottom). Virginia Tech Mach 2.4, Pr=14.	135
Figure 5.51. Comparison of the CFD C_p plots along the tunnel centerline for the three configurations. (a) Over the whole computational domain. (b) Detail of the low-pressure region where the secondary injectors are located. Virginia Tech Mach 2.4, Pr=14.	136
Figure 5.52. Comparison of the CFD C_p mapping for the Primary jet only case (top) and the primary jet plus Group 1 secondary jets case (bottom). Virginia Tech Mach 2.4, Pr=14.	137
Figure 5.53. Comparison of C_p plots along the tunnel centerline for the experimental and numerical data sets. Virginia Tech, Mach 2.4, Pr=14.	139
Figure 5.54. Comparison of C_p plots along the tunnel centerline for the experimental and numerical data sets with only the Primary jet. Virginia Tech, Mach 2.4, Pr=14.	140

Figure 5.55. Comparison of C_p plots along the tunnel centerline for the experimental and numerical data sets with both Group 1 secondary jet. Virginia Tech, Mach 2.4, Pr=14.....	140
Figure 5.56. Comparison of C_p plots along the tunnel centerline for the experimental and numerical data sets with both Group 1 and Group 2 secondary jets. Virginia Tech, Mach 2.4, Pr=14.....	141
Figure 5.57. Schlieren photograph of the flowfield produced by the case with only the primary jet activated [84]. Virginia Tech, Mach 2.4, Pr=14.....	142
Figure 5.58. Comparison of the experimental (top) and CFD (bottom) C_p mapping for the case with only the Primary injector activated. Virginia Tech Mach 2.4, Pr=14.....	144
Figure 5.59. Comparison of the experimental (top) and CFD (bottom) C_p mapping for the case with the Primary injector and the secondary injectors of Group 1 activated. Virginia Tech Mach 2.4, Pr=14.	145
Figure 5.60. Comparison of the experimental (top) and CFD (bottom) C_p mapping for the case with the primary and secondary injectors of Group 1 and Group 2 activated. Virginia Tech, Mach 2.4, Pr=14.	146
Figure 5.61. Perspective view of the overall grid topology employed for the Virginia Tech Mach 4.0 cases. It is composed of 13-zone some of which are H-type and others are C-type grid topology. The C-type grids wrap around the primary injector to optimize the grid refinement in this area. The total number of cells varied depending on the case: 1,544,098 for the case with only the primary injector activated and 2,073,024 cells for the case with the primary and secondary injectors activated). Not all grid lines are shown. The dashed rectangle shows the location of the block that was replaced with a Chimera grid when the secondary jet was activated. The area inside the rectangle is shown in more detail in Figure 5.62.	149
Figure 5.62. Comparison of the regular grid used in the case with only the primary injector and of the Chimera grid used for the case with the primary and secondary injector. Virginia Tech, Mach 4.0, Pr=532.	150
Figure 5.63. Details of the Chimera grid around the Primary jet and the secondary jet of Group 2. Virginia Tech, Mach 4.0, Pr=532 test cases.	152
Figure 5.64. Comparison of the normal force, F_y , acting on the flat plate for the two Virginia Tech, Mach 4.0, Pr 532 test cases.....	155
Figure 5.65. Comparison of the pitching moment, M_z , acting on the flat plate for the two Virginia Tech, Mach 4.0, Pr 532 test cases.....	155
Figure 5.66. Comparison of the CFD C_p mapping for the Primary jet only case (top) and the primary jet plus 1 secondary jet case (bottom). Virginia Tech, Mach 4.0, Pr 532.	157
Figure 5.67. Comparison of the C_p plots along the tunnel centerline for the primary jet only case and the Primary + Group 2 jet case. Virginia Tech, Mach 4.0, PR 532.	158
Figure 5.68. Comparison of the CFD Mach contours on the plane of symmetry for the primary jet only case (top) and the primary jet plus 1 secondary jet case (bottom). Virginia Tech, Mach 4.0, Pr=532.	159
Figure 5.69. Comparison of the pressure coefficient along the same spanwise location as the secondary injector for the medium and fine sequences of the Chimera grid. The	

- top figure shows in detail the line along which the C_p is plotted. Virginia Tech, Mach 4.0, Pr=532 with secondary injector. 160
- Figure 5.70. Locations of the C_p plots of Figure 5.71 and Figure 5.72 superimposed on the experimental C_p mapping for the case with only the primary jet. Virginia Tech, Mach 4.0, Pr=532..... 163
- Figure 5.71. Comparison of the experimental and numerical spanwise C_p plots ahead of the separation region at $x/d = -8.0$ for the case with only the primary jet. Virginia Tech, Mach 4.0, Pr=532..... 163
- Figure 5.72. Comparison of the experimental and numerical longitudinal C_p plots at $z/d = -15.0$ for the case with only the primary jet. Virginia Tech, Mach 4.0, Pr=532..... 164
- Figure 5.73. Comparison of the experimental (top) and numerical (bottom) C_p mappings on the surface of the flat plate for the case with only the primary jet switched on. Virginia Tech, Mach 4.0, Pr=532. 167
- Figure 5.74. Pressure coefficient plots from the numerical solution (solid line) and from the experimental (dashed line with error bars) for the case with only the primary injector. Virginia Tech, Mach 4.0, Pr=532. 168
- Figure 5.75. Comparison of the experimental (top) and numerical (bottom) C_p mappings on the surface of the flat plate for the case with both the primary and secondary jets activated. Virginia Tech, Mach 4.0, Pr=532. 169
- Figure 5.76. Pressure coefficient plots from the numerical solution (solid line) and from the experimental (dashed line with error bars) for the case with the primary and secondary injectors. Virginia Tech, Mach 4.0, Pr=532. 170
- Figure 5.77. Shadowgraph of the flowfield generated by the primary jet only. Virginia Tech, Mach 4.0, Pr=532. From Wallis [84]..... 171
- Figure 5.78. Schlieren photograph of the flowfield generated by the primary jet only. Virginia Tech, Mach 4.0, Pr=532. From Wallis [84]..... 172
- Figure 5.79. Schlieren photograph of the flowfield generated by the primary jet only. Virginia Tech, Mach 4.0, Pr=532. From Wallis [84]..... 172
- Figure 5.80. Visual comparison of the Schlieren picture with the flowfield features from the CFD solution on the plane of symmetry; the CFD contours represent the spatial derivative of the density. Primary injector only. (see Figure 5.68). Virginia Tech, Mach 4.0, Pr=532..... 173
- Figure 5.81. Visual comparison of the Schlieren picture with the flowfield from the CFD solution on the plane of symmetry for the case with the primary and secondary injectors. (see Figure 5.68). Virginia Tech, Mach 4.0, Pr=532. 173
- Figure 6.1. Isometric view of the oblique barrel shock with two groups of streamlines highlighting the flow out of the recirculation region ahead of the injector. The contours on the plane of symmetry are Mach number contours, the colors on the flat plate surface are C_p contours and the contours on the crossplane are Mach number contours with velocity vectors ($y-z$ projection) superimposed. Virginia Tech, Mach 4.0, Pr=532, Primary jet only..... 175
- Figure 6.2. Analysis of the jet interaction flowfield produced by the Virginia Tech, Mach 4.0 case with only the primary jet switched on. (Pr=532). 176
- Figure 6.3. Isometric view of the oblique barrel shock with the groups of streamlines identifying the main rotational motion. The contours on the plane of symmetry are

Mach number contours, the contours on the flat plate surface are C_p contours and the contours on the crossplane are vorticity magnitude contours. Virginia Tech, Mach 4.0, Pr=532, Primary jet only.....	182
Figure 6.4. Velocity vectors and Mach number contours on the plane of symmetry in the separation region just ahead of the injector. Virginia Tech, Mach 4.0, Pr=532, Primary jet only.....	183
Figure 6.5. Schematic of the flowfield generated by an under-expanded sonic jet exhausting in a quiescent medium [95].	184
Figure 6.6. Crossplane mappings of vorticity magnitude (left) and Mach number (right) with velocity vectors superimposed at a location of $x/d=15.00$ downstream of the injector. Virginia Tech, Mach 4.0, Pr=532. ($y/d: 0-10.0, z/d: 0-5.0$).	184
Figure 6.7. Crossplane mappings of vorticity magnitude (left) and Mach number (right) with velocity vectors superimposed at a location of $x/d=15.00$ downstream of the injector. Virginia Tech, Mach 4.0, Pr=532. ($y/d: 0-10.0, z/d: 0-5.0$).	185
Figure 6.8. Crossplane mappings of vorticity magnitude (left) with projected velocity vectors and Mach number (right) with velocity vectors superimposed at a location of $x/d=3.5$ downstream of the injector. Virginia Tech, Mach 4.0, Pr=532.	186
Figure 6.9. Crossplane mappings of vorticity magnitude (left) and Mach number (right) at different x/D . Virginia Tech, Mach 4.0, Pr=532. ($y/d: 0-32.0, z/d: 0-24.0$).	187
Figure 6.10. Blown-up crossplane mappings of vorticity magnitude (left) and Mach number (right) with velocity vectors superimposed at different x/D . Virginia Tech, Mach 4.0, Pr=532. ($y/d: 0-21.0, z/d: 0-10.0$).	189
Figure 6.11. Planar mappings of vorticity magnitude (left) and Mach number (right) at different heights over the flat plate surface (y/D). Virginia Tech, Mach 4.0, Pr=532. ($x/d: -8 \rightarrow 39.0, z/d: 0 \rightarrow 24.0$).	192
Figure 6.12. Streamlines above the flat plate simulating oil surface flow visualization with pressure coefficient mapping superimposed. Virginia Tech, Mach 4.0, Pr=532. ($x/d: -7 \rightarrow 40.0, z/d: 0 \rightarrow 24.0$).	195

List of Tables

Table 2.1 Computational work on Jet interaction flow fields.....	20
Table 5.1. Jet-interaction numerical simulations (a) laminar (b) turbulent (all turbulent calculations employed Wilcox’s $k-\omega$ turbulence model [91]).	53
Table 5.2. Summary of flow parameters.....	73
Table 5.3. Flat plate dimensions.	79
Table 5.4. Summary of flow parameters.....	80
Table 5.5. Flat plate dimensions for the Cubbison case.	87
Table 5.6. Summary of flow parameters for the Cubbison case.	88
Table 5.7. Comparison of the solution on the three grid levels with the solution obtained with the “Mixed 1 st +2 nd Order Extrapolation”. “ ϵ ” is the discretization error in the solution.....	90
Table 5.8. Comparison of the experimental to CFD force and moment for the Cubbison case.....	90
Table 5.9. Summary of flow parameters for the Letko experiments.	98
Table 5.10. Flat plate and injector dimensions for the Letko experiment.	98
Table 5.11. Comparison of the experimental to CFD force and moment for the Letko case with a discharge coefficient of 1.00.....	101
Table 5.12. Comparison of the solution on the three grid levels with the solution obtained with the “Mixed 1 st +2 nd Order Extrapolation” for the Letko case with a discharge coefficient of 1.00. “ ϵ ” is the discretization error in the solution.	101
Table 5.13. Comparison of the order of accuracy, p , calculated using the first three grid sequences and the last three grid sequences. Letko case with a discharge coefficient of 1.00.	101
Table 5.14. Comparison of the experimental and CFD force and moment for the Cubbison (laminar) and the Letko (turbulent) experiment.	108
Table 5.15. Comparison of the experimental to CFD force and moment for the Letko case with a discharge coefficient of 0.78.....	114
Table 5.16. Comparison of the solution on the three grid levels with the solution obtained with the “Mixed 1 st +2 nd Order Extrapolation” for the Letko case with a discharge coefficient of 0.78. “ ϵ ” is the discretization error in the solution.	114
Table 5.17. Summary of flow parameters for the Letko Multiple Jet case.....	118
Table 5.18. Flat plate and injector dimensions for the Letko Multiple Jet case.	118
Table 5.19. Comparison of the forces and moments for Letko case with only the primary jet and the Letko case with a simulated secondary injector.....	121
Table 5.20. Longitudinal distance (x) of the secondary injector groups from the primary injector. The distance is measured between the jet axes. The Mach 2.4 cases simulated the Primary jet alone, Primary +Group 1, and Primary + Group 1&2. The Mach 4.0 cases simulated the Primary jet alone and the Primary + Group 2.	123
Table 5.21. Summary of flow parameters for the Virginia Tech Mach 2.40 experiments.	126
Table 5.22. Flat plate and injector dimensions for the Virginia Tech experiment.	127

Table 5.23. Comparison of the solution on the three grid levels with the solution obtained with the “Mixed 1 st +2 nd Order Extrapolation” for the Virginia Tech case with a freestream Mach number of 2.40. “ ϵ ” is the discretization error in the solution....	129
Table 5.24. Increase in (a) normal force and (b) pitching moment due to the action of the secondary jets without taking into consideration the thrust of the jets. On the right column are the results from the experiment and on the left are the results from the numerical simulations. Virginia Tech cases with a freestream Mach number of 2.40. Note that $\delta C_{()}$ represents the augmentation of the parameter $C_{()}$ with respect to the case with the primary injector only. No jet thrust.....	130
Table 5.25. Increase in (a) normal force and (b) pitching moment due to the action of the secondary jets taking into consideration also the thrust of the jets. On the right column are the results from the experiment and on the left are the results from the numerical simulations. Virginia Tech cases with a freestream Mach number of 2.40. Note that $\delta C_{()}$ represents the augmentation of the parameter $C_{()}$ with respect to the case with the primary injector only. No jet thrust.....	131
Table 5.26. Comparison of the experimental to CFD force and for the Virginia Tech case with a freestream Mach number of 2.40.	143
Table 5.27. Flat plate and injector dimensions for the Virginia Tech experiment.	147
Table 5.28. Summary of flow parameters for the Virginia Tech Mach 4.0 (PR=532) experiments.	148
Table 5.29. Comparison of the solution on the three grid levels with the solution obtained with the “Mixed 1 st +2 nd Order Extrapolation” for the Virginia Tech case with a freestream Mach number of 4.0. “ ϵ ” is the discretization error in the solution.....	153
Table 5.30. Comparison of the experimental and numerical results for the normal force and pitching moment. Virginia Tech Mach 4.0, PR 532. The limit of integration for these calculations, in meters, are $-0.037 < x < 0.041$ and $-0.07 < z < 0.00$	161
Table 5.31. Increase in (a) normal force and (b) pitching moment due to the action of the secondary jets without taking into consideration the jet thrust. On the right column are the results from the experiment and on the left are the results from the numerical simulations. Virginia Tech cases with a freestream Mach number of 2.40. Note that $\delta C_{()}$ represents the increase of the parameter $C_{()}$ with respect to the case with the primary injector only.....	165
Table 5.32. Increase in (a) normal force and (b) pitching moment due to the action of the secondary jets taking into consideration the contribution of the jet thrust. On the right column are the results from the experiment and on the left are the results from the numerical simulations. Virginia Tech Mach 4.0. Note that $\delta C_{()}$ represents the increase of the parameter $C_{()}$ with respect to the case with the primary injector only.	165
Table B.1. Comparison of the solution on the three grid levels with the solution obtained with the “Mixed 1 st +2 nd Order Extrapolation” for the Virginia Tech case with a freestream Mach number of 2.40. “ ϵ ” is the discretization error in the solution....	213
Table B.2. Comparison of the solution on the three grid levels with the solution obtained with the “Mixed 1 st +2 nd Order Extrapolation” for the Virginia Tech case with a freestream Mach number of 4.0. “ ϵ ” is the discretization error in the solution.....	214

Nomenclature

Roman Symbols

a	Speed of sound	[m/s]
A	Plate area	[m ²]
C _{Fy}	Normal force coefficient	
C _{Fx}	Axial force coefficient	
C _{Mz}	Pitching moment coefficient	
C _p	Pressure coefficient	
D	Jet diameter	[m]
F _y	Normal force	[N]
F _x	Axial force	[N]
H	Height of the barrel shock from the tunnel floor	[m]
k	Turbulent kinetic energy (also TKE)	[m ² /s ²]
L	Axial (x-) length of plate	[m]
Ma	Mach number	
M _z	Pitching moment	[Nm]
P	Static pressure	[Pa]
P _o	Total pressure	[Pa]
Pr	Prandtl number (Pr _{Perfect Gas} =0.72)	
PR	Pressure Ratio (P _{o,j} /P _∞)	
Re	Reynolds number	
t	Time	[s]
T	Static temperature	[K]
T _o	Total temperature	[K]
u,v,w	Cartesian velocity components	[m/s]
x,y,z	Cartesian coordinates	[m]

Greek Symbols

β	Angle between the zero-C _p line and the tunnel centerline	[Deg]
δ	Boundary layer thickness	[m]
ε	Turbulence dissipation rate	[m ² /s ²]
γ	Specific heat ratio (γ _{Perfect Gas} =1.40)	
λ	Second bulk viscosity coefficient	[Ns/m ²]
μ	Laminar (molecular) viscosity (First bulk viscosity coefficient)	[Ns/m ²]
μ _T	Turbulent (eddy) viscosity	[Ns/m ²]

ν	Kinematic viscosity	$[\text{m}^2/\text{s}]$
θ_1	Inclination of the bow shock to the tunnel floor	$[\text{Deg}]$
θ_2	Inclination of the barrel shock to the tunnel floor	$[\text{Deg}]$
ρ	Density	$[\text{kg}/\text{m}^3]$
τ	Shear stress	$[\text{N}/\text{m}^2]$
ω	Turbulent frequency	$[\text{m}^3/\text{s}^3]$

Subscripts

j	jet condition
jet	jet condition
inf	freestream condition
∞	freestream condition
wall	wall condition
*	non-dimensionalized value

Superscripts

\sim	Mean Value of Favre'-averaged Variable
-	Time-averaged Values
“	Fluctuating Value of Favre'-averaged Variable

Chapter 1

Introduction

1.1 Background

The jet interaction flow field produced by a jet exhausting in a crossflow (see Figure 1.1 for a schematic) is a complex fluid dynamics problem that can be found in several real life applications. Reference [1] gives an ample and detailed review of the field. Examples of applications of the jet interaction principles range from the very low-speed regimes of a chimney plume in a crossflow to the very high-speed of scramjet combustion and hypersonic missile control systems, from the low mass flow of boundary layer control systems to the high mass flow of V/STOL aircraft [1]. The basic problem of a gas injected into a crossflow has several variations depending on the application it is used for [1]. Examples of these variables are the yaw angle and the pitch angle of the injector, the flow conditions of the jet (subsonic, choked, supersonic), and on the freestream conditions (subsonic, supersonic, laminar, turbulent), not to mention the chemical composition of the gases (single or multiple-phase, non-reacting mixture, reacting mixture etc.).

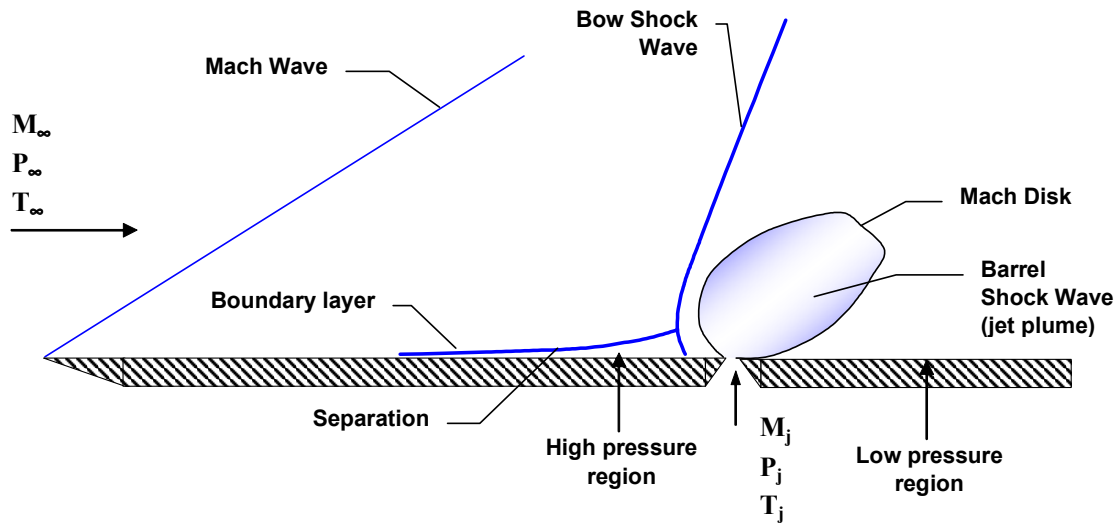
The present study focuses on the case of normal injection of a perfect gas through a sonic circular jet into a perfect gas supersonic turbulent crossflow. This configuration is representative of a typical exterior arrangement of reaction control systems installed on the hypersonic vehicles such as experimental aircraft (e.g. North American X-15), re-entry vehicles (e.g. Space Shuttle, any future re-usable launch system, ICBMs) and missiles (e.g. National Missile Defense interceptors or other high-altitude SAMs). Note that when jet thrusters are used for directional control, they are usually applied on the outside surface of the vehicle. However, thrusters can also be used as directional control units when they are inserted in the exhaust nozzle of a rocket-powered vehicles [86]. In this application, a secondary jet is introduced into the primary exhaust flow of the nozzle. The jet interaction of the secondary jet with the primary flow creates an asymmetric thrust and therefore a force normal to the flight direction of the vehicle. This normal force is usually larger than the thrust of the secondary jet.

The main reasons for the use of reaction control systems on these fast-moving vehicles lie in the large forces that can be produced by jet thrusters and by their fast reaction time. Both of these characteristics of reaction control systems are essential when the medium the vehicle is moving in is very rarified making conventional control surfaces ineffective and when trying to intercept an extremely fast-moving object with a fast-moving interceptor. The extremely low-density of the upper layers of the atmosphere brings the flow conditions near the theoretical boundary between the continuous flow and slip flow conditions. In this study, continuous flow is assumed to exist for all the test conditions

examined. In reaction control systems, normal injection is usually chosen over angled injection because it maximizes the lateral force produced by the thrust of the jet. Two primary mechanisms contribute to the production of the lateral force. The first contribution comes from the thrust produced by the jet (remember that the thrust is simply the momentum of the injectant plus the pressure force acting on the cross-sectional area of the injector exit). The second contribution is a subtler one and is produced by the complex interaction of the jet with the cross-flow. In fact the injected gas acts as an obstruction to the primary flow and, as such, produces a shock wave in the primary flow (see Figure 1.1). The shock wave produces an adverse pressure gradient that causes the boundary layer on the wall to form a separation region ahead of the injector. The high pressures typical of recirculated flows (see pressure plot of Figure 1.2) augment the lateral force produced by the thrust of the jet. Therefore, a jet operating with a crossflow will produce a larger force than if it was exhausting into a quiescent medium. However, at the same time, a large low-pressure region forms aft of the injector (Figure 1.2). The low-pressure region has two main effects on the forces and moments produced by the jet on the flat plate. The first effect is to decrease the normal force on the plate created by the combined effects of the thrust of the jet and of the high-pressure region ahead of the injector. Note that the low-pressure region effectively creates a suction behind the jet. Even though the pressure is not significantly lower than freestream pressure, it acts over a large area behind the injector, thus creating a strong negative force. The second and in many aspects most detrimental effect is to form a couple with the high-pressure region ahead of the jet to produce a nose-down moment about the injector. The contribution to the nose-down moment from the low-pressure region is particularly high since, as mentioned above, this region extends far aft of the injector, therefore its moment arm is relatively large.

1.2 Flowfield Description

A better understanding of the flowfield created by the jet interaction is obtained when the problem is analyzed in three dimensions. To simplify the problem and to highlight the basic physics that govern the problem, we considered here the injector in a flat plate instead of a body of revolution. A typical static pressure distribution along the plate centerline associated with the three-dimensional jet interaction field is shown in Figure 1.2. A schematic of the three-dimensional flow field formed by normal injection into a supersonic cross flow over a flat plate is shown in Figure 1.5. This flowfield model was created after the description of Santiago and Dutton [63] and Chenault, et al. [15] and Wallis [84][85] and after analyzing several of the flowfields obtained from the numerical simulations presented in this work. The injected gas enters through a circular sonic nozzle at a much higher static pressure than the freestream. The gas immediately expands through a Prandtl-Meyer expansion fan and is turned downstream by the incoming crossflow. The over-expanded gas is recompressed through a barrel shock wave and a Mach disk, and trails in the jet plume far downstream of the injection location.



$$\text{Jet Pressure ratio (PR)} = P_{T,j}/P_{s,\infty}$$

Figure 1.1. Schematic cut along the tunnel centerline. The definition of the jet pressure ratio (PR) as given by Cubbison [22] is consistently used as the primary injection parameter all through the present work.

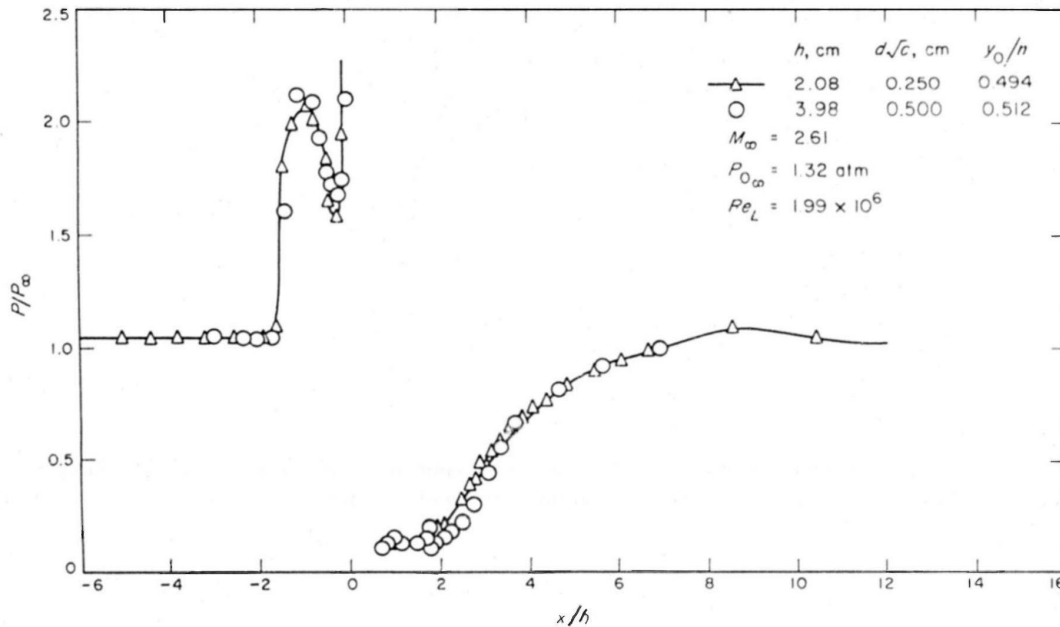


Figure 1.2. Typical pressure distribution along the plate centerline for a three-dimensional jet interaction flowfield created by the normal injection of a gas into a supersonic crossflow. From the experimental work of Spaid, et al. [70].

A system of five pairs of counter-rotating vortices form in the recirculation region, along the barrel shock wave and immediately downstream of the Mach disk (see Figure 1.4). Of these ten vortices, eight form in the recirculation region and the other pair is formed by the recompression in the Mach disk (the so-called kidney-shaped vortex). The horseshoe vortex and the trailing upper vortex systems form and immediately move away from the centerline of the plate. The horseshoe vortex moves along the solid surface and away from the symmetry plane while the upper vortex moves along the symmetry plane and away from the flat plate surface (see Figure 1.4). The longitudinal vortices form in the recirculation region but gain in strength as they are convected downstream and upwards along the barrel shock plume. The trailing lower vortices also form in the recirculation region but remain close to the flat plate surface and to the tunnel centerline. The kidney-shaped counter-rotating vortices form downstream of the jet plume and are the major contributor to the mixing of the injectant with the freestream (mainly by entrainment of the freestream in the vortices). Both the horseshoe and the upper vortex systems trail downstream isolated from other vortex systems not mixing with the other vortices, therefore they remain clear and easy to locate far downstream of the injection location. The lower trailing vortex remains attached to the solid surface as it entrains fluid from the surrounding boundary layer. The other two vortex systems, the longitudinal, and kidney-shaped vortex systems, merge aft of the Mach disk into one strong vortex with its core trailing downstream along a constant cross-plane location.

As discussed for the description of the flow along the tunnel centerline (Figure 1.1 and Figure 1.2), the barrel shock wave creates an obstruction to the crossflow. The similarity between the jet plume and a solid obstruction to the flow is such that analytical models of the jet interaction problems proposed by Zukoski and Spaid [70] and Glagolev, Zubkov and Panov [30] and Voitenko, Zubkov and Panov [83] actually approximated the shock patterns produced by the injection of a gas with those produced by blunt axi-symmetric solid bodies. Such an obstruction creates a region of very high-pressure gradients where the boundary layer separates. Depending on the type of incoming boundary layer, the separation will have different characteristics. A laminar boundary layer produces a separation region that extends further ahead of the injector than a turbulent boundary layer. However, the separation region for the laminar boundary layer is thinner and with lower static pressures than for a turbulent boundary layer. The fluid in the recirculation region cannot flow directly downstream along the tunnel centerline due the obstruction of the jet plume. This trapped fluid, therefore, forms a horseshoe vortex that starts in the recirculation region and trails downstream on both sides of the barrel shock (Figure 1.5). The rapid expansion of the injectant creates regions of flow with very high Mach number.

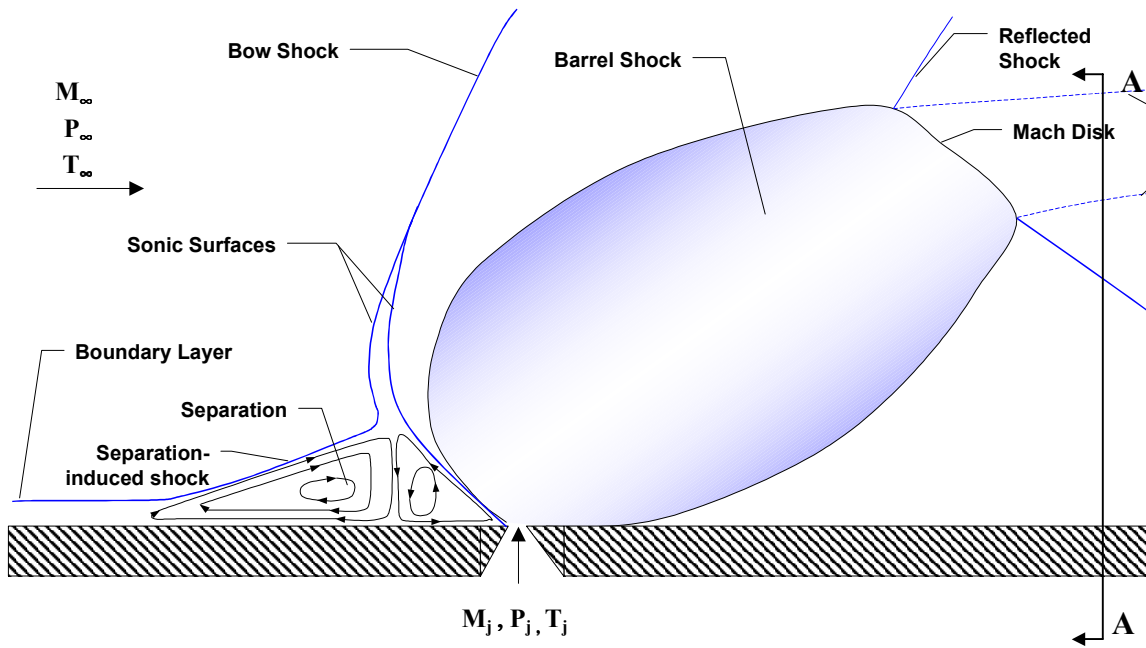


Figure 1.3. Detail of the separation-jet plume region along the tunnel centerline.

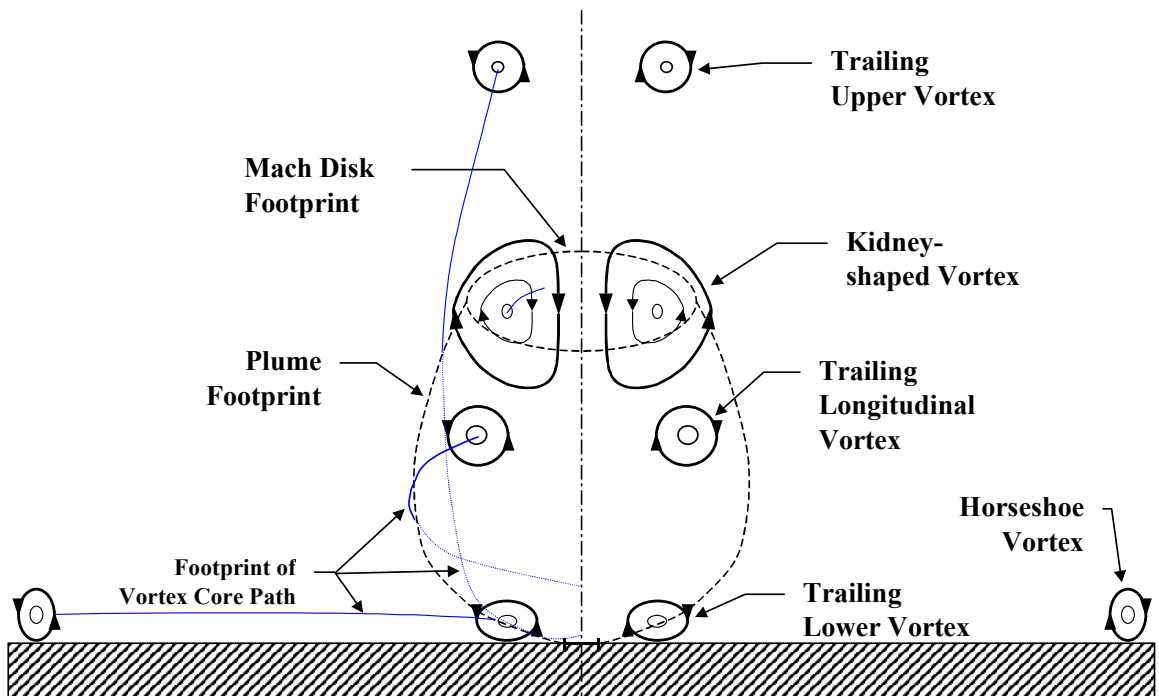


Figure 1.4. Schematic view of the flowfield at section AA (Figure 1.3).

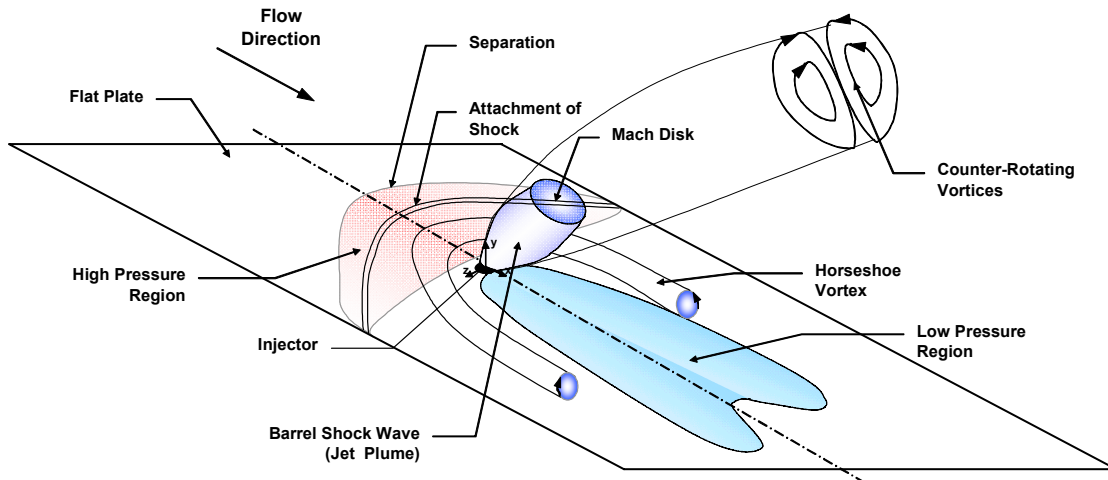


Figure 1.5. Three-dimensional schematic view of the jet interaction problem with a single circular jet normally injecting into a supersonic cross flow.

1.3 Motivation

As mentioned above, in control systems applications, the region of negative pressure aft of the primary jet causes both a decrease in the normal force (F_y) and a nose-down pitching moment acting on the vehicle (see Figure 1.6). The decrease in normal force can be easily compensated for by increasing the total thrust of the jet. On the other hand the nose-down pitching moment cannot be corrected so easily. To counterbalance the nose-down moment, it is necessary either to suppress the nose-down moment itself or to create a nose-up moment that will cancel out the nose-down moment on the vehicle. The most intuitive way to create a nose-up moment, is to add a thruster far aft of the center of gravity of the vehicle. This design philosophy is applied to modern hypersonic vehicles and it has been proven to work. However, this configuration has some drawbacks. The main one is the additional complexity and cost associated with the second thruster. The additional nozzle would be roughly the same size and mass as the main thruster, thus increasing the fuel requirements for the control system and decreasing the useful payload of the vehicle. For missiles other issues associated with a large secondary jet located far aft of the main injector concern the packaging of the control system in a very tight space and the breaking up of a large payload bay into two separate sections by the insertion of a secondary thruster.

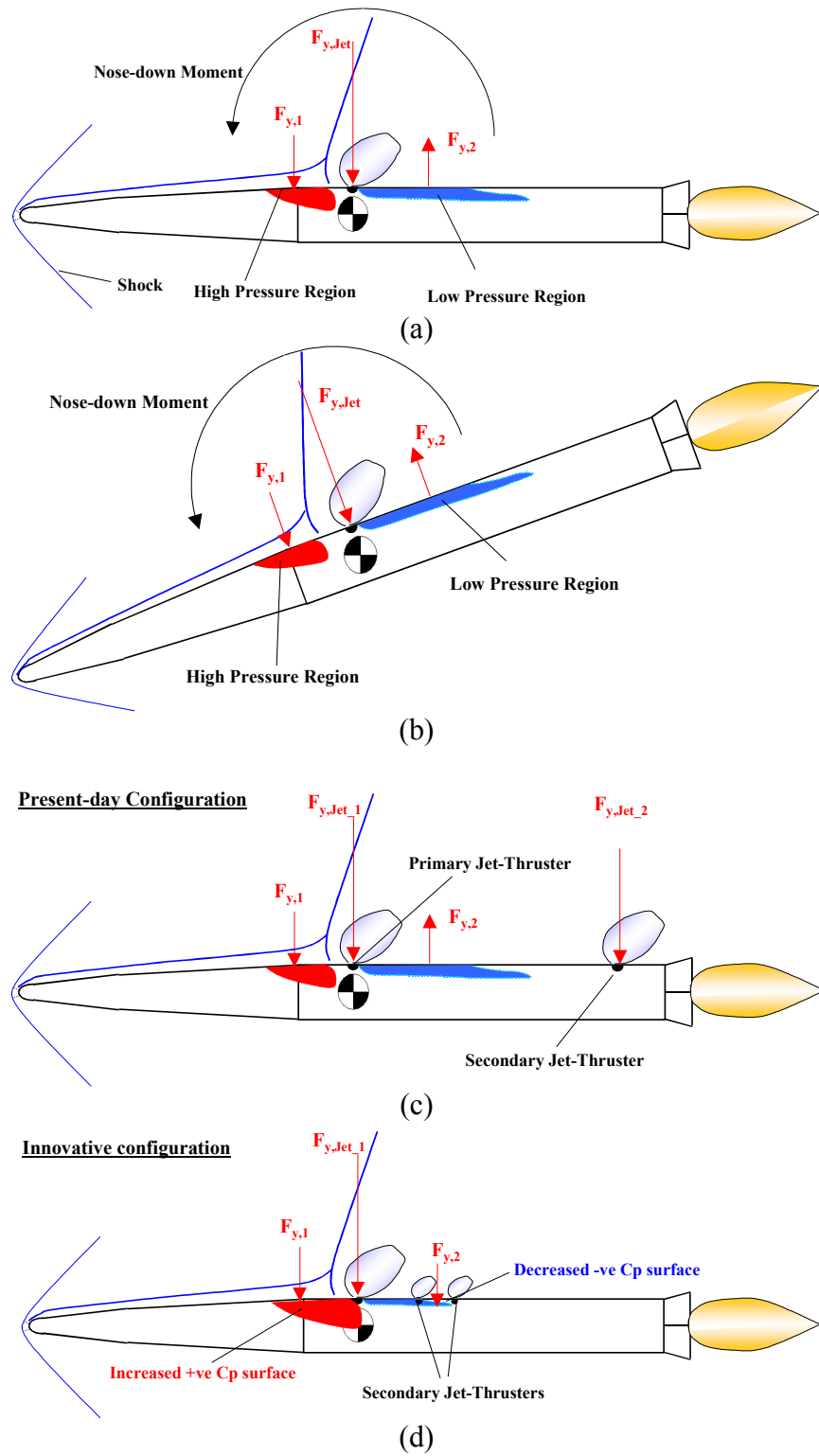


Figure 1.6. (a) Model of the effect of a jet thruster on a hypersonic vehicle. (b) The effect of the nose-down moment. (d) Modern control system configuration. (e) Innovative configuration.

A way to eliminate the disadvantages of the double-thruster configuration is to develop a design with a single thruster that minimizes or cancels the region of negative pressure aft of the injector. In 1998, a team at Virginia Tech, (J. A. Schetz, S. Cox-Stouffer, R. Fuller [67]) while performing experimental work in fuel mixing for scramjet engines discovered an interesting feature of multiple-injector configurations. In an array of jets located to form an “aerodynamic ramp”, the influence of the injectors located in the second row of the array was to suppress the area of negative C_p behind the first row of injectors. This finding suggested that a secondary jet, smaller than and carefully located behind the primary thruster, could help reduce the region of negative C_p and in this way it could obviate the aforementioned problems created by the use of two similarly sized thrusters. A study was then initiated in the Aerospace and Ocean Engineering Department of Virginia Tech to determine the feasibility of the idea, to study the fluid dynamics phenomena governing the flow-field, and to establish the optimal location of the secondary jets. The effort was both experimental, taking advantage of the availability of the supersonic wind tunnel in the Aerospace and Ocean Engineering Department at Virginia Tech, and numerical, using the computing resources of the Interdisciplinary Center for Applied Mathematics (ICAM) of Virginia Tech and of AeroSoft, Inc. This work concerns the Computational Fluid Dynamics (CFD) aspect of the study.

1.4 Approach to the problem

The combined effort of an experimental and a computational investigation to study fluid phenomena seems a logical choice when dealing with very complex flowfields such as the three-dimensional jet interaction one (see Ref. [67]). While experiments provide data about the flow, they often lack the possibility of having a direct and detailed insight into the physics of the flowfield. Often the physics of the flow are indirectly inferred from the experimental measurements of mean flow variables or of surface conditions. However, this method leaves quite a large uncertainty about the exact nature and the interaction of the phenomena that ultimately produce the data measured by the experimentalist. The shortcomings of the experimental data are due both to the inherent nature of experimental work and to the technological limitations of the measuring techniques and equipment. An example of the first category of problems affecting experimental work is the need to insert a probe to obtain measurements of the pressure at a given location in a flowfield. The probe itself alters the flowfield and hence the data that it is supposed to measure. These types of problems that the experimentalist faces have been and are often solved by the development of new measuring techniques or more advanced measuring equipment. An example is the advent of Laser Doppler Velocimetry, a non-intrusive measuring technique that allows the measurement of the velocity almost everywhere in the flowfield without the need of an intruding Pitot tube. Another example is the advent of the Pressure Sensitive Paint (PSP) that allows a continuous mapping of the pressure field on a solid surface. Before the PSP became practical, an experimentalist would have tried to create a pressure mapping on a solid surface by using a large number of pressure orifices embedded in the surface. Each orifice would have produced a discrete data-point and the

whole collection of pressure data would have provided the researcher with a crude description of the rapidly varying pressure field.

On the other hand, numerical simulations produce a continuous solution all through the computational domain. In this way, any flow variable can be probed at any point of the flowfield and mappings can be produced on any real surface or imaginary cutting plane. This almost infinite wealth of information generated by a CFD solution provides the researcher with a deep insight into the flow physics and therefore a better understanding of those processes and their interaction that ultimately produce the phenomena the experiment can measure. Furthermore, numerical simulations offer the advantage of reduced costs and, often, reduced times between the generation of a design and the preliminary results when compared to experiments. However, numerical simulations too are affected by some drawbacks and are far from being a perfect tool that can replace experiments. The main problem of numerical calculations is the simulation of turbulence. Common numerical models simulating turbulence are based on the Boussinesq approximation and are defined as “first-order models”. The fundamental assumption of the Boussinesq approximation states that “the principal axes of the Reynolds stress tensor, τ_{ij} , are coincident with those of the mean strain-rate tensor, S_{ij} , at all points in a turbulent flow...[and], the constant of proportionality between τ_{ij} and, S_{ij} , is the eddy viscosity, μ_t ”[91]. First-order turbulence models can be further divided into three other sub-groups, depending on the number of equations used to simulate turbulent phenomena: zero-equation (algebraic) models, one-equation models and two-equation models. The implementation of a turbulence model in a numerical code requires the solution of extra equations in addition to the five basic Navier-Stokes equations. A one-equation turbulence model will require the solution of the five Navier-Stokes equations plus a single equation for the turbulent quantity. Similarly, the implementation of a two-equation model will require the solution of a total of seven equations. In general the more equations are used to simulate turbulence, the more accurate the model, and the more computational resources are needed. One step more complex than the first-order models are the second-order models, such as the Reynolds Stress turbulence model, that do not use the Boussinesq assumption and model each component of the Reynolds Stress tensor individually. The implementation of second-order models in numerical codes need the solution of the five Navier-Stokes equations plus six equations for the Reynolds stress tensor (one equation per component) and one equation for the turbulence length scale, for a total of twelve coupled equations. First-order models have been extensively used by the engineering community since they provide reasonably accurate turbulence predictions when used for specific flow fields and, more important, because they require significantly less computational resources than second-order models. As computational speed, memory and archival resources of computers have been increasing over the past years, the trend in the engineering community has been to routinely use more complex and more capable turbulence models. When initial jet interaction simulations were attempted in the late 80’s and early 90’s [89][78][17][94] the turbulence model used was the zero-equation Baldwin-Lomax [8]. Later, most of the jet interaction simulations used either the one-equation model of Spalart-Allmaras or different two-equations models such as the k - ϵ or the k - ω models. Only recently, researchers have also made use of Reynolds Stress

models [14][15][16] to simulate turbulence in jet interaction flowfields. However, the use of second-order turbulence models is still very limited, mainly because the required additional computational resources make this class of turbulence models impractical for routine engineering use. The present work makes use of the Wilcox 1988 $k-\omega$ turbulence model [93]. The $k-\omega$ turbulence model was chosen over other two-equation turbulence models because of its better performance in wall-bounded and free-shear compressible flows. Also, it adds only two equations for turbulence modeling to the set of the five Navier-Stokes equations, thus keeping the need for computer resources lower than a Reynolds Stress model which would have required seven additional equations for turbulence modeling. Furthermore, the goal of this investigation is to provide a better understanding of the flow physics that affect the forces and moments on the solid surface. These integrated quantities and the macro-scale flow structures that produce them are not so greatly affected by the individual component of the turbulent Reynolds stresses as to require the additional complexity and cost of second-order turbulence models. This study used the CFD code General Aerodynamic Simulation Program (GASP) developed by AeroSoft Inc., in both the 3.2 and 4.0 releases. The code solves the RANS equations numerically and it offers the choice of several first-order turbulence models. Note that the use of the RANS equations implies that a continuous flow is assumed to exist for all the test conditions under consideration.

1.5 Objectives

The main objectives of this study were:

- 1) Assess the capability of CFD codes that solve the Reynolds averaged Navier-Stokes (RANS) equations with a practical turbulence model to properly simulate the physics of the three-dimensional jet interaction flowfield.
- 2) Gain a better understanding of the jet interaction flowfield created by a single sonic jet and by multiple sonic jets exhausting normally into a supersonic cross flow through the use of numerical simulations.
- 3) Use the numerical simulations to assess the validity of the proposed idea to use a multiple-jet configuration to improve the design of present-day jet thrusters.
- 4) Support the jet interaction experiments performed at Virginia Tech by providing an insight into the flow physics in order to interpret more effectively the experimental data.

1.6 Overview of the Document

This document starts with a description of the jet interaction problem, its relevance for selected aerodynamics applications and the problem related to its implementation. Following the current section is a review of the relevant research work in jet interaction flowfields of the past sixty years. The review is divided into two parts, one dealing with experimental and analytical studies and the other dealing with numerical simulations. More specifically, this collection of past works focuses on those studies that considered the jet interaction flowfield produced by reaction jet control systems rather than by fuel injectors.

The section after the review of the past work deals with the governing equations, namely the Navier-Stokes equations (NS), the averaging of these governing equations using Reynolds and Favre' averaging procedures to reduce the NS equations to the Reynolds Averaged Navier-Stokes equations (RANS) and the turbulence modeling. The NS equations are derived in the conservative form and are re-arranged in the matrix form which is more convenient when solving them numerically. Turbulence modeling and the closure problem are described and discussed in this section and the $k-\omega$ turbulence model is presented in more detail, being the model consistently used in this work. Also, the numerical code used to numerically solve the finite volume form of the RANS, AeroSoft's GASP, is presented.

The Results section presents the main computational results and their comparison to the experimental data. The results are presented in a logical order (that also matches the chronological order) starting with the preliminary laminar-flow jet interaction calculations simulating the Schetz [65] experiment, with a pressure ratio of 60, and the Cubbison experiment [22] with a pressure ratio of 677. Then, the first turbulent-flow jet interaction calculation performed in this study is presented. This calculation simulated the Letko experiment [42] with a pressure ratio of 680. The exhaustive grid-convergence study performed on the Letko case is shown in this section together with the simulation of the nozzle flow performed to estimate the discharge coefficient of the injector. Finally, the calculations simulating the Virginia Tech experiments are presented [84] [85]. Two sets of computations were run: the first one simulating the Virginia Tech cases with a freestream Mach number of 2.4 and a pressure ration of 14.0 and the second one simulating the Virginia Tech cases with a freestream Mach number of 4.0 and a pressure ratio of 532. In both cases the results of the numerical simulations run with only the primary jet and with both the primary and one or two secondary jets are presented. The CFD results for the case with only the primary injector are compared with the CFD results for the cases with the primary and one or two secondary jets. The numerical solutions are also compared to the experimental results. The comparison involves several parameters: the forces and moments, the pressure mappings on the surface of the flat plate, the flowfield features visible in Schlieren photographs. The Results section is concluded with a deeper study of the physics involved in the jet interaction flowfield.

The last chapters of the document are the Conclusions section, in which the major finding of the study are summarized and recommendations are made for future studies and the Bibliography. An appendix section follows with the presentation of raw data and of some additional research activity performed during the evolvement of this study.

Chapter 2

Literature Review

As discussed in the previous section, jet interaction flowfields are encountered in a large range of practical applications. At the extremes of this range there is the very low-pressure ratios and low crossflow velocity encountered in the case of a smokestack with a crosswind and, at the other extreme, the very high-pressure ratios and high Mach number encountered in reaction control systems. However, many of the studies of jet interaction flow-fields concern fuel injection in ramjet and scramjet engines. These fuel injection cases include injection with normal or angled injection, subsonic, sonic or supersonic nozzle conditions and, usually, supersonic crossflow. Often, it is difficult to discern or precisely categorize the range of applications a jet interaction test case can apply to. The imaginary boundaries that define the conditions for which a jet can be used in fuel injection applications overlap those defining the regime in which a jet is used as a reaction control system. Also, many of the flow structures observed with the lower-pressure ratio injection cases are essentially the same for higher-pressure ratios, the main difference being the intensity level at which they occur. An example of the overlapping of the fuel-injection regime with the jet-thruster regime, at least in the research field, is the work of Clark and Chan [17] that, in spite of the low-pressure ratio of the jet interaction case they considered, was intended as a study of supersonic aerodynamic control.

2.1 Experimental Work

As is often the case in engineering, many numerical calculations simulate physical problems that were extensively studied with experiments and analytical models before the advent of modern computational capabilities. The jet interaction problem is no exception to this pattern. In particular, the jet interaction problem with a supersonic crossflow and a sonic or supersonic jet started to raise interest in the scientific community after the Second World War. The interest was stirred by the advent of supersonic, and eventually hypersonic flight with re-entry vehicles and the related requirement for powerful control systems that would be effective also in the thin air of the upper atmosphere. At the same time, progress in rocket design made quantum steps thus favoring the use of small rockets as control system thrusters. Preliminary work was performed by the then young NASA in 1959 on a body of revolution [37][82], but it was not until the work of Cubbison in 1960 [22] that a more thorough study of the jet interaction problem was performed.

Cubbison studied the jet interaction problem of a sonic jet exiting normal to the surface of a flat plate and an arrow wing in a crossflow with a laminar boundary layer, Mach

numbers that ranged from 2.92 to 6.40 and pressure ratios that varied from 677 up to 5,453. Cubbison reported pressure coefficient (C_p) mappings and C_p plots along the tunnel centerline for several pressure ratios and two freestream Mach numbers. His definition of pressure ratio (PR) as the ratio of the jet total pressure to the freestream static pressure is used consistently through the present work. Also, he published Schlieren photographs of the interaction flow. He concluded that freestream Mach number had a large effect on the pressure level whereas the pressure ratio greatly affected the pressure field distribution. On the other hand, effects of Reynolds number at constant pressure ratio seemed to be very limited. He also concluded that since the interaction field can be extensive, in any application it would be necessary to know the detailed vehicle geometry to estimate the overall degree of thrust augmentation.

Letko in 1963 [42] tested the effects of sonic and supersonic jets injecting normal to a flat plate with a turbulent boundary layer and a freestream Mach number of 4.5 over a range of pressure ratios. He reported C_p plots along the tunnel centerline and pressure mappings on the flat plate and computed the thrust augmentation created by the jet interaction. He concluded that a supersonic nozzle is more effective than a sonic nozzle as a control thruster and, very relevant to the present study, he discussed the benefits of eliminating the areas of negative C_p behind the injector. In particular, he estimated that a 12% increase in effectiveness could be attained by eliminating the zones of negative C_p . To attain such a goal he suggested cutting the plate following the zero- C_p contour.

Both the Cubbison and the Letko experiments were aimed at an estimation of trends in forces and pressure fields as the flow parameters were changed. No detailed study of the flowfield or an analysis of the flow physics was attempted. In 1963 and 1966, a joint effort of the Jet Propulsion Laboratory and Caltech led by Spaid and Zukoski [70] [100] provided an extensive and detailed study of the jet interaction problem. They used normal sonic injection of Nitrogen, Argon and Helium through a circular port into a freestream Mach number of 1.38, 2.56 (with laminar or turbulent boundary layer) and 4.56 (turbulent boundary layer only). The pressure ratio was changed as well as the injector diameter. The primary goal of their work was to obtain fundamental information about the jet interaction problem and to develop an analytical model of the process that could correlate the flow conditions and a scaling parameter to the forces on the flat plate. They were partially successful, since the correlation they developed would work well for a very restricted number of cases, only for some flow regions and for turbulent boundary layers only. However, the extensive amount of pressure data, Schlieren photographs and velocity profiles they reported form an excellent database for the validation and comparison of jet interaction numerical calculations [14]. Also, they briefly experimented with multiple (two) injectors [70] of equal dimensions and with the centerlines aligned normal to the flow direction. They concluded that the interaction of the two jets increased the values in the region of high- C_p ahead of the injectors and decreased the values in the region of low- C_p behind the injectors.

In 1963, Strike and Schueler [72] experimented with slot (i.e. two-dimensional), single and multiple circular injectors with sonic conditions on a flat plate and an ogive in a supersonic crossflow. They successfully developed a method to estimate, within generous

error margins, the normal force on the flat plate. They initially approached the jet interaction problem in two dimensions and developed a force-correlation formula that combined the inviscid normal force contribution (basically the force produced by a lateral jet without an approaching boundary layer) with the viscous contribution (i.e. the force produced by the boundary layer separation). They then extended the model to three dimensional flow fields. This work also determined the importance of three-dimensional effects on the force on the flat plate and the strong influence on the normal force of the type of boundary layer (with laminar boundary layers producing higher normal forces than turbulent ones).

An attempt to develop an analogy between the well-understood case of an under-expanded jet in a quiescent medium and the jet interaction problem was done by Schetz, et al. in 1966 [65]. In this work, Schetz proposed the use of the “effective back pressure”, previously introduced by the same author [66], as the correlation parameter. However, the correlation focused on the penetration and structure of the jet plume for fuel injection applications rather than on the pressure distribution and the forces acting on the flat plate. For this reason, the paper reported a Schlieren picture of the laminar jet interaction case under study (freestream Mach number of 2.1 and a pressure ratio of 60) but not the corresponding pressure data. The laminar boundary layer and the low-pressure ratio used in this work made it suitable to be used in the initial stages of this study as a trial calculation. The preliminary simulation of this case was used to assess the capability of the numerical code of simulating three dimensional jet interaction flow-fields.

A large amount of experimental data was accumulated between 1968 and 1979 by Russian researchers at the Institute of Mechanics of the University of Moscow. Glagolev, et al. [30] performed a detailed study of the three-dimensional jet interaction flow field. Analyzing the case of normal sonic injection into a Mach 3 flow with turbulent boundary layer and using pressure measurements and flow visualization (Schlieren photographs and oil patterns on the flat plate) they were able to produce a detailed model of the flow field (see Figure 2.1). In particular, they described the mechanism that forms the horseshoes vortices ahead of the injector and the absence of a recirculation region immediately aft of the injector due to the expansion of the injectant. In another publication Glagolev, et al. [31] focused on the structure of the jet instead of the external flow-field. They managed to successfully correlate the geometry of the jet plume to the pressure ratio, but no attempt was made to describe the complex system of expansion fans and compression shocks within the jet. Zubkov, et al. [99] studied the effects of boundary layer thickness and surface curvature for the three-dimensional jet interaction problem. Their work concluded that as the boundary layer thickness is increased, the extent of the separation region ahead of the injector increased while the peak pressure along the tunnel centerline decreased. Also, they established that the jet interaction flow field produced by a jet on curved surfaces is qualitatively the same as that produced on a flat plate. However, they differ quantitatively, a negative curvature producing a stronger separation and therefore higher forces than a positive (i.e. a cone) curvature. Finally, they analyzed the effect of injector inclination to the freestream; their conclusion was that the

maximum force magnification is obtained when the injector is inclined to the flat plate surface at an angle of 63° (the normal injection case being inclined at 90°).

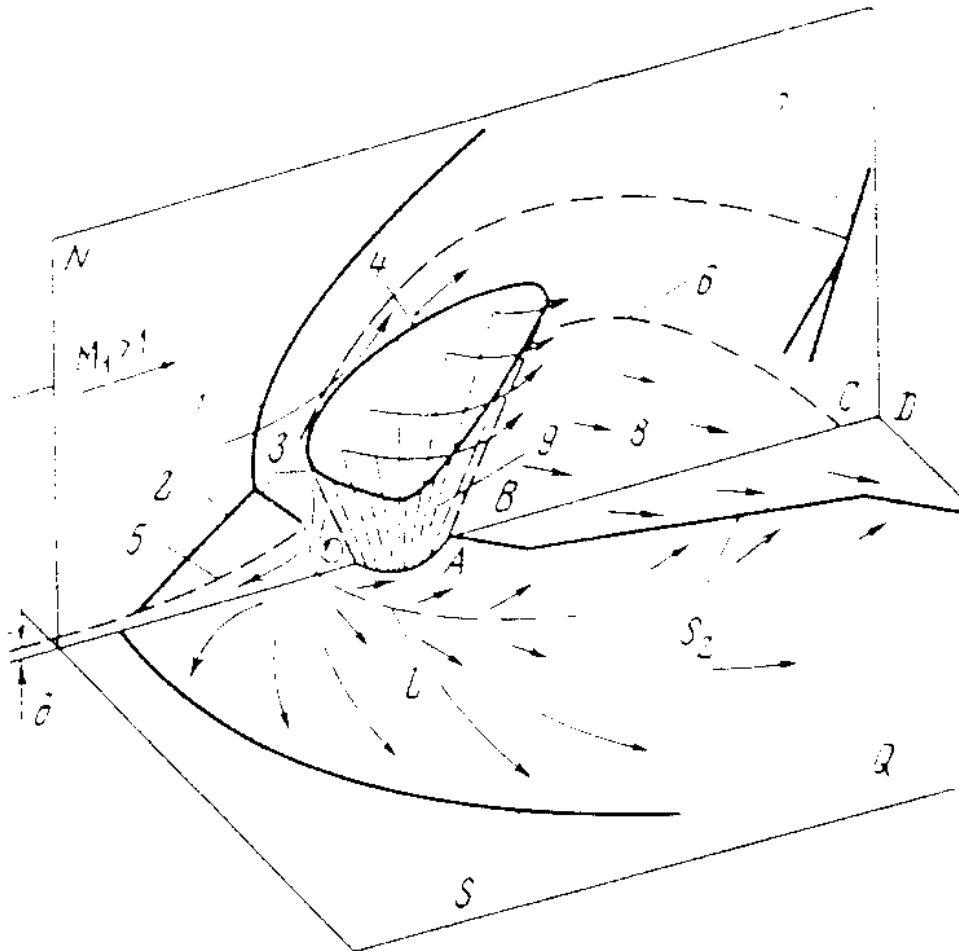


Figure 2.1. The three-dimensional schematic view of the jet interaction problem with a single circular jet normally injecting into a supersonic cross flow as proposed by Glagolev, et al. [30].

Aso, et al. in Japan carried out an extensive experimental investigation of the two- and three-dimensional jet interaction flow-field on a flat plate. In particular, they wanted to produce a pressure and geometry database for numerical code validation. In 1991, they started analyzing the two-dimensional jet interaction flow field on a flat plate [5]. They investigated the effects of changing the pressure ratio as well as changing the slot width. They reached the conclusion that for the same nozzle geometry, as the pressure ratio was increased the shape of the bow shock wave, Mach disk and barrel shock were kept in geometric similarity. The separation region increased in extent with increasing pressure ratio, linearly for the lower pressure ratio range and then for the higher-pressure ratio range not linearly. As reported by Chenault, et al. [14], the Aso experiment was probably affected by three-dimensional effects and the pressure orifice system in the flat plate was

not adequate to produce a detailed pressure plot. In fact, the Aso experiments failed to capture the pressure peak just ahead of the injector for the lower pressure ratio range. In 1993, Aso, et al. [6] [7] extended the database for two-dimensional jet interaction flow-fields to include three-dimensional ones. Through the use of Schlieren photographs, surface oil-flow visualization and pressure mappings they assessed the large differences between two and three-dimensional jet interaction flow fields and located the existence of a horseshoe vortex emanating from the separation region ahead of the injector. They also investigated the effect of injecting nitrogen versus helium concluding that qualitatively the flow-field remained the same, even though the Helium produced smaller separation regions than the nitrogen for the same conditions.

A more recent body of work is that produced by researchers in the Department of Mechanical Engineering at the University of Illinois at Urbana-Champaign. VanLerberghe, et al. [79] used surface oil flow visualization, planar Mie scattering and planar laser-induced fluorescence to qualitatively study the jet interaction flow-field created by normal injection of a single sonic nozzle into a Mach 1.6 crossflow. Their study confirmed the existence of a horseshoe vortex ahead of the injector as well as a primary and a secondary recirculation region. The flow-field was found to be independent of the injected gas as long as the momentum ratio (i.e. the ratio of the momentum of the jet to the momentum of the crossflow, $(\rho V^2)_{Jet}/(\rho V^2)_{\infty}$) was kept constant. They observed large turbulent structures at the interface between the jet and the crossflow that tended to penetrate far into the crossflow and to engulf large portions of it. The shape and rotation of these structures were an indication that the jet fluid was moving faster than the crossflow fluid at the interface. Also, the flow-field was found to be highly symmetric in the spanwise direction and, quite surprisingly and in disagreement with previous observations [53], steady. Santiago and Dutton [63] used Laser Doppler Velocimetry (LDV) measurements of the mean velocity fields to study the development of the crossflow vortices. They developed the three-dimensional jet interaction model shown in Figure 2.2 and focused on the streamwise development of the counter-rotating “kidney-shaped” vortex pair generated by the jet plume. They asserted that this pair of vortices is the primary source of entrainment of the surrounding inflow air into the injectant. Also the crossflow vector fields showed how the two kidney-shaped vortices are constrained by each other and by the wall in the near jet region and as they are convected downstream and move away from the wall they become elliptical in shape and behave more like free vortices. Importantly, they measured an asymmetry in the up-wash velocity of the vortices about the vortex core. The vortex asymmetry was attributed to the fact that the flow is highly three-dimensional and compressible.

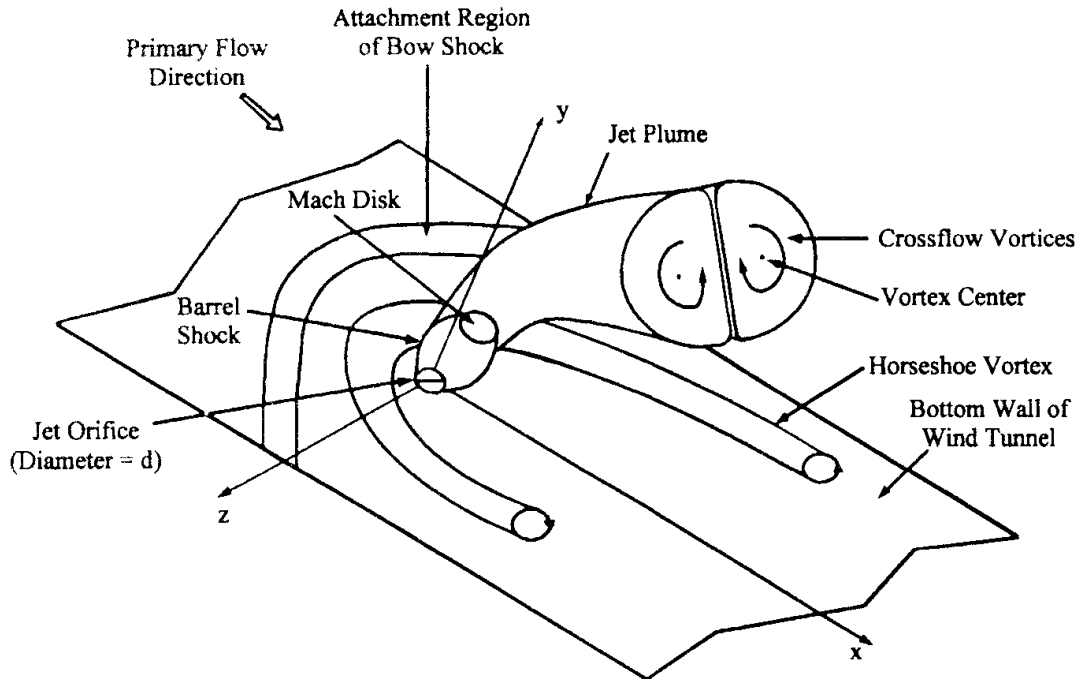


Figure 2.2. Three-dimensional schematic view of the jet interaction problem with a single circular jet normally injecting into a supersonic cross flow as proposed by Santiago and Dutton [63].

McCann and Bowersox [44] measured mean flow quantities and turbulence quantities using film anemometry of a low-angled supersonic injector exhausting in a Mach 2.9 crossflow. They measured the strength of the “kidney-shaped” vortices and attributed their generation to two main mechanisms. The first mechanism is the low-pressure region behind the jet plume that induces rotation in the crossflow fluid wrapping around the jet plume. The second mechanism is the turning of the jet flow into the crossflow direction that adds energy to the secondary flow (rotational motion) in an analogous way as the secondary flow in curved ducts. They detected a third smaller vortex near the wall surface, below one of the counter-rotating vortices. They explained the existence of this smaller vortex with the asymmetry in the spanwise location and strength of the counter-rotating vortices, but they did not provide an explanation for the asymmetry itself. Turbulent kinetic energy measurements showed the existence of two peaks coincident with the vortices. This was explained by the increased production that in turn is due to the effects of the three-dimensional, dilatational strain rates and by entrainment of high turbulence intensity boundary layer fluid. The structure of the shear stress distribution in the jet plume was found to be highly three-dimensional and quite complicated, especially because of the interaction of the expansion with the vortices and the convected turbulent structures. Also, it was assessed that compressibility accounts for 67-75% of the total Reynolds shear stress.

2.2 Numerical Work

This section is a non-exhaustive review and discussion of representative examples of numerical works in jet interaction flowfields as listed in Table 2.1. Numerical studies of the jet interaction flow field started in the late 70's with the work of Drummond [24] but they were mainly aimed at fuel injection applications. Fuel injection applications employ lower pressure ratios than those for control systems and focus on the prediction of the mixing of the gas species rather than on the prediction of the pressure field. Weidner and Drummond [89] performed a parametric study of two-dimensional staged injection on a flat surface. They reported pressure data on the surface of the flat plate only for a single-jet validation case, and the result was an under-prediction of the extent of the separation region ahead of the injector and failure to correctly predict the pressure distribution behind the injector. The disagreement between the numerical calculation and the experimental data was primarily blamed on the algebraic turbulence model (Baldwin-Lomax [8]). However, the parametric study indicated that the two injectors had to be far apart to see a difference in the flow fields produced by differently sized injectors.

Thompson [78] compared a numerical solution obtained with the Baldwin-Lomax turbulence model to the experimental data from Zukoski and Spaid [100]. Thompson chose a two-dimensional test case with normal sonic injection into a freestream with a Mach number of 2.61 and a test pressure ratio of 24. An adaptive grid was used for the numerical solution. The comparison with the experiment of the pressure on the flat plate surface was "fair", with the numerical solution again under-predicting the separation region and failing to properly capture the pressure well aft of the injector. Thompson attributed the deficiencies in the computational solution to the Baldwin-Lomax turbulence model as well as to the limiter used in the calculations. It was pointed out that the adapted grid greatly enhanced the quality of the solution.

Rizzetta in 1992 [57] simulated the Aso, et al. two-dimensional experiment [5]. Rizzetta employed the k - ϵ turbulence model and compared the numerical solution to the experiment in terms of surface static pressure, separation region length and height of the Mach disk for different slot widths and pressure ratios. Agreement was reasonably good for the smaller slot width and the lower pressure ratio cases, the major disparity being the higher peak pressure levels predicted by the numerical simulations. Comparisons for the larger slot widths and higher-pressure ratios were not so favorable. Rizzetta attributed this disparity to the lack of knowledge of the turbulence properties at the nozzle exit. It is noted that the imposed boundary conditions at the nozzle exit can be expected to remain physically realistic only when they impact a small region in the immediate vicinity of the slot. This condition is not satisfied for large slots or for high-pressure ratios.

Author	2D/ 3D	M_∞	M_j	PR	Lam/ Turb	Re_L [m^{-1}]	Normal/ Inclined Inj.	Gas	Turbul. Model	Experimental Comparison	Comparison of
Weidner, Drummond, 1981 [89]	2D	2.61	1.0	38.0	Turb	1.72×10^8	Multiple/ Normal	He/ Air	B-L	Same authors	C_p centerline, Pressure in BL, He fraction
Thompson 1989 [78]	2D	2.61	1.0	23.5	Turb	1.15×10^8	Normal	Air/ Air	B-L	Zukoski	C_p centerline
Fuller 1991 [26]	3D	6.0	1.7	26.7	Turb	5.42×10^7	Inclined 15deg	He/ Air	B-L	Same authors	He concentration
Rizzetta 1992 [57]	2D	3.70	1.0	10.1 60.6	Turb	5.83×10^6	Normal	Air/ Air	$k-\epsilon$	Aso [5]	C_p centerline
Clark, Chan, 1992 [17]	2D	3.71	1.0	31.7	Turb	6.27×10^7	Normal	N/ Air	B-L	Aso [5]	C_p centerline
Garlinger, et al., 1994 [29]	2D	3.71	1.0	31.7 43.0 50.2	Turb	6.27×10^7	Normal	H ₂ , N /Air	q- ω ($k^2-\omega$)	Aso [5]	C_p centerline, N fraction, Pressure in BL
Williams et Al., 1996 [94]	3D	2.00	1.5	7.8	Turb	4.88×10^7	Inclined 30, 45, 60deg	Air /Air	B-L	No comparison	N/A
Chenault et Al., 1998 [14]	2D	3.75	1.0	9.2 47.6	Turb	6.27×10^7	Normal	Air /Air	$k-\epsilon$ R-S	Aso [5]	C_p centerline, Separation Length
Chenault et Al., same as previous	2D	3.50	1.0	16.5 120.2	Turb	1.34×10^7	Normal	Air /Air	$k-\epsilon$ R-S	Zukoski [70]	C_p centerl., Separat. Length
Chenault et Al., 1999 [15]	3D	2.90	1.8	60.0	Turb	1.50×10^7	Inclined 25deg	Air /Air	$k-\epsilon$ R-S	McCann, Bowersox [44]	C_p centerl., Vorticity
Wang 2000, [87]	3D	0.5	1.5	0.8	Turb	6.59×10^7	Inclined 35deg	Air /Air	S-A	Pietrzyk, et al. [56]	C_p centerl., Vorticity
Kennedy 2000, [40]	3D	1.6	1	8.4	Turb	3.49×10^7	Normal	Air /Air	$k-\epsilon$	Same authors	C_p mapping., Velocity

Table 2.1 Computational work on Jet interaction flow fields.

The two-dimensional Aso, et al. data was again used for a validation of a numerical code by Clark and Chan [17]. In this work the authors used a modified Baldwin-Lomax turbulence model to perform a parametric study on the influence of the angle of the injector to the freestream on the pressure field and on the force on the flat plate. A grid convergence study showed the importance of refining the mesh in the region around the injector. This was especially important ahead of the injector, since the grid density greatly affected the extent of the separation region. A comparison of the pressure distribution along the flat plate between the numerical solution and the experiment data revealed a bias in the Aso et al data. The measured pressure on the flat plate never reached the freestream value even when measured at stations much ahead of the separation region. In spite of this concern, Clark and Chan went on with the comparison that showed a partial agreement with the data in the separation region ahead of the injector and a good agreement in the region aft of the injector. Clark and Chan also performed a parametric study on the effect of the injection angle on the normal force. The study showed that canting the injector 60° forward (i.e. into the freestream), produces a normal force which is 15% greater than that produced by a normal injector (90°) for the same mass flow.

Garlinger, et al. [29] simulated the two-dimensional Aso experiment using the $q-\omega$ turbulence model, a modification of the $k-\omega$ developed by Coakley [18]. They experimented with several modifications to the original $q-\omega$ model and obtained reasonable agreement for the pressure distribution along the flat plate, particularly in the region ahead of the injector. Their numerical predictions always tended to under-predict the extent of the separation region, the pressure peak due to the bow shock, and to greatly over-predict a pressure peak just ahead of the injector. They also verified that changing the turbulence intensity of the jet fluid does not have an impact on the overall flow-field.

Williams, et al. [94] performed a numerical study of three-dimensional angled injection using Baldwin-Lomax turbulence model. They confirmed the presence of “kidney-shaped” vortices trailing behind the injector and their importance in the mixing of the jet fluid with the crossflow fluid. Also, the solution well predicted the low-pressure region just aft of the injector, which is one of the major concerns of this study.

A notable amount of work in numerical simulations of the jet interaction flowfield was performed at the Wright-Patterson Air Force base by Chenault, Beran and Bowersox and presented in two separate papers in 1998-1999. The work of these authors is significant to the present effort, since it covers the jet interaction flow-field in greater detail than any other previous work and it presents the first application of a Reynolds Stress turbulence model to this type of problems. Chenault and Beran [14] carried out a thorough comparison of numerical simulations to the two-dimensional experiments of the Aso, et al. [5] and Spaid and Zukoski [70], both with sonic normal injection. Chenault and Beran modeled the turbulent effects with $k-\epsilon$ and Reynolds stress turbulence models developed by Zhang, et al. [98] and additionally compared their results to the numerical results obtained by Rizzetta [57] with the Jones-Launder $k-\epsilon$ model for the Aso experiments. They used a Cartesian grid and verified the grid convergence of their results. They found

a poor agreement of the numerical solutions with the experimental data of the Aso, et al. experiment and attributed the disagreement to the poor quality of the experimental data. In particular, they point out that the Aso, et al. data is affected by three-dimensional effects because of the lack of fences at the side of the plate, lack of an appropriate number of pressure orifices to capture the characteristics of the flow details, and a “choppy” nature of the static pressure profiles ahead of the injector, an indication of shock/boundary layer interaction ahead of the primary separation (this shortcoming in the Aso et al. data was mentioned also by Clark and Chan [17], see above). Nevertheless, the comparison of the three turbulence models indicated that both the k - ϵ and Reynolds stress Zhang, et al. turbulence models performed quite well for the lower pressure ratios, but as the pressure ratio was increased their accuracy degraded. On the other side, the Jones-Lauder k - ϵ model performed better with the higher-pressure ratios, predicting more accurately the separation location and the plume height than the other two turbulence models. A better agreement is exhibited by the comparison between the Chenault and Beran numerical solutions and the Spaid and Zukoski data, mainly because of the better quality of the experimental data. Again, both the k - ϵ and Reynolds stress turbulence models predict the pressure distribution on the wall quite well for the lower pressure ratios. However, as the pressure ratio is increased toward the maximum value of 120 the disagreement between computed and experimental values increases. Both models under-predict the length of the separation region (24% for the Reynolds stress turbulence model and 28% for the k - ϵ model) and over-predict the pressure peak ahead of the injector produced by the bow shock. Specifically, the k - ϵ model better predicts the pressure distribution in the region aft of the injector, whereas the Reynolds stress model better predicts the pressure distribution in the region ahead of the injector. With their calculations, Chenault and Beran also confirmed the observation made by Spaid and Zukoski that the boundary-layer separation distance is about four plume penetration heights upstream of the jet. The analysis of the turbulence data showed how both the k - ϵ and Reynolds stress turbulence models satisfy the law of the wall for flat plates and that both models predicted similar shear stress values. However, the two models predict significantly different results in the vicinity of shock and at the interfaces of flow structures, especially when there are large differences in flow direction and pressure. Chenault and Beran attribute the discrepancy of the shear stresses predicted by the two models to the k - ϵ model not modeling the second-order pressure-velocity gradient term and because of the k - ϵ model employing an isotropic formulation of the turbulence dissipation rates. All these factors cause the k - ϵ model to predict a non-physical behavior at the interface of the two strong recirculation vortices ahead of the injector.

Chenault, et al. [15] also performed a numerical analysis of the three-dimensional jet interaction flowfield with angled supersonic injection studied by McCann and Bowersox [44]. The authors used the Zhang, et al. [98] k - ϵ and Reynolds stress turbulence models and, in order to investigate any asymmetric behavior of the flowfield, the computational domain encompassed the wind tunnel on both sides of the centerline, thus avoiding the assumption of the symmetry plane. The need to avoid the symmetry plane assumption stemmed from minor asymmetric behavior in the experimental data of McCann and Bowersox. However, the numerical results did not show any type of asymmetry,

indicating that the asymmetric behaviors noted in the experiments were probably due to a combination of imperfections in the test section and nozzle, systematic errors in the test setup and to the coarseness of the data collection matrix. Also, the unsteadiness of the flowfield and some unstable transients that are damped out of the numerical solutions could be the cause of the asymmetries in the experiment. The comparison of the two turbulence models showed that both were able to satisfactorily predict the mean flow variables. However, as expected, the Reynolds stress model showed a better agreement with the experimental data in both the distribution and magnitude of the shear stresses, especially in the region downstream of the injector. The analysis of the flowfield evaluated with the Reynolds stress turbulence model highlighted the highly three-dimensional pattern of alternating expansion and compression waves present in the plume and the complex rotational motion downstream of the injector. The plume featured the typical characteristics of under-expanded jets, with a diamond shock pattern and a Mach disk (in this case the Mach disk was very small due to the low-pressure ratio of the jet). The rotational motion present in the region downstream of the injector was found to be produced by the interaction of the oblique barrel shock and the upwash of the freestream fluid colliding along the plane of symmetry immediately aft of the jet plume. This interaction modified the barrel shock as it detached from the flat plate surface, with the upwash along the centerline creating an indentation in the base of the diamond-shaped plume (see Figure 2.3).

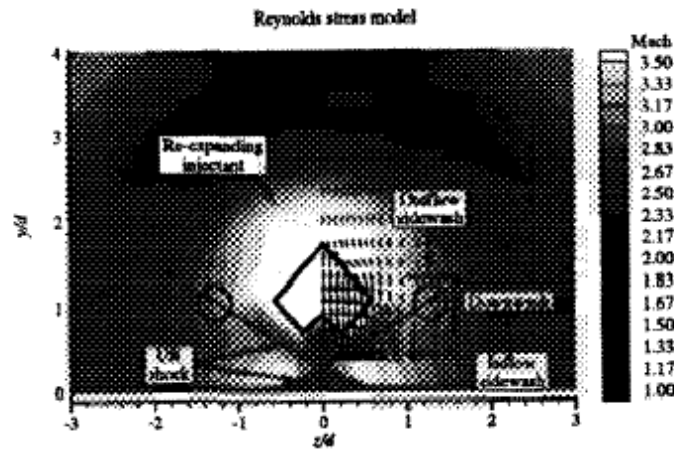


Figure 2.3. Mach contours at 4 diameters downstream of the injection location. In this case the injection is inclined to the surface of the flat plate and the jet conditions are supersonic. [15]

Wang [87] used the one-equation turbulence model of Spalart and Allmaras to determine the influence of the eddy viscosity of the injectant on the three-dimensional jet interaction flowfield. In spite of the low crossflow Mach number (0.5), the low-pressure ratio (0.78) and the angled injector with supersonic conditions used in this experiment, it is informative to study the general behavior of the flowfield with a variation in eddy viscosity of the injected gas. Wang showed that increasing the magnitude of the eddy

viscosity changed the magnitudes and directions of the crossflow velocity components as well as reducing the vorticity level near the injector and inducing vorticity oscillation at downstream locations.

Kennedy, et al. [40] analyzed the three-dimensional flowfield of a normal sonic jet exhausting in a supersonic crossflow. They used the k - ϵ turbulence model to produce numerical solutions that were then compared to the Laser Doppler Velocimetry (LDV) and Pressure Sensitive Paint (PSP) data produced by the same authors. The comparison of the pressure mapping on the flat plate surface obtained with the numerical solution and the PSP data shows, quite surprisingly, a near-perfect agreement in the separation region with some discrepancies occurring aft of the injector along the centerline. The largest difference was along the edge of the injector, and this was attributed to the “slug flow” assumption for the jet boundary condition. The authors propose a simulation of the entire sonic nozzle of the injector to better reproduce the real flowfield. The comparison with the LDV-measured velocity field shows that the numerical solution over-predicts the expansion of the jet core with lower pressures and higher core Mach number than the experiment. Kennedy, et al. attribute the discrepancy to the perfect gas assumption made in the calculations. Interestingly, the authors report a lack of symmetry in the flow field measured in the experiment which is in disagreement with previous observations of jet interactions. As discussed by Chenault, et al. [15] the lack of symmetry in the experimental data is probably due to imperfections in the test apparatus that cause asymmetry in the flow or in transient flow features that are washed away in the steady-state numerical simulation. However, Kennedy, et al. also stress the necessity to use time-accurate solutions to accurately reproduce all the flow details.

Similar in scope to the experimental study of Zubkov, et al. [99], the numerical work of Roger, et al. [60], is an attempt to determine the effect of the boundary layer thickness and of the jet Mach number on the jet penetration height. The computations simulated a square injector exhausting normal to the surface of a flat plate and into a Mach 5.0 crossflow. The study concluded that for those flows where the jet plume is of the same order of magnitude as the boundary layer, and for fixed jet total conditions, the jet penetration height does not increase with increasing jet Mach number. However, for jet plumes that are larger than the order of magnitude of the boundary layer, the penetration height increases with jet Mach number. In addition to the above, Roger also confirmed that, as previously shown by Zubkov, et al. [99], penetration height increases with thicker boundary layers.

Chapter 3

Governing Equations and Numerical Solvers

The numerical solver used in this study was AeroSoft's General Aerodynamics Simulation Program (GASP). In the initial stages of this study GASP Version 3.2 was used and as GASP Version 4.0 became available all the numerical simulations were switched to the newer version. GASP was chosen because it is a mature program with a proven reliability record in simulations of turbulent flows [60], vortical flows [50], jets [36], shock-vortex interaction [49] and jet interaction flows [45]. Furthermore AeroSoft Inc. of Blacksburg, the developer of GASP, was one of the subcontractors to the Air Force grant and made available its computational and human resources to support the project. The following is a brief description of GASP and of its features.

3.1 GASP

AeroSoft's GASP solves the integral form of the time-dependent Reynolds-Averaged Navier-Stokes (RANS) equations in three dimensions. The main difference between GASP Version 3.2 and GASP Version 4.0 exercised during this effort is that Version 4.0 implements a fully implicit three-dimensional solution algorithm whereas Version 3.2 implements a plane implicit solver. Other new features of GASP Version 4.0 used in this efforts are that Version 4.0 offers the possibility of using overset (Chimera) grids, a more efficient parallel computing capability and a generally more user-friendly environment than Version 3.2.

GASP is capable of solving subsets of the RANS equations including two-dimensional and axi-symmetric problems, the Thin-Layer Navier-Stokes equations, the Parabolized Navier-Stokes equations and the Euler equations. The code is applicable to flows from subsonic to hypersonic speed and has options for thermo-chemical equilibrium and thermo-chemical non-equilibrium.

The code requires multi-block structured grids with point-to-point matching or non-matching at the block interfaces. Grid-sequencing is implemented. The solution is driven to a steady-state using relaxation algorithms (sweeping over a plane) or full 3-D solvers (Symmetric Block Gauss Seidel, Block Jacobi, GMRES). The inviscid fluxes are computed using the full flux option, scalar dissipation models or two flux-splitting methods: the flux-difference splitting of Roe or the flux-vector difference of Van Leer. The Monotonic Upstream-centered Scheme for Conservation Laws (MUSCL) scheme is used to interpolate the primitive variables at the cells interfaces. Through the MUSCL scheme, the spatial accuracy can be selected to be first-order, second-order fully upwind, second-order upwind biased and third-order upwind bias. The limiter can be chosen from the Van Albada, Min-Mod, Spekreijse-Venkat, Modified ENO and SuperBee limiter. The

viscous terms are discretized using a standard 2nd order accurate central differencing scheme. Most of the numerical simulations performed in this study used the 3rd order accurate Roe flux with the Min-Mod limiter in all three spatial directions. An exception to this flux combination was the replacement in only one computational direction of the Roe flux with the Van Leer flux leaving all the other parameters unchanged to avoid the “carbuncle effect” (see Ref. [55]) since the plume of the jet acts as a solid blunt obstruction to the incoming flow [100]. Several turbulence models have been implemented in GASP including a zero-equation model (Baldwin-Lomax) a one-equation model (Spalart-Allmaras) and two-equation models (high Reynolds number k -epsilon, Lam-Bremhorst and Chien k -epsilon, Wilcox-1988 k - ω , Wilcox-1998 k - ω).

3.2 Governing Equations

The flow of a viscous, heat conducting, compressible, single-species, non-reacting fluid can be described using the mass continuity equation (conservation of mass), Newton’s second law of motion (conservation of momentum) and the first law of thermodynamics (conservation of energy). The combined system of equations is generally known as the Navier-Stokes equations. The individual equations representing the conservation of each physical parameter are:

Conservation of mass:

$$\frac{\partial \rho}{\partial t} + \frac{\partial(\rho u_i)}{\partial x_i} = 0 \quad (3.1)$$

Conservation of momentum:

$$\frac{\partial \rho u_i}{\partial t} + \frac{\partial}{\partial x_i}(\rho u_i u_i + p \delta_{ij}) = \frac{\partial}{\partial x_i}(\tau_{ij}) + \rho f_i \quad (3.2)$$

Conservation of energy:

$$\frac{\partial \rho e_o}{\partial t} + \frac{\partial}{\partial x_i}(\rho e_o u_i + p u_i + \rho e_o u_i) = \frac{\partial}{\partial x_i}(\tau_{ij} u_j) - \frac{\partial q_i}{\partial x_i} + \rho(u_j f_j) + \rho \dot{q} \quad (3.3)$$

where

$$e_o = e + \frac{1}{2}u_i u_i \quad (3.4)$$

The above equations are in tensor form and are valid in any coordinate system. The term u_i is a vector representing the three velocity components, u_1, u_2, u_3 , in the three spatial directions defined by x_i , that is x_1, x_2, x_3 . The term τ_{ij} is a tensor representing the viscous stresses. The term δ_{ij} is the Kronecker delta that takes the value of 1 if $i=j$ or the value of 0 if $i \neq j$. Note that the system of equations contains five equations in terms of six flowfields variables, $\rho, p, u_1, u_2, u_3, e$. Therefore it is necessary to introduce one more equation to close the system. Usually this additional equation is the equation of state. For a gas that does not behave like a perfect gas or for a mixture of gases, solving the equation of state can be quite complicated. However, for a thermally perfect gas the thermal equation of state can be used as the sixth equation to close the system:

$$p = \rho RT \quad (3.5)$$

Note that one more unknown, the temperature T , has been introduced. The entire system can be closed with a thermodynamic relation between state variables such as:

$$e = e(T, p) \quad (3.6)$$

If the gas is both thermally and calorically perfect (i.e. it obeys the thermal equation of state, Eq. (3.5) and the specific heats are constant [81]) the situation is greatly simplified since the above equation reduces to a linear relationship such as:

$$e = C_v T \quad (3.7)$$

The above equations can be re-written in matrix form and using Cartesian coordinates (i.e. replacing the general coordinates x_1, x_2, x_3 with the linear coordinates x, y and z) as:

$$\frac{\partial \mathbf{Q}}{\partial t} + \frac{\partial \mathbf{F}'}{\partial x} + \frac{\partial \mathbf{G}'}{\partial y} + \frac{\partial \mathbf{H}'}{\partial z} = \mathbf{J} \quad (3.8)$$

where \mathbf{F}' , \mathbf{G}' and \mathbf{H}' are column vectors also called flux terms and \mathbf{J} is the “source term” which is zero if body forces can be neglected. The above form of the equation is called the strong conservation form since all the terms are buried inside the derivatives, and all the spatial derivative terms can be identified as a divergence. Sometimes it is convenient

for clarity to divide the viscous terms (or viscous fluxes) from the inviscid fluxes. By doing so Eq. (3.8) becomes:

$$\frac{\partial \mathbf{Q}}{\partial t} + \left(\frac{\partial \mathbf{F}}{\partial x} + \frac{\partial \mathbf{G}}{\partial y} + \frac{\partial \mathbf{H}}{\partial z} \right) = \left(\frac{\partial \mathbf{F}_v}{\partial x} + \frac{\partial \mathbf{G}_v}{\partial y} + \frac{\partial \mathbf{H}_v}{\partial z} \right) + \mathbf{J} \quad (3.9)$$

where \mathbf{Q} is the vector of the conserved variables:

$$\mathbf{Q} = \left\{ \begin{array}{c} \rho \\ \rho u \\ \rho v \\ \rho w \\ \rho e_o \end{array} \right\} \quad (3.10)$$

F, G and H are the inviscid flux vectors:

$$\mathbf{F} = \left\{ \begin{array}{c} \rho u \\ \rho u^2 + p \\ \rho uv \\ \rho uw \\ \rho uh_o \end{array} \right\},$$

$$\mathbf{G} = \left\{ \begin{array}{c} \rho v \\ \rho uv \\ \rho v^2 + p \\ \rho vw \\ \rho vh_o \end{array} \right\},$$

$$\mathbf{H} = \left\{ \begin{array}{c} \rho w \\ \rho uw \\ \rho vw \\ \rho w^2 + p \\ \rho wh_o \end{array} \right\} \quad (3.11)$$

F_v , G_v and H_v are the inviscid flux vectors:

$$\begin{aligned}
 \mathbf{F}_v &= \left\{ \begin{array}{c} 0 \\ \tau_{xx} \\ \tau_{xy} \\ \tau_{xz} \\ u\tau_{xx} + v\tau_{xy} + w\tau_{xz} - q_x \end{array} \right\} \\
 \mathbf{G}_v &= \left\{ \begin{array}{c} 0 \\ \tau_{xy} \\ \tau_{yy} \\ \tau_{yz} \\ u\tau_{xy} + v\tau_{yy} + w\tau_{yz} - q_y \end{array} \right\} \\
 \mathbf{H}_v &= \left\{ \begin{array}{c} 0 \\ \tau_{xz} \\ \tau_{yz} \\ \tau_{zz} \\ u\tau_{xz} + v\tau_{yz} + w\tau_{zz} - q_z \end{array} \right\}
 \end{aligned} \tag{3.12}$$

and \mathbf{J} is the source term vector:

$$\mathbf{J} = \left\{ \begin{array}{c} 0 \\ \rho f_x \\ \rho f_y \\ \rho f_z \\ \rho (uf_x + vf_y + wf_z) \end{array} \right\} \tag{3.13}$$

where h_0 is the stagnation enthalpy per unit mass given by:

$$h_0 = h + \frac{V^2}{2} = e + \frac{p}{\rho} + \frac{V^2}{2} = e_0 + \frac{p}{\rho} \tag{3.14}$$

Note that the vector of the primitive variables used in GASP is:

$$\mathbf{U} = \begin{Bmatrix} \rho \\ u \\ v \\ w \\ p \end{Bmatrix} \quad (3.15)$$

Now, collecting the inviscid flux vectors as:

$$\mathbf{F}(\mathbf{Q}) = (\mathbf{F} + \mathbf{G} + \mathbf{H}) \quad (3.16)$$

and the viscous flux vectors as:

$$\mathbf{F}_v(\mathbf{Q}) = (\mathbf{F}_v + \mathbf{G}_v + \mathbf{H}_v) \quad (3.17)$$

Eq (3.9) becomes:

$$\frac{\partial \mathbf{Q}}{\partial t} + \nabla \mathbf{F}(\mathbf{Q}) = \nabla \mathbf{F}_v(\mathbf{Q}) + \mathbf{J} \quad (3.18)$$

Moving the viscous flux vector to the left-hand side and integrating over a volume V we get the integral form of the governing equations:

$$\iiint \left[\frac{\partial \mathbf{Q}}{\partial t} + \nabla \mathbf{F}(\mathbf{Q}) - \nabla \mathbf{F}_v(\mathbf{Q}) \right] dV = \iiint \mathbf{J} dV \quad (3.19)$$

GASP (as most of present-day fluid-dynamics numerical solvers) treats the above integral form of the Navier-Stokes equations. All of the above equations are in the differential form and need to be re-arranged into the integral form. This can be readily done using Gauss theorem. The theorem states that for a vector \mathbf{F} with continuous partial derivatives in a domain V enclosed by the surface S with a normal vector \mathbf{n} [39]:

$$\iiint \nabla \mathbf{F} dV = \iint \mathbf{F} \cdot \mathbf{n} dS \quad (3.20)$$

Applying Gauss' theorem to the inviscid and viscous flux vectors in Eq. (3.19) we obtain the usual integral form of the Navier-Stokes equations for a viscous, heat-conducting, compressible, non-reacting, single-species fluid:

$$\frac{\partial}{\partial t} \iiint \mathbf{Q} dV + \iint [\mathbf{F}(\mathbf{Q}) - \mathbf{F}_v(\mathbf{Q})] \cdot \mathbf{n} dA = \iiint \mathbf{J} dV \quad (3.21)$$

3.3 Non-dimensional Form of the Governing Equations

The governing equations are often non-dimensionalized using reference quantities. The advantages of non-dimensionalization are several. First, the potential round-off error associated with the machine finite-precision is minimized. Second, characteristic parameters such as the Mach number, the Reynolds number and the Prandtl number can be varied independently. Many different non-dimensionalizing procedures are possible some using freestream values to non-dimensionalize the governing equations and some others using set reference values. In GASP non-dimensionalization is carried out using reference values that can be set close or equal to the freestream values. As it is common use, non-dimensionalized parameters are denoted by an asterisk, $(.)^*$. The non-dimensionalized parameters are defined in the following list.

$$\begin{aligned}
 x^* &= \frac{x}{L_{ref}}, & y^* &= \frac{y}{L_{ref}}, & z^* &= \frac{z}{L_{ref}}, & t^* &= \frac{t}{t_{ref}} \\
 u^* &= \frac{u}{V_{ref}}, & v^* &= \frac{v}{V_{ref}}, & w^* &= \frac{w}{V_{ref}} \\
 \mu^* &= \frac{\mu}{\mu_{ref}}, & k^* &= \frac{k}{k_{ref}} \\
 \rho^* &= \frac{\rho}{\rho_{ref}}, & p^* &= \frac{p}{\rho_{ref} V_{ref}^2}, & f_i^* &= \frac{f_i}{\rho_{ref} V_{ref}^2 L_{ref}^2} \\
 T^* &= \frac{T}{T_{ref}}, & e^* &= \frac{e}{V_{ref}^2}
 \end{aligned} \tag{3.22}$$

The reference quantities:

$$\rho_{ref}, V_{ref}, T_{ref}, L_{ref} \tag{3.23}$$

are input by the user and the other reference quantities are calculated from:

$$\begin{aligned}
 t_{ref} &= \frac{L_{ref}}{V_{ref}} \\
 \mu_{ref} &= \rho_{ref} V_{ref} L_{ref} \\
 k_{ref} &= \frac{\rho_{ref} V_{ref}^2 L_{ref}}{T_{ref}}
 \end{aligned} \tag{3.24}$$

The turbulent quantities such as the turbulent kinetic energy k and the turbulence frequency ω that will be derived in the subsequent section are normalized as

$$\begin{aligned}\kappa^* &= \frac{\kappa}{\kappa_{ref}} \\ \omega^* &= \frac{\omega}{\omega_{ref}}\end{aligned}\tag{3.25}$$

where

$$\begin{aligned}\kappa_{ref} &= V_{ref}^2 \\ \omega_{ref} &= \frac{V_{ref}}{L_{ref}}\end{aligned}\tag{3.26}$$

Using the above non-dimensional parameters and non-dimensional groups the governing equation in strong conservation form, Eq. (3.9), becomes:

$$\frac{\partial \mathbf{Q}^*}{\partial t^*} + \left(\frac{\partial \mathbf{F}^*}{\partial x^*} + \frac{\partial \mathbf{G}^*}{\partial y^*} + \frac{\partial \mathbf{H}^*}{\partial z^*} \right) = \left(\frac{\partial \mathbf{F}_v^*}{\partial x^*} + \frac{\partial \mathbf{G}_v^*}{\partial y^*} + \frac{\partial \mathbf{H}_v^*}{\partial z^*} \right) + \mathbf{J}^*\tag{3.27}$$

The column vectors will then be re-written as:

$$\mathbf{Q}^* = \begin{Bmatrix} \rho^* \\ \rho^* u^* \\ \rho^* v^* \\ \rho^* w^* \\ \rho^* e_o^* \end{Bmatrix}\tag{3.28}$$

$$\begin{aligned}
 \mathbf{F}^* &= \begin{Bmatrix} \rho^* u^* \\ \rho^* u^{*2} + p^* \\ \rho^* u^* v^* \\ \rho^* u^* w^* \\ \rho^* u^* h_o^* \end{Bmatrix} \\
 \mathbf{G}^* &= \begin{Bmatrix} \rho^* v^* \\ \rho^* u^* v^* \\ \rho^* v^{*2} + p^* \\ \rho^* v^* w^* \\ \rho^* v^* h_o^* \end{Bmatrix} \\
 \mathbf{H}^* &= \begin{Bmatrix} \rho^* w^* \\ \rho^* u^* w^* \\ \rho^* v^* w^* \\ \rho^* w^{*2} + p^* \\ \rho^* w^* h_o^* \end{Bmatrix}
 \end{aligned} \tag{3.29}$$

where the non-dimensionalized total enthalpy per unit mass is:

$$h_o^* = e_o^* + \frac{p^*}{\rho^*} = \left(e^* + \frac{u^{*2} + v^{*2} + w^{*2}}{2} \right) + \frac{p^*}{\rho^*} \tag{3.30}$$

The non-dimensionalized viscous terms are:

$$\begin{aligned}
 \mathbf{F}_v^* &= \left\{ \begin{array}{c} 0 \\ \tau_{xx}^* \\ \tau_{xy}^* \\ \tau_{xz}^* \\ u^* \tau_{xx}^* + v^* \tau_{xx}^* + w^* \tau_{xx}^* - q_x^* \end{array} \right\} \\
 \mathbf{G}_v^* &= \left\{ \begin{array}{c} 0 \\ \tau_{xy}^* \\ \tau_{yy}^* \\ \tau_{yz}^* \\ u^* \tau_{xy}^* + v^* \tau_{yy}^* + w^* \tau_{yz}^* - q_y^* \end{array} \right\} \\
 \mathbf{H}_v^* &= \left\{ \begin{array}{c} 0 \\ \tau_{xz}^* \\ \tau_{yz}^* \\ \tau_{zz}^* \\ u^* \tau_{xz}^* + v^* \tau_{yz}^* + w^* \tau_{zz}^* - q_z^* \end{array} \right\}
 \end{aligned} \tag{3.31}$$

and the non-dimensionalized source term is given by:

$$\mathbf{J}^* = \left\{ \begin{array}{c} 0 \\ \rho^* f_x^* \\ \rho^* f_y^* \\ \rho^* f_z^* \\ \rho^* (u^* f_x^* + v^* f_y^* + w^* f_z^*) \end{array} \right\} \tag{3.32}$$

Finally, the perfect gas equation of state, Eq.(3.6), becomes:

$$p^* = (\gamma - 1) \rho^* e^* \tag{3.33}$$

3.4 The Reynolds Averaged and Favre Averaged form of the Governing Equations

Most of present-day CFD codes including GASP numerically integrate the Reynolds-Averaged Navier-Stokes equations. These governing equations can be written using time-averaged (Reynolds averaged) values of the density and pressure and mass-weighted (Favre') averages for the velocity components and temperature. The Reynolds averaged values (indicated by an over bar) are defined as:

$$\bar{f} \equiv \frac{1}{\Delta t} \int_{t_0}^{t_0+\Delta t} f dt \quad (3.34)$$

It follows that the randomly changing flow variables can be replaced by the Reynolds averages plus the fluctuations about the average (Reynolds decomposition). We may then write:

$$f = \bar{f} + f' \quad (3.35)$$

where f is the randomly changing flow variable and f' is the fluctuation about the average. The Favre'-averaged values are convenient for treatment of compressible flows and mixtures of gases since the density variation of the fluid comes into play in the averaging process. The Favre'-averaged values (indicated by a tilde) are defined by:

$$\tilde{f} \equiv \frac{\overline{\rho f}}{\bar{\rho}} \quad (3.36)$$

Using the above definitions and identities the Reynolds Averaged Navier-Stokes equations (RANS) become:

Conservation of mass:

$$\frac{\partial \bar{\rho}}{\partial t} + \frac{\partial (\bar{\rho} u_i)}{\partial x_i} = 0 \quad (3.37)$$

Conservation of momentum:

$$\frac{\partial \bar{\rho} \tilde{u}_i}{\partial t} + \frac{\partial}{\partial x_i} (\bar{\rho} \tilde{u}_i \tilde{u}_i + \bar{p} \delta_{ij}) = \frac{\partial}{\partial x_i} (\tilde{\tau}_{ij} + \bar{\tau}_{ij}') - \frac{\partial}{\partial x_i} (\bar{\rho} \tilde{u}_i \tilde{u}_i'') \quad (3.38)$$

Conservation of energy:

$$\frac{\partial \bar{\rho} \tilde{e}_o}{\partial t} + \frac{\partial}{\partial x_i} (\bar{\rho} \tilde{e}_o \tilde{u}_i + \overline{p u_i} + \bar{\rho} \widetilde{e_o'' u_i''}) = \frac{\partial}{\partial x_i} (\overline{\tau_{ij} u_j}) - \frac{\partial q_i''}{\partial x_i} \quad (3.39)$$

where

$$\tilde{e}_o = \bar{C}_v \tilde{T} + \frac{1}{2} \tilde{u}_i \tilde{u}_i + \frac{1}{2} \widetilde{u_i'' u_i''} \quad (3.40)$$

The perfect-gas law becomes:

$$\bar{p} = \bar{\rho} R \tilde{T} \quad (3.41)$$

Eq (3.38) shows that aside from replacement of instantaneous variables by mean values, the only difference between the time (Reynolds) averaged and instantaneous momentum equation is the appearance of the correlation

$$\tau_{ij} = -\bar{\rho} \widetilde{u_i'' u_j''} \quad (3.42)$$

also known as the Reynolds stress tensor. This is a symmetric tensor and thus has six independent components, all of which are unknown. Therefore as a consequence of time-averaging, six more unknowns have been introduced without gaining any additional equations to close the system. For a general three-dimensional flow, these unknowns add to the five mean unknown flow properties, nominally the pressure, the three velocity components and the enthalpy to produce a system of 11 unknowns and five equations (conservation of mass, momentum and energy). This disparity between the number of unknowns and of equations is the closure problem of turbulent flows and it is commonly handled through turbulence modeling.

3.5 Turbulence Modeling

Turbulence models to close the RANS can be divided into two broad categories, according to whether or not the Reynolds stress tensor is simulated using a combination of assumptions and physical relations (first-order models) or it is directly resolved into its six components (second-order models). First-order models, also known as eddy viscosity models, make use of the Boussinesq assumption. The Boussinesq assumption states that, in analogy to the laminar viscous diffusion terms, the turbulent shearing stresses are related to the rate of mean strain through and apparent scalar turbulent viscosity. In mathematical terms this is:

$$-\overline{\rho u_i'' u_j''} = \mu_T \left(\frac{\partial \tilde{u}_i}{\partial x_j} + \frac{\partial \tilde{u}_j}{\partial x_i} - \frac{2}{3} \delta_{ij} \frac{\partial \tilde{u}_k}{\partial x_k} \right) - \frac{2}{3} \delta_{ij} \overline{\rho} k \quad (3.43)$$

where μ_T is the turbulent viscosity and k is the kinetic energy of the turbulent fluctuations or turbulent kinetic energy (TKE):

$$k = \frac{1}{2} \overline{u_i'' u_i''} = \frac{1}{2} \frac{\overline{\rho u_i'' u_i''}}{\overline{\rho}} \quad (3.44)$$

In contrast to the molecular viscosity which is an intrinsic property of the fluid state, the turbulent viscosity depends upon the mean flow. On the other hand, second-order models do not make use of the Boussinesq assumption and solve the transport equations for the individual stress components directly, rather than using an algebraic relationship for the stresses. For these reasons, second-order models are more general than first-order models for flows with sudden changes in the mean strain rate or with effects such as streamline curvature or gradients in the Reynolds normal stresses.

With the exception of some preliminary laminar calculations performed to test the grid quality, to prove the code capability, and to understand the basic physics of the jet interaction problem, all the numerical calculations performed in this study were turbulent calculations. GASP offers the choice of zero, one and two-equation turbulence models. However, no second-order turbulence models have been implemented in the code at this time. The choice of the turbulence model was restricted to one of the two-equation models since they perform better in separated flows than zero or one-equations models. More specifically Wilcox's $k-\omega$ model [91] was selected over $k-\epsilon$. The $k-\omega$ model was chosen because of its good capability in predicting separation and in dealing with adverse pressure gradients and separated flows when compared to other two-equation models [1] [54].

5.5.1 k - ω

As described above, the k - ω model is a first-order turbulence model. It uses the kinetic energy of the turbulence, k , as one of its turbulence parameters and the dissipation per unit turbulent kinetic energy, ω , as the second turbulence parameter. ω is normally referred to as the turbulent frequency having units of 1/second. The k - ω model used in this study is the Wilcox 1988 [92] [93] in the GASP Version 3.2 and Version 4.0 implementation. In this model, the equations governing the turbulent parameters are:

Eddy viscosity:

$$\mu_T = C_\mu \frac{\bar{\rho}k}{\omega} \quad (3.45)$$

Turbulent Kinetic Energy:

$$\bar{\rho} \frac{\partial k}{\partial t} + \bar{\rho} U_j \frac{\partial k}{\partial x_j} = \tau_{ij} \frac{\partial U_i}{\partial x_j} - \beta^* \bar{\rho} k \omega + \frac{\partial}{\partial x_j} \left[(\mu + \sigma^* \mu_T) \frac{\partial k}{\partial x_j} \right] \quad (3.46)$$

Specific Dissipation Rate:

$$\bar{\rho} \frac{\partial \omega}{\partial t} + \bar{\rho} U_j \frac{\partial \omega}{\partial x_j} = \alpha \frac{\omega}{k} \tau_{ij} \frac{\partial U_i}{\partial x_j} - \beta \rho \omega^2 + \frac{\partial}{\partial x_j} \left[(\mu + \sigma \mu_T) \frac{\partial \omega}{\partial x_j} \right] \quad (3.47)$$

The empirical closure coefficients for Wilcox's 1988 model are:

$$\alpha = 5/9 \quad \beta = 3/40 \quad \beta^* = 9/100 \quad \sigma = \sigma^* = 1/2 \quad C_\mu = 1.00 \quad (3.48)$$

Chapter 4

Boundary Conditions and Computational Grids.

An important part of numerical simulations is the definition of appropriate boundary conditions and the creation of a computational grid with discretized volumes small enough to resolve the flow physics in detail. It is noteworthy to recognize that, while all the fluid problems are governed by the same equations, namely the full Navier-Stokes equations, what distinguishes one flow from another are the boundary conditions. This perspective makes evident the importance of using the correct boundary conditions.

While the importance of the boundary conditions is dictated directly by the type of governing equations, the relevance of the computational domain comes from the type of method used to solve the governing equations. As discussed in Chapter 3, this study makes use of the finite-volume formulation of the RANS to numerically solve the flowfield. Therefore, a discretized computational space over which the RANS can be numerically solved has to be generated using appropriate software. The computational space, usually called domain, needs to describe correctly the geometry of the problem. At the same time the individual discretized volumes (cells) that compose the domain have to be small enough to capture the details of the flow physics. However, the total number of cells cannot be too large due to memory and CPU run time concerns. Therefore, a balance has to be found between the need for a fine grid and the limitations imposed by the computational resources available.

This section discusses the current treatment of the boundary conditions for the jet interaction flowfield and the generation and adaptation process of the computational grids.

4.1 Boundary Conditions

The computational domain for the flat plate with normal injection consisted of a six-sided box (see Figure 4.1). The lower plane, i.e. the plane defined by $y/d=0.00$, corresponds to the solid surface of the flat plate. The upper plane is not simulating a solid surface. The same is valid for the longitudinal plane far away from the plane of symmetry ($z/d=0.00$) and for the exit plane. One plane is defining the entry boundary conditions that are set at freestream conditions. An entry boundary layer can be simulated. Due to the fact that several experiments were simulated, specific freestream and jet conditions are reported in the Results section for each experiment. Data from the simulated experiments as used for all quantities when available. In some cases not all the necessary data was available and therefore assumptions had to be made. Notable examples of missing information about the exact boundary conditions are: the details of the jet exit flow, including the discharge coefficient and the inlet boundary layer profiles. The following is a general description of the applied boundary conditions.

Wall

The no-slip condition ($u=v=w=0.00$) is imposed on the flat plate along with $\partial p/\partial y=0.00$ and the adiabatic wall condition, $\partial T/\partial y=0.00$. The surface is assumed to be smooth.

Primary Jet

The injector is cut in the surface of the flat plate. The origin of the reference axes is at the center of the injector. For each case investigated, the nozzle was choked and the total conditions of the jet were known. Therefore, sonic conditions were applied at the cells simulating the jet ($Ma_J=1.00$, $\rho_J=\rho_{sonic}$, $u_J=w_J=0.00$ m/s, $v_J=a$, $p_J=p_{sonic}$). The jet was assumed to have a flat step profile i.e. no boundary layer in the nozzle was simulated. However, the area of the simulated jet is smaller than the real jet and the ratio of the two areas is equal to the discharge coefficient ($C_{d,J}$) of the real nozzle. In this way the mass flow rate and the thrust of the simulated jet was the same as the real jet. The discharge coefficient is defined by the relation:

$$C_{d,J} = \frac{\dot{m}_{actual}}{\dot{m}_{ideal}} = \frac{\dot{m}_{actual}}{v_J \rho_J A_J} \quad (3.49)$$

Notice that the primary injector is cut in half by the symmetry plane.

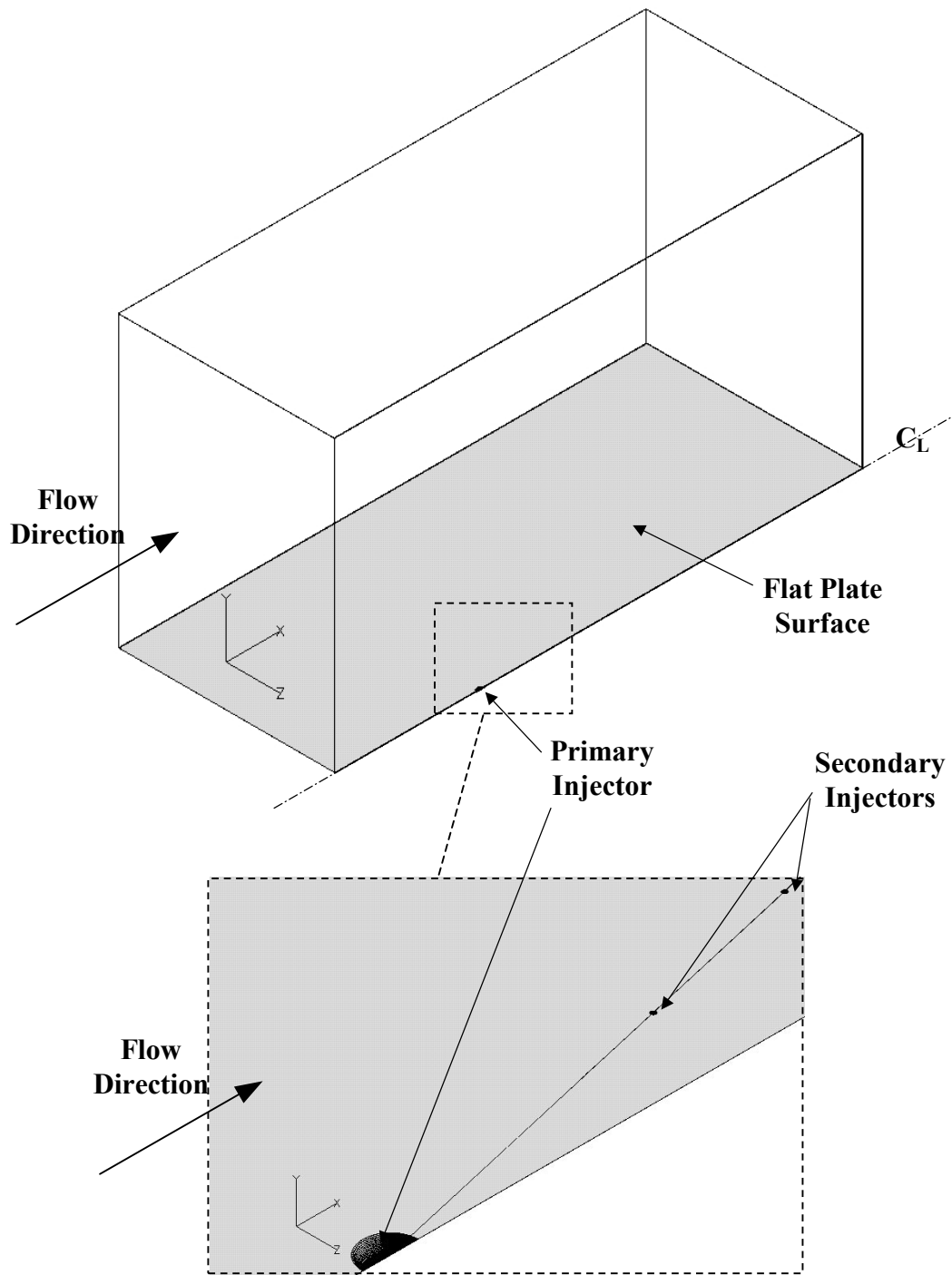


Figure 4.1. Computational domain for the flat plate with normal injection. The surface of the flat plate is highlighted in gray. The arrangement of the computational domain is the same for all the calculations even though the dimensions of the plate and of the injector changed from case to case.

Secondary Jet

The computations that involved secondary jets were either simulated cases that did not model an actual experiment (Section 5.5.3, “*Letko Turbulent case with Simulated Secondary Jet*”) or they were experiments run at Virginia Tech (the Virginia Tech Mach 2.4 and Virginia Tech Mach 4.0 cases) for which detailed information about the jet exit conditions was available. The secondary injectors are cut in the surface of the flat plate. The same total conditions as the primary jet were applied to the secondary jets. The main difference between the two jets is the area of the injector. The area of the secondary injector (and therefore also the mass flow rate since the same total conditions are applied to the two jets) is $1/100^{\text{th}}$ the area of the primary injector. Also, the discharge coefficient was the same for both injectors. Note that unlike the primary jet, the secondary injectors do not lie along the plane of symmetry of the computational domain and therefore the whole jet has to be simulated.

Entry Conditions

The flow upstream of the injector is supersonic. The flat plate can however, be mounted on supports and away from the tunnel floor, [65] [22] [42], or flush to the tunnel floor in the Virginia Tech cases. In the latter case, an entry boundary layer had to be simulated. All the dependent variables on the entry plane outside the boundary layer were assigned their respective freestream value. The known freestream quantities from the experiment usually are the Mach number and the total pressure. From knowledge of these two quantities and using isentropic relations for a perfect gas with $\gamma=1.40$ and the specific heat at constant volume, C_v , equal to 717.25 J Kg/K , all the other freestream quantities were derived. For the turbulence quantities (for the k - ω , k , the turbulent kinetic energy, and ω , the turbulent frequency) two assumptions had to be made since the exact turbulence level inside the wind tunnel for the Virginia Tech experiments was not known. First, due to the lack of actual turbulence measurements for each case, the freestream turbulence intensity (TI) was assumed to be 5%. Second the mixing length, l_T , had to be assumed. The initial guess for the freestream mixing length was driven by stability considerations for the k - ω turbulence model. In fact the k - ω model shows a more stable behavior when the initial conditions for the turbulent viscosity, μ_T , is less than the laminar viscosity, μ . Therefore the mixing length was chosen so that the turbulent viscosity would be slightly less than the laminar viscosity. From the assumed values of TI and l_T , the freestream k and ω could be derived using:

$$TI_{\infty} = \frac{\sqrt{k_{\infty}}}{V_{\infty}} \quad (3.50)$$

and

$$\omega = \frac{\sqrt{k}}{l_T} \quad (3.51)$$

As discussed above the turbulent viscosity is related to the mixing length through ω by virtue of the relationship:

$$\mu_T = \frac{C_\mu \rho k}{\omega} \quad (3.52)$$

When an inlet boundary layer was simulated such as for the Virginia Tech cases [84] [85], the known parameters were the freestream conditions and the boundary layer thickness, δ_o , the latter obtained from Schlieren pictures of the tunnel flow. The turbulent velocity boundary layer profile was then assumed to follow the simple relationship [68]:

$$\frac{U}{U_e} = \left(\frac{y}{\delta} \right)^{\frac{1}{7}} \quad (3.53)$$

where U_e is the edge, or freestream, velocity.

Plane of Symmetry

The three dimensional computational domain simulated only half of the experimental setup. Assuming that no erroneous asymmetries are present in the wind tunnel flow, the flow field is symmetric about the centerline of the flat plate. The symmetry plane is represented by the x-y plane. The symmetry boundary condition ensures that the primitive variables are reflected across this plane. The Cartesian velocity component which is changing sign for this symmetry plane is the w component.

Extrapolation from the Interior

The three remaining sides of the computational domain (the exit plane, the top surface and the longitudinal plane opposite the symmetry plane) do not represent any physical surface. The top surface and the side wall of the wind tunnels were assumed [65] [22] [42] or actually measured [84] [85] to be distant enough from the injector not to interfere with the flowfield of interest. Therefore, a first-order extrapolation boundary condition was applied to these surfaces. The first-order extrapolation boundary condition applies the conditions at boundary cells inside the computational domain to the first and second ghost cells. In this way the gradients along the first-order extrapolation boundary condition are always zero.

Zonal Boundaries

A zonal boundary is the surface along which two blocks are connected. In GASP this can be a point-to-point match or a non-matching connection, i.e. not all the points of the two blocks are matching up. The zonal boundaries allow information to be transferred from one computational grid to the next one, and vice-versa.

4.2 Computational grids

GASP uses a finite-volume, structured grid to discretized and solve the governing equations. The grid has to be input into GASP as a Plot3D format file, and it needs to be generated using a separate grid-generation software. In this study, GRIDGEN Version 13.3 [32] was employed to generate the multi-block structured grid. The computational grids used in these calculations were developed in several consecutive stages. As calculations proceeded and a better understanding of the flow-field was obtained, the grid was adapted to better resolve the salient characteristics of the flow without drastically increasing the total number of cells.

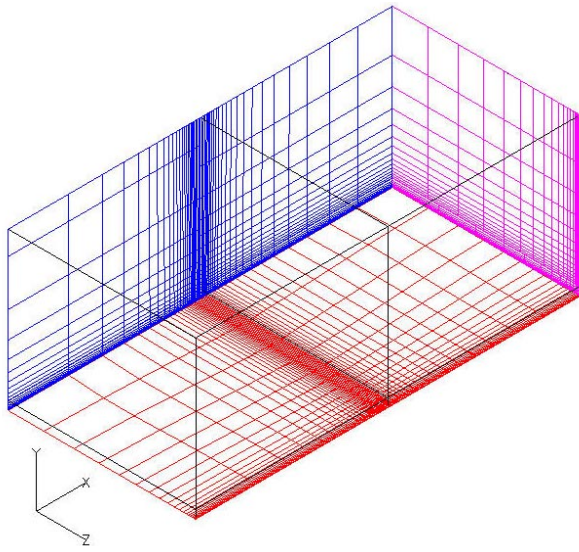
The initial grid was a standard H-type grid with clustering around the injector and near the wall. (see Figure 4.2 (a)). The H-grid topology is the most widely used in other numerical studies of jet interaction on a flat plate (see Ref.[24] through [87]). This grid topology requires the least amount of time to develop, its geometric parameters are quite easy to modify and comparisons between grids of different size are easily performed. However, the main disadvantage of this type of topology is the low efficiency of the cell clustering. Finely spaced cells around the injector mean that the fine mesh has to propagate in the three dimensions away from the injector, thus resulting in an overly refined mesh in regions where the flow is at freestream conditions.

From the simple H-type topology, the grid evolved into a more complex combination of H-type and C-type grids with better cell clustering in the injector and jet plume regions (see Figure 4.2 (b)). A C-type grid can wrap around the injector, and any cell clustering will not be propagated far away from the injector but will stay concentrated around the jet. In fact, the complicated flow physics and the steep pressure gradients found in this region require a finely spaced grid to be accurately resolved. A further and final grid-adaptation step produced an H-type and C-type grid combination with contoured zonal boundaries (Figure 4.2 (c)). The contoured zonal boundaries improved the cell distribution all through the C-grid surrounding the jet thus improving the grid quality. Figure 4.2 (d) shows the outline of the last adaptation process of the grid with a further optimized grid topology and a computational domain now divided into 14 zones to improve the computational efficiency of the grid when using parallel-processing.

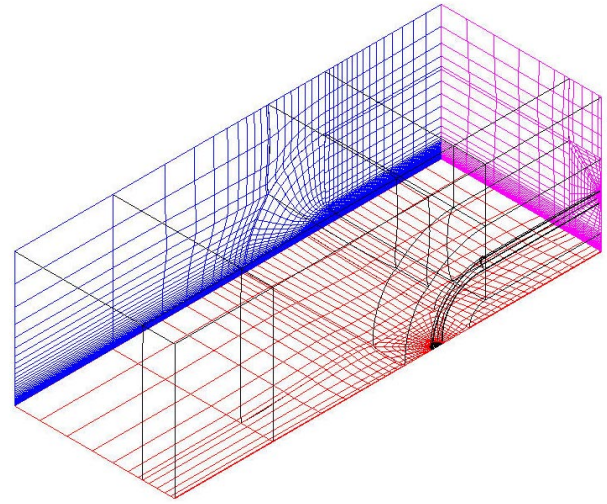
Figure 4.3 shows details of the different computational grids in the region around the primary injector. Figure 4.3 (a) shows the simulations of the primary injector in the H-type grid of Figure 4.2 (a). The injector was simulated by shaping the grid on the surface of the plate in a circular pattern. Note the orthogonality of the grid lines surrounding the injector. In Figure 4.3 (b) the injector simulated in one of the first mixed H- and C-type grids without contouring of the zonal boundaries is shown (the whole grid is shown in Figure 4.2 (b)). Note that the injector surface corresponds to one of the sides of a grid block that extends from the surface of the injector and curves into the direction of the crossflow. The grid that wraps around the jet is a C-type grid. The radial lines of the grid extend from the injector toward the outer boundary of the C-type grid. This outer

boundary maps onto the other H-type blocks. Note that the interface, the zonal boundary, between the C-type grid and the H-type grid is rectangular. Also, note how the C-type topology allows to optimize the clustering of the cells around the injector and compare this distribution to the less-efficient cell distribution of the H-type topology of Figure 4.3. The final large optimization process performed on the grid was to contour the outer boundary of the C-type grid in a circular shape as shown in Figure 4.3 (c) (the mesh detail corresponds to the grids shown in Figure 4.2 (c) and (d)). Again, the grid consists of a mixed H- and C-type topology but the contouring of the zonal boundaries allowed an improved cell distribution when compared to the grid shown in Figure 4.3 (b). Note that the C-type grid encloses the flat plate region where the strongest pressure gradients are found.

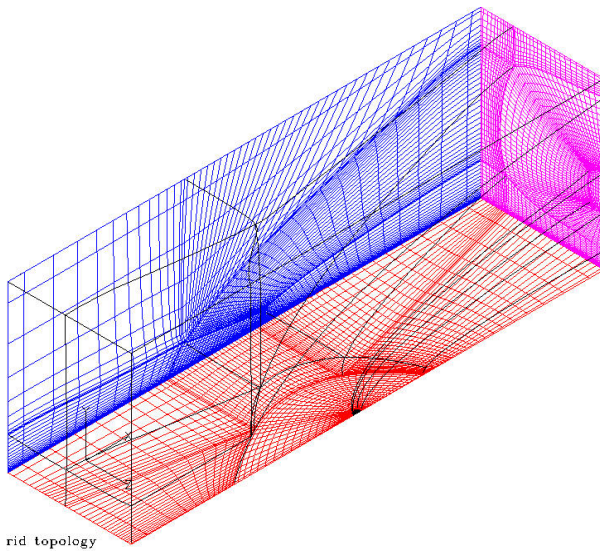
Due to the fact that each experiment had different entry lengths and different injector dimensions, the grids had to be modified each time to match the physical dimensions of the plate and of the injector. The multi-block nature of the grid (i.e. the fact that the physical space simulated by the computational domain is subdivided into several computational sub-domains) allowed the extension of the flat plate by simply inserting an additional zone ahead of the original computational domain, when necessary. The grid size ranged from 1.0 million cells to 1.5 million cells. The grid size was dictated by the need to find a balance between the grid refinement and the time to converge a solution to a steady state. On average, it would take 2090 total CPU hours using SGI Origin CPUs to converge a turbulent calculation using a 1.5 million-cell grid. It was therefore paramount to optimize the cell clustering without increasing the number of grid cells. The original grids were sequenced twice so that three grid sequences would be produced: the fine, the medium and the coarse grid. Sequencing was automatically performed by the CFD code by eliminating every other grid point in the three spatial directions. In this way, the number of cells in the fine grid was 8 times (i.e. $2 \times 2 \times 2$) larger than the number of cells in the medium grid and 64 times ($4 \times 4 \times 4$) larger than the coarse grid. Sequencing is beneficial to the convergence of a solution for several reasons: (a) it allows the use of a higher CFL number, (b) it provides a higher level of absolute convergence since the relative tolerance is based on the interpolated solution and not on the solution from the initial conditions, and (c) it speeds up overall convergence thus requiring less CPU time [27].



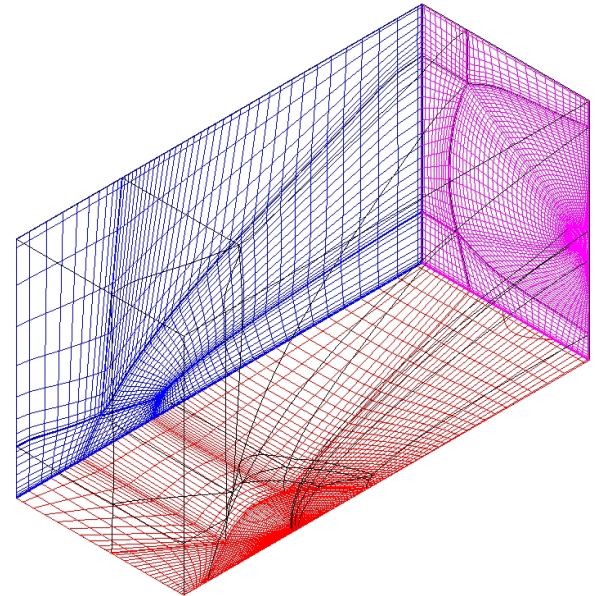
(a) H-Type grid, 967,680 cells, used in the Schetz laminar case.



(b) H- and C-Type grid, 766,488 cells, used in the Cubbison laminar case.

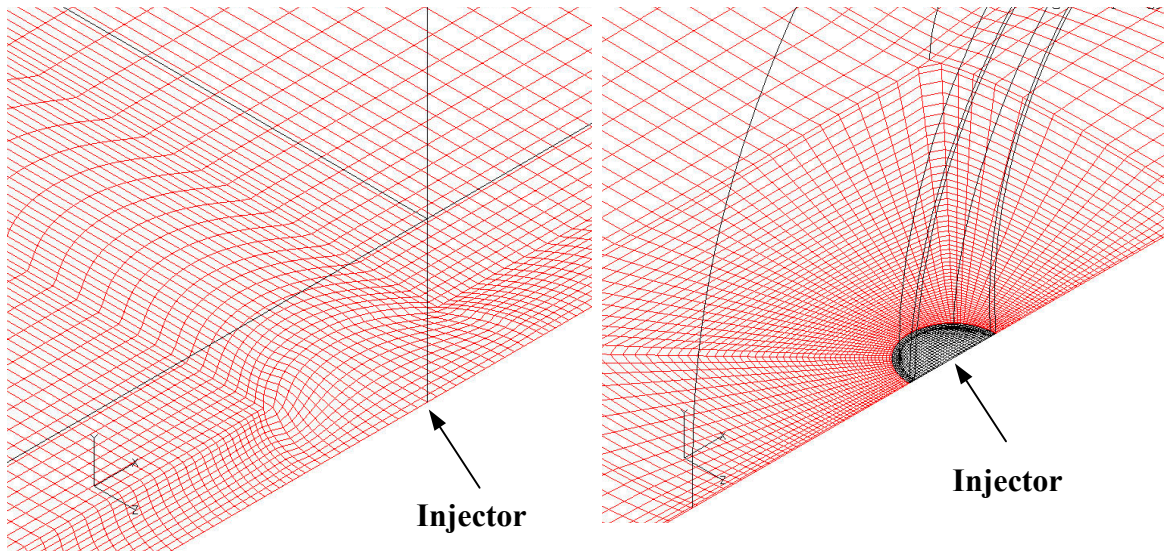


(c) H- and C-Type grid, 902,240 cells, used in the Letko turbulent case.



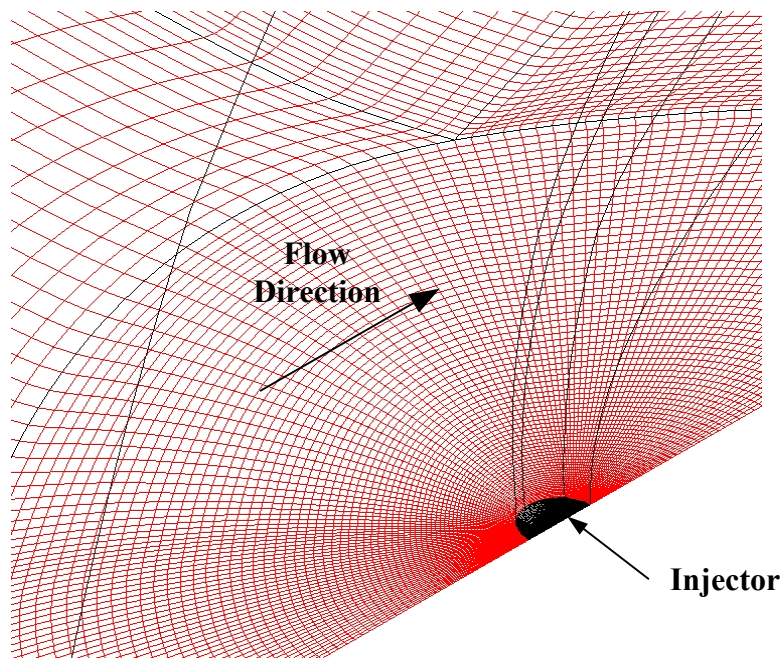
(d) H- and C-Type grid, 1,460,672 cells, used in the Virginia Tech Mach 2.4 and Mach 4.0 turbulent cases.

Figure 4.2. Overview of the adaptation of the computational grid.



(a) simple H-type grid (Schetz laminar case)

(b) combination of H-type and C-type grids (Cubbison laminar case)



(c) combination of H-type and C-type grids with contoured zonal boundaries (Letko and Virginia Tech Mach 2.4 and 4.0 turbulent cases)

Figure 4.3. Comparison of the grids wrapping around the injector for the three grid topologies. See also the previous figure for comparison.

Specific details about each individual grid are given in the Results section concerning the specific numerical calculation. Some common features of all the grids can be listed here:

- 1) The computational domain covered only half of the flat plate, since it was assumed that a longitudinal plane of symmetry passing through the primary jet centerline existed. This is a common assumption in the study of normal injection, and it is validated by experimental evidence.
- 2) The origin of the right-handed coordinate axes used in all of the jet interaction simulations is located at the center of the primary injector. The positive X-coordinate is downstream, the positive Y-coordinate is away from the top surface of the flat plate.
- 3) In the normal direction, away from the wall, initial spacing Δy was determined using the relation:

$$\Delta y = \frac{0.7L}{\sqrt{\text{Re}_L}} \quad (3.54)$$

The adequacy of the normal spacing was then assessed by calculating the y^+ for the cells on the flat plate surface ahead of the separation region. All the cells adjacent to the solid surface were below a y^+ of 1.0. This spacing close to the wall is a widely accepted value for accurate predictions using the $k-\omega$ turbulent model in wall-bounded turbulent flows.

- 4) One-dimensional hyperbolic tangent stretching [80] was used in all regions to distribute the cells along the grid connectors. This type of stretching has been used in several numerical works [15], since it provides an effective way to smoothly vary the cell spacing along a line.
- 5) An elliptic solver was run on all the planes of the computational domain. The elliptic solver improves the orthogonality (quality) of the mesh, especially in those regions where the blocks intersect with sharp or convex corners. Orthogonality is also very important on the plane of symmetry since skewing will create a strong grid-dependence on this plane.
- 6) The injector was simulated by cells on the surface of the flat plate with imposed pressure and velocity equal to the jet total conditions (see Figure 4.3). Due to the plane of symmetry of the problem only half of the injector was simulated.

The simulated injector has the same circular shape as the real nozzle, but its dimensions are slightly smaller. The area ratio of the simulated to the real injector corresponds to the discharge coefficient measured during the experiments. By reducing the area of the simulated injector the viscous effects of the flow through the real nozzle were taken into consideration and the mass flow through the simulated injector is the same as that of the real injector (see also Section Chapter 55.4.35.4.3).

In only one case, (the Virginia Tech Mach 4.0 case, see Section 5.7) a Chimera grid was used to simulate the secondary injectors. The Chimera grid was used to substitute a regular block of the original computational domain. The block that was substituted and the Chimera grid that replaced it are shown in Figure 5.62 (a) and (b), respectively. The Chimera grid was considerably finer than the original block (179,564 cells versus 814,044 cells) since one of the goals of the substitution was to better resolve the flow details in the region around the secondary injector and to perform a localized grid convergence study.

Chimera is a well-known method in CFD [77][9][76] that uses multi-block overlapping structured grids to model complicated geometries and resolve flow physics where most needed without re-gridding the entire computational domain. A Chimera grid is essentially a grid that does not require a point-to-point boundary with the neighboring grids as usually is the case in multi-block grids. Furthermore, the boundaries between the Chimera grid or block and the other blocks do not have to be fixed at the same location, but they can move with time. A Chimera grid can be completely embedded inside another grid so as to provide a very fine grid in a localized region without having to increase the number of cells in all the rest of the domain. The Chimera or overset grid method is a capability made available in GASP starting with GASP Version 4.0.

Usually Chimera boundaries are non-conservative [38] and issues are often raised about the error introduced by the Chimera boundaries in the numerical solutions. There are two opposing lines of thought about the conservation error. The first one states that as long as the grid is fine enough, then the numerical solution is a valid physical answer. The second line of thought states that conservation is necessary to obtain a valid numerical solution no matter how fine the grid is. It has been shown [88] that if the Chimera boundaries are far from discontinuities then the solution is not affected by the conservation error and that the error decreases as the grid is refined.

Chapter 5

Results

5.1 Overview of Considered Cases

In this section the salient results of the computational work and their comparison to the experimental data are presented in detail. The results are presented in a logical order (that roughly also matches the chronological order in which the calculations were performed) starting from the simplest jet interaction cases with a laminar boundary layer and the lowest pressure ratio and ending with the most complicated jet interaction cases with a turbulent boundary layer and multiple injectors. Table 5.1 is a description of the numerical computations performed, each computation named after the author of the experimental work that it simulated.

In all of these experiments and calculations, the freestream flow had supersonic conditions. The primary and secondary injectors were circular in shape, injected normal to the flat plate surface and had sonic conditions at the exit. The types of comparison between the experiments and the CFD solutions were limited to the type of experimental data reported by the authors. Schetz, et al. [65] reported only a Schlieren picture of the barrel shock, therefore the comparison of the numerical solution to the experiment was limited to the visual comparison of the photographed and computed interaction shock and barrel shock. Cubbison [42] reported both Schlieren photographs of the barrel shock and pressure mappings on the surface of the flat plate. Therefore, the comparison of the experimental data to the numerical solution involved both the visual comparison of the shape of the interaction and barrel shocks and the comparison of the C_p mapping on the surface of the flat plate. Furthermore from the pressure mappings, the normal force and pitching moment acting on the plate could be estimated. The computation of the experimental forces and moments was performed by discretizing the mappings into small areas, computing the normal force and moments acting on each individual area element and then integrating the individual contributions over the entire area of the flat plate. In this way, the computed and experimentally measured normal force (F_y) and pitching moment (M_z) acting on the plate could be compared. The same type of comparisons as the Cubbison case were carried out for the Letko [22] case with the exception of the visual comparisons, since no Schlieren photographs were reported in the original Letko paper.

The most comprehensive set of information was available for the Virginia Tech cases [84][85], since a close collaboration between the author of this work and the researcher carrying out the experiments (Scott Wallis) was present since the beginning of this study. The numerical study was intended to guide the development and the design of the experimental setup. In a coordinated effort, the numerical study would indicate the

location of the secondary jet that produces the most desirable results. It would also provide the researchers with an insight into the physics that govern the complicated flow field and that produce those phenomena of which the experiment can only measure the final effects (i.e. pressure field, skin friction, force and moments, shocks etc.). With this knowledge available, the experimentalist could design the experimental setup and validate (or confute) the numerical results. The benefits of this integrated and coordinated experimental-numerical approach to the study of a complex flow field is described and discussed in detail by Schetz, et al. [67]. Another advantage of the Virginia Tech experiments results over the other experimental works was the use of the Pressure Sensitive Paint (PSP) to create a continuous mapping of the pressure field acting over the flat plate surface. PSP technology enabled a direct and thorough comparison of the experimental and numerical pressure field on the flat plate without the need, for the experimentalist, to create isobar lines by interpolating between the discrete data available at the pressure orifices. Force and moment balances were not mounted on the Virginia Tech experimental setup but again, these quantities could be calculated using the pressure mappings on the surface of the flat plate. Also, Schlieren photographs were available for a visual comparison of the shape and location of the barrel and bow shocks.

Simulation Name	2D/3D	M_∞	M_j	PR	Lam/Turb	Re_L [m^{-1}]	Normal/Inclined Inj.	Gas	Turbul. Model	Experiment	Comparison of
Schetz	3D	2.10	1.0	60	Lam	1.24×10^7	Normal	Air/Air	N/A	Schetz, 1966 [65]	Schlieren photograph
Cubbison	3D	2.92	1.0	677	Lam	2.76×10^6	Normal	Air/Air	N/A	Cubbison, 1960 [22]	Schlieren photograph Pressure Mapping
Letko	3D	4.5	1.0	680	Turb	1.74×10^7	Normal	Air/Air	$k-\omega$	Letko, 1963 [42]	Pressure Mapping
Virginia Tech Mach 2.4 Primary Jet Alone Primary Jet + Group 1 Jets Primary Jet + Group 1 & 2 Jets	3D	2.4	1.0	14	Turb	4.03×10^7	Normal	Air/Air	$k-\omega$	Virginia Tech, 2000 [84]	Pressure Mapping Forces and Moment on Flat Plate
Virginia Tech Mach 4.0 Primary Jet Alone Primary Jet + Group 2 Jets	3D	4.0	1.0	532	Turb	5.14×10^7	Normal	Air/Air	$k-\omega$	Virginia Tech, 2001 [84]	Pressure Mapping Forces and Moment on Flat Plate
Virginia Tech Ramp Cases	3D	3.92	1.0	474	Turb	5.57×10^7	Normal	Air/Air	$k-\omega$	Virginia Tech, 2001 (Ramp cases)	Pressure Mapping Forces and Moment on Flat Plate

Table 5.1. Jet-interaction numerical simulations (a) laminar (b) turbulent (all turbulent calculations employed Wilcox's $k-\omega$ turbulence model [91]).

5.2 Definition of Parameters.

As mentioned above, depending on the information available for the experiments, the comparison of the flowfield observed in the experiment to the numerical solution involved a visual-qualitative comparison of the flow features and a quantitative comparison of such parameters as the forces and moments acting on the flat plate or the distribution of the pressure and skin friction coefficients. These parameters are very common to most readers, since they are fundamental quantities of fluid-dynamics. However, for completeness and to avoid any confusion regarding the definition of these parameters in this work, their definitions are presented in this section.

The pressure coefficient, C_p , is one of the most basic parameters in the study of fluid-dynamics. It is defined as:

$$C_p = \frac{p - p_\infty}{q} \quad (5.1)$$

where q is the dynamic pressure defined as:

$$q = \frac{1}{2} \rho_\infty V_\infty^2 \quad (5.2)$$

The skin friction coefficient, C_f , is defined as:

$$C_f = \frac{F_x}{qA} \quad (5.3)$$

where A is a reference area and F_x is the viscous force component in the same direction as the freestream.

The normal force acting on the flat plate, F_y , is obtained by integrating the pressure coefficient over a given area A :

$$F_y = q \cdot \oint C_p dA \quad (5.4)$$

Note that when integrating only the pressure p instead of the pressure coefficient, the result is the force that would be produced if on the opposite side of the flat plate there was just a vacuum. Similarly to the force, the pitching moment, M_z , is given by:

$$M_z = q \cdot \oint (C_p \cdot x) dA \quad (5.5)$$

where x is the longitudinal distance along the flat plate with the origin of the axes located at the center of the injector. It is important to remember that these forces and moment do not include the contributions produced by the thrust of the primary and secondary injectors. Furthermore, when integrating the pressure coefficient to obtain forces and moments, the projected area of the injector was excluded from the integration altogether so that only the pressure force acting on the solid surface of the plate was taken into consideration.

The normal force coefficient, C_{F_y} , is obtained dividing F_y by the thrust of the primary jet:

$$C_{F_y} = \frac{F_y}{\text{primary jet thrust}} \quad (5.6)$$

The pitching moment coefficient, C_{M_z} , is obtained normalizing M_z by the jet thrust and the jet diameter, d_j :

$$C_{M_z} = \frac{M_z}{\text{primary jet thrust} \cdot d_j} \quad (5.7)$$

Note that according to the coordinate axis used to define the computational domain in this study, a negative pitching moment about the center of the primary jet indicates a nose-down moment. This convention is schematized in Figure 5.1.

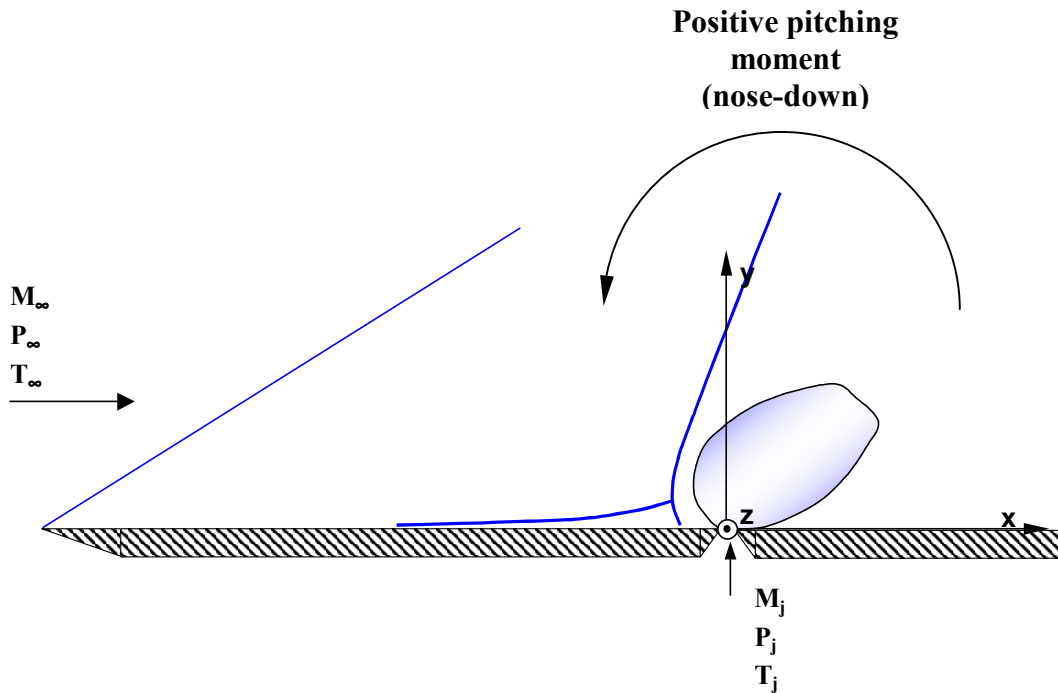


Figure 5.1. Reference coordinate system and pitching moment sign convention for the jet interaction problem. Note also the pressure ratio definition used in this work. The definition comes from Cubbison '61 [22].

Another important factor to keep in mind is that the normal forces and pitching moment depend on the area of integration. Therefore both parameters can vary largely depending on the selected area of integration. The pitching moment is particularly sensitive to this issue since if the integration includes a large area in front of the injector where there are freestream conditions this would produce a strong nose-down moment. Also, the limits of integration depend on the dimensions of the flat plate used in the experiments. Therefore, it is not possible to compare one set of force and moment coefficients obtained for one test case with another since the area of integration will be different for the two experiments. The influence of the limit of integration on the normal force and pitching moment is illustrated in Figure 5.2. In this plot, the force and moments are normalized using the area of integration and the dynamic pressure instead of the jet thrust as before. These new force and moment coefficients are identified by the dash sign (.') and are defined as $C_{F_y}' = Fy/(q A)$ and $C_{M_z}' = Mz/(q A d_j)$, respectively. The normal force coefficient (solid squares) shows that when no jet is activated (dashed line with solid rectangles), the force coefficient is independent of the limits of integration; this is easily explained by the fact that the freestream pressure is constant over the flat plate and therefore, when normalized using the area of integration, it will produce a constant values. When the injector is switched on (solid line with solid squares), the force coefficient is higher when the limits of integration are closer to the injection location. As the limits of integration are moved away from the injector, the force coefficient decreases asymptotically to a value which is the summation of the contribution coming from the

freestream pressure (the dashed line with the solid squares) and the jet interaction flowfield. The effects of the jet interaction flowfield mainly influence the region in the immediate surroundings of the injection location as shown by the negative slope of the curve corresponding to the case with the jet on. The negative slope indicates that as the integration limits are moved further downstream, the normal force augmentation factor remains approximately constant indicating that the flow-physics causing the increase in normal force exist in the immediate surroundings of the injector. The same conclusions can be drawn from the plot of the pitching moment coefficient. When the jet is not activated, the pitching moment coefficient shows a constant negative slope as the limits of integration are extended further downstream. This behavior is explained by noting that forces acting aft of the injector produce a negative pitching moment. Therefore, when the limits of integration are extended downstream, there will be a larger force acting at a longer moment arm aft of the injector, creating a more negative pitching moment. When the jet is activated (solid line with solid rhomboids), the slope of the line becomes more negative in the region nearby the injector. As the limits of integration are extended downstream, the slope goes back to the no-jet value. As in the case of the normal force coefficients, this behavior indicates that the jet-interaction flow-physics responsible for the decrease in the pitching moment are concentrated around the injector location and the downstream flowfield does not influence the pitching moment to a high degree.

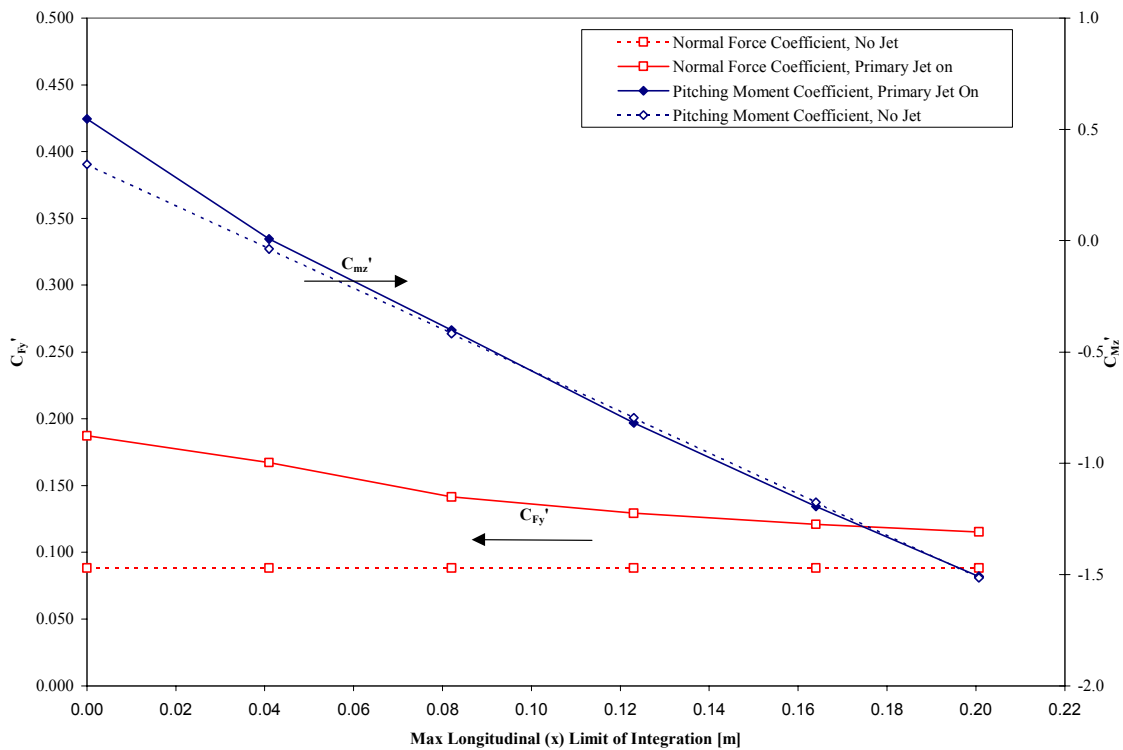


Figure 5.2. Reference coordinate system and pitching moment sign convention for the jet interaction problem. Note also the pressure ratio definition used in this work. The definition comes from Cubbison '61 [22].

5.3 Sources of Error in the Numerical Simulations.

Numerical simulations of complex flow fields are sometimes regarded with skepticism by the scientific community. This skepticism finds foundations in the results of “numerous blind validation studies” [62] that undermine the credibility of numerical simulations. In order to increase the confidence of researchers and, in particular, of experimentalists in CFD it is essential to perform a careful and thorough study of the accuracy of the numerical solution. The uncertainty level in CFD solutions should be assessed using the latest developments in error analysis for numerical schemes. The present discussion is a review of the analysis presented by Roy [62] with additional details from Roache [58][59] and Hosder, et al. [35].

The uncertainty, or error, of numerical simulations can be divided into two broad areas, namely verification and validation. Verification deals with the mathematics of the set of equations that are being solved and can be thought of as “solving the equations right” [62]. Errors under this topic include iterative convergence errors, grid-convergence (discretization) errors, coding (or human) errors, and computer round-off errors. Validation deals with the physical modeling of the problem and can be thought of as “solving the right equations” [62]. Errors due to the inaccuracy of the physical models (i.e. the governing equations) to describe the flow physics and inaccuracies in the boundary solutions and in the geometry modeling of the problem fall under the validation group. Verification must be performed before validation since for the comparison of the numerical results to the experimental results to be meaningful, the reliability and accuracy of the numerics must be ascertained first. However, in practice it is extremely difficult to separate the two types of uncertainties, especially for complex flow problems such as the present jet interaction flowfield. In the current work both the verification and validation errors associated with the numerical simulations of the jet interaction flowfield are analyzed and estimated. However, due to the difficulty of the estimation of the experimental uncertainty, the errors in the physical modeling are just discussed without attempting to quantify them. The methods employed in this study to reduce the numerical uncertainty are presented and discussed.

5.3.1 Iterative convergence of the numerical solutions.

The convergence of the calculations was determined by checking the change of several flow parameters over time. An approximate indication of the convergence of the solution was given by the plot of the normalized residual against the iteration number (Figure 5.3). In general, the smaller the residual the closer the solution is to convergence. However, convergence of the residual does not imply convergence of the flow, and many flow characteristics continue to evolve also after the residual has reached a constant value. If the focus of the numerical study is a particular flow variable or integrated quantity, then it is reasonable to consider the calculation converged, at least for the scope of the study, when that parameter has leveled off or oscillates about a fixed value. In this study, three primary integrated quantities were constantly checked for convergence: the normal force over the flat plate, the pitching moment and the axial force (drag). These quantities are plotted versus the iteration number in Figure 5.4 for the Virginia Tech Mach 4.0 case with only the primary jet activated. While the normal force and pitching moment are parameters governed mainly by inviscid flow features, basically the pressure distribution on the surface of the flat plate, the axial force depends on the viscous features that develop in the boundary layer, mainly the skin friction. Since viscous effects tend to be slower to form and converge than inviscid features, the axial force is a more reliable indication of convergence than the normal force or the pitching moment. Still since forces and moments are integrated quantities, they indicate the general level of convergence of the whole flowfield smoothing out differences in convergence level between different flow features and different locations. An example of such a difference in convergence level is the separation region. In the jet interaction flowfield, the separation location is particularly slow to converge, since it is created by the complex viscous interaction of the incoming boundary layer with the bow shock that, in turn, depends on the barrel shock. To assess the convergence of the numerical solution in the separation region, the distribution of the pressure coefficient and of the skin friction coefficient on the flat plate surface along the tunnel centerline were plotted versus the iteration number (see Figure 5.5).

The iteration number does not literally correspond to any specific physical time. It is anyway an indication of the level of advancement of the iterative process. How fast the convergence is for a specific problem depends on two main factors, these being the speed of the CPU and the largest admissible CFL number. The speed of the CPU concerns the real physical time (also called wall-clock time) that the machine needs to run one iteration. The CFL number (CFL stand for Courant, Friedrichs and Lewy, Ref. [20]) concerns the time needed in an iteration to reach a steady-state solution. The CFL number establishes a relationship between the characteristic size of the discretized space (i.e. Δx) and a time step (i.e. Δt).

The relationship between these two quantities is given by:

$$CFL = c \frac{\Delta t}{\Delta x} \quad (5.8)$$

where c is a constant of proportionality depending on the numerics of the problem. The maximum admissible CFL number is fixed for a given problem according to the ‘‘CFL condition’’ that takes into consideration the stability of the iterative process. In general, the stability of the numerical scheme employed in the iterative process can be analyzed using a Von Neumann stability analysis (note that a Von Neumann stability analysis is valid only for linear differential equations while the RANS equations are not linear and only a rough estimate of the stability conditions can be obtained from this type of approach). The CFL condition indicates what is the maximum allowable CFL that will produce a stable convergence behavior for the numerical scheme being employed in the iterative process. Note that the parameter ‘‘ c ’’ too is fixed by the flow conditions and the iterative process. Therefore, the smaller the grid size, represented by Δx , the smaller the allowable time Δt . Small time steps mean that more iterations will be needed to reach a converged solution. In GASP, the time step is calculated from

$$\Delta t = \frac{CFL \Delta x}{c} \quad (5.9)$$

where the CFL number, is input by the user. GASP calculates the group $c/\Delta x$ from:

$$\frac{c}{\Delta x} = \frac{\oint (|\mathbf{V} \cdot \hat{\mathbf{n}}| + a) dA}{Vol} \quad (5.10)$$

GASP has the option of time-stepping using three different strategies. The first one obtains the group $c/\Delta x$ by calculating the characteristic speed $|\mathbf{V} \cdot \hat{\mathbf{n}}| + a$ with freestream quantities. In this way, the fastest free-stream characteristic speed, $q_\infty + a_\infty$ is used in the calculation of the time step. The second strategy uses the local quantities to compute the characteristic speed and therefore the fastest local characteristic speed, $q + a$, is used to compute Δt at each cell. The third option employs a physical time stepping, i.e. Δt is input by the user as one value for all the cells. The first option is useful only in certain situations, since it tends to slow down the convergence of the solution in the viscous layers where the characteristic speed would be much lower than the freestream. The second option, employing the local characteristic speed, is the quickest way to reach convergence for most applications, since the fastest characteristic speed for each cell is used. However, it is clear that when employing these two options the time step changes from cell to cell, therefore a non-converged solution does not represent an instantaneous flow snapshot since different parts of the domain will be at a different physical time. Only the third option produces a flow solution that is at the same physical time all through the domain and therefore is the most realistic, especially when the converged

solution is unsteady. In this study, the solution was converged using a local or a freestream characteristic speed, depending on the stability of the calculation. After convergence was reached, a few iterations were run using the characteristic time stepping option to guarantee that the flow was at the same physical time all over the domain. In light of the above observations and noting that the CFL could be changed during a calculation depending upon stability considerations, it is clear that the iteration number does not indicate the physical-time a calculation has been running. However, in the convergence plots shown here the iteration number can be conveniently used as an indicator of the level of advancement of the calculation. Also, since one iteration corresponds to a given wall-clock time, knowing the time it takes a given machine to run one iteration, the iteration number can indicate how expensive a calculation is to converge.

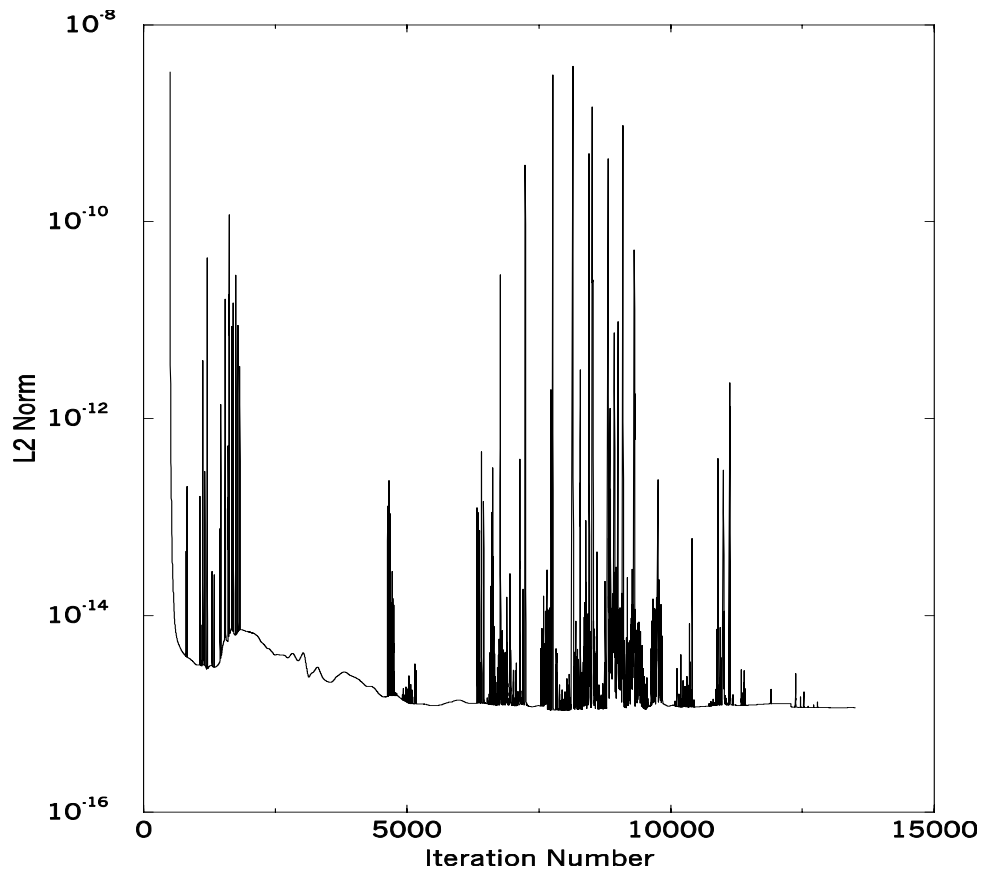
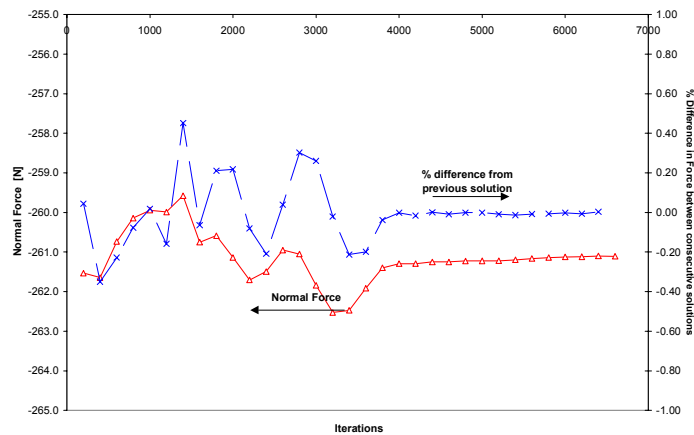
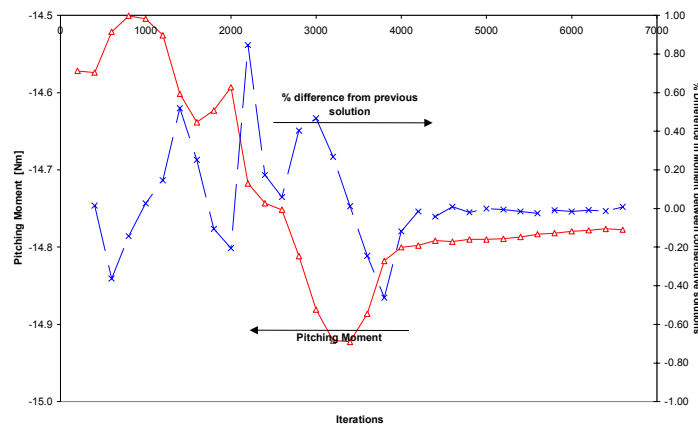


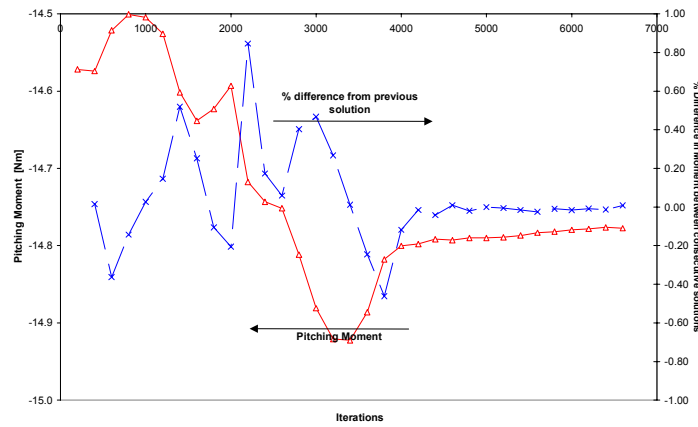
Figure 5.3. Residual history for the medium grid sequence of the Virginia Tech Mach 4.0 case with only the primary jet activated.



(a) Normal Force (F_y)

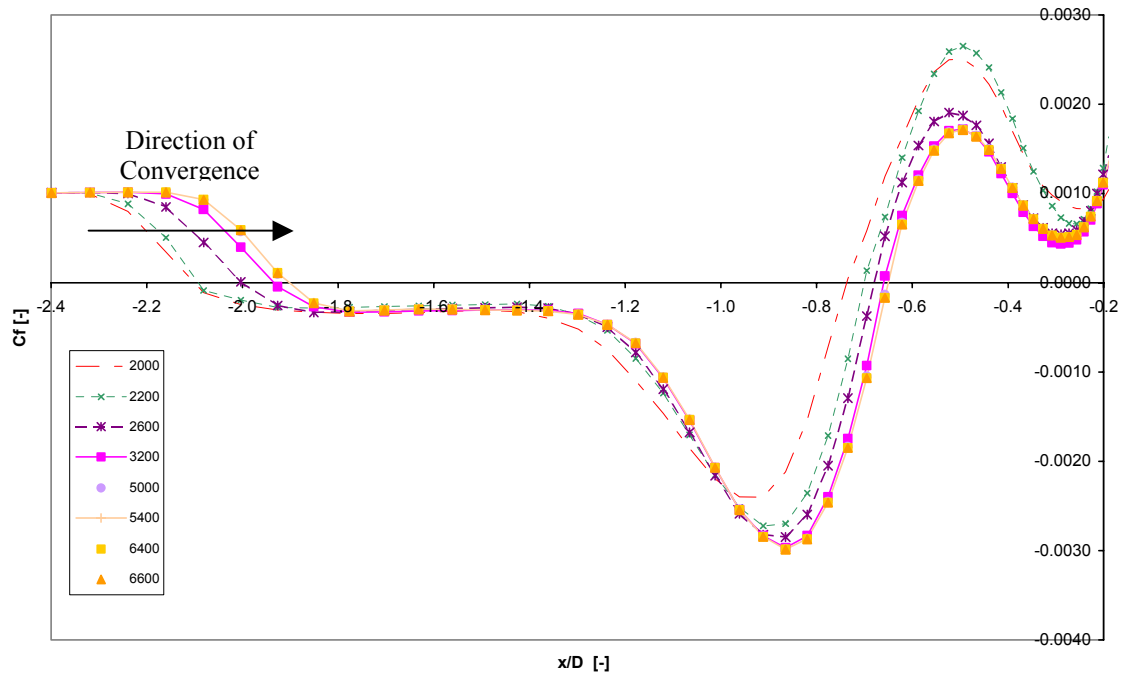


(b) Pitching Moment (M_z)

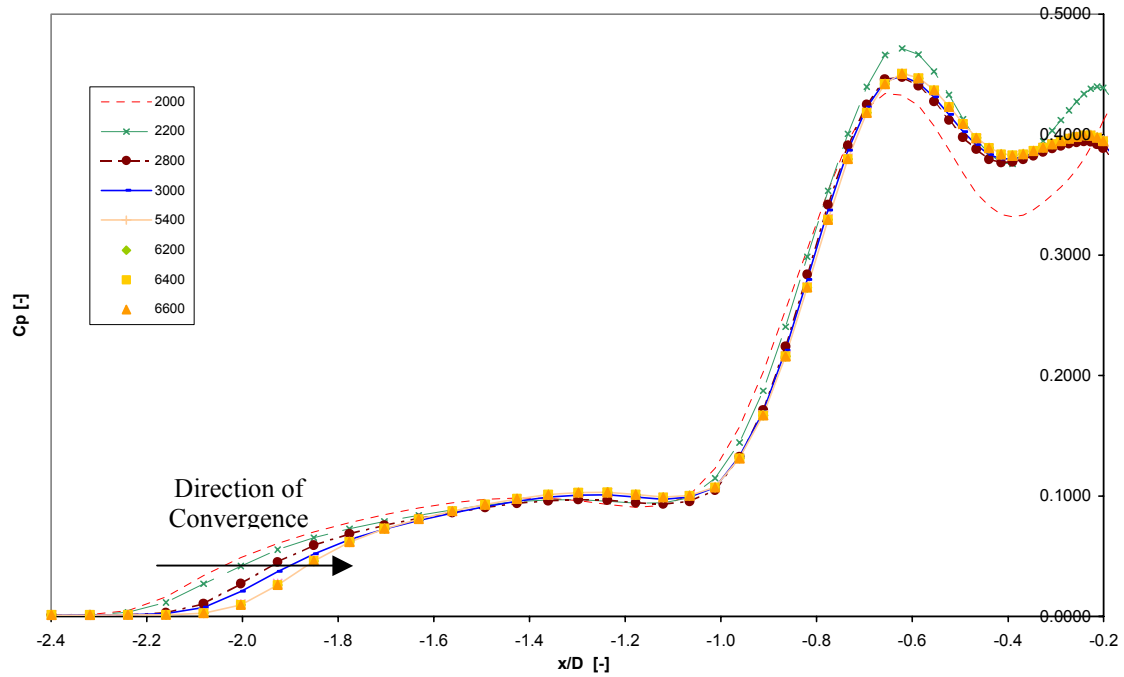


(b) Axial force (F_x)

Figure 5.4. History of the convergence of the numerical solution. The three main parameters used to check for convergence were (a) the normal force, (b) the pitching moment and (c) the axial force. This history is for the Virginia Tech Mach 4.0 case with only the primary jet activated.



(a) Skin friction coefficient (C_f)



(b) Pressure coefficient (C_p)

Figure 5.5. Residual history for the Virginia Tech Mach 4.0 case with only the primary jet activated.

5.3.2 Grid-convergence error.

The most widespread and reliable methods to assess the grid-convergence for complex numerical problems are based on the Richardson extrapolation [58]. The starting point is a grid refinement study with at least a converged solution on two grid sequences, the ratio between the number of the cells on the two sequences being variable. In its general form, the Richardson extrapolation uses the solution on the two grid sequences and the knowledge of the nominal order of accuracy of the numerical scheme to produce an error estimate in the numerical solution. However, this approach can be misleading in that the nominal order of accuracy can be quite different from the real or observed order of accuracy. This discrepancy between the nominal and observed order of accuracy is particularly large for high-speed compressible flows that have shocks. In most commercial numerical codes, the numerical methods used to tackle high-speed compressible flows are second-order, characteristic-based, upwind schemes, mainly due to their accuracy and stability properties. However, in order to avoid non-physical oscillations around shocks, limiters are used. Limiters reduce the order of accuracy of the scheme to first-order in the regions across the shock. All of the simulations performed in this study with GASP used a third-order spatially accurate scheme for the inviscid terms. The min-mod limiter was used consistently with third-order schemes to reduce the oscillations. This mixed order of accuracy greatly increases the difficulty in performing grid-convergence analysis, since it produces a non-monotonic convergence of some of the flow properties as the grid is refined [61]. The non-monotonic behavior of the convergence is further exacerbated by the use of the κ - ω turbulence model [35]. It was, therefore, necessary to use the Generalized Richardson Extrapolation by Roache [58] that employs the discrete solutions on three different grid sequences called the ‘‘Mixed 1st + 2nd Order Extrapolation’’. An ideal error estimator would produce an error that is both very close to the real error and that has a statistical measure of the confidence that the error will be conservative (usually a 2σ or 95% confidence band). However, for complex non-linear, multi-dimensional problems such as the jet interaction flowfield, it is almost impossible to prove and to assess such an error band. The researcher is then forced to rely a not-so-rigorous and heuristic method, such as the one here presented, to determine discretization errors.

General Richardson extrapolation

The Richardson extrapolation procedure is based on a series expansion of the discretization error, DE, on the grid level k :

$$DE_k = f_k - f_{exact} \quad (5.11)$$

where f_{exact} is the exact solution and f_k is the solution on grid level k . On a uniform grid the series expansion for the solution can be written as:

$$f_k = f_{exact} + g_1 h_k + g_2 h_k^2 + g_3 h_k^3 + O(h_k^3) \quad (5.12)$$

where g_i is the i th order error term coefficient and h_k is a measure of the grid spacing in sequence k . Then, the above equation is written for a number of grid sequences solved for an approximate f_{exact} and the error term coefficients, g_i . In certain cases, an error term of an “observed” order p will be used and the equation solved for both the error term coefficients and p . The fine grid spacing can be normalized to unity so that a grid refinement factor for sequence k , r_k , can be introduced, r_k being defined as:

$$r_{k,k+1} = \frac{h_{k+1}}{h_k} \quad (5.13)$$

For example, in a three-dimensional domain, if the number of cells is doubled in each of the three spatial directions, the total number of cells will increase by 8 (i.e. 2x2x2) and the grid refinement factor will be 8. For convenience, define also the difference between the solution of two successive grid sequences, ϵ , as:

$$\epsilon_{k+1k} = f_{k+1} - f_k \quad (5.14)$$

Richardson extrapolation can be generalized following Roache [58] to a general grid refinement factor r and order p . In this case the series expansion of Eq (5.12) is written as:

$$\begin{aligned} f_1 &= f_{exact} + g_p h_1^p + O(h_1^{p+1}) \\ f_2 &= f_{exact} + g_p h_2^p + O(h_2^{p+1}) \end{aligned} \quad (5.15)$$

The above equations can be used to find the p^{th} order error coefficient g_p and the exact solution, f_{exact} , by dropping the higher-order terms, to give:

$$\begin{aligned} \tilde{g}_p &= \frac{\epsilon_{21}}{r^p - 1} \\ \tilde{f}_{exact} &= f_1 - \frac{\epsilon_{21}}{r^p - 1} \end{aligned} \quad (5.16)$$

where the order of the discretization p must be assumed since only two solutions are used. In general, the nominal order of accuracy is used as p . In order to estimate the real order of accuracy, at least three solutions are needed. These three solutions should be monotonic as the grid is refined and, to recover the nominal order of accuracy, the solutions should be in the asymptotic grid convergence range. If all these conditions are met, then we can write, in the same fashion as Eq (5.12):

$$\begin{aligned}
f_1 &= f_{exact} + g_p h_1^p + O(h_1^{p+1}) \\
f_2 &= f_{exact} + g_p h_2^p + O(h_2^{p+1}) \\
f_3 &= f_{exact} + g_p h_3^p + O(h_3^{p+1})
\end{aligned} \tag{5.17}$$

Neglecting the higher-order terms, the above equations can be solved for approximations to the order p , the error coefficient g_p and the exact solution f_{exact} as:

$$\begin{aligned}
\frac{r_{12}^p - 1}{r_{12}^p r_{23}^p - 1} &= \frac{\mathcal{E}_{21}}{\mathcal{E}_{21} - \mathcal{E}_{32}} \\
\tilde{g}_p &= \frac{\mathcal{E}_{21}}{r^p - 1} \\
\tilde{f}_{exact} &= f_1 - \frac{\mathcal{E}_{21}}{r^p - 1}
\end{aligned} \tag{5.18}$$

The top line of the previous equation has to be solved iteratively since it is implicit in p . If the refinement factor r is constant for the three grid sequences, then the equation for p can be reduced to:

$$p = \frac{\ln(\mathcal{E}_{32} / \mathcal{E}_{21})}{\ln(r)} \tag{5.19}$$

Problems arise when the solutions do not converge monotonically as the grid is refined. In this case the ratio $\mathcal{E}_{32}/\mathcal{E}_{21}$ is less than zero and p is undefined. This issue has been heuristically solved by Celik and Karatekin [13] by adding a negative sign in front of the negative \mathcal{E} term so that the natural logarithmic is defined. However, although the method provides an order of accuracy p for no-monotone solutions, no mathematical justification for this procedure was provided.

Mixed 1st+2nd order Richardson extrapolation

The Richardson extrapolation procedure is based on a series expansion of the discretization error, DE, on the grid level k :

$$DE_k = f_k - f_{exact} \tag{5.20}$$

where f_{exact} is the exact solution and f_k is the solution on grid level k .

On a uniform grid the series expansion for the solution can be written as:

$$f_k = f_{exact} + g_1 h_k + g_2 h_k^2 + g_3 h_k^3 + O(h_k^3) \quad (5.21)$$

where g_i is the i th order error term coefficient and h_k is a measure of the grid spacing in sequence k . Then, the above equation is written for a number of grid sequences solved for an approximate f_{exact} and the error term coefficients, g_i . In certain cases, an error term of an “observed” order p will be used and the equation solved for both the error term coefficients and p . The fine grid spacing can be normalized to unity so that a grid refinement factor for sequence k , r_k , can be introduced, r_k being defined as:

$$r_{k,k+1} = \frac{h_{k+1}}{h_k} \quad (5.22)$$

For example, in a three-dimensional domain, if the number of cells is doubled in each of the three spatial directions, the total number of cells will increase by 8 (i.e. 2x2x2) and the grid refinement factor will be 8. For convenience, define also the difference between the solution of two successive grid sequences, ϵ , as:

$$\epsilon_{k+1k} = f_{k+1} - f_k \quad (5.23)$$

The “Mixed 1st+2nd Order Extrapolation” method requires the solution on three different grid sequences, which is the usual number of grid sequences used in this study to converge a solution on the fine grid. The solution on the each grid sequence can be written as a series expansion from (5.21) as:

$$\begin{aligned} f_1 &= f_{exact} + g_1 h_1 + g_2 h_1^2 + O(h_1^3) \\ f_2 &= f_{exact} + g_1 h_2 + g_2 h_2^2 + O(h_2^3) \\ f_3 &= f_{exact} + g_1 h_3 + g_2 h_3^2 + O(h_3^3) \end{aligned} \quad (5.24)$$

The above equation can then be solved for approximations to g_1 , g_2 , and f_{exact} , the approximation being indicated by a tilde over the symbol of the parameter:

$$\begin{aligned}
\tilde{g}_1 &= \frac{\varepsilon_{32}(1-r_{12}^2) + \varepsilon_{21}r_{12}^2(r_{23}^2 - 1)}{r_{12}(r_{12} - 1)(r_{23} - 1)(r_{12}r_{23} - 1)} \\
\tilde{g}_2 &= \frac{\varepsilon_{32}(r_{12} - 1) - \varepsilon_{21}r_{12}(r_{23} - 1)}{r_{12}(r_{12} - 1)(r_{23} - 1)(r_{12}r_{23} - 1)} \\
\tilde{f}_{exact} &= f_1 + \frac{\varepsilon_{32}(r_{12} - 1) - \varepsilon_{21}(r_{12}r_{23}^2 - r_{12} - r_{23} - 1)}{(r_{12} - 1)(r_{23} - 1)(r_{12}r_{23} - 1)}
\end{aligned} \tag{5.25}$$

For the case of a constant grid refinement factor, i.e.:

$$r_{12} = r_{23} \tag{5.26}$$

the above equations reduce to:

$$\begin{aligned}
\tilde{g}_1 &= \frac{\varepsilon_{21}r_{12}^2 - \varepsilon_{32}}{r(r-1)} \\
\tilde{g}_2 &= \frac{\varepsilon_{32} - r\varepsilon_{21}}{r(r+1)(r-1)^2} \\
\tilde{f}_{exact} &= f_1 + \frac{\varepsilon_{32} - \varepsilon_{21}(r^2 + r - 1)}{(r+1)(r-1)^2}
\end{aligned} \tag{5.27}$$

According to Roy [62] the ‘‘Mixed 1st+2nd Order Method’’ produces the best error estimation for non-monotonic, mixed-order solutions by best implying it is the most conservative and that it is the closest to the true error. In the grid sequencing performed in this study, r is theoretically constant since the number of grid points is halved/doubled in each spatial direction between two consecutive grid levels. Thus, the overall refinement factor is 8 (2x2x2) between two grid levels. Equation (5.25) is used to compute the approximate exact solution, \tilde{f}_{exact} . Once this is known, the discretization error, DE, on sequence k can be calculated as suggested by Roy [62] using:

$$|DE| = F_s \left| \frac{f_k - \tilde{f}_{exact}}{\tilde{f}_{exact}} \right| \tag{5.28}$$

where F_s is the ‘‘factor of safety’’ added by Roy to ensure a wider confidence band for the error estimate. Roy suggests taking F_s to be 3 and this value is used in the error estimation of this study. Note that f_k can be the solution of either a flow parameter at a point in the domain or an integrated quantity.

5.3.3 Discretization error and round-off error

The round-off error is the error that results from the substitution of an exact number with a finite-precision number. An example is the substitution of the fractional exact number $1/3$ by the decimal number $0.33\bar{3}$ where the overbar indicates that the 3 is repeated to infinity. In this case, if the 3 could be repeated to infinity, both numbers would be exact. However, since computers use finite-precision numbers stored as bytes, the decimal number needs to be truncated at a decimal place. Where the number is truncated depends on the precision of the machine being used. Obviously, the more precision that is required, the more CPU and memory-expensive any operation on the number will be. The round-off error is usually very small, since modern machines use 64-bit precision that give ten decimal place of accuracy. Also, the accuracy of the machine can be adjusted to double precision or to adjustable precision so that a number can be described by many decimal points. As already mentioned, increasing the precision increases the memory requirement as well as the CPU time required to run any operation on the number. However, since the numerical solution of the governing equations is iterative, round-off errors tend to accumulate. Furthermore, as the size of the grid cells is refined (i.e. as the discretization error is reduced) the round-off error becomes a more important source of error.

The round-off error can be related to the discretization error in the following way. The present discussion follows the treatment of the round-off error by Anderson [90]. If we let NS describe the exact analytical solution to the Navier-Stokes equations, DNS describe the exact solution to the discretized Navier-Stokes equations and N be the numerical solution produced by a finite-accuracy computer then we can write:

$$\begin{aligned}\text{Discretization error} &= \text{NS} - \text{DNS} \\ \text{Round-off error} &= \text{N} - \text{DNS}\end{aligned}$$

and:

$$\text{N} = \text{DNS} + \text{Round-off error}$$

According to the above, the numerical solution of the discretized Navier-Stokes equations produced by a finite-precision machine correspond to the exact solution of the Navier-Stokes equations plus the round-off error. For a more exhaustive treatment of the round-off error the reader is referred to Ref. [73].

5.3.4 Perfect gas assumption

All of the calculations performed in this study assumed that the freestream flow and the injectant behaved as a perfect gas (i.e. a gas which is both thermally and calorically perfect) with a specific heat ratio (γ) of 1.40 and a perfect gas constant of 286.9 J/(kg K) [27]. The perfect gas assumption was justified by the fact that in most of the flowfield the thermodynamic conditions are such that the specific thermal heats for air vary very little and can be considered to be constant. However, the injectant undergoes a very rapid expansion as it exits the nozzle and forms the barrel shock. For the higher pressure ratios investigated here the static temperature reached minimum values of 10 K in some small areas of the plume. The low temperature predicted inside the barrel shock, well below both the Nitrogen and Oxygen freezing point, raised the issue of having frozen gases in the jet plume and how this would affect the flowfield. This issue concerned both the experimental results and the computational solution. During July 2000, Frank Spaid, the author of Ref. [70] was contacted by Dr. Schetz to inquire about any eventual measurement that they carried out during the experiment to assess whether or not condensation occurred during the experiment. Spaid replied that he assumed that no phase change of the gas occurred during the experiment. Spaid justified this assumption with the finite-rate kinetics of condensation. Basically Spaid and the other authors of the experimental work assumed that a gas particle would be exposed to the very low temperatures and low pressures for an extremely short time interval over which any phase change would not have enough time to occur. The numerical solutions offered the possibility of easily measuring the average time interval that it would take an injectant particle to flow through the barrel shock. The calculation was performed along the longest possible particle path inside the barrel shock. Along this particle path, called AB in Figure 5.6, the velocity magnitude and temperature are known from the numerical solution. Knowing the distribution of the velocity magnitude and the length of the particle path AB (see Figure 5.7), the average velocity could be calculated and used to estimate the average time necessary for a particle of injected gas to flow through the barrel shock. Using the average values shown in Table 5.2 and calculating the average time as:

$$t_{avg} = \frac{\Delta S}{V_{avg}} = \frac{0.03}{750} = 4 \times 10^{-5} s \quad (5.29)$$

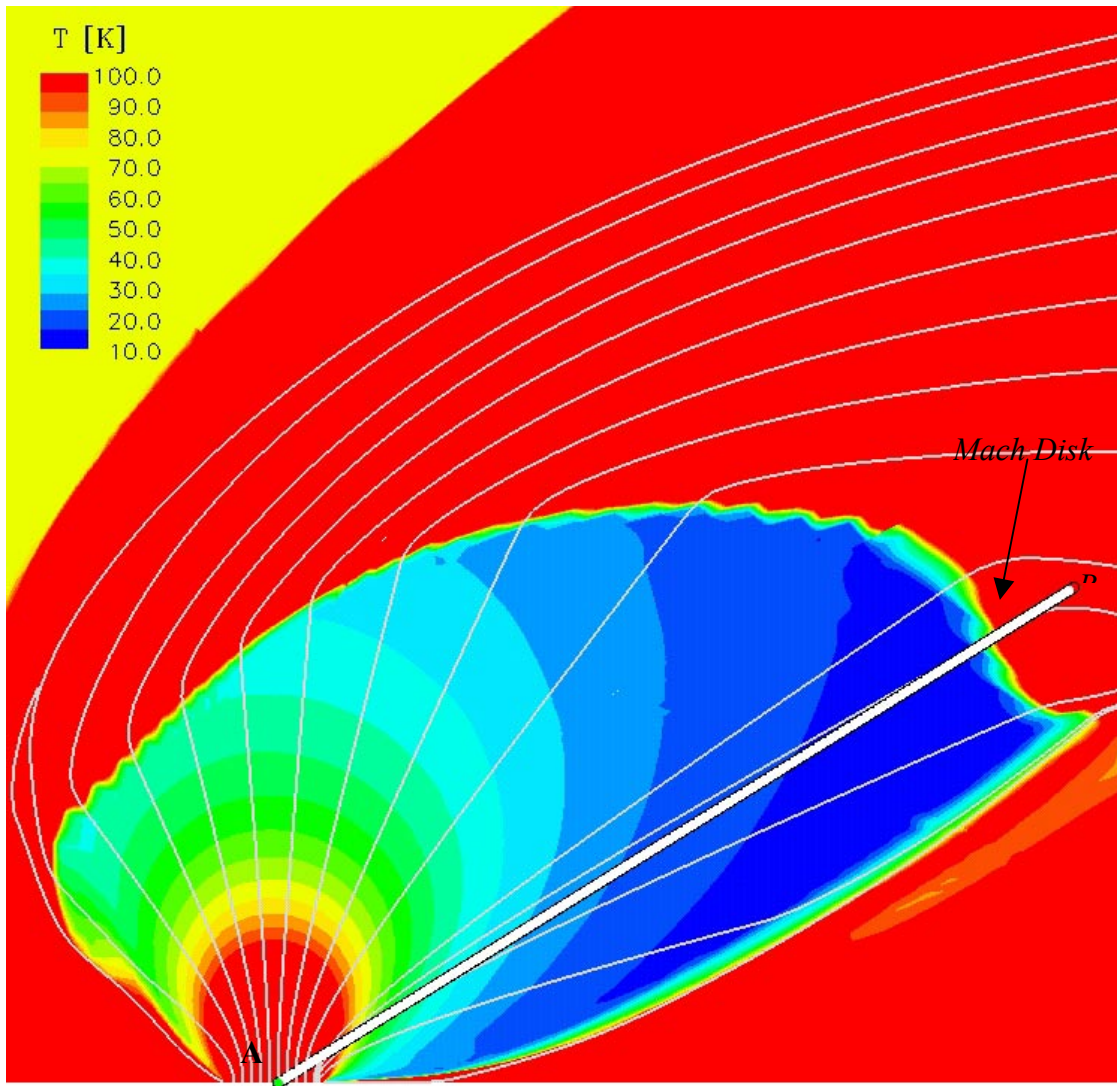


Figure 5.6. Temperature contours and streamlines inside the barrel shock. The white thick diagonal line represents the line along which the velocity magnitude is plotted in Figure 5.7. This calculation is representative of all the other jet interaction cases and uses flowfield data of the Virginia Tech case with only the primary jet activated.

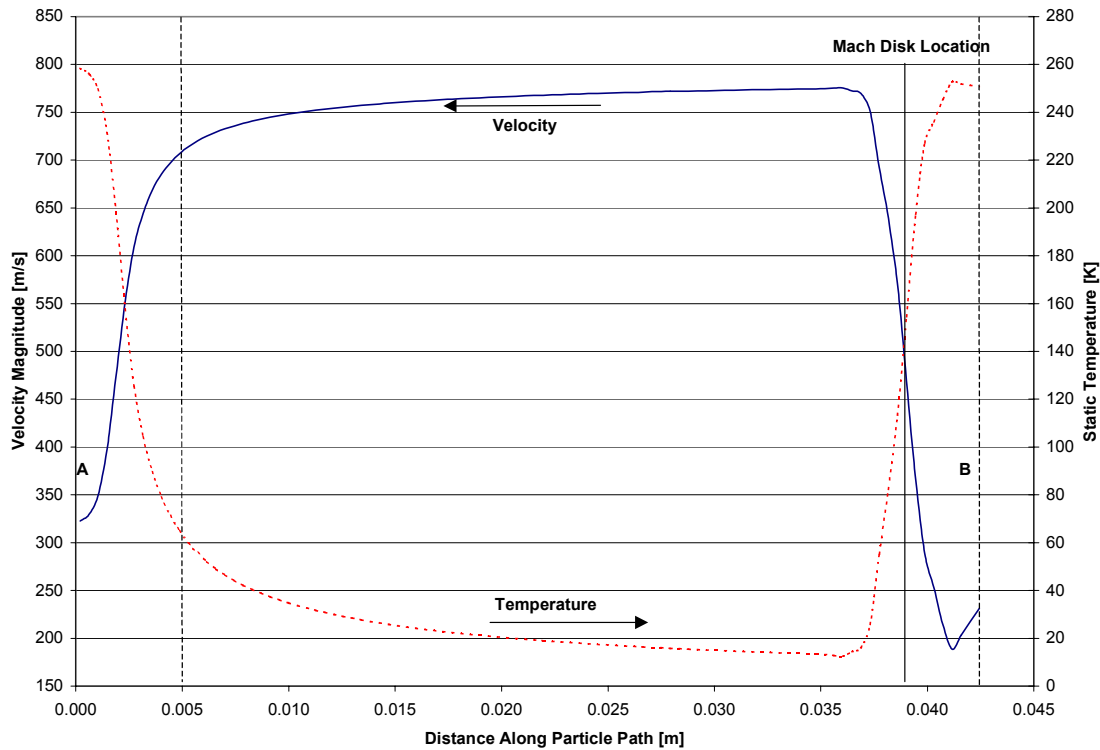


Figure 5.7. Velocity magnitude and static temperature distribution along the particle path AB (see Figure 5.6).

Parameter	
V_{avg}	750 m/s
ΔS	0.03 m
T_{avg}	25 K
T_{min}	10 K

Table 5.2. Summary of flow parameters.

The estimated average time for a particle to flow through the longest possible path inside the plume at a temperature below the freezing temperature of Nitrogen and Oxygen is 4.0×10^{-5} second. This time interval is short compared to the rate at which phase changes are likely to occur, and it validates the assumption first made by Spaid and then used throughout the present work. Daum in 1963 [23] noted that in hypersonic wind tunnel flows large amounts of super-saturation could occur. As a result of this phenomenon, single-phase isentropic flow might be obtained also at conditions considerably past the theoretical ones required for obtaining condensation-free flow with no super-saturation. Stever and Rathbun [71] reported that “oxygen and nitrogen condense on nuclei of impurities rather than on the self-generated nuclei postulated in the pure-vapor theory”. This would mean that while in theory substantial levels of super-saturation can be

reached before running into condensation phenomena, in a real experiment where particles impurities are present in the injectant, condensation would occur at much lower levels of super-saturation. The subject is further complicated by the fact that condensation can start both on impurities or on self-generated nuclei of liquid. However, not all of the nuclei will act as catalysts for the condensation process since this also depends on the curvature of the interface between the drops and the gas as it was shown by Thompson [74]. This subject is quite vast and would require a complex analysis of the flow. For the primary goal of this study condensation does not seem to sensibly affect the results. However, further investigation into the condensation effects is recommended for future studies possibly using a real-gas chemistry model that includes real-gas effects and condensation effects. Examples of condensation models can be found in the work of Masuda, et al. [43] and Eppard, et al. [25].

5.3.5 Accuracy of boundary conditions

Apart from the error introduced in the numerical solution by the treatment of the boundary conditions there is also an error associated with the representation of the physical boundary condition with a simplified model. A typical example of this type error is the simulation of an entry boundary layer as an inlet boundary condition. In the Virginia Tech cases [84] [85], the flat plate was mounted flush to the tunnel floor. A turbulent boundary layer could be observed in the Schlieren pictures of the flowfield. From these pictures, it was possible to measure the boundary layer thickness at the start of the flat plate surface. However, since no boundary layer velocity profiles were measured, the velocity distribution in the boundary layer had to be assumed. As discussed in the Boundary Conditions section, Section 4.1, the boundary layer velocity profile was assumed to follow the simple distribution [68]:

$$\frac{U}{U_e} = \left(\frac{y}{\delta} \right)^{\frac{1}{7}} \quad (5.30)$$

where U_e is the edge, or freestream, velocity. The static pressure and the total temperature were assumed to stay constant through the boundary layer, the static temperature and density varying as functions of the other parameters. Turbulent quantities were extrapolated from the interior cells and therefore did not require any assumption. Obviously, the assumed boundary layer profile will introduce some error in the numerical solution even though the governing equations will tend to adjust the flow to its physical state thus reducing the error introduced by the inlet boundary conditions.

Another numerical boundary condition prone to error is the jet boundary condition. Apart from the discharge coefficient issue discussed before, the calculations assumed a jet with a step-profile. In reality, a boundary layer would form on the walls of the nozzle, and there would be a velocity profile exiting the nozzle. Other researchers found the step profile to be a source of instability [14] [15]. In this study, a velocity profile and a step-

profile were used for the simulation of a methane-injection case on a flat plate. As long as the mass flow of the two jets was kept the same no noticeable differences in the flowfield were noticed and both simulations had the same stability and convergence behavior. The discrepancy of the behaviors observed by Chenault, et al. [14] [15] and during the current study could be attributable to the grid refinement and to the grid topology. Chenault, et al. used a simple H-type orthogonal grid all through the computational domain while the present study employed a much more elaborate and adapted grid topology that might have alleviated any instability generated by the step profile of the jet.

The plane of symmetry is a reasonable assumption. Some experimental studies [44] showed the existence of minor flow asymmetries in the jet interaction flowfield. However, these asymmetries do not have any physical basis that justifies their existence. In a following numerical study [15] Chenault, et al. attributed these asymmetries in the jet interaction flowfield to flow asymmetries generated by a combination of imperfections in the tunnel walls, systematic errors in the data collection apparatus and to the coarseness of the measurement matrix.

The solid surface of the flat plate was assumed to be adiabatic and smooth. While these two assumptions are reasonable for any type of engineering calculations they are approximations to the real conditions on the surface. As shown by the Schlieren pictures of the flowfield (see Figure 5.12 for the Schetz case or Figure 5.57 and Figure 5.77 for the Virginia Tech cases) usually a weak shock existed ahead of the injector. The shock was produced by the leading edge of the flat plate (Schetz, Cubbison and Letko and cases) or by imperfections in the tunnel floor (Virginia Tech cases).

5.4 Sources of Error of the Experimental Data Used for Comparison with the Numerical Solutions.

The numerical simulation of the experiments required a full knowledge of the freestream and jet conditions as well as the geometry of the flat plate and of the injector. However, especially for the experimental cases taken from the earlier literature (Schetz, Cubbison and Letko) some important information about the flow conditions was missing and had to be estimated, introducing an additional source of uncertainty. Also, in most of the experiments, an estimate of the experimental error/uncertainty was missing thus making the comparison with the numerical solution more difficult. Following is a detailed analysis of the major sources of uncertainty and discrepancy in the comparison of the numerical results to the experimental data.

5.4.1 Experimental Uncertainty

All the experimental measurements are subject to a certain degree of uncertainty that can be decreased by using very accurate instrumentation and by a careful experimental setup, but it cannot be completely eliminated. The experimental uncertainty affects the direct measurements, and it is propagated through the derived quantities. A proper analysis of the experimental uncertainty requires the knowledge of the uncertainty in each individual reading. Unfortunately, few of the experimental works considered in this study reported any uncertainty information for the experimental conditions and measurements. Assuming that the experiment was properly setup, that the experimental equipment worked according to its specifications, and that no human errors were made, it is reasonable to assume an experimental uncertainty of $\pm 10\%$ for pressure coefficient data. Assuming an uncertainty of $\pm 5\%$ in the measurement of the tunnel dynamic pressure and negligible errors in the geometric measurement of the plate dimensions (moment arm, surface area), the uncertainty in the forces and moments acting on the plate would be $\pm 11\%$ according to the uncertainty propagation theory explained by Coleman and Steele [19].

5.4.2 Pressure Mapping Uncertainty

It must be noted that in the experimental pressure mappings reported by Cubbison and Letko the experimental uncertainty is particularly high. The high level of uncertainty is due to the fact that the authors generated a continuous mapping of the pressure field by curve-fitting the discrete pressure data they measured at a limited number of stations on the flat plate. The flat plate setup with the distribution of the pressure orifices used by Cubbison is shown in Figure 5.8. Therefore, a large human error is introduced by the curve fitting procedure into the mapping and, as a consequence, in the calculation of the normal force and pitching moment from the pressure data. In addition to all this, the calculation of forces and moment by integration of the pressure mapping is also affected

by a discretization error. It is not unreasonable to assume a final uncertainty in the computed experimental forces and moments in the region of $\pm 20\%$. Nevertheless, the pressure mappings can give a good and useful overview of the pressure field that one can expect in a jet interaction case.

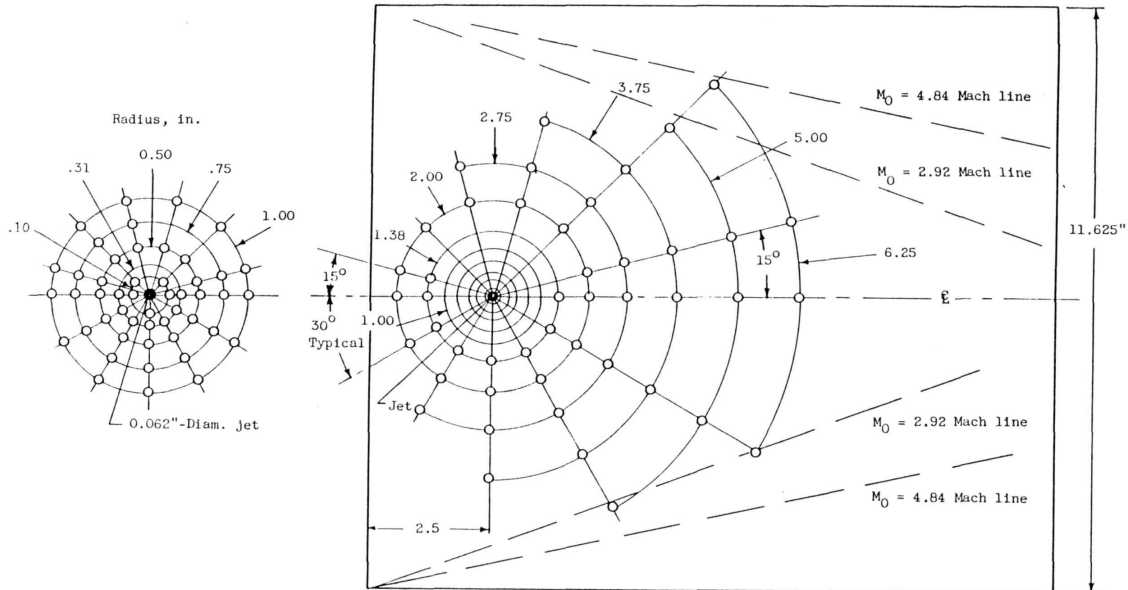


Figure 5.8. Plan-view of the flat plate used by Cubbison [22] in his jet interaction experiments. The pressure orifices used to draw the pressure contours of Figure 5.22 are shown as circles. The drawing on the left is a detailed drawing of the locations of the pressure orifices in the area around the injector. All dimensions in inches. From Ref. [22].

Also in the Virginia Tech cases the experimental results had a high level of uncertainty. The uncertainty is due to the difficulty of calibrating the Pressure Sensitive Paint (PSP) correctly and in eliminating any bias in the reading due to the angle at which the CCD camera is inclined to the surface of the flat plate (see Section 5.6.1). In the Virginia Tech experimental setup (Figure 5.44) the PSP was sprayed on the surface of the flat plate. the presence of some pressure orifices in the flat plate surface allowed for an “*in situ*” calibration of the PSP. However, as shown by spanwise plots of the static pressure ahead of the separation, i.e. where the flow is smooth and homogeneous, the PSP data presented a clear bias (see Figure 5.53). Error estimation in the pressure readings was performed using these spanwise pressure distributions and assuming that the maximum error is given by the difference between the highest and lowest pressure value, with the average value being considered the real static pressure. By performing such an error estimation, uncertainty in the static pressure readings was $\pm 15\%$. This uncertainty was then propagated into the calculation of the pressure coefficient and into the calculation of the forces and moment generating much larger errors.

5.4.3 Discharge Coefficient Uncertainty

Another large source of uncertainty at least for the Schetz, Cubbison and Letko cases is the lack of information about the discharge coefficient of the injectors. The definition of discharge coefficient of the jet, $C_{d,j}$, is here repeated for completeness:

$$C_{d,J} = \frac{\dot{m}_{actual}}{\dot{m}_{ideal}} = \frac{\dot{m}_{actual}}{v_J \rho_J A_J} \quad (5.31)$$

This quantity is an indication of the actual mass flow through the nozzle compared to the isentropic mass flow that neglects any loss due to viscous effects or to geometric imperfection. In general, the total conditions of the jet are reported by the authors and, knowing that the nozzle is choked, all the other jet conditions can be calculated. However, it is not known exactly where the total conditions were measured or, more important, what the mass flow of the jet was. The location of the total conditions affects the discharge coefficient of the injector since the longer the distance between the measurement location and the nozzle, the larger the viscous losses and the lower the mass flow through the injector (i.e. the smaller the discharge coefficient). The lower the jet mass flow, the smaller the barrel shock and the weaker the bow shock and the smaller the normal force acting on the solid surface. So for an accurate comparison of the experiments with the numerical solutions, it is essential to know the actual mass flow of the jet. In order to alleviate this problem numerical simulations of the flow inside the injector for the Letko case were run to estimate the losses. Initial calculations assumed an isentropic flow through the nozzle and a discharge coefficient of 1.00. More detailed information about the calculations of the jet flow and the relative results are given when discussing the Letko case. Information about the discharge coefficient is available for the Virginia Tech cases, since the mass flow through both the primary and the secondary injectors were measured during the experiments.

5.5 Laminar Cases

Laminar calculations were run to simulate the Schetz [65] and then the Cubbison [22] experiments; both experiments reported a laminar boundary layer before separation occurred. The goal of the two laminar calculations was to prove the capability of the numerical approach to accurately describe the jet interaction flowfield without the added computational burden and the added complication of a turbulence model. Laminar calculations in fact do not require the solution to any additional equations beyond the five basic governing equations as discussed in Chapter 3. Furthermore, since laminar calculations do not have to resolve the fine flow structures in the laminar sub-layer as is the case for turbulent calculations, the boundary layer can be resolved with fewer grid cells than a turbulent calculation, thus reducing the computational load and speeding up convergence. It is interesting to note the scarcity of experimental works in jet interaction flowfields with laminar boundary layers. The only other three dimensional jet interaction experimental work with a laminar boundary layer found is that of Zukoski [100]. This shortage is probably due to the low possibility of encountering a laminar boundary layer in any practical applications of jet thrusters. Nevertheless, in spite of the very high flow speeds, laminar conditions can be encountered when a vehicle is flying at very high altitudes where the atmospheric density is very low to reduce the Reynolds number below transition.

5.5.1 Schetz Laminar Case (PR62, Mach 2.10)

This initial laminar simulation was performed to validate the GASP capability to simulate the main flow features. The selected case is the experimental study of a circular sonic jet in a Mach 2.1 supersonic crossflow described by Schetz in Ref. [65]. The nozzle is cut in the solid surface of a flat plate mounted on a sting (Figure 5.9). The boundary layer is laminar (see Table 5.4 and Table 5.3 for the flow conditions and the plate dimensions) and the pressure ratio is relatively low compared to the flight conditions of a real jet thruster. Nevertheless the flowfield presents all those features typical of a jet interaction problem such as the shock-induced boundary layer separation, the bow shock and the barrel shock. The comparison was quite useful in that it showed GASP was able to resolve most of the flow features produced by the boundary-layer-jet interaction.

Parameter	
Flat plate entry length, x_0	5.08 cm
Injector diameter, d_j	0.389 cm
x_0/d_j	13.1

Table 5.3. Flat plate dimensions.

Parameter	
Gas	Air, perfect gas ($\gamma=1.40$)
M_∞	2.1
$P_{\infty, t}$	101.5 kPa
P_∞	11.1 kPa
T_∞	159 K
Type of boundary layer	Laminar

(a) Free-stream

Parameter	
Gas	Air, perfect gas ($\gamma=1.40$)
M_J	1.0
$P_{J, t}$	690.5 kPa
P_J	364.8 kPa
T_J	250 K
$P_{J, t} / P_\infty$	62

(b) Jet

Table 5.4. Summary of flow parameters.

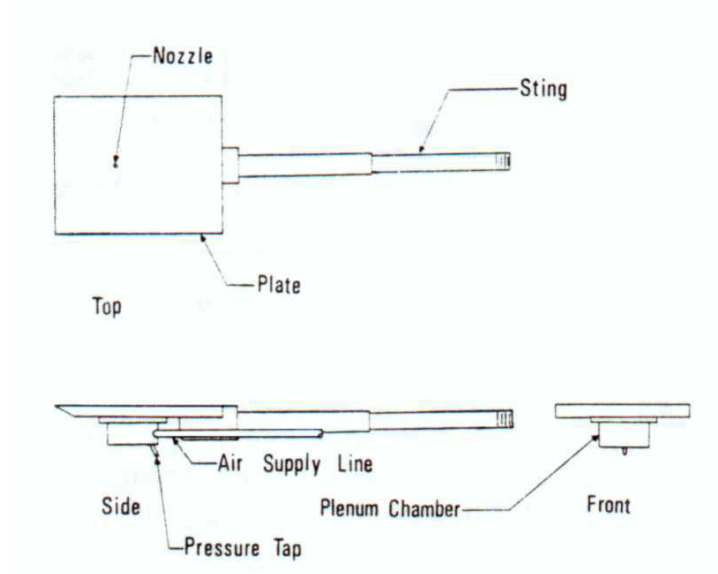


Figure 5.9. Experimental set up of the Schetz experiment (from Ref. [65]).

The computational domain for this problem consisted of a standard H-type grid divided into a four-zone, six-sided rectangular box as shown in Figure 5.10 (a). Figure 5.10 (b) shows a side view of the computational domain together with a view of the sharp-edged flat plate. The overall grid dimensions are $144 \times 120 \times 56$ for a total number of cells of 967,680. Since the physical problem is symmetrical with respect to the XY-plane, the

computational domain simulated only half of the wind tunnel width. The grid was generated using GRIDGEN v. 12. The grid features a highly refined mesh in two regions: the near wall region to capture the viscous boundary layer and in the region around the jet where very high pressure gradients are found (Figure 5.10 (b)). One-dimensional Tanh stretching was used in all regions, and an elliptic solver was run on the domains around the injector. The elliptic solver was useful to blend the curved lines defining the injector surface with the straight lines describing the plate surface (see Figure 5.11). All zones except the one immediately downstream of the jet (zone 4) were run using third-order accuracy for the inviscid fluxes, and the Min-Mod limiter. All viscous fluxes were second-order accurate, and the Roe-flux was used for the inviscid fluxes in all the four zones. This numerical calculation was run using all the 4 CPUs of AeroSoft's Cray J90 and it took 35 wall-clock hours to reach convergence.

Figure 5.12 and Figure 5.13 show the comparison between the experimental Schlieren picture and the CFD results. The comparison was performed by visually analyzing the main features that could be observed in the Schlieren picture and then by superimposing them onto the CFD solution. The major flow features can be clearly picked out in the Schlieren picture and lines describing the shock waves, the jet plume and the boundary layer can be easily drawn. All superimposed lines are subject to an error due to human judgment. On the other hand, the large bands describing shock waves and the boundary layer in the CFD results are somewhat more inclined to the subjective judgment of what line best describes a flow feature. For this reason the comparison will focus on the superposition of the lines of the main flow details drawn from the Schlieren photographs onto computational solution (Figure 5.13). As shown by Figure 5.13, the simulation is in good agreement with the experimental results. Both the boundary layer thickness and shock wave position and inclination were correctly predicted by the numerical solution, an indication that most of the flow physics are captured by the simulation. However, it was not possible to fully validate such agreement between the experiment and the simulation, since the original paper reported only the Schlieren picture. In the visual comparison, it is important to note that the Schlieren photograph is a two-dimensional representation of a three-dimensional flowfield. Therefore, all the flow features within the camera field of view and present at different z -locations integrated onto one plane. It is important to bear in mind this factor in the visual comparison of the experiment to the numerical solution since the numerical results shown in Figure 5.13 are the two-dimensional mapping of the flow on just the plane of symmetry. Another *caveat* of the visual comparison is the fact that the Schlieren picture highlights the zones of higher (whiter) and lower (darker) density gradient. The post-processing package used in this study (FieldView) does not have the capability of displaying density gradient contours. After some trials and error, it was found that the mapping of the Mach contours on the plane of symmetry best highlighted the salient features of the flowfield. Therefore, Mach number contours were chosen as the parameter to be mapped on the plane of symmetry for the visual inspection of the numerical solution throughout this study.

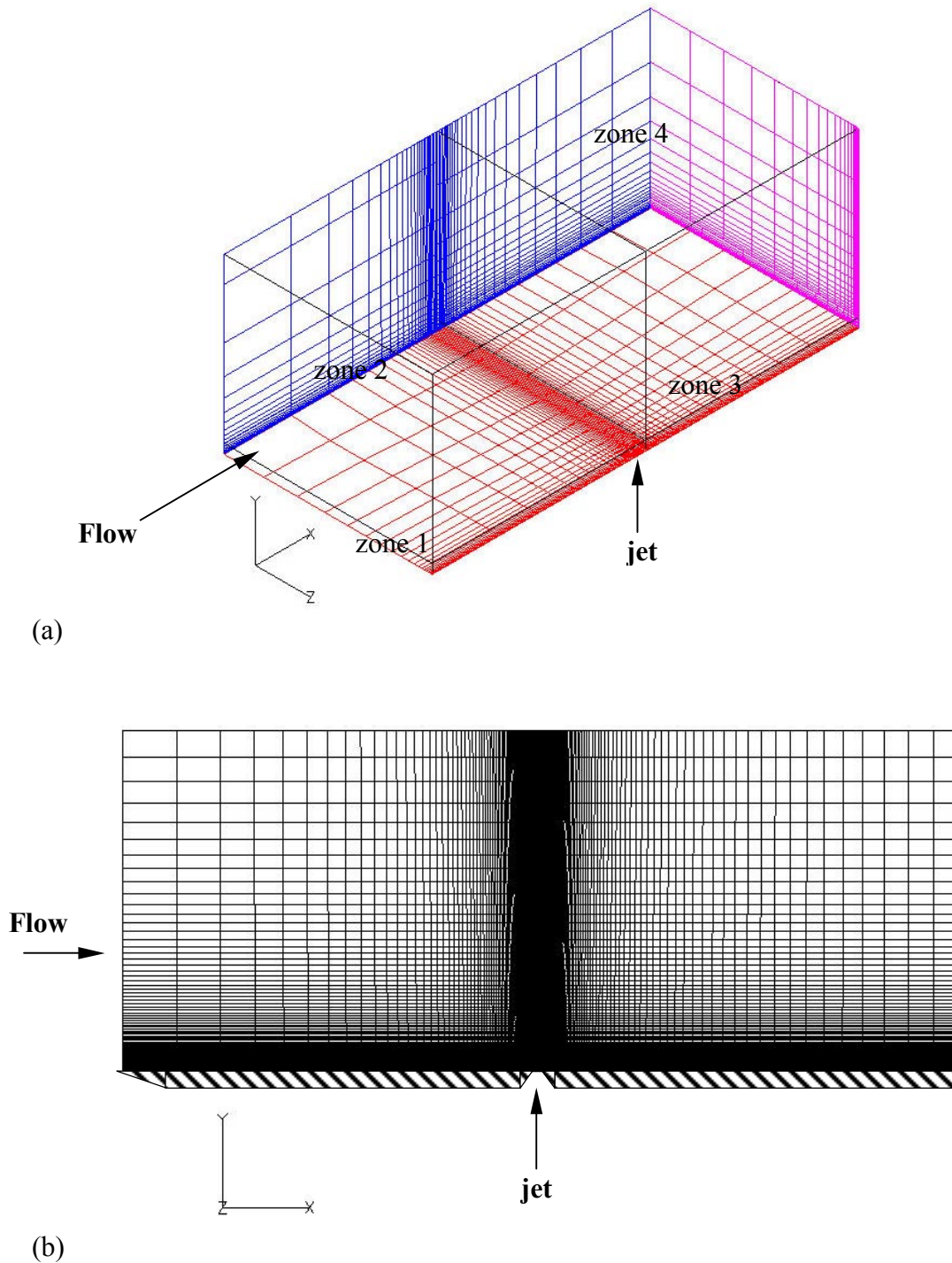


Figure 5.10. (a) Perspective and (b) side view of the 4-zone computational grid. The grid dimensions (nodes) of the four zones are $(73 \times 65 \times 57)$ for zone 1 and 3 and $(73 \times 57 \times 57)$ for zone 2 and 4 for a total of 967,680 cells.

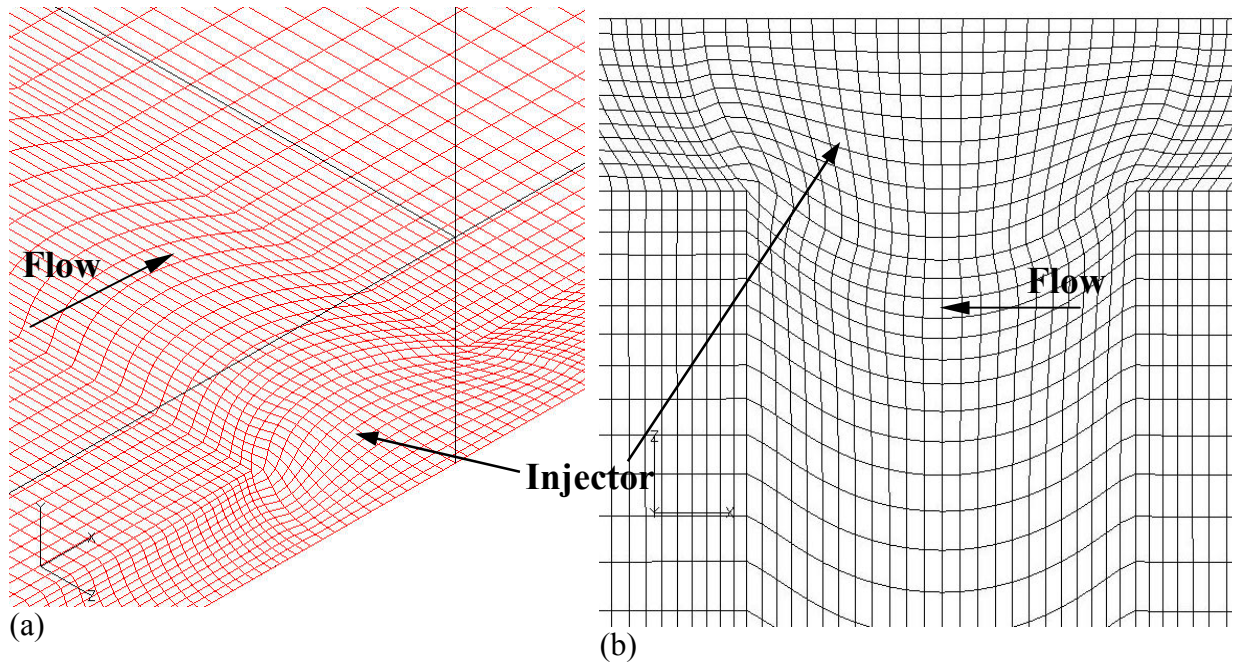


Figure 5.11. (a) Perspective and (b) top view of the of the surface mesh around the injector.

As a means of comparison of different jet interaction test cases and to prove the correctness of a theory to predict the height of the jet plume, Schetz used a logarithmic plot of a modified pressure ratio versus the barrel shock height, h . The plot is shown in Figure 5.14 (a) with the definition of the barrel shock height presented in Figure 5.14 (b). Superimposed on the plot is the data point indicating the height of the plume produced by the simulation (star). As might have been expected by the examination of the comparison of the Schlieren photograph with the Mach number contours produced by the numerical solution (Figure 5.13), the simulation result falls right on top of the experimental data point corresponding to the same test case. Note that the vertical axis of Figure 5.14 (a) plots the ratio P_j/P_{eb} . As usual, P_j is the static pressure of the jet. P_{eb} is the “*effective back pressure*”, a concept introduced by Schetz [66] that relates the case of a jet in a crossflow to the case of a jet exhausting in a quiescent medium. In the plot of Figure 5.14 (a) the effective back-pressure was calculated as 80% of the total pressure behind a normal shock. Note that the current study instead of using the effective back-pressure as a parameter to define the strength of the injection the jet pressure ratio, PR , as defined by Cubbison [22] was used.

Figure 5.13 shows that the numerical solution presents some grid-dependence issues. The Mach number contours inside the barrel shock (Figure 5.13) seem to follow the orthogonal pattern of the gridlines in the region near the injection location. However, the rest of the flowfield is free of any grid-dependence issue. This isolated case might be

exacerbated by the combined effects of some localized grid-dependence issues and the high pressure gradients encountered at the nozzle exit. The localized grid-dependence issue can be attributed (see Figure 5.10 (b)) to the extremely fine longitudinal grid spacing near the injector that becomes abruptly coarser. However, the goal of this simulation was not to obtain an accurate solution and to perform an extensive comparison with the experiment. The primary goal was just to assess the capability of the numerical code to properly simulate the jet interaction flowfield and, also, to familiarize the author with the numerical code. Therefore the grid-dependence issue concerning this test case was not studied any further. However, care was taken in the development of the other grids used in the jet interaction flowfield to avoid abrupt changes in the grid spacing especially in regions of high pressure gradients.

Overall the H-type grid was found to be numerically inefficient due to the clustering of cells in regions where the variable gradients were very small. In fact the fine mesh that can be observed in the Figure 4.2 (a) extends all across the width of the plate up to the furthest side of the computational domain. The calculations showed that in this region all the variables have a constant value, the free-stream values. A more efficient grid, with a combination of C-type and H-type grid topologies that allows cell clustering only around the jet, would enable the use of a smaller number of cells to produce the same accuracy as the current grid, thus increasing the computational efficiency.

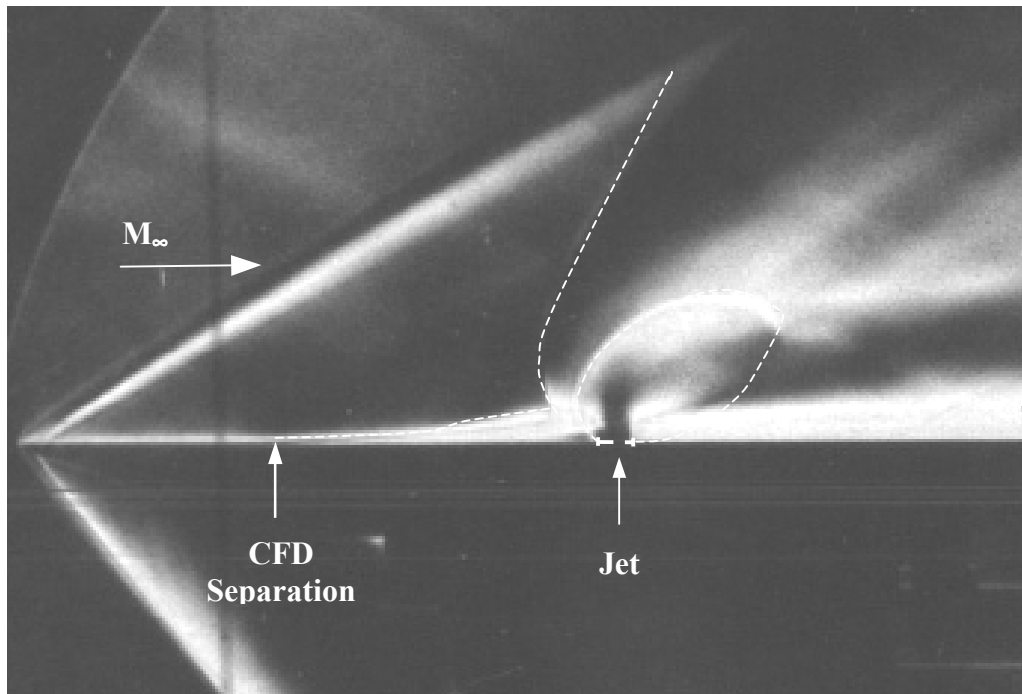


Figure 5.12. Schlieren picture with superimposed major flow features obtained with the CFD calculations.

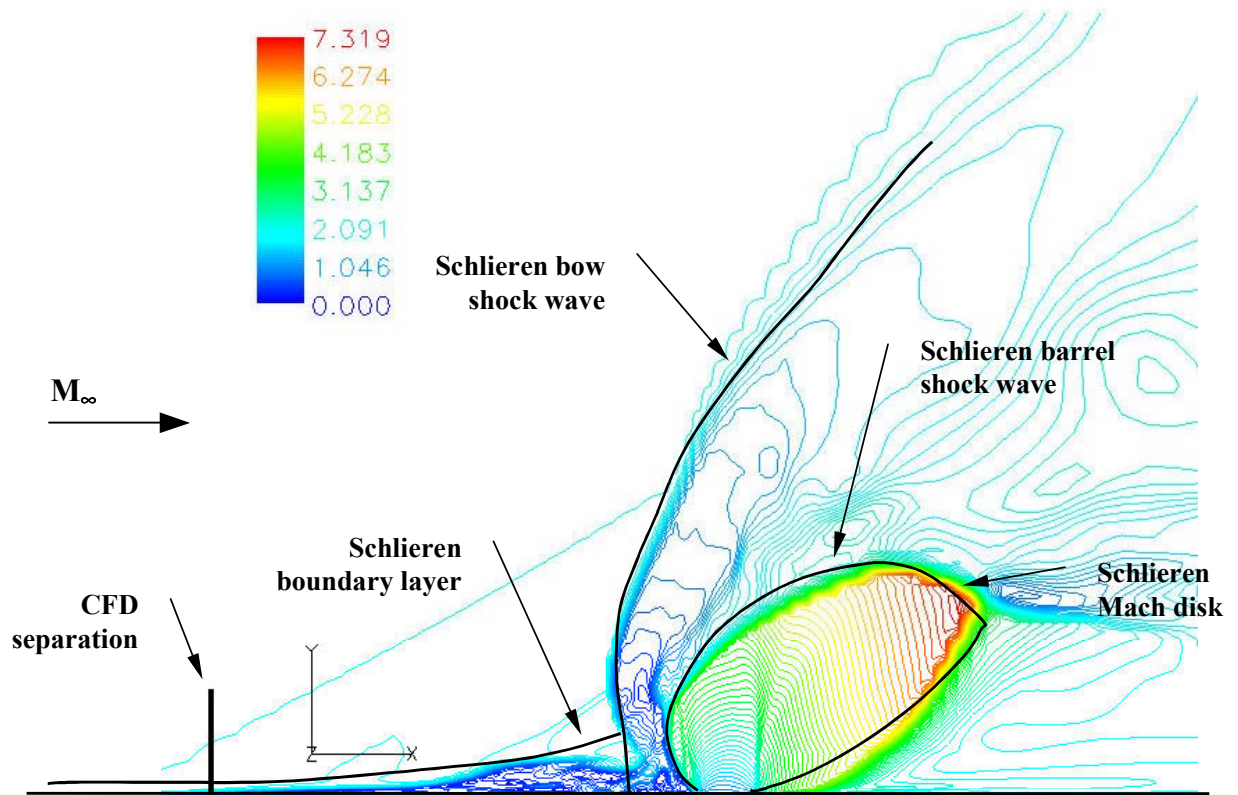


Figure 5.13. Mach number contour lines as predicted by the CFD calculations. The solid black lines represent the shock waves, jet plume and boundary layer thickness that can be observed in the Schlieren picture of Figure 5.12.

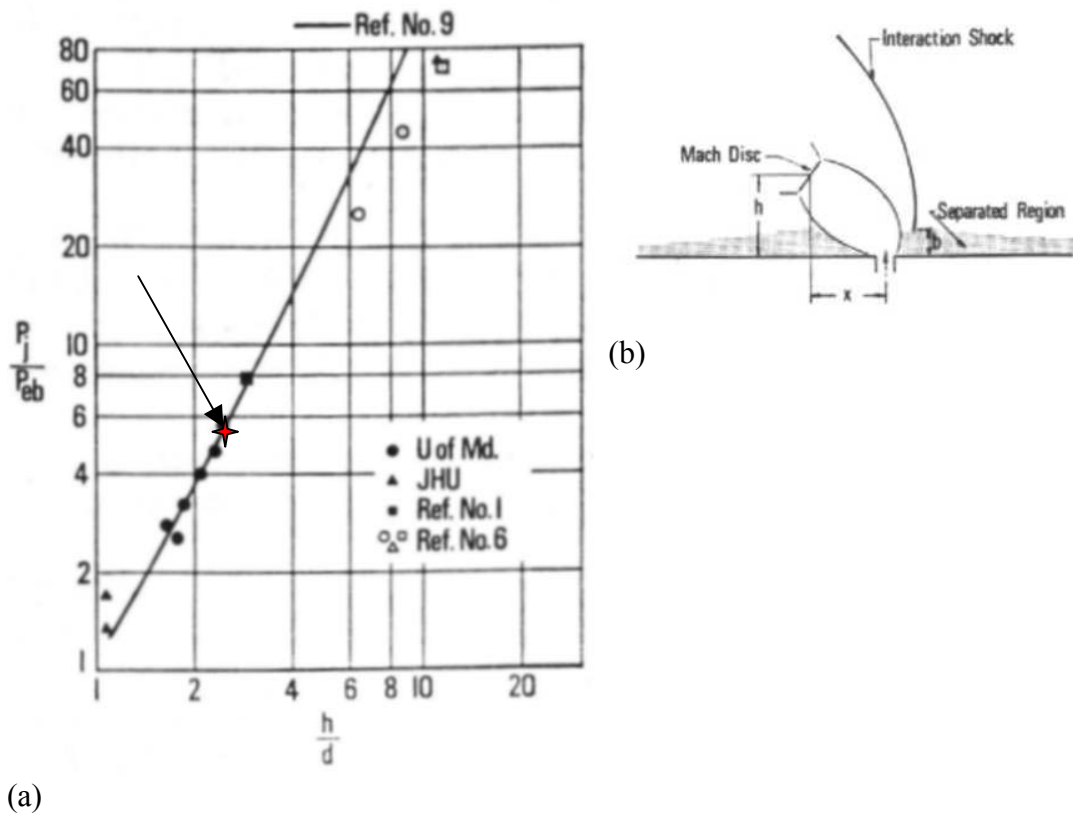


Figure 5.14. (a) Plume height comparison for the Schetz experiment (from Ref. [65]). The arrow indicates where the data point corresponding to the experiment simulated in this work. The star is the data point corresponding to the numerical simulation. As expected from looking at Figure 5.13 the height of the plume for the numerical calculation and the experiment are exactly the same. (b) Definition of plume height.

5.5.2 Cubbison Laminar Case (PR677, Mach 2.92)

The Schetz case described above proved that a numerical solution with approximately 1,000,000 cells could capture most of the flow physics of the jet interaction problem; this is for a flow with a laminar boundary layer and a relatively low-pressure ratio. Also, the experience gained by generating the grid and the subsequent analysis of the flowfield, showed that the simple orthogonal H-grid topology is not very efficient to resolve the flow details. To extend the range of conditions over which the code was tested it was decided that the next calculation should have a much higher-pressure ratio. Also a new grid should be developed to improve on the clustering efficiency of the orthogonal H-type grid. The new grid should feature a combination of C-type and H-type zones to increase the clustering around the injector without significantly increasing the overall number of cells. However, for consistency with the previous calculation and to avoid adding extra complications, the new simulation should still be laminar. Following all these objectives, the Cubbison experiment [22] was chosen as the test case. This experiment had a much higher-pressure ratio than the Schetz case (677 versus 62), a higher Mach number (2.92 versus 2.1) but it still featured a laminar boundary layer and a sonic injector. The dimensions of the flat plate and of the injector are shown in Table 5.5, and the whole set of test conditions is presented in Table 5.6. A schematic of the experimental setup from the original Cubbison paper is shown in Figure 5.15



Figure 5.15. Experimental flat plate configuration for the Cubbison test case as shown in Ref. [22].

Parameter	
Flat plate entry length, x_0	6.35 cm
Injector diameter, d_j	0.1575 cm
x_0/d_j	40.3

Table 5.5. Flat plate dimensions for the Cubbison case.

Parameter	
Gas	Air, perfect gas ($\gamma=1.40$)
M_∞	2.92
$P_{\infty, t}$	34.2 kPa
P_∞	1.05 kPa
T_∞	107.6 K
Type of boundary layer	Laminar

(a) Free-stream

Parameter	
Gas	Air, perfect gas ($\gamma=1.40$)
M_J	1.0
$P_{J, t}$	710.5 kPa
P_J	375.4 kPa
T_J	280 K
$P_{J, t} / P_\infty$	677
Jet mass flow	0.00305 Kg/s
Jet thrust	1.02 N

(b) Jet

Table 5.6. Summary of flow parameters for the Cubbison case.

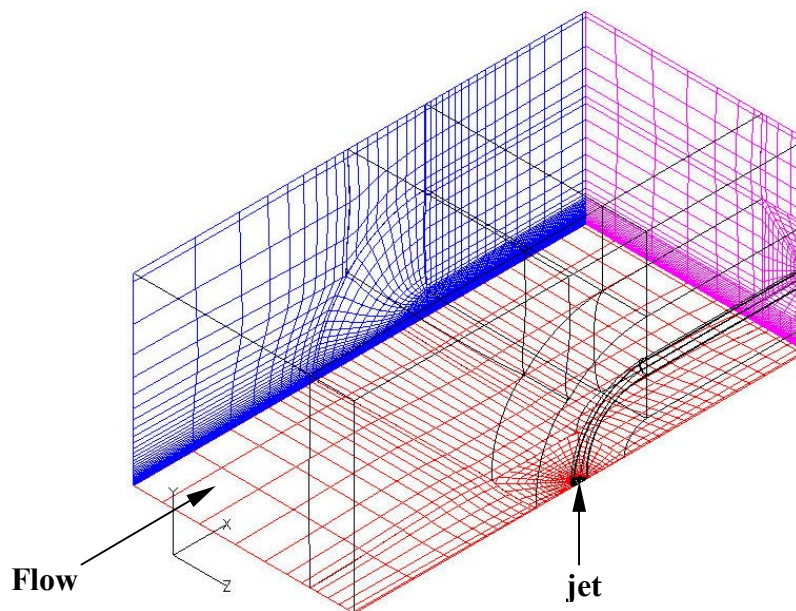


Figure 5.16. Perspective view of the computational domain for the Cubbison case (not all gridlines are shown). The flat plate surface (no-slip adiabatic) is in red, the injector (fixed jet conditions) is in black, the back-plane (extrapolation) is in purple and the far cross-plane (extrapolation) is in blue.

The new grid developed for this test case was composed of a total of 12 zones (see Figure 5.16). Both H-type and C-type grid topologies were used together to improve the clustering around the injector area where most of the flow physics (very high-pressure gradients, barrel shock, bow shock, Mach disk, separation) occur. The injector was simulated by an H-type grid and the flat plate in the immediate surrounding of the injector was simulated with a C-type grid that wraps around the nozzle as shown in Figure 5.17. This mixed configuration allows a finely clustered grid around the injector, and, as the distance from the injector increases, the cells fan out and map onto a much wider area decreasing the clustering. The domain had to be subdivided into 12 zones to accommodate the mixed topology and to help increase the clustering around the injector. The final result was a quite complicated grid layout in three dimensions (Figure 5.16) that required a considerable effort to generate. The total number of cells for this configuration was 766,488. The grid was sequenced twice by eliminating every other grid cell to generate three grid levels, fine (level 1 with 766,488 cells), medium (level 2 with 110,382 cells) and coarse (level 3 with 18,308 cells).

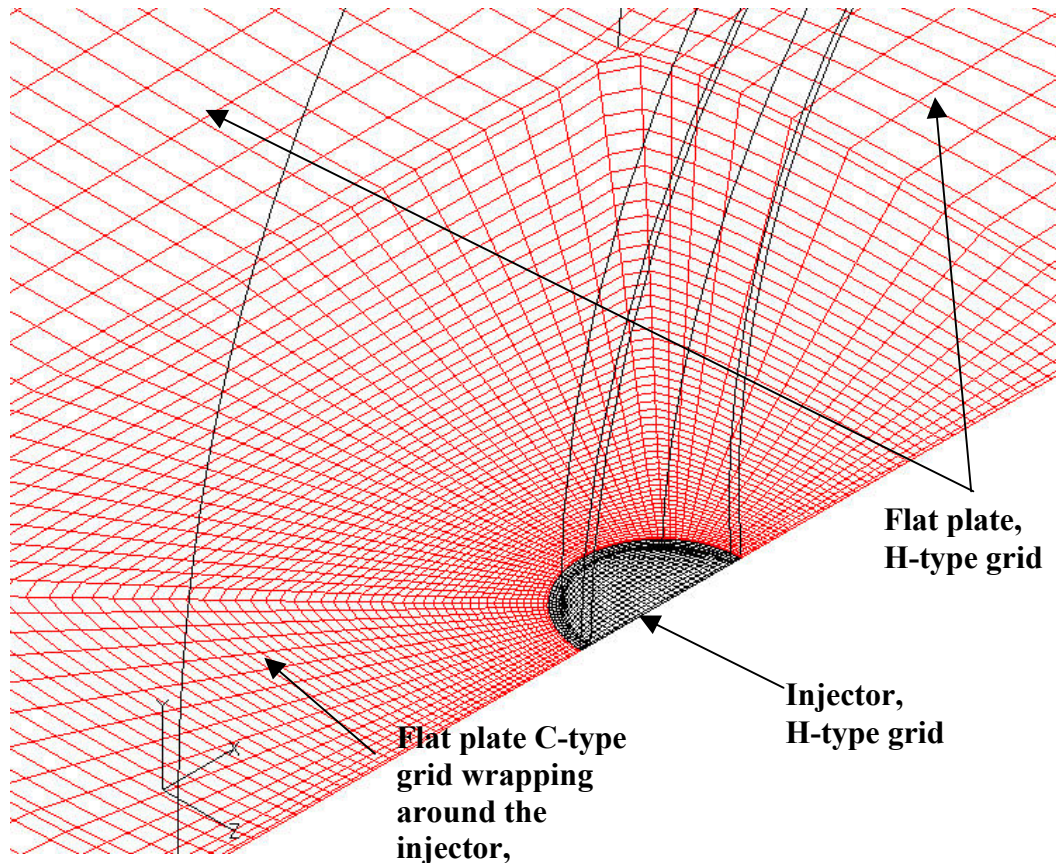


Figure 5.17. Detail of the grid laying on the flat plate surface and around the injector. Note how the C-type grid (in red) wraps around the injector (in black) and how it allows a much more efficient clustering than the H-type grid since it “fans-out” the finely spaced cells near the injector to a larger area.

The solution was converged on the three grid levels, and the results were compared to assess the level of grid-convergence. The normal force coefficients and the pitching moment coefficients for the three grid levels are plotted and compared in Figure 5.18 and Figure 5.19, respectively. In these plots, the experimental quantities are also shown with an error band representing the estimated experimental uncertainty. For the Cubbison case, the experimental uncertainty in the integrated forces and moment was assumed to be $\pm 20\%$ which, taking into consideration the experimental uncertainty and the error in the calculation of the pressure force as described in Section 5.4 is likely a conservative estimate. The force and the moment plots show two behaviors that at first sight might seem in contradiction, but that after deeper analysis of the results show a common trend. While the moment features a monotonic convergence, Figure 5.18 shows that the force does not converge monotonically as the difference between the fine sequence and the medium sequence is greater than that between the medium and coarse sequences as shown in Table 5.7. This non-monotonic convergence makes necessary the use of the “Mixed 1st and 2nd Order Extrapolation” (see Section 5.3.2) instead of the “Generalized Richardson Extrapolation” to compute the discretization error (see Table 5.7). The discretization error on the fine grid level is 31% for the normal force and a low 4% for the pitching moment. Note that both the normal force and the pitching moment results obtained on the fine grid already fall within the uncertainty band of the experimental measurements. However, the normal force on the coarse and medium grid sequences is well beyond the uncertainty band of the experiment. On the other hand, the pitching moment results on the three grid sequences are all within the experimental uncertainty bands and, unexpectedly, the difference with the experimental value increases as the grid is refined. The small discretization error and the trend in the pitching moment might indicate that the converged numerical solution would approximately differ by 20% from the experimental value.

Sequence	Number of Cells	Richardson Extrapolation		CFD		$\epsilon C_{Fy} \%$	$\epsilon C_{Mz} \%$
		C_{Fy}	C_{Mz}	C_{Fy}	C_{Mz}		
3	18,308	0.636	12.282	0.214	10.925	66	-11
2	110,382			0.236	11.198	63	-9
1	766,488			0.571	12.106	10	-1

Table 5.7. Comparison of the solution on the three grid levels with the solution obtained with the “Mixed 1st +2nd Order Extrapolation”. “ ϵ ” is the discretization error in the solution.

Sequence	Number of Cells	Experiment		CFD		$\Delta C_{Fy} \%$	$\Delta C_{Mz} \%$
		C_{Fy}	C_{Mz}	C_{Fy}	C_{Mz}		
3	18,308	0.472	10.268	0.214	10.925	-55	6
2	110,382			0.236	11.198	-50	9
1	766,488			0.571	12.106	21	18

Table 5.8. Comparison of the experimental to CFD force and moment for the Cubbison case.

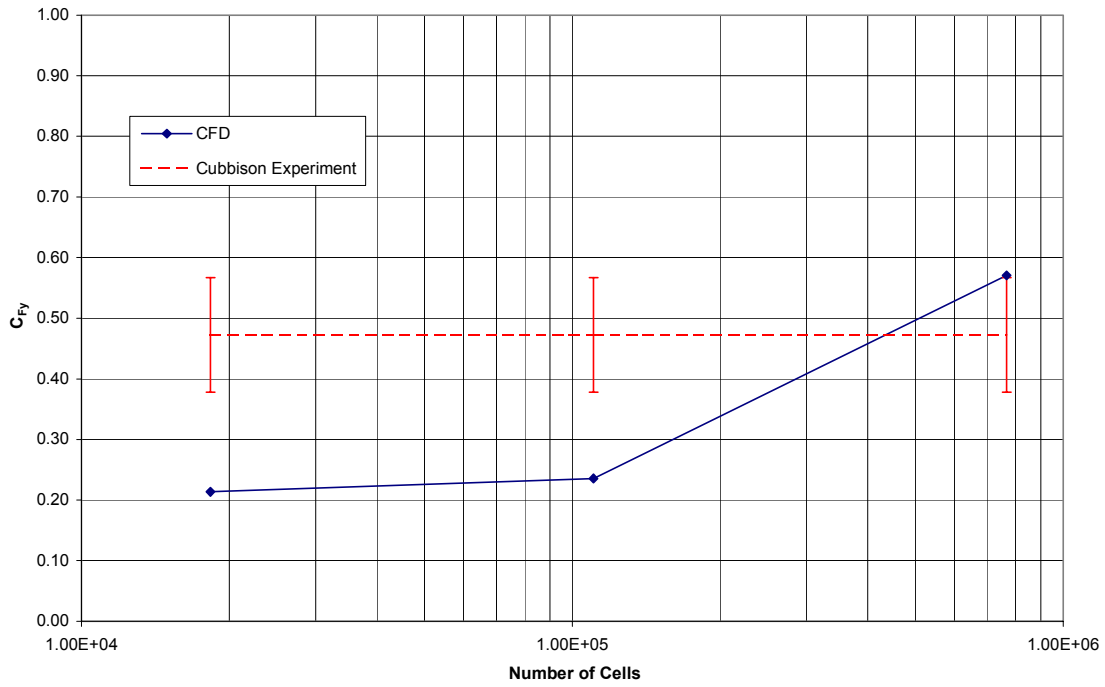


Figure 5.18. Comparison of the experimental and CFD force for the three grid sequences.

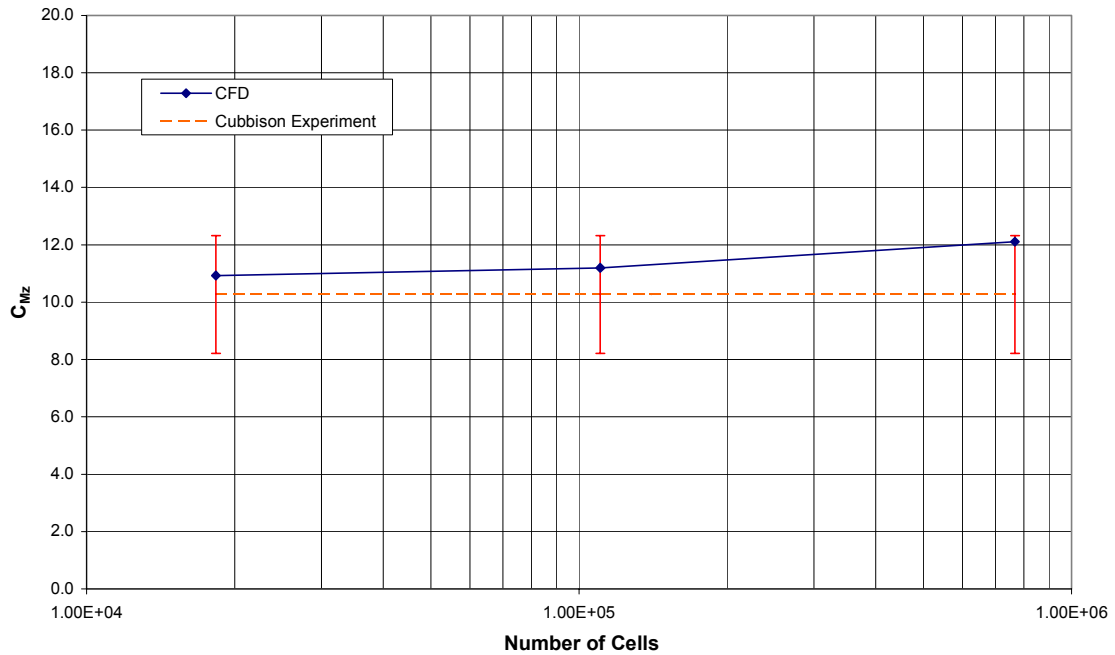


Figure 5.19. Comparison of the experimental moment and the CFD moment for the three grid sequences.

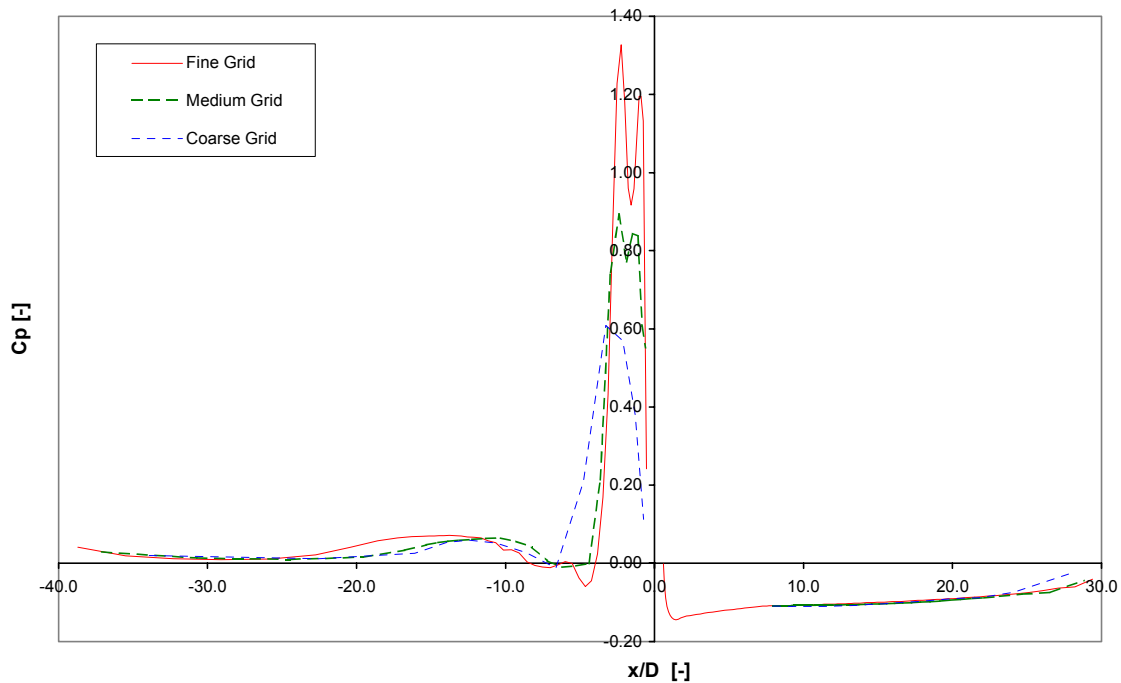


Figure 5.20. Comparison of the experimental and the CFD (for the three sequences) C_p distribution along the centerline. Mach 2.92, PR=1247.

The trend of an increase with grid refinement in both the normal force and the pitching moment is confirmed by the plot of the pressure coefficient along the tunnel centerline in Figure 5.20. While the C_p in the region aft of the injector is converged on all the grid sequences, the separation region ahead of the injector increases in extent and in intensity, as the grid is refined. This increase in pressure coefficient ahead of the injector as the grid is refined causes both the augmentation in normal force shown in Figure 5.18 and the increase in the nose-down moment shown in Figure 5.19. Clearly, Figure 5.20 indicates that the area in the computational domain that needs more grid cells to improve the grid convergence is the separation region, since the changes in the C_p distribution between the grid sequences are concentrated in this region. The comparison of the three grid sequences shows that the grid employed in the Cubbison test case was not fine enough to produce a grid-converged solution. In particular the non-monotonic convergence of the normal force raised questions about the grid quality and the grid clustering around the injector that had to be taken into consideration in the generation of the next grid.

The Mach contours from the numerical solution are qualitatively compared to the flowfield shown by the shadowgraph taken by Cubbison during the experiment in Figure 5.21. and to the C_p mapping on the flat plate surface in Figure 5.22. The CFD and the experimental results show an overall good agreement with the shadowgraph lines closely matching the Mach contour lines of the CFD solution. Also, the C_p distribution computed with GASP shows a good agreement with the experimental distribution.

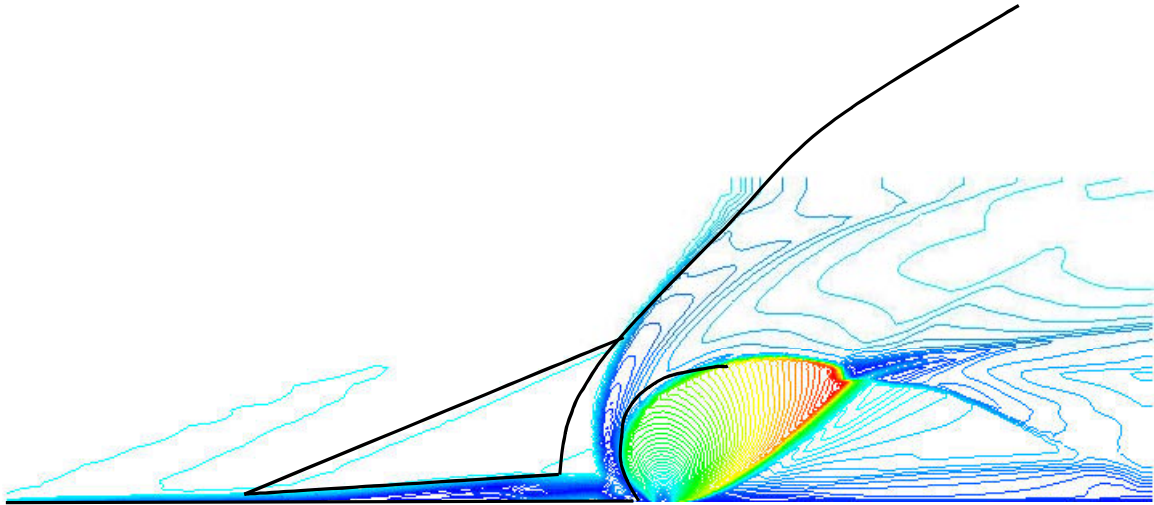


Figure 5.21. Mach number contour lines on the plane of symmetry. Mach 2.92, PR=677, sequence 1(709,161 cells).

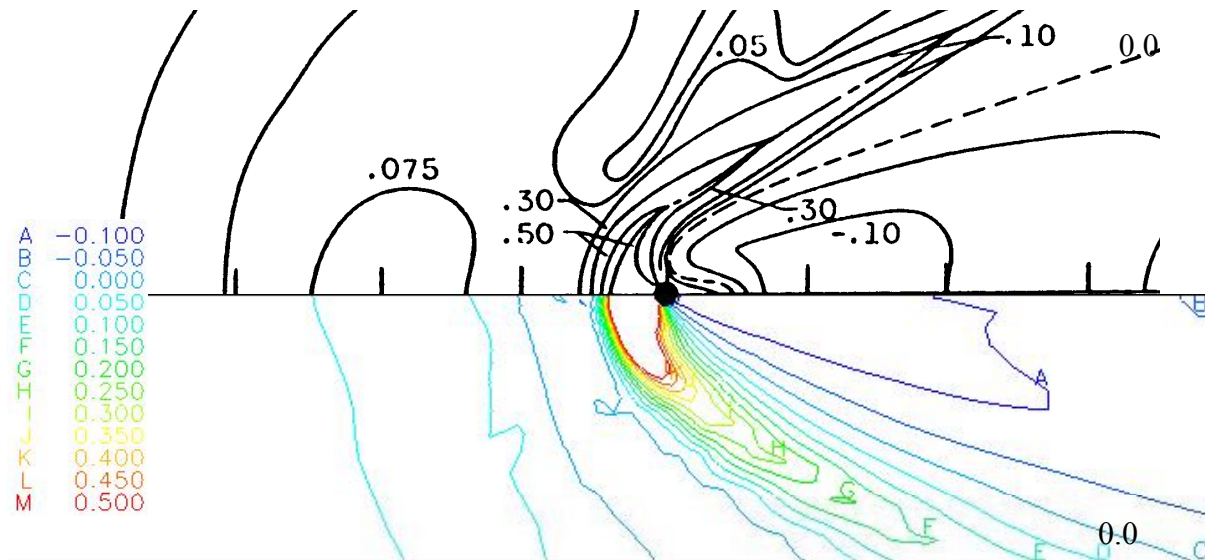


Figure 5.22. C_p contour lines on the flat plate surface. Mach 2.92, PR=677.

The comparison of the experimental force and moment with the three grid sequences is shown in Figure 5.18 and Figure 5.19, respectively. Note that the experimental force and moments were calculated by integration of the C_p plot as found in the original Cubbison paper. It is important to remember that, as discussed in Section 5.4.2, due the limited number of pressure orifices on the surface of the flat plate the experimental pressure mapping was drawn by interpolating the isobars from one point to the other. This interpolation process necessarily creates a data-reduction uncertainty that is added to the experimental uncertainty. The combined effect of the uncertainty in the measurements and in the data-reduction affects the values for the experimental normal force and pitching moment.

In spite of the similarity in the shape of the isobars of the pressure mappings on the flat plate surface (Figure 5.22) the force and moments plots (Figure 5.18 and Figure 5.19) and data (Table 5.8) show the need to improve the number of cells in the grid. Note in fact how the force and moment values are still changing considerably between the medium (sequence 2) and the fine (sequence 1) grids. Figure 5.20 shows a comparison of the C_p distribution. Again it is noticeable the change in the solution between the three different grid sequences. Note how the fine grid can resolve much better the flow in the region just ahead of the injector. These laminar calculations showed the need for an improved grid with more grid cells. Also it was found out that in order to assure the stability of the problem the calculations have to be run with a constant time step instead of a constant CFL number. Using a constant time step slows down the convergence but assures stability. Once the problem has been settled on the fine grid it was possible to ramp up the time step and to speed up the convergence again.

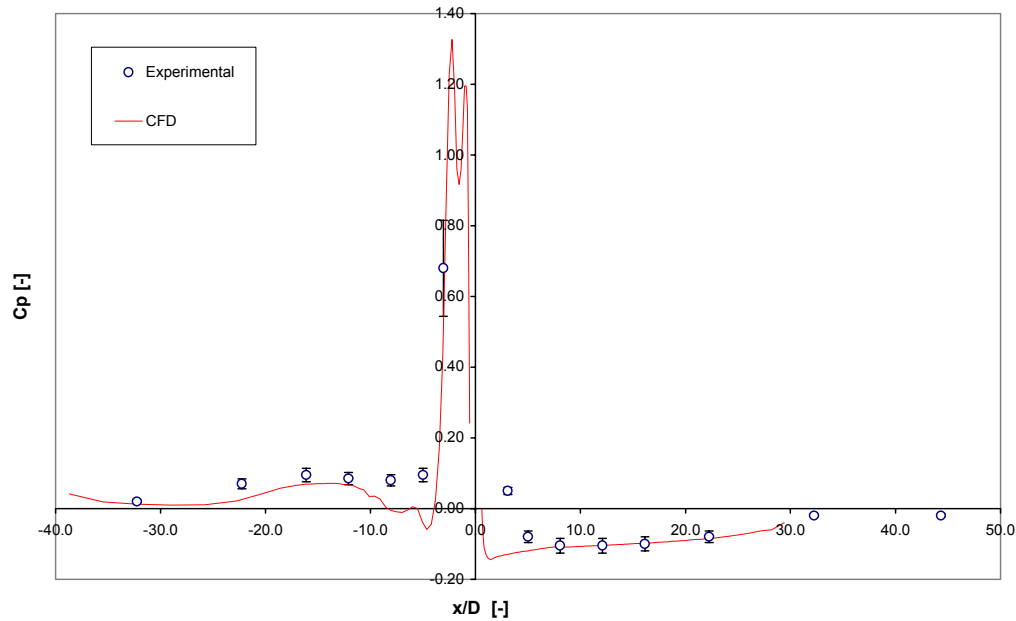
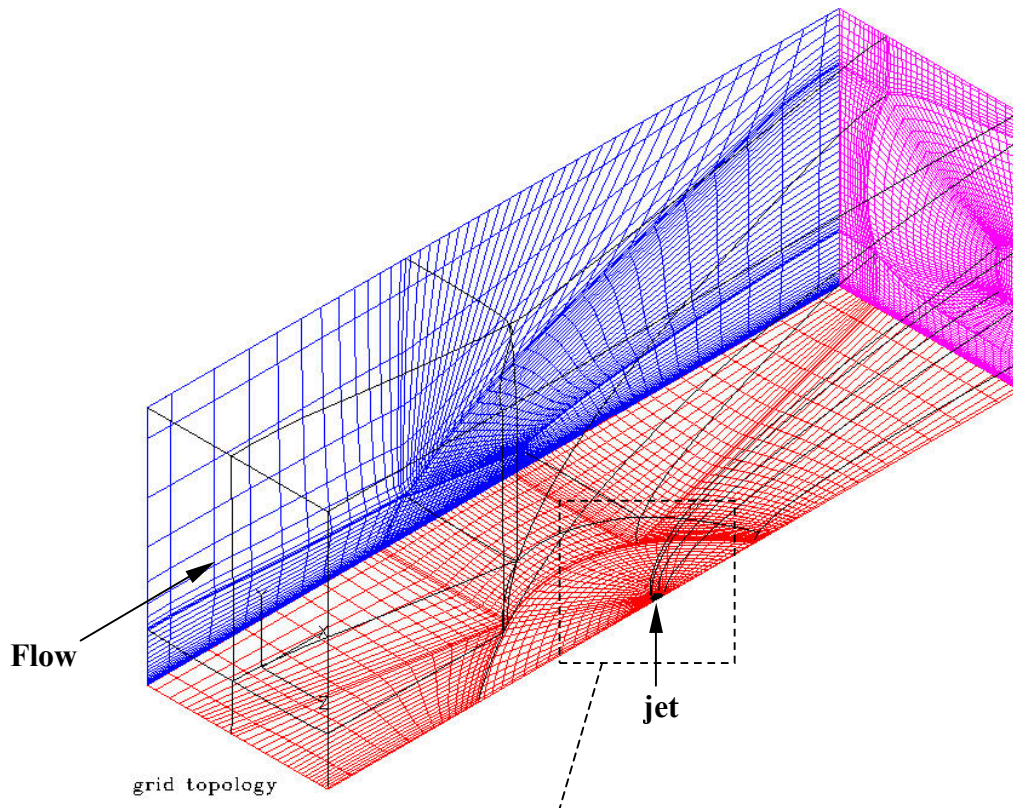


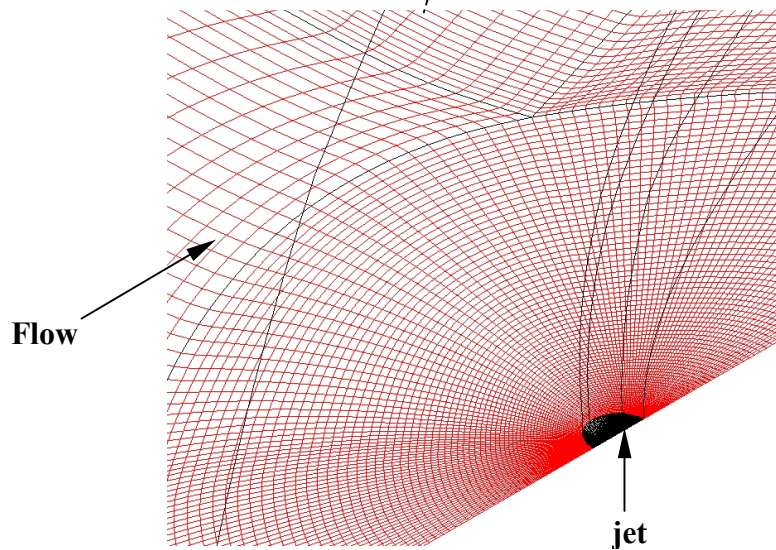
Figure 5.23. Comparison of the experimental and the C_p distribution along the centerline. Cubbison case, Mach 2.92, PR=677.

Turbulent Cases

The laminar calculations showed a good overall agreement with the experiment. More important, they showed that the numerical solution could adequately describe the flow physics of the complex three-dimensional jet interaction flowfield. A few areas for improvement were highlighted, the main one being the need for a finer grid especially in the separation region. The grid used for the simulation of the Cubbison experiment comprised 766,488 cells on the fine sequence. The challenge now was to decrease the cell size around the injector without affecting the rest of the grid and without greatly increasing the overall number of cells. In addition to these requirements that were pointed out by the laminar calculations, the grid now had to have a fine enough spacing at the wall to handle a turbulent boundary layer. To meet the above requirements, the mixed H- and C-type grid topology was retained, but the zones were re-shaped to optimize the cell distribution around the injector and in the separation region. The zones in the new grid smoothly blended one into the other with the C-type grid around the injector having a curved outer boundary rather than a rectangular one as in the old grid (see Figure 5.16). The new grid is shown in Figure 5.24. This grid topology will be used consistently for the turbulent Letko case and then for all the other Virginia Tech cases. However, the total number of cells will change due to the need to improve the refinement in one region or another or due to a longer entry length. As discussed in Chapter 3 the turbulence model chosen for the calculations was the $k-\omega$ model as developed by Wilcox in its 1988 version [92] [93]. Wilcox [93] listed the main deficiencies of the $k-\epsilon$ model as being its ill-behavior approaching a solid surface and its inaccuracy for flows with adverse pressure gradients. The first issue is usually addressed by the use of damping functions but they make the model stiff. The second issue cannot be solved since, as shown by Wilcox, the $k-\epsilon$ model's "defect-layer structure is consistent with measurements only for constant-pressure turbulent boundary layers" [93]. On the other hand, the $k-\omega$'s defect-layer model has been proven to be consistent with experimental data in all types of pressure gradients. In addition to this, the $k-\omega$ model can be integrated all the way to the wall without the use of complicated viscous damping functions. Ultimately, Wilcox's $k-\omega$ model was chosen because of its proven reliability and for its better performance than the $k-\epsilon$ model for compressible wall-bounded flows and adverse pressure gradients. [11] [54].



(a) The entire computational grid



(b) Detail of the injector

Figure 5.24. (a) Perspective view of the new grid topology used for the Letko case.(b) Detailed view of the grid around the injector. Letko case, Mach 4.50, PR=680.

5.5.3 Letko turbulent case (Mach 4.50, PR680)

The first turbulent test case to be simulated was the Letko experiment [42] from 1963. This experiment was chosen as an intermediate step between the laminar cases and the Virginia Tech experiments mainly because the latter were still in the process of being set up and the exact test conditions were not known. The simulations were first run on a fine grid with 902,204 cells. However, to perform a more exhaustive grid-convergence study, the grid was refined further in the freestream direction. The new grid feature 1,769,280 cells and was called “superfine sequence” to distinguish it from the fine sequence. So, a total of four grid sequences were available to assess the discretization error. Since the Letko paper did not report any mass flow through the nozzle but only the geometric dimensions and the flow conditions, the grid convergence study assumed a discharge coefficient of 1.00. This assumption does not affect the validity of the grid convergence study since the discretization error is a pure mathematical issue and it is independent of the errors in the physical modeling. However, as shown further below, the comparison of the numerical solution with a discharge coefficient of 1.00 and the experiment was not favorable and showed that a better estimate of the discharge coefficient was needed to simulate the real flowfield. To address this, simulations were run of the internal flow through the sonic nozzle as will be shown in the following sections. The new discharge coefficient was calculated to be 0.78. Once this better estimate for the discharge coefficient was available, the simulation of the Letko experiment was run again with the new nozzle mass flow on the coarse, medium and fine grid sequences (see the section “*Comparison of CFD calculations with a jet discharge coefficient of 0.78 to Experiment.*”). As expected, the comparison with the experimental results showed a better agreement than the numerical solution employing a discharge coefficient of 1.00. The flow conditions were the same for all the simulations of the Letko experiment and they are shown in Table 5.9 and Table 5.10. The flat plate model used in the experiment is shown in Figure 5.25.

The Letko experiment was also used as a test case to assess the effect that adding a small secondary injector behind the primary injector would have on the forces and moments acting on the flat plate. Because this calculation was only meant to indicate trends in the flow parameters, it was run only on the coarse and medium grid sequences.

Parameter	
Gas	Air, perfect gas ($\gamma=1.40$)
M_∞	4.5
$P_{\infty, t}$	587.75 kPa
P_∞	2.03 kPa
T_∞	66.8 K
Type of boundary layer	Turbulent (Wilcox $k-\omega$)

(a) Free-stream

Parameter	
Gas	Air, perfect gas ($\gamma=1.40$)
M_J	1.0
$P_{J,t}$	1,380.95 kPa
P_J	729.53 kPa
T_J	298 K
$P_{J,t} / P_\infty$	680
Jet mass flow ($C_d=1.00$)	0.5384 Kg/s *
Jet thrust ($C_d=1.00$)	186.31 N *

(b) Jet. * These values were not reported by Letko but were calculated assuming isentropic flow through the nozzle and a discharge coefficient of unity.

Table 5.9. Summary of flow parameters for the Letko experiments.

Parameter	
Flat plate entry length, x_0	37.5 cm
Injector diameter, d_j	1.52 cm
x_0/d_j	24.6

Table 5.10. Flat plate and injector dimensions for the Letko experiment.

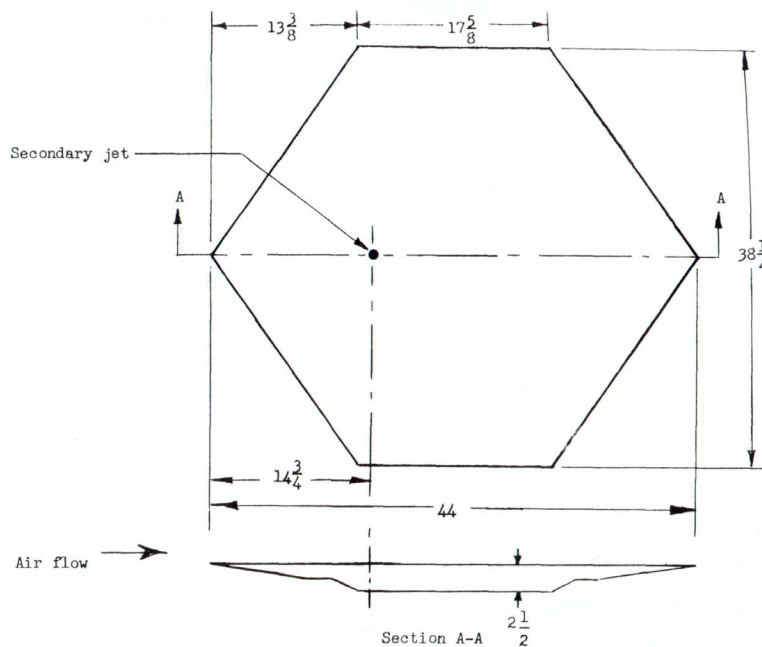


Figure 5.25. Experimental flat plate configuration for the Letko test case as presented in Ref. [42].

Grid-Convergence Study with a discharge coefficient of 1.00

In order to assess with more accuracy the discretization error and the level of grid convergence for a jet interaction case, the numerical solution of the Letko experiment was converged on four grid levels instead of the usual three. The baseline grid from which the other three grid sequences were obtained was the fine grid with 902,240 cells. This grid was sequenced twice in the usual way as described in Sections 5.5.2 i.e. by eliminating every other grid cell in the three spatial dimensions. The result was a coarse sequence with 20,362 cells and a medium grid sequence with 127,976 cells. The fourth grid sequence was obtained by refining the fine grid sequence thus obtaining a “*super-fine*” grid sequence. Due to computational limitations it was not possible to double the number of cells in the three spatial dimensions since this “super-fine” grid level would have had more than 7 million cells. The fine grid spacing in the spanwise direction and in the directions normal to the surface of the flat plate (the cell adjacent to the surface is well below a y^+ of 1.00) were proved to be more than adequate to resolve the pressure gradients encountered in these directions. Also, the previous calculations showed that the area of major need of refinement was the separation region which was mostly affected by the longitudinal (x-direction) spacing of the cells in this region. Therefore, the number of cells was doubled only in the longitudinal direction (the freestream direction). The resulting “super-fine” grid level had 1,769,280 cells. For this reason the grid factor between the fine and superfine grid sequences is 2.

Even though the main goal of this calculation was to perform a grid convergence study, the numerical solution is compared to the experimental forces and moment for completeness. Note how the force predicted by the simulation over-predicted the experimental value by as much as 61% while the pitching moment was under-predicted by roughly 50%. Figure 5.26, Figure 5.27 and Table 5.12 show the results of the grid convergence study. The forces and moments on each grid level are compared to the “approximate exact solution”: obtained from the “Mixed 1st +2nd Order Extrapolation”. Note that the convergence of both the force and moment is not monotonic. This behavior is the same as observed by Hosder [35] when employing Wilcox’s $k-\omega$ turbulence model. However, the discretization error is quite small for both the fine and superfine grid sequences as it ranges between 0% and 2% for the force and 2% and 10% for the pitching moment (Table 5.12). When the discretization error is so small, other types of errors in the numerical solution become important, such as the round-off error and even the error produced by the iterative convergence. The force data for the superfine grid indicates a slight decrease in force. As seen before for the Cubbison case, the convergence is critical in the separation region indicating that probably this non-monotonic behavior of the Letko calculation is caused by changes in the separation region. The convergence of the moment results shown in Figure 5.27, indicates the same trend as the convergence of the force. In fact, a decrease in the force ahead of the injector and in the separation region would cause a more negative pitching moment.

The order of accuracy p for the first three sequences (coarse, medium and fine) and for the last three grid sequences (medium, fine and super-fine) are compared in Table 5.13. The order of accuracy was calculated following the procedure described in Section 5.3.2. The two calculated orders of accuracy were found to be quite close, differing by 5%. This behavior indicates that the solution is in the asymptotic convergence region. Note that the real order of accuracy of the computational solution is first-order rather than somewhere in between the nominal second-order for the viscous fluxes and third-order for the inviscid fluxes. The reduction of the order of accuracy to first-order is due to the presence in the solution of shocks. Due to the use of flux-limiters, the accuracy of the solution is effectively reduced to first-order in the regions where shocks exist. Even though limiters reduce the order of accuracy of the solution to first-order only in the regions near the shocks, this local change greatly affects all the rest of the computational domain as shown by the calculated first-order accuracy.

It is difficult to find a clear trend for the C_p distribution ahead of the injector for the fine and superfine grid sequences as shown in Figure 5.28. The pressure coefficient for the fine grid appears to be slightly higher than the superfine grid in the region between a x/D of -2.0 and -0.5.

But, the reverse is true for the region between a x/D of -4.5 and -2.0. On the other hand, the comparative behavior of the C_p distribution on the coarse, medium and fine grid indicates a monotonic convergence of the C_p . The trend in the C_p distribution corresponds to the trend of the forces and moments of Figure 5.26 and Figure 5.27. As the pressure coefficient in the separation region increases with grid refinement, so does the normal force (higher C_p means higher pressure force on the flat plate). Also, since the increase in normal force occurs ahead of the injector, it creates a more positive (nose-down) pitching moment and again this is verified by the trend of the curve in Figure 5.27.

An even more accurate test for grid convergence is the convergence of the skin friction coefficient since it involves the derivative of the velocity with respect to the spatial direction normal to the solid surface. The C_f distribution ahead of the injector is shown in Figure 5.29. This plot basically mimics the convergence of the pressure coefficient. There are clear trends towards convergence in the coarse and medium grids, but the C_f distribution for the fine and superfine grids is virtually the same. Figure 5.29 also shows the separation location for the four grid levels. Note the small change between the medium and fine grid and the negligible difference between the fine and superfine sequences.

Sequence	Number of Cells	Experiment		CFD		$\epsilon C_{Fy} \%$	$\epsilon C_{Mz} \%$
		C_{Fy}	C_{Mz}	C_{Fy}	C_{Mz}		
3	20,362	0.501	-3.170	0.774	-1.713	54	-46
2	127,976			0.800	-1.638	59	-48
1	902,240			0.810	-1.588	62	-50
0	1,769,280			0.806	-1.635	61	-48

Table 5.11. Comparison of the experimental to CFD force and moment for the Letko case with a discharge coefficient of 1.00.

Sequence	Number of Cells	Richardson Extrapolation		CFD		$\epsilon C_{Fy} \%$	$\epsilon C_{Mz} \%$
		C_{Fy}	C_{Mz}	C_{Fy}	C_{Mz}		
3	20,363	0.805	-1.645	0.774	-1.713	-4	4
2	127,976			0.800	-1.638	-1	0
1	902,240			0.810	-1.588	1	-3
0	1,769,280			0.805	-1.635	0	-1

Table 5.12. Comparison of the solution on the three grid levels with the solution obtained with the “Mixed 1st +2nd Order Extrapolation” for the Letko case with a discharge coefficient of 1.00. “ ϵ ” is the discretization error in the solution.

Sequence	Number of Cells	Order of Accuracy, p
3	20,363	0.96
2	127,976	
1	902,240	
0	1,769,280	0.91

Table 5.13. Comparison of the order of accuracy, p , calculated using the first three grid sequences and the last three grid sequences. Letko case with a discharge coefficient of 1.00.

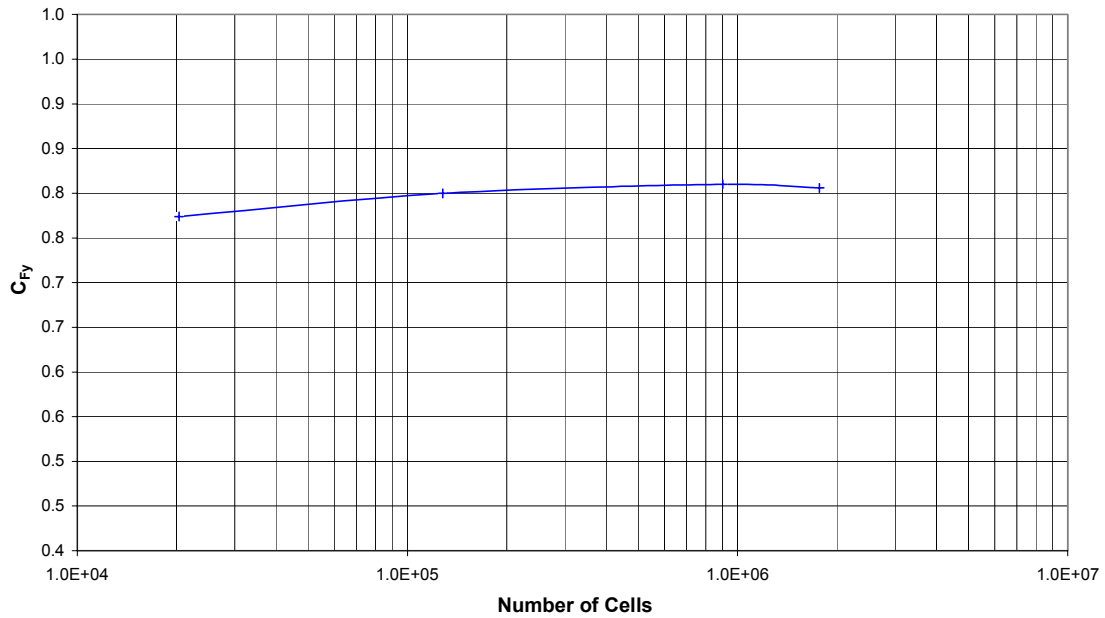


Figure 5.26. Comparison of the normal force coefficient on the four grid sequences for the Letko case.

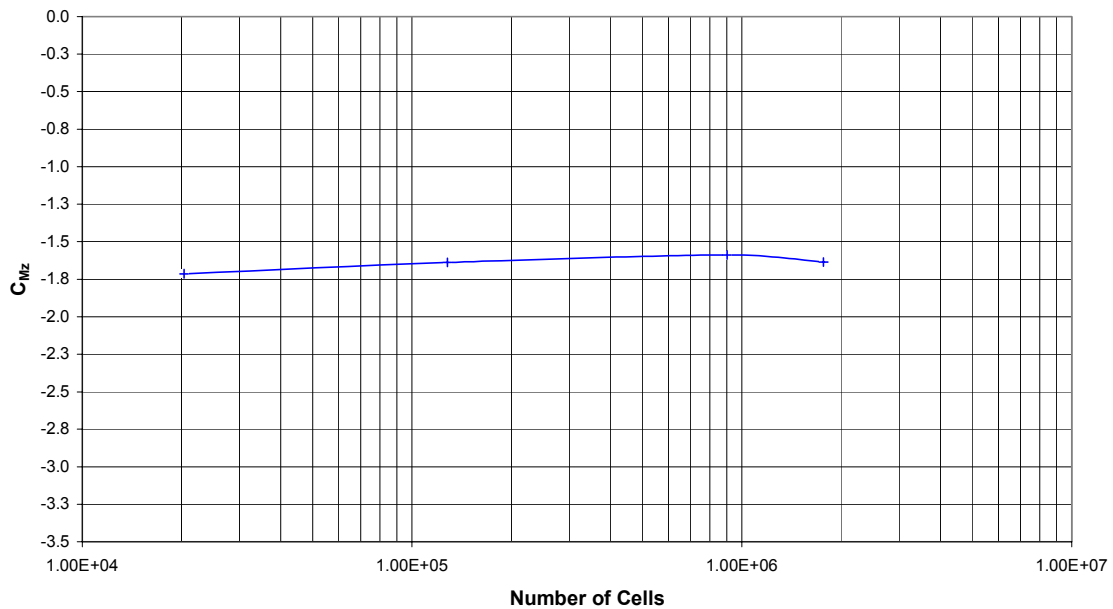


Figure 5.27. Comparison of the pitching moment coefficient on the four grid sequences for the Letko case.

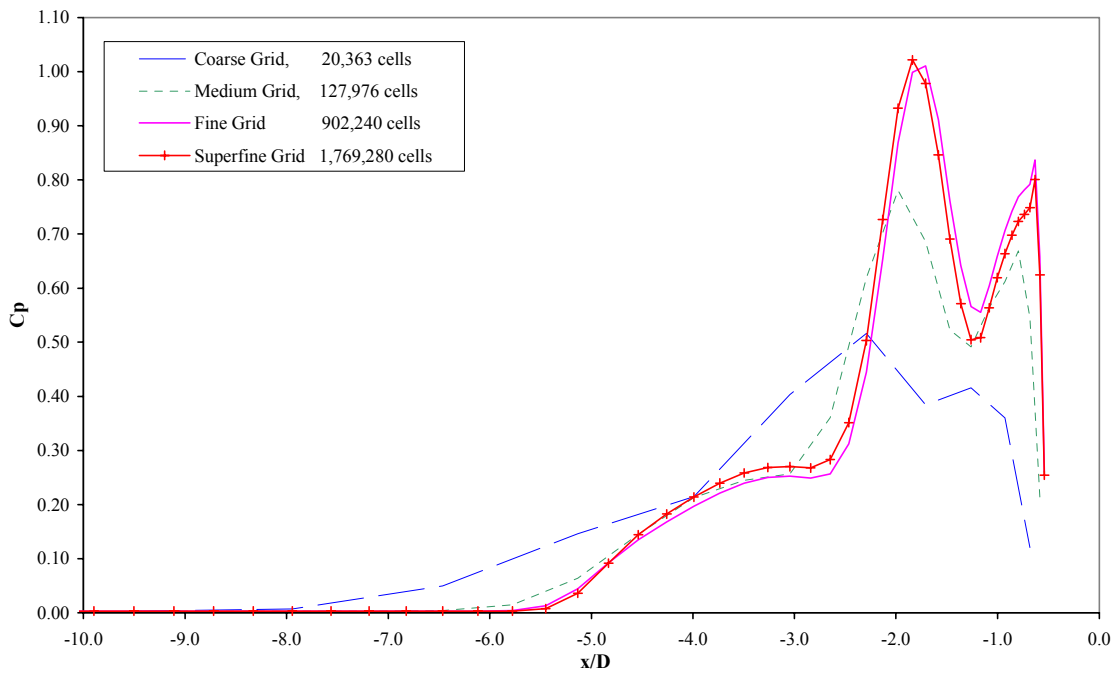


Figure 5.28. Comparison of the pressure coefficient just ahead of the injector for the four grid sequences.

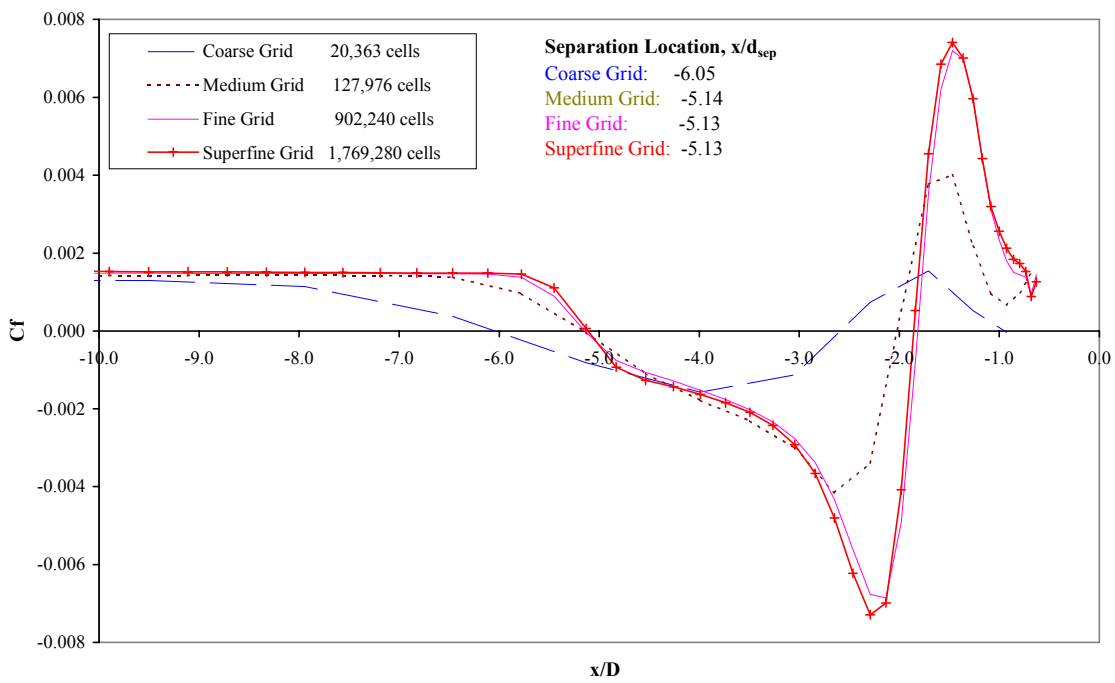
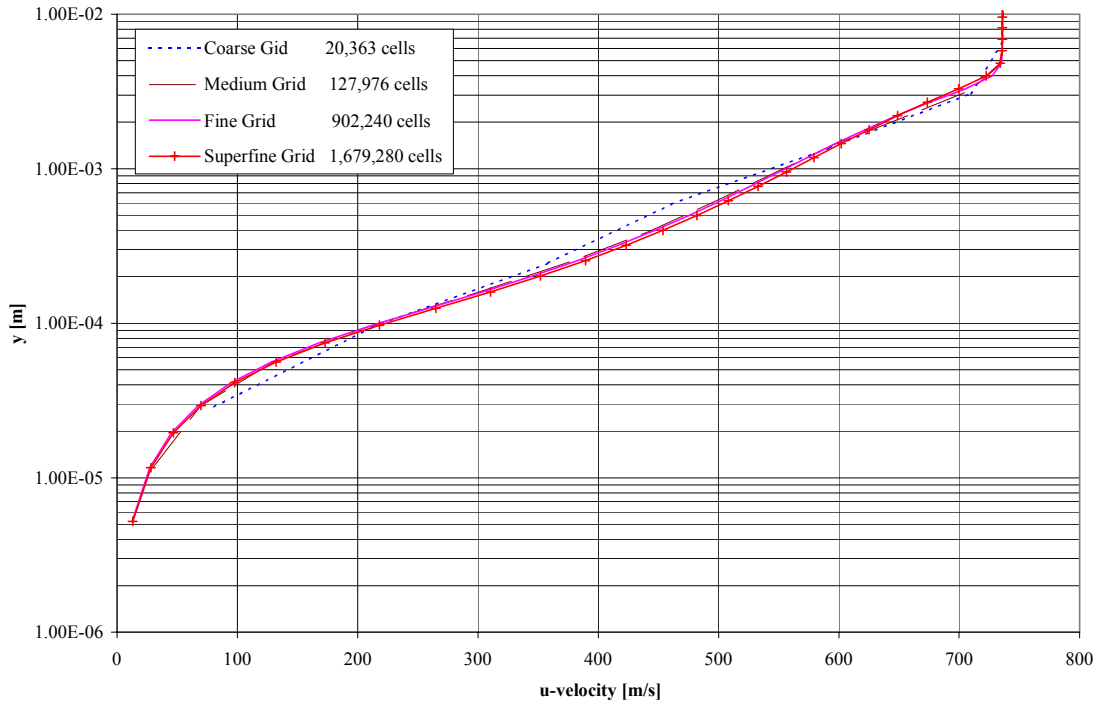
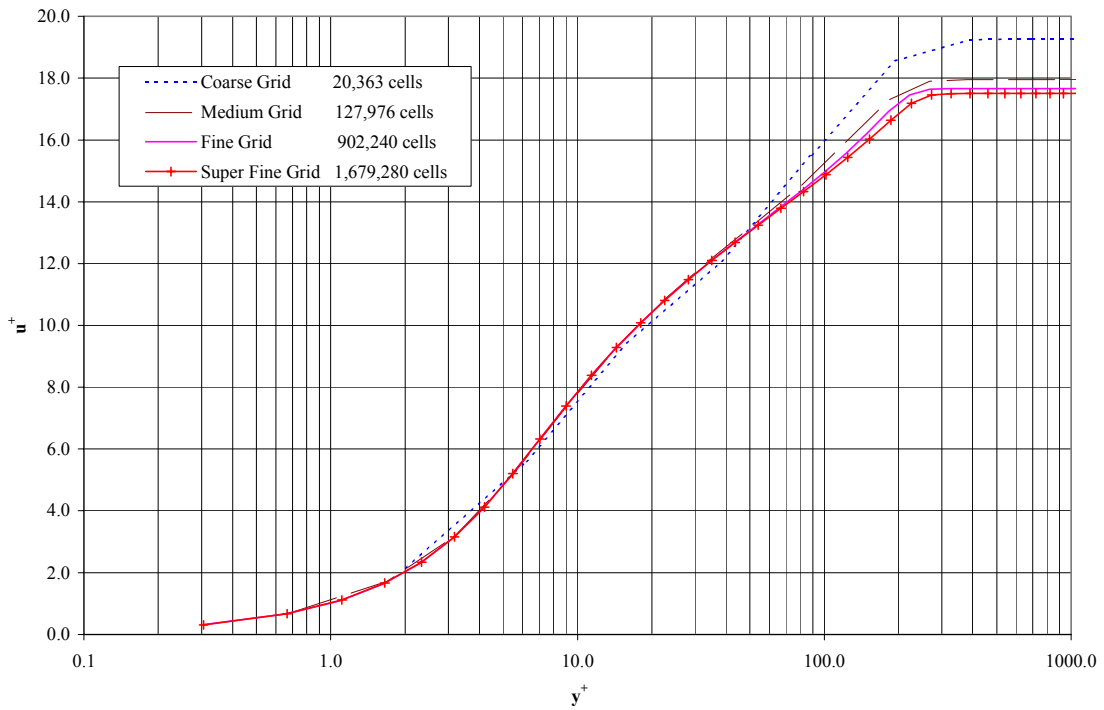


Figure 5.29 Comparison of the skin friction coefficient just ahead of the injector for the four grid sequences.



a) dimensional velocity profiles.



b) wall law plot.

Figure 5.30 Comparison of the (a) dimensional plot of the boundary layer velocity profiles and of (b) the wall law plot just ahead of the separation ($x/d=-8.5$) on the symmetry plane for the four grid sequences.

The above remarks concerning the overall grid convergence of the fine grid level are further confirmed by the boundary layer profiles shown in Figure 5.30. Note that the velocity distribution and the y^+ distribution for the medium, fine and superfine grid sequences are virtually unchanged while that of the coarse grid shows some differences.

To complete the grid convergence study, a visual comparison was carried out of the main flowfield features on the four grid sequences. Figure 5.31 compares the Mach contours on the four grids and it also introduces the bow shock angle, θ_1 , the plume angle, θ_2 , and the plume height, h , as comparison parameters to assess the grid convergence. The bow shock angle, θ_1 , is the angle formed by a line with the same inclination as the bow shock and the flat plate surface (see Figure 5.31). The plume angle, θ_2 , is the angle formed by a line drawn between the center of the injector and a point halfway across the Mach disk of the plume (Figure 5.31). The plume height, h , is simply the distance from the flat plate of the center of the Mach disk. There is virtually no difference between the medium, fine and superfine grids. The solution on the coarse grid can capture most of the inviscid flow physics but as shown by the C_p and C_f plots, it does not perform well in predicting the separation region.

Figure 5.32 is a comparison of the pressure distribution on the flat plate for the four grid sequences. The angle formed by the zero- C_p line and the plane of symmetry is defined as the zero- C_p line angle, β . This angle does not change considerably between the medium, fine and superfine sequences. However, these plots show some interesting trends. First of all, the separation region ahead of the injector becomes more defined as the grid is refined. It also extends further across the plate with increasing cell number. This was expected from the C_p plots shown in Figure 5.28. Second is the change in the pressure distribution in the region contained by the zero- C_p line. The C_p plots along the centerline did not indicate any change in this area. However, the mapping on the whole plate indicates that, as the grid is refined, the location of the zero- C_p line remains constant but the C_p values inside this line become more negative. The negative pressure coefficient means a stronger suction region aft of the injector that adds to the effect of the stronger separation ahead of the injector to increase the nose down pitching moment seen in Figure 5.27.

The grid convergence study showed how the medium and fine grid can capture most of the flow characteristics and can produce reliable force and moment estimates. As shown by the contour lines in Figure 5.31 and Figure 5.32, the salient flow details are adequately resolved by the medium and fine grid, with very small differences between the solution on these two grid sequences and the superfine grid. The force and moment data plots shown in Figure 5.26 and Figure 5.27 respectively confirm the adequacy of the coarser grid sequences in estimating the integrated quantities. A stricter grid-convergence test than the one provided by the integrated quantities is the comparison of the C_p and the C_f on the flat plate in the separation region. Figure 5.28 and Figure 5.29 show the comparison of the C_p and C_f for the four grid sequences. It is apparent how, when considering such sensitive convergence parameter, the fine grid is producing much more accurate results than the coarser sequences. Note the general closeness of the solutions

obtained from the fine and superfine grids and the relative larger difference between the coarse, medium and fine grid solutions. The same conclusions can be drawn from the comparison of the boundary layer velocity profiles shown in Figure 5.30. Thus the “fine” grid is adequate for single jet calculations

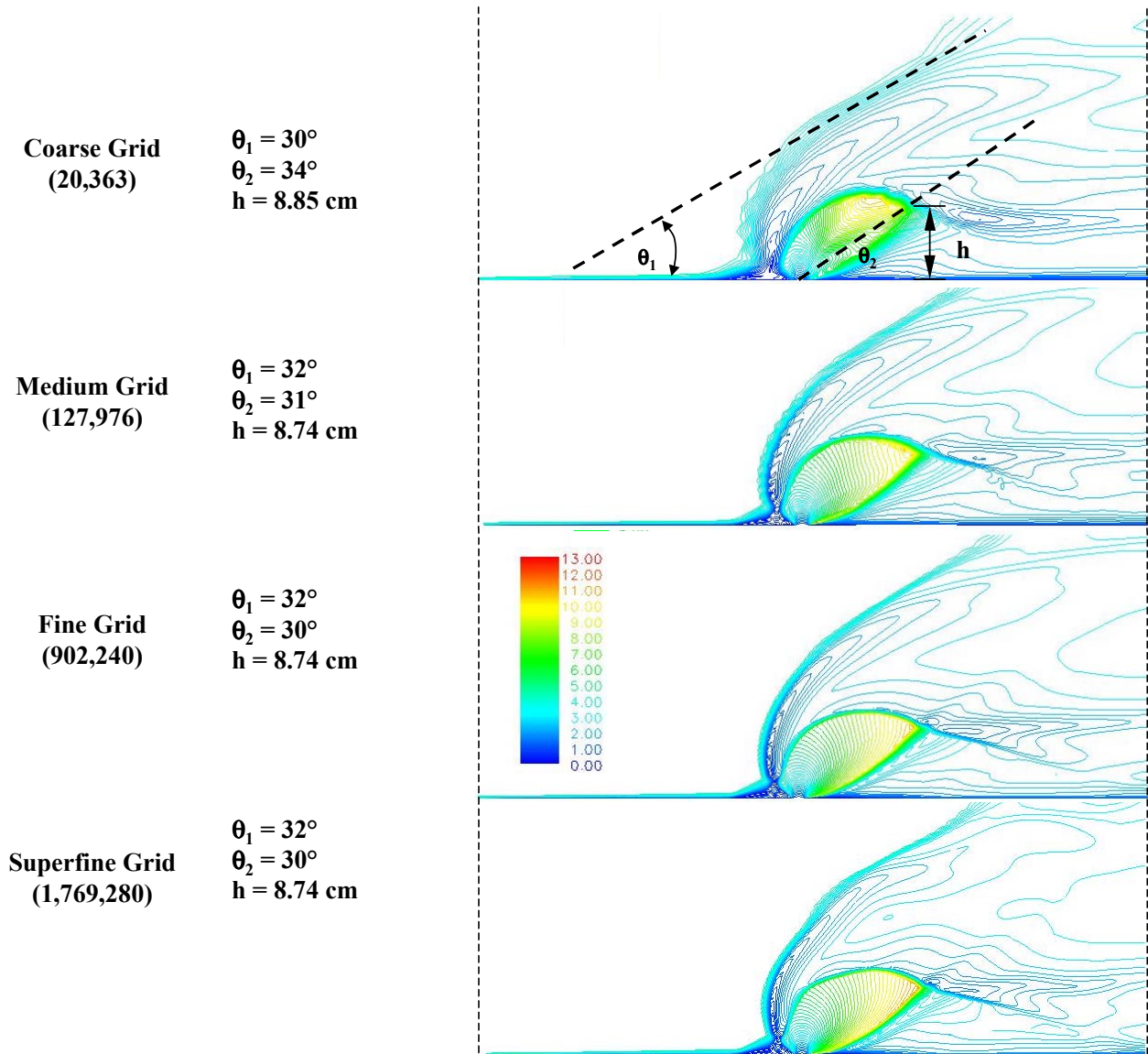


Figure 5.31. Comparison of the Mach number contour lines on the plane of symmetry for the four grid sequences. Some of the main flow parameters, such as the penetration height and the plume angle were measured and compared.

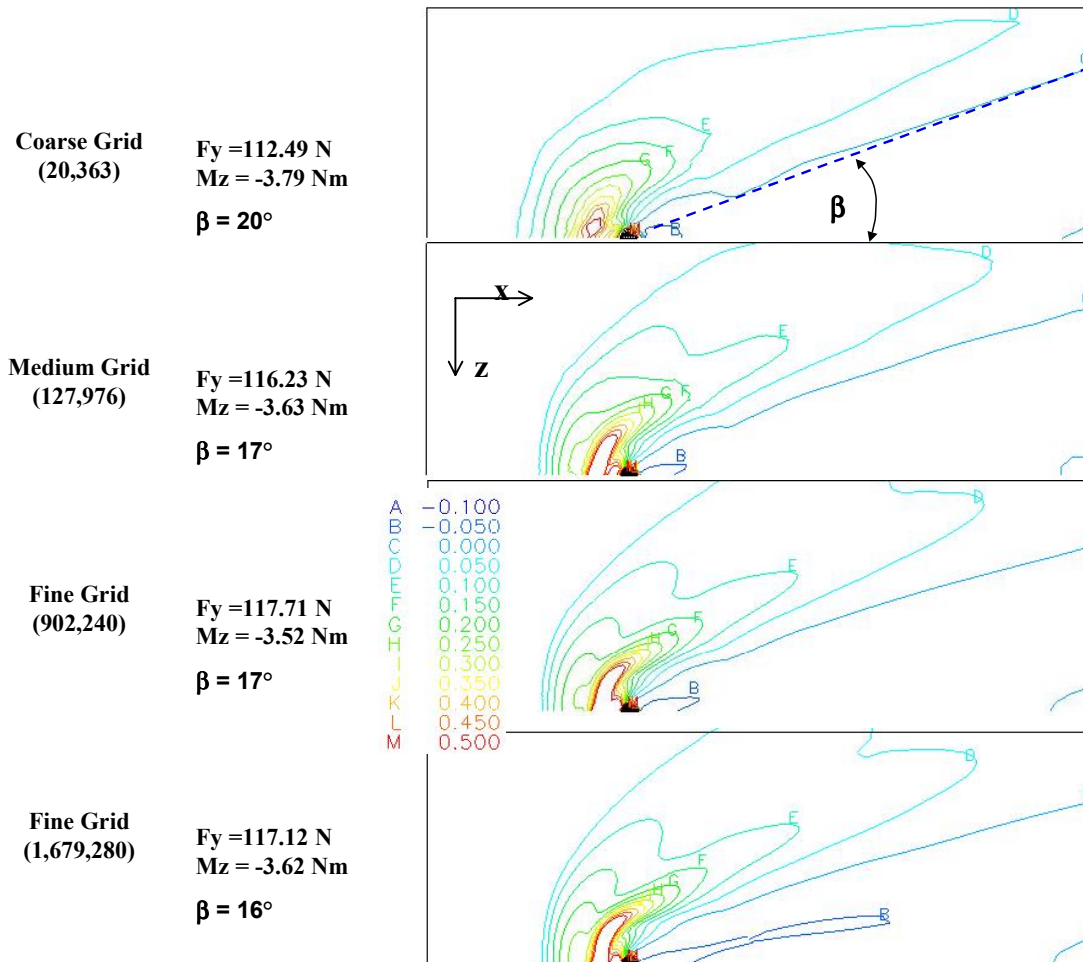


Figure 5.32. Comparison of the C_p contour lines on the flat plate for the four grid sequences. The angle formed by the zero- C_p line and the flow direction was measured and compared (β). Other parameters used for comparison are the normal force on the flat plate (F_y) and the moment about the z-axis (M_z).

Calculation of Discharge Coefficient for the Injector

The numerical simulations for the laminar (Cubbison) and the turbulent (Letko) cases overestimated the experimental normal force acting on the flat plate (see Table 5.14). Consideration of all the factors that might create a consistent over-estimation of the normal force highlighted the lack of knowledge of the discharge coefficient (C_d) of the nozzle and the inadequacy of the assumption of isentropic flow through the nozzle (i.e. the discharge coefficient was assumed to be 1.00 in all the numerical simulations up to this point). Since the discharge coefficient is a measure of the mass flow of the jet, a change in this parameter directly affects the pressure distribution on the flat plate (see the discussion about the uncertainty due to the C_d in Section 5.4.3). The forces and moments presented are obtained by integrating the static pressure over the surface of the flat plate. Therefore, both the jet thrust and the pressure force of the primary and secondary jets are not included in the computations of the forces and moments. However, an increase in the jet mass flow creates a larger barrel shock wave that in turns creates a stronger bow shock and a stronger separation thus altering the pressure field on the flat plate. Neither the Cubbison [22] or the Letko [42] papers provided any information about the mass flow of the jet.

Experiment	Experiment		CFD		$\Delta C_{Fy} \%$	$\Delta C_{Mz} \%$
	C_{Fy}	C_{Mz}	C_{Fy}	C_{Mz}		
Cubbison	0.472	10.268	0.571	12.106	+21	+18
Letko	0.501	-3.170	0.810	-1.588	+62	-50

Table 5.14. Comparison of the experimental and CFD force and moment for the Cubbison (laminar) and the Letko (turbulent) experiment.

Both papers gave information about the jet total conditions and stated that the nozzles were sonic, but they lacked detailed information about where the jet conditions were measured. Flow conditions might have been measured in a plenum or they might have been measured along a duct leading the pressurized air to the nozzle or in the nozzle itself. The location of the measurements is important since it affects the viscous losses and hence the true mass-flow through the nozzle.

To address this lack of information about the location where the flow conditions were measured and to determine the mass flow of the jet, several numerical calculations of the flow inside the nozzle were run. Schematics of all the flow conditions that were considered are shown in Figure 5.33 as well as the geometry of the nozzle as presented by Letko. Each calculation simulated a different scenario such as that of a uniform velocity profile entering the nozzle or a fully-developed velocity profile or the flow from a plenum chamber through a converging pipe. In addition to the changes in nozzle geometry, the back-pressure, the turbulent model (Baldwin-Lomax vs. $k-\omega$) and the flux type (full-flux vs. split flux) at the sonic exit boundary condition were changed to verify the effect of these parameters on the discharge coefficient. The results of all the GASP calculations are presented in Figure 5.34. It is clear that the largest effect on the discharge

coefficient is produced by the type of inlet boundary condition. Although possible, it is unlikely that the conditions were measured along a pipe leading the pressurized air to the nozzle. It is most likely that the pressurized air would be drawn from a plenum (or settling chamber) so as to reduce losses and turbulence in the jet. Because of this, the calculations involving a plenum are considered to be more representative of what the real experimental setup was. The plenum was simulated by building a large reservoir with smooth walls that gradually lead to the smaller nozzle. Note that Figure 5.33 is a schematic of the geometry used in the calculations, is not drawn to scale, and does not represent the plenum geometry used in the calculations. The estimated value for the discharge coefficient was obtained by averaging the results of the calculations that simulated a plenum. The final averaged discharge coefficient was then chosen to be 0.78. Note in Figure 5.34 the small effect that the turbulence model or the back-pressure have on the discharge coefficient. A discharge coefficient of 0.78 indicates that the true mass flow through the injector is 78% the mass flow of an ideal nozzle with no losses.

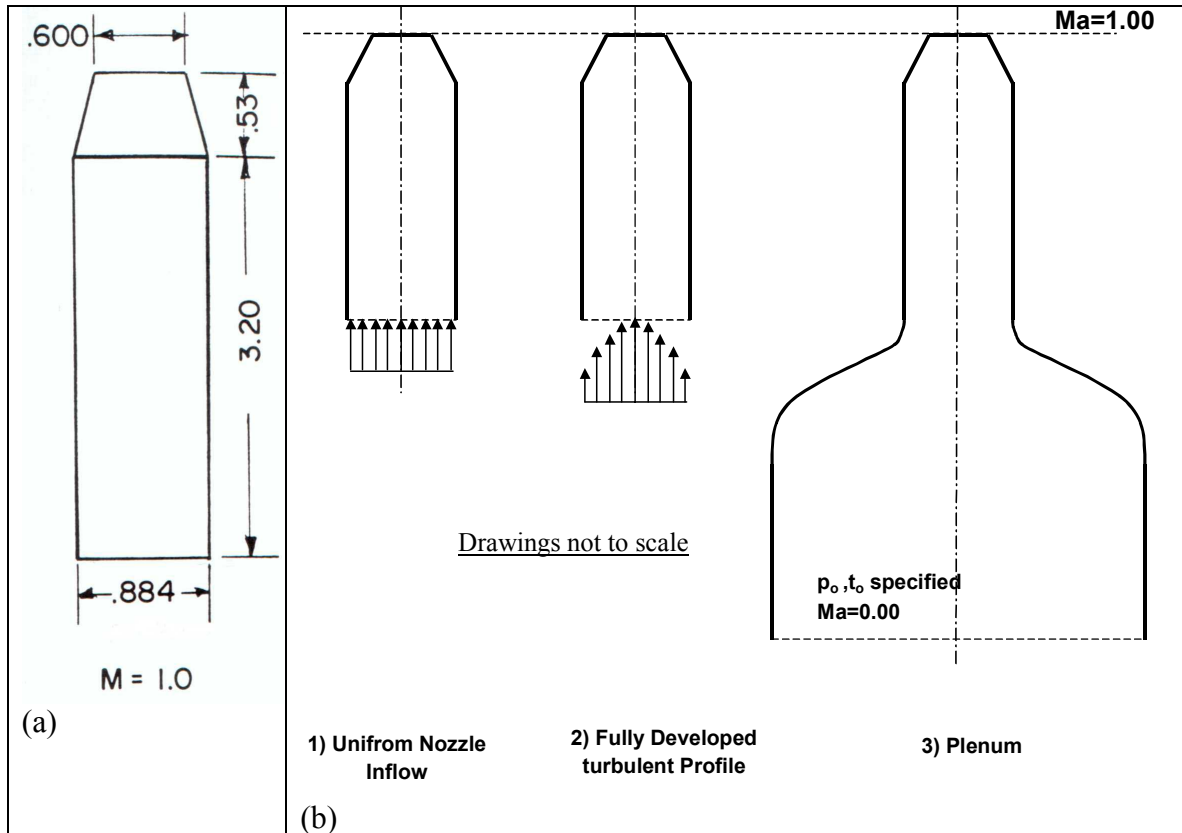


Figure 5.33. (a) The nozzle drawing from the original Letko paper [42] (all dimensions in inches). (b) The different inflow conditions that were used to calculate the nozzle flow. Drawings not to scale.

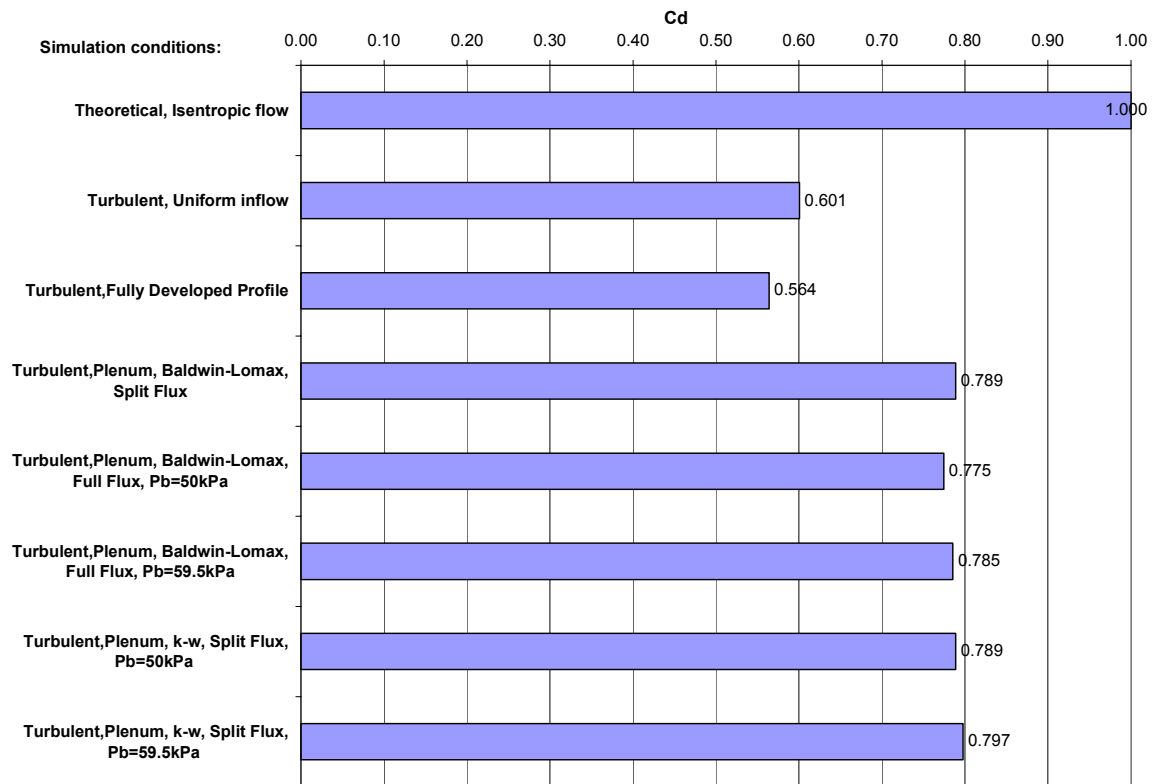


Figure 5.34. Discharge coefficient (C_d) results of the GASP calculations with the different flow conditions.

Comparison of CFD calculations with a jet discharge coefficient of 0.78 to Experiment.

The discharge coefficient obtained from the simulations of the sonic injector was then used to modify the mass flow rate of the nozzle of the Letko case. This was obtained by reducing the area of the injector by 22% of its original dimensions and keeping the total conditions of the jet the same as before. This approach created an injector area smaller than the physical jet it simulated even though the mass flow was the same. The jet kept its step-profile; no boundary layer profile inside the nozzle was simulated. This approach was followed since no detailed information about the jet exit velocity profile was provided.

The simulation was re-started on the coarse grid sequence from the solution of the flowfield with a discharge coefficient of 1.00. All the other flow parameters and grid topology were the same as for the Letko case with a discharge coefficient of 1.00. The force and moment results obtained from the solutions on the three grid sequences are shown in Figure 5.35 and Figure 5.36. The comparison shows a better agreement between the experimental measurements and the CFD calculations with a C_d of 0.78. Table 5.15 shows that the numerical results for the simulation with a C_d of 0.78 differ from the experiment by -25% for the normal force (ΔF_y) and by 45% for the pitching moment (ΔM_z). These discrepancies compare with those obtained for the numerical solution with a discharge coefficient of 1.00, 62% and -48% for the normal force and moment respectively (Table 5.11). Both the simulation with a C_d of 0.78 and the simulation with a C_d of 1.00 showed the same grid convergence trend. In both calculations, as the grid was refined, the normal force and the pitching moment converged to values that are less in agreement with the experimental results than the coarser grid calculations (see Figure 5.35 and Figure 5.36).

The comparison of the pressure mappings on the surface of the flat plate are shown in Figure 5.37. The general shape and trend of the isobars is predicted fairly well by the CFD. The predicted zero- C_p line (line "C") is in very good agreement with the experiment. The experimental mapping presents some non-physical features that are difficult to explain. For example, the lobes of positive C_p immediately ahead of the injector should extend to the symmetry plane instead of curving back and creating an almost oval lobe. These arguable features in the experimental mapping are probably the result of too few pressure ports to draw reliable pressure mappings. The small number of pressure ports is confirmed by the pressure plot along the tunnel centerline shown in Figure 5.23. Note that especially ahead of the injector there are only five pressure orifices. In order to draw the continuous pressure mapping of Figure 5.37, the experimentalist had to make some assumptions about the shape of the iso-surfaces thus increasing the level of uncertainty in the pressure mappings. From looking at Figure 5.23, it appears clear that the computations under-predicted the extent of the separation region even though it appears that the maximum C_p values were over-predicted by the CFD. As seen also in the simulation of the Cubbison experiment there is very good agreement between the experiment and the CFD in the region aft of the primary injector where the negative pressure coefficient slowly recovers to the freestream value at a x/d of 23.0.

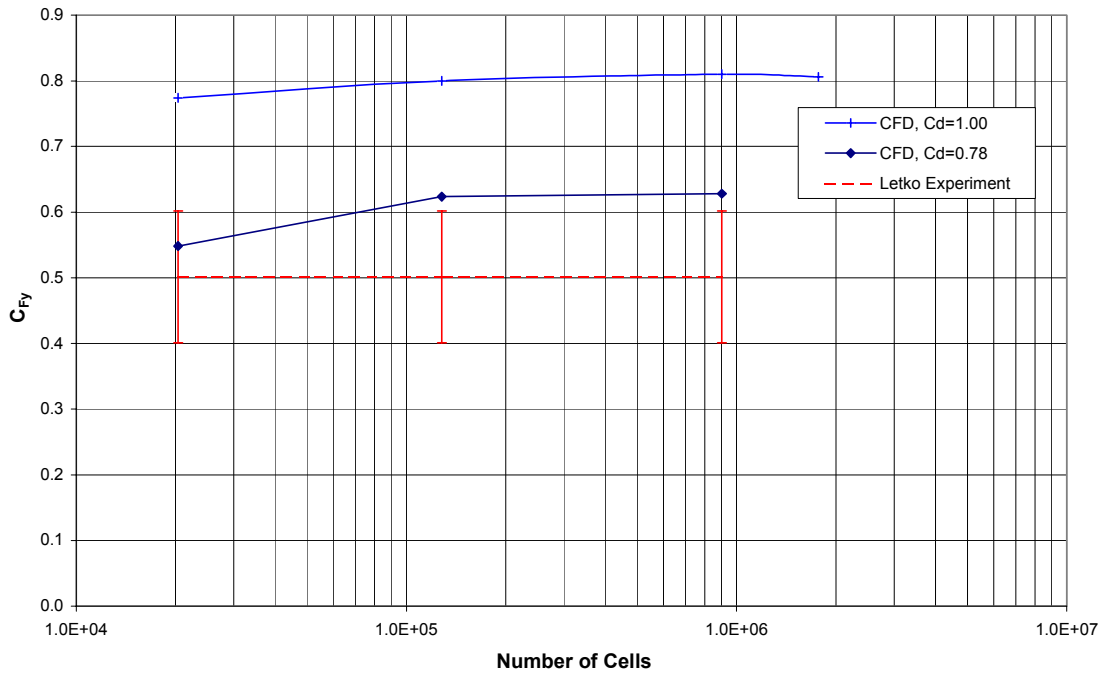


Figure 5.35. Comparison of the force on the flat plate obtained from the solution on the three sequences of Grid 5 for the Letko case with a discharge coefficient of 1.00 and 0.78.

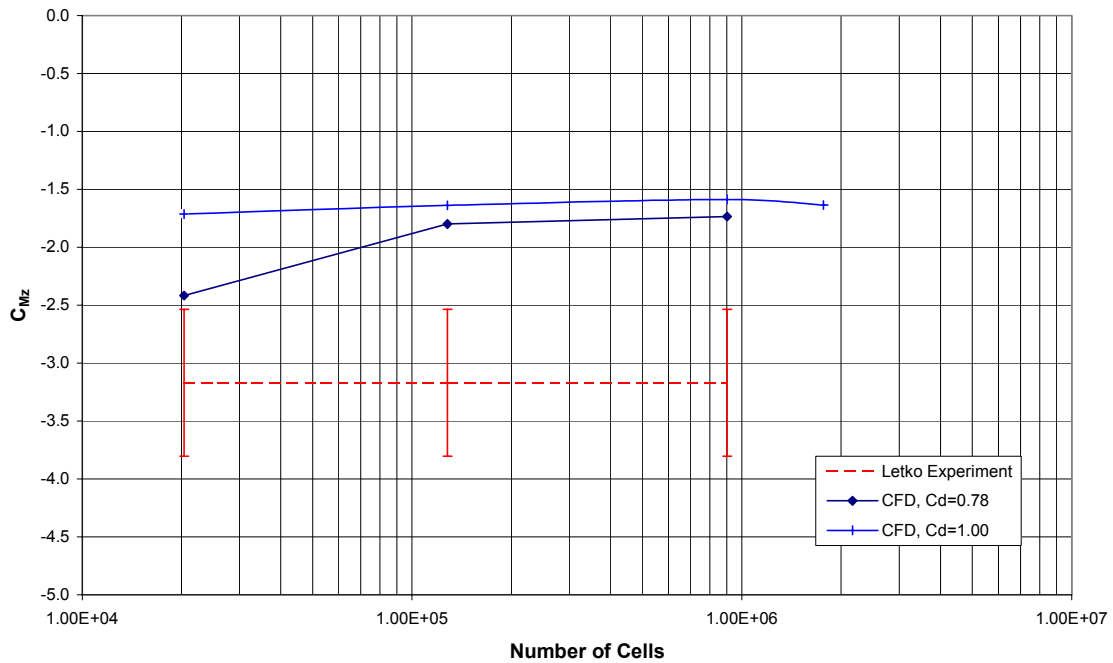


Figure 5.36. Comparison of the moment obtained from the solution on the three sequences of Grid 5 for the Letko case with a discharge coefficient of 1.00 and 0.78.

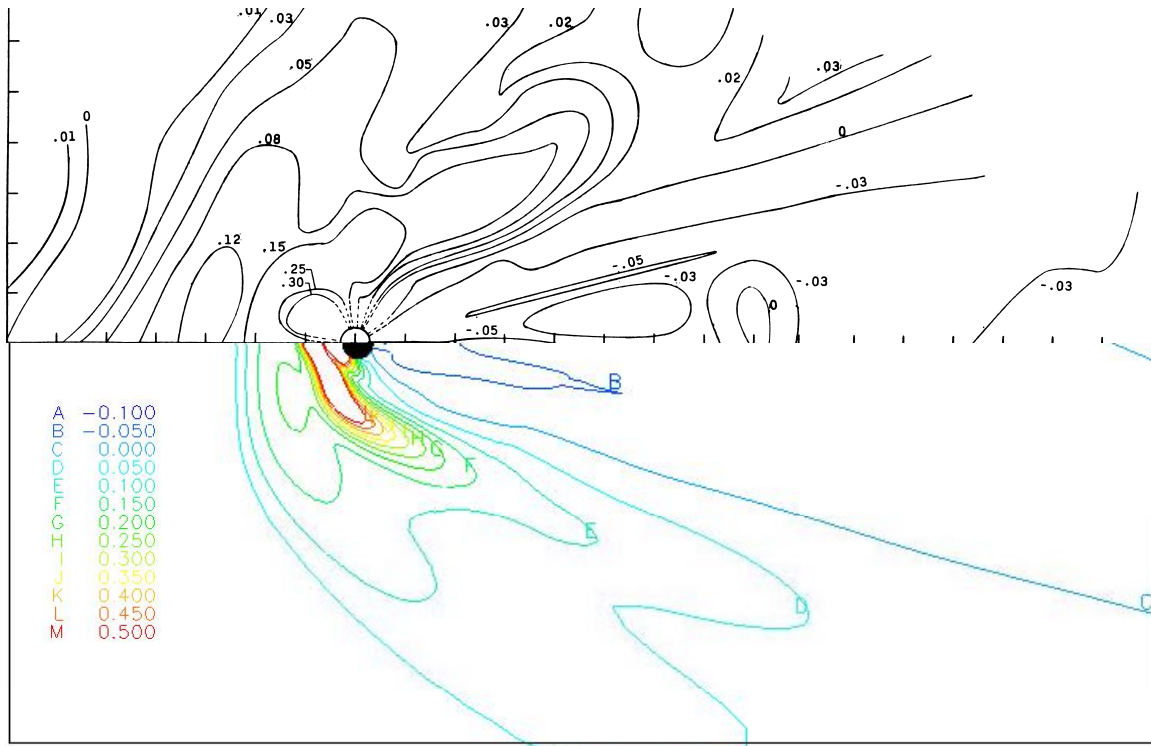


Figure 5.37. Comparison of the C_p mapping on the surface of the flat plate for the Letko experiment (top) and the numerical simulation (bottom) with a discharge coefficient of 0.78.

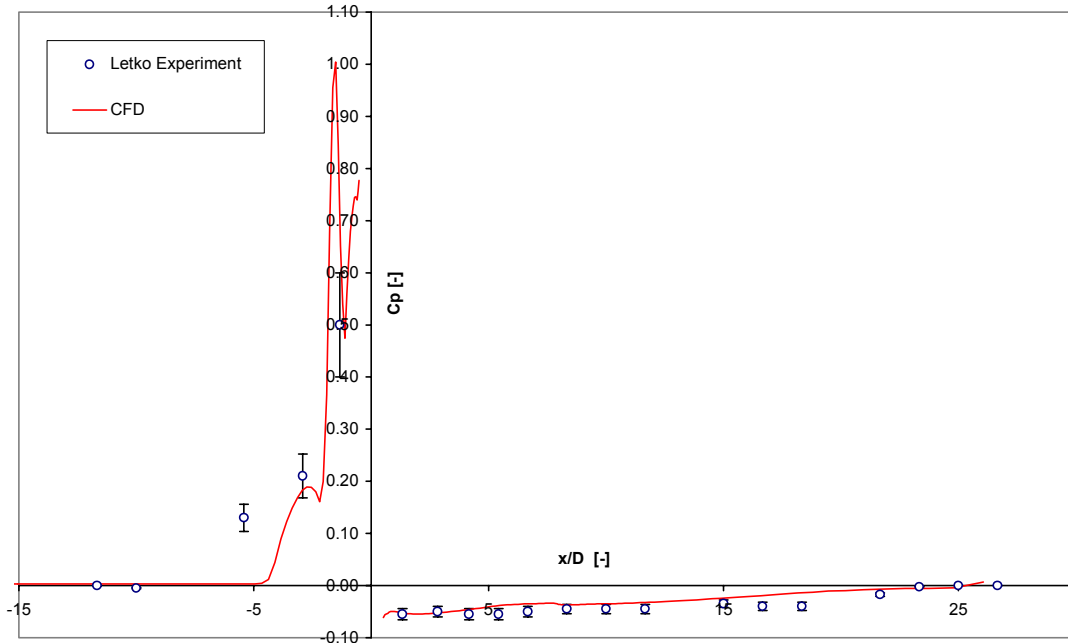


Figure 5.38. Comparison of the experimental and the C_p distribution along the centerline. Letko case, Mach 4.50, PR=680.

Sequence	Number of Cells	Experiment		CFD		$\Delta C_{Fy} \%$	$\Delta C_{Mz} \%$
		C_{Fy}	C_{Mz}	C_{Fy}	C_{Mz}		
3	20,364	0.501	-3.170	0.548	-2.418	9	-24
2	127,976			0.624	-1.799	24	-43
1	902,240			0.628	-1.734	25	-45

Table 5.15. Comparison of the experimental to CFD force and moment for the Letko case with a discharge coefficient of 0.78.

In order to assess the discretization error of this calculation, the solution was converged to a steady state on the three grid sequences. The discretization error was calculated using the “Mixed 1st and 2nd order” extrapolation method and the results are shown in Table 5.16. The small discretization error of the fine grid sequence (0% for the normal force and 2% for the pitching moment) is an indication that the mesh is very refined and that the solution is grid. As in the grid convergence study with a discharge coefficient of 1.00, the Mach contours on the plane of symmetry for the three grid levels are compared in Figure 5.39. There exist a noticeable difference in the plume shape and in the definition of the bow shock between the coarse and medium grid levels. On the other hand, the Mach contours of the solutions on the medium and fine grids are almost the same, thus confirming the force and moment convergence of Table 5.16.

Sequence	Number of Cells	Richardson Extrapolation		CFD		$\epsilon C_{Fy} \%$	$\epsilon C_{Mz} \%$
		C_{Fy}	C_{Mz}	C_{Fy}	C_{Mz}		
3	20,364	0.629	-1.725	0.548	-2.418	-13	40
2	127,976			0.624	-1.799	-1	4
1	902,240			0.628	-1.734	0	1

Table 5.16. Comparison of the solution on the three grid levels with the solution obtained with the “Mixed 1st +2nd Order Extrapolation” for the Letko case with a discharge coefficient of 0.78. “ ϵ ” is the discretization error in the solution.

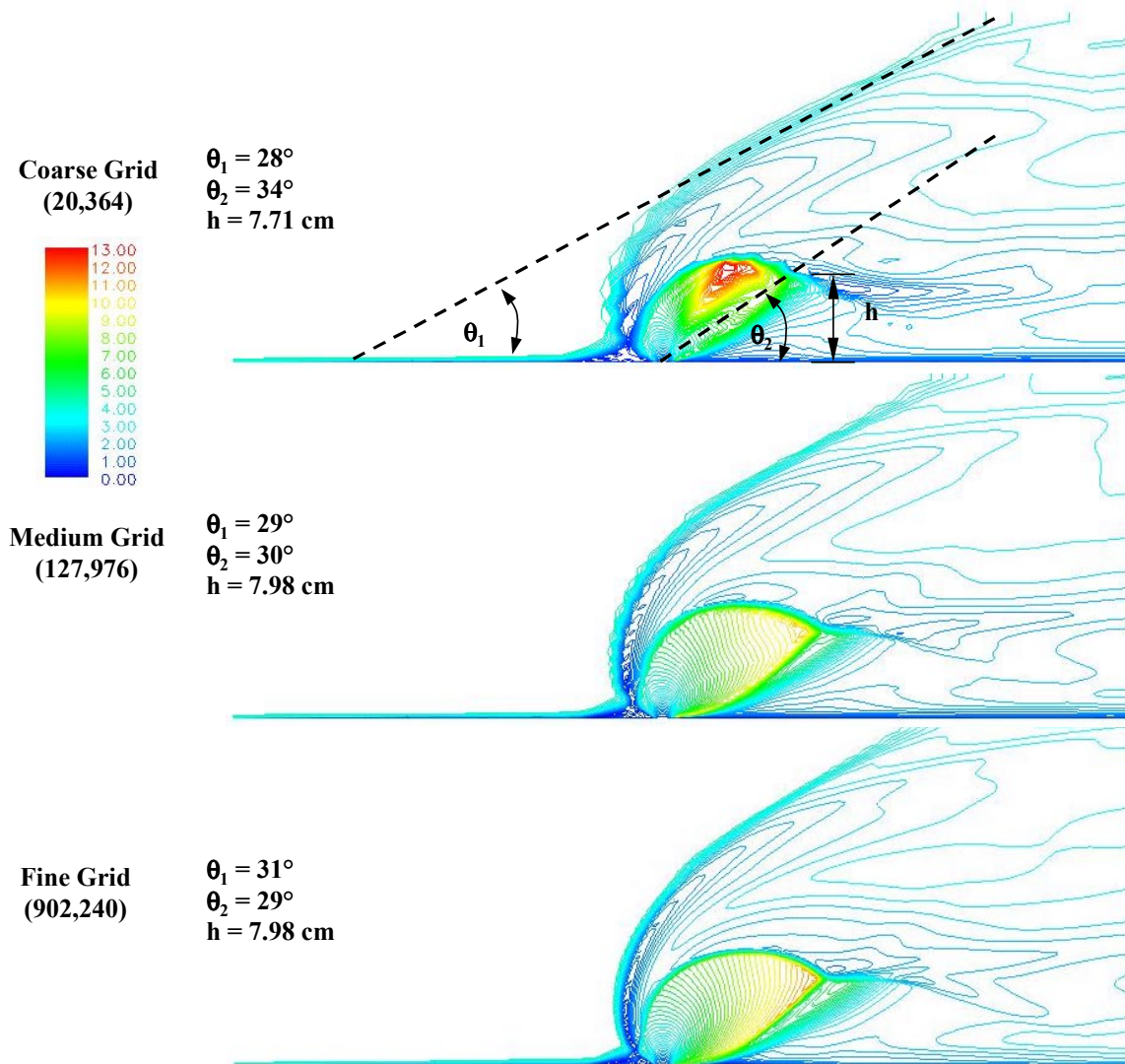


Figure 5.39. Comparison of the Mach contours on the plane of symmetry on the three grid sequences of the Letko calculation with a discharge coefficient of 0.78. Letko case, Mach 4.50, PR=680.

Letko Turbulent case with Simulated Secondary Jets

The complex boundary-layer-shock-plume interaction found in the transverse injection cases such as in the Cubbison and Letko experiments generate a C_p pattern on the surface of the flat plate that can be roughly divided into two main regions (see Figure 5.40). The first region is where positive values of C_p dominate; it covers the area just in front of the injector and it follows the lateral patterns of the bow shock. The second region develops immediately behind the injector and is characterized by negative C_p values. The latter region is working against the effect of the main jet since it is creating a force in the opposite direction of the desired control force. As mentioned in the Motivation section (Section 1.3), one of the main goals of this study was to find ways to reduce the magnitude of the negative C_p values in this region and the size of this region itself. In this study the use of small secondary injectors in this area of negative C_p is considered:

In this particular “proof of concept” calculations a smaller secondary jet was inserted aft of the main injector. The computational grid used in this study was the same as the baseline Letko case. The location of the secondary injectors was chosen according to the set up of the flat-plate experiment that was being manufactured at Virginia Tech. The experimental set up was designed to have all the secondary jets inside the region of negative C_p as shown in Figure 5.40. The reason for choosing these locations for the secondary jets was that a jet inside the region of negative C_p would create a smaller jet interaction flowfield with an area of increased pressure ahead of the injector. The interaction of several jets, it was hoped, would have the net effect of eliminating the region of negative C_p . The jets were located along a straight line that radiates from the center of the primary injector and trails downstream forming an angle of 12 degrees with the tunnel centerline.

To simplify and speed up the grid development, the secondary jet was simulated by switching the boundary condition on some cells that initially simulated the flat plate surface from no-slip adiabatic to a point-wise boundary condition with the same conditions as the primary jet. In this way, the cross section of the secondary jets was not circular as the primary jet but rather it followed the contours of the grid lines that defined the secondary jets as shown in Figure 5.41. The area ratio of the primary jet to the secondary jets was 10. The grid was then slightly modified to better capture the effect of the secondary jet by clustering cells around the location of the jets. The conditions of the freestream and of the primary and secondary jets are shown in Table 5.17 and Table 5.18. Note that all the flow conditions are the same as the Letko case with the primary jet only discussed earlier and that the primary and secondary jets have exactly the same flow conditions.

Due to the fact that no experimental data exists for this simulated multiple jet case, the main goal of this calculation was to obtain a qualitative result and to highlight the trend in the forces and moments on the flat plate generated by the secondary jets behind the primary injector. For this reason, the discharge coefficient of both the primary and secondary jets was set at 1.00.

The solution was converged only on the coarse and medium grid sequences (24,065 and 137,200 cells respectively) since, as shown by the previous grid convergence study, the medium grid can capture most of the flow details and accurately predicts the trend of forces and moments. The two solutions, one for the case with only the primary jet activated and the other one for the case where both the primary jet and one of the secondary jet pair were activated, were compared to each other on the corresponding grid sequences.

The flowfield generated by the interaction of the two jets with the free stream is shown in Figure 5.42 for two cross plane locations. The plume of the secondary jet impinges on the lower side of the barrel shock of the primary jet. The barrel shock generated by the primary jet is forced to move into a more vertical position than in the case with only the primary jet (see Figure 5.31). The movement of the barrel shock creates a stronger bow shock since the flow is now “seeing” a larger obstacle (the barrel shock). In the region behind the primary injector, a small area of positive C_p is formed by the presence of the leading edge of the plume of the secondary jet. However, a relatively large area of negative C_p forms behind the secondary jet in the same way as the area of negative C_p forms behind the primary jet. The overall effect of the secondary jet is to increase the normal force with the combined effect of:

- the stronger bow shock
- the region of positive C_p between the primary and secondary injector.
- the overall reduced area of negative C_p behind the primary injector

Figure 5.43 and Table 5.19 show the comparison of the predicted C_p mapping for the Letko case with only the primary jet on and for the case with both the primary and secondary jet on. Note how the force has been increased by 9% in the case with the secondary jet on. The moment too has been increased in magnitude and the trend indicated by the values confirms the trend expected after inspection of the C_p mapping. These preliminary results are encouraging since they confirm the idea that lays behind the philosophy of the entire project; that the area of negative pressure can be decreased by inserting small secondary injectors at convenient locations behind the primary jet.

Parameter	
Gas	Air, perfect gas ($\gamma=1.40$)
M_∞	4.5
$P_{\infty, t}$	587.75 kPa
P_∞	2.03 kPa
T_∞	66.8 K
Type of boundary layer	Turbulent (Wilcox $k-\omega$)

(a) Free-stream

Parameter	
Gas	Air, perfect gas ($\gamma=1.40$)
M_j	1.0
$P_{j, t}$	1,380.95 kPa
P_j	729.53 kPa
T_j	298 K
$P_{j, t} / P_\infty$	680
Jet mass flow ($C_d=1.00$)	0.5384 Kg/s *
Jet thrust ($C_d=1.00$)	186.31 N *

(b) Jet.

Table 5.17. Summary of flow parameters for the Letko Multiple Jet case.

Parameter	
Flat plate entry length, x_0	37.5 cm
Injector diameter, d_j	1.52 cm
$A_{j, primary} / A_{j, secondary}$	10
x_0 / d_j	24.6

Table 5.18. Flat plate and injector dimensions for the Letko Multiple Jet case.

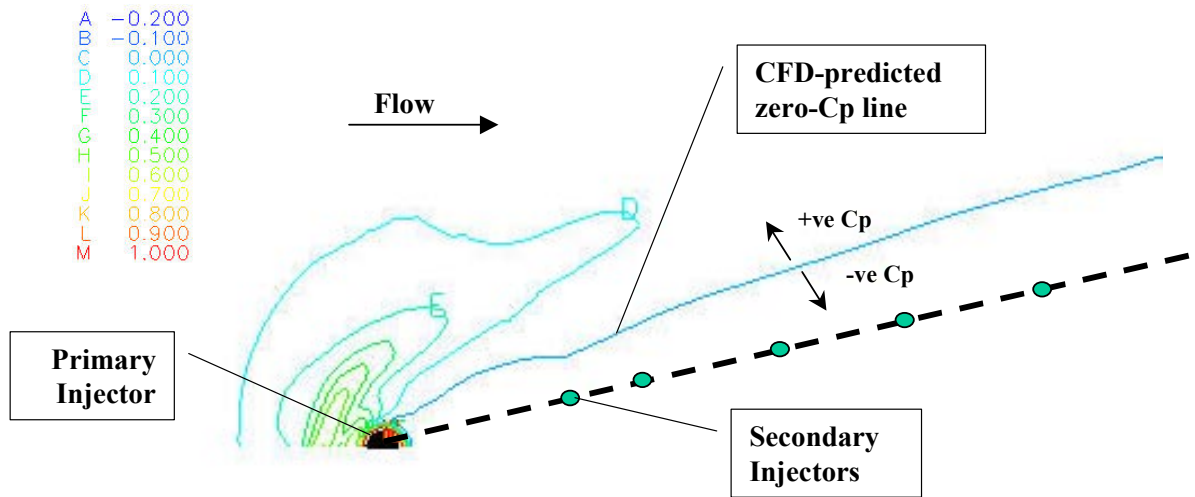


Figure 5.40. Plan view of the location of the secondary injectors with superimposed the C_p mapping of the Cubbison case [22].

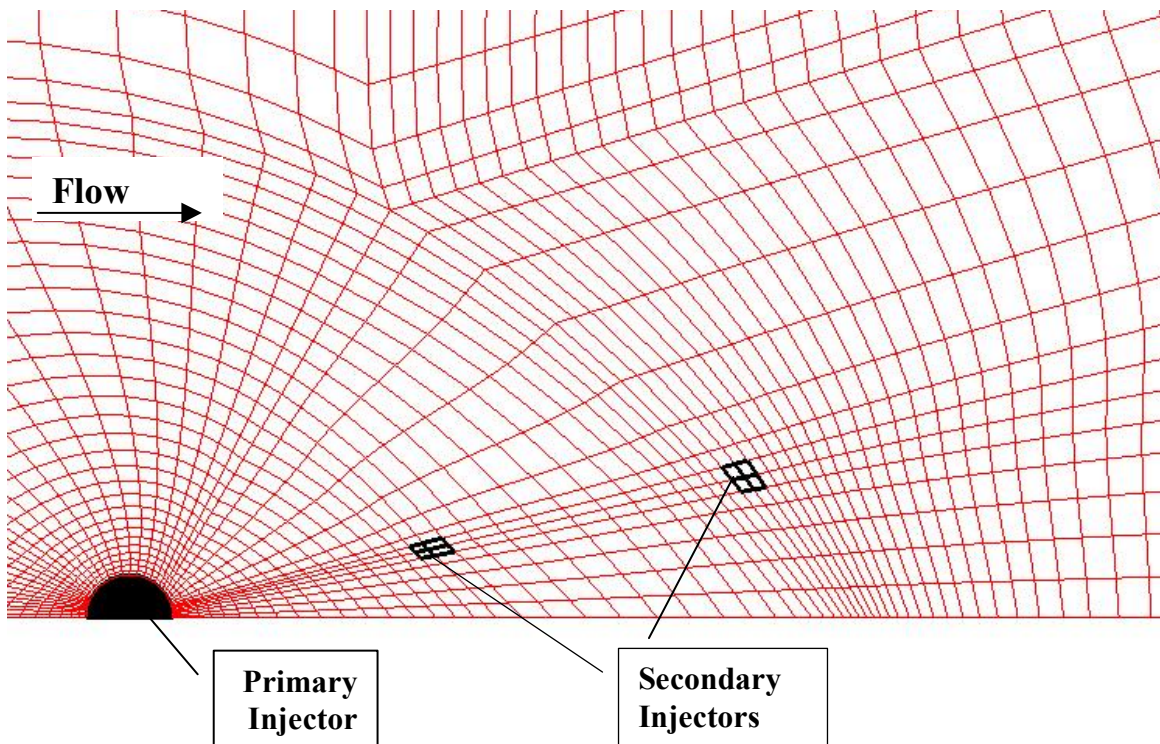


Figure 5.41. Plan view of the grid on the surface of the flat plate in the region behind the main injector. The secondary injectors were created by specifying a flow-rate for some cells on the surface of the flat plate. Not all gridlines shown.

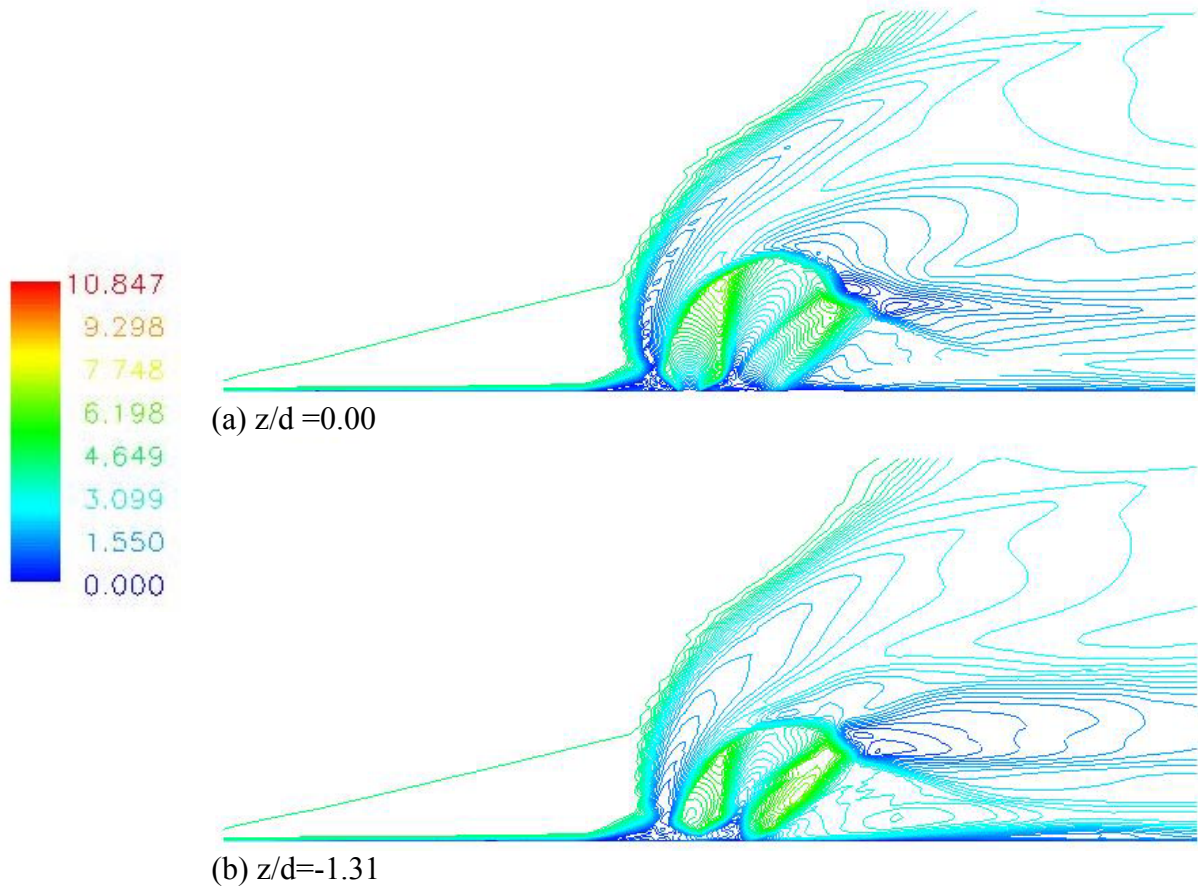


Figure 5.42. Mach number contours for the Letko case with simulated secondary injector. Top view is on the plane of symmetry ($z/d = 0.00$) and the one at the bottom is on the longitudinal plane intersecting the secondary jet axis ($x/d = -1.31$).

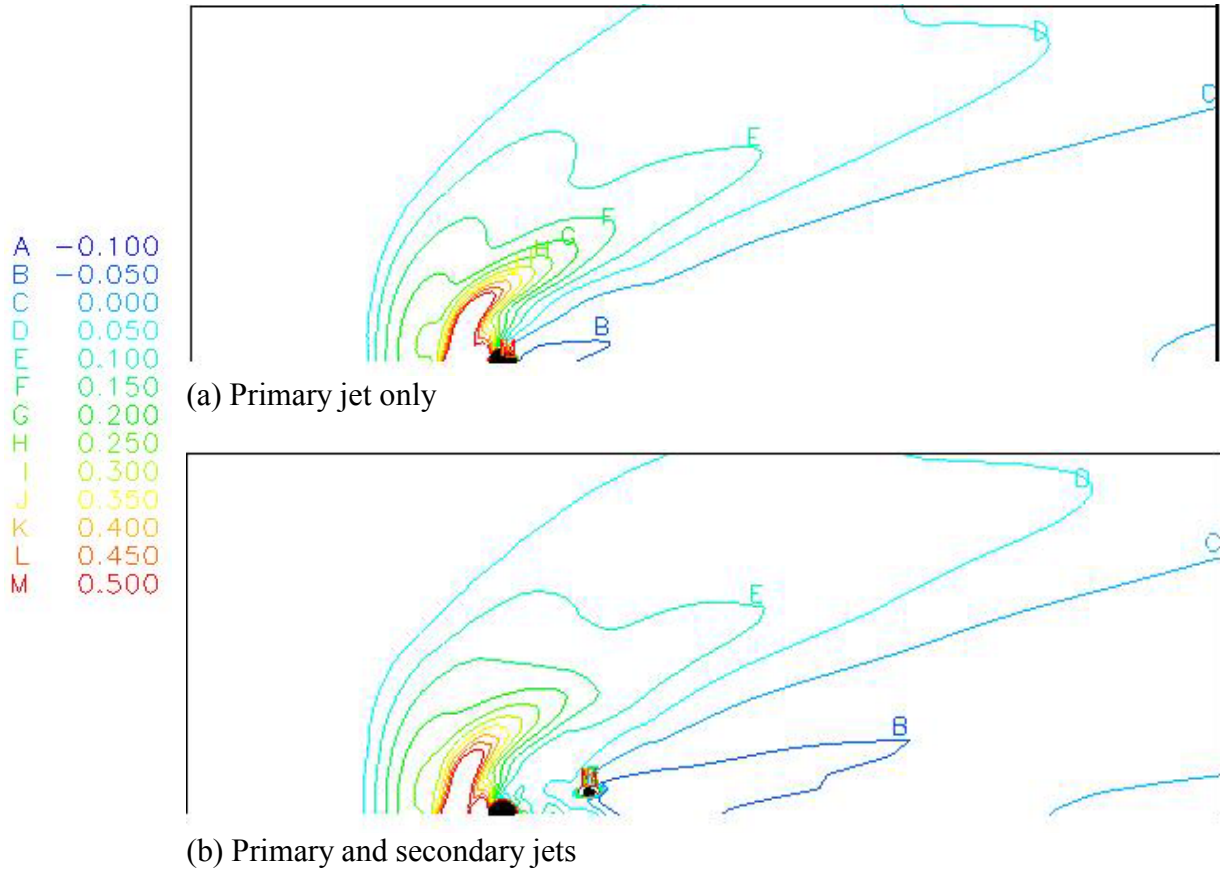


Figure 5.43. Comparison of the C_p for the Letko case with only the primary jet on and the Letko case with both the primary and the secondary jet on (medium grid sequence, 127,976 cells).

Case	C_{Fy}	$\delta C_{Fy} \%$	C_{Mz}	$\delta C_{Mz} \%$
Primary jet only	0.91	0	3.99	0
Primary jet + 1 pair of Secondary jets	0.99	9	4.94	24

Table 5.19. Comparison of the forces and moments for Letko case with only the primary jet and the Letko case with a simulated secondary injector.

5.6 Virginia Tech Mach 2.4, Turbulent (PR 14)

Following the encouraging results of the Letko case with a simulated secondary jet, an experimental investigation was set up in the supersonic wind tunnel of the Aerospace and Ocean Engineering department at Virginia Tech. The main goal of the experiments was to further investigate the effect of inserting smaller secondary injectors aft of the primary injector. The experiments were trials to prove the feasibility of the concept, and the layout of the primary and secondary injectors was not optimized. The numerical investigation is here used to both provide support to the analysis of the flowfield and to optimize the configuration in order to reduce the nose-down pitching moment produced by the primary jet alone.

In the initial stages of the experimental study a proof-of-concept test was run with a relatively low freestream Mach number (2.4) and pressure ratio (14). This test case is here referred to as the Virginia Tech Mach 2.4 case. The Mach 2.4 experiment was an interim step while the wind tunnel piping was upgraded to withstand the high-pressures required to run the cases with a higher freestream Mach number (4.0) and a higher pressure ratio (532). That case is then referred as the Virginia Tech Mach 4.0 case. The experimental setup and procedures for both the Virginia Tech 2.4 and the Virginia Tech 4.0 cases are the same and are thoroughly described by Wallis [84] and Wallis and Schetz [85]. Following is a brief description of the experimental set up and of the pressure-sensitive paint (PSP) used to map the pressure field on the flat plate during the experiment.

5.6.1 Description of the experiment

The Virginia Tech supersonic wind tunnel is of the blow-down type with a working section measuring 23x23 cm. Contrary to the previous experiments that were simulated in this study where the flat plate was had a sharp leading edge, the flat plate for the Virginia Tech cases was mounted flush to the tunnel wall. This set up means that a developed turbulent boundary layer existed at the leading edge of the flat plate. The thickness of the boundary layer was measured from the Schlieren pictures and a boundary layer velocity profile had to be assumed as discussed in Section 4.1. The boundary layer profile was then used as an inlet boundary condition to the numerical calculations. Also, the fact that the flat plate was mounted flush to the tunnel floor introduced another source of uncertainty in the comparison of the experiment to the numerical results. In fact, a small misalignment existed at the fitting of the tunnel with the surface of the flat plate. The effects of this gap on the flow conditions are not certain but, as shown by the shadowgraph photograph of the flow (see Figure 5.57) a weak shock existed ahead of the bow shock produced by the jet interaction flowfield. This weak shock seems to be produced by the joint between the plate and the tunnel floor and was not included in the numerical simulations. But, the shock could be strong enough to make the isentropic conditions in the freestream invalid thus effectively changing the flow conditions for the experiment and introducing another source of discrepancy between the experimental results and the numerical solution. The flat plate had one primary injector drilled in its

surface and five pairs of secondary injectors drilled behind the primary one. The secondary injectors were drilled along a straight line on the surface of the plate that formed an angle of 12 degrees with the plate centerline (Figure 5.44). The pairs of secondary injectors are identified by a "Group" number; "Group 1" is located 1.78 cm behind the primary injector, "Group 2" is 2.54 cm behind the primary injector and so on. The distance between two injectors was measured from the axis of one of the injectors to the axis of the other. The plate dimensions are 30.48 cm long and 22.86 cm wide.

Secondary injector group	x [cm]	x/d_j	z [cm]	z/d_j
Group 1	1.78	1.520	-0.4398	-0.923
Group 2	2.54	2.169	-0.5864	-1.231
Group 3	3.81	3.254	-0.8796	-1.847
Group 4	5.08	4.338	-1.1728	-2.463
Group 5	7.62	6.507	-1.7592	-3.694

Table 5.20. Longitudinal distance (x) of the secondary injector groups from the primary injector. The distance is measured between the jet axes. The Mach 2.4 cases simulated the Primary jet alone, Primary + Group 1, and Primary + Group 1&2. The Mach 4.0 cases simulated the Primary jet alone and the Primary + Group 2.

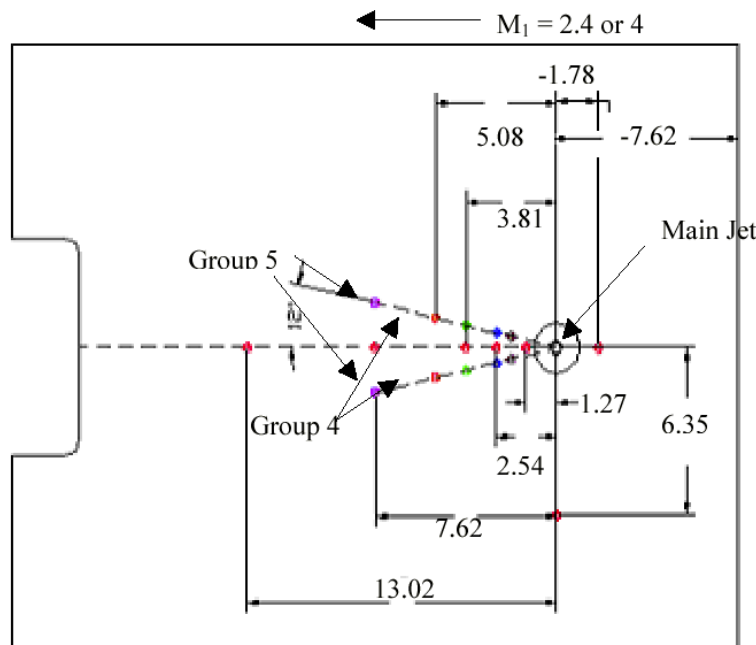


Figure 5.44. Top view of the flat plate used in the Virginia Tech jet interaction experiments. The primary and secondary injectors are highlighted. All dimensions in centimeter [84].

The origin of the axes of reference is at the center of the primary injector which is found at -7.62 cm from the leading edge of the flat plate and at 11.43 cm from the sides of the plate. Both the primary and the secondary injectors were converging nozzles drilled through the thickness of the flat plate. The high-pressure air and the converging geometry of the injectors assured sonic conditions at the nozzle exit.

High-pressure air was supplied to the nozzles from either the tunnel plenum chamber (Mach 2.4 cases) or from pressurized air in industrial gas cylinders through a manifold, a heavy-duty piping system, a dome regulator and switch valve that could cut off the flow through the injector (Mach 4.0 cases).

The discharge coefficient for the primary nozzle was measured by Wallis [84] [85] to be 0.75 and 0.78 with a freestream Mach number of 2.4 and 4.0 respectively. The discharge coefficient for the secondary injectors was measured to be 0.80 at both freestream Mach numbers.

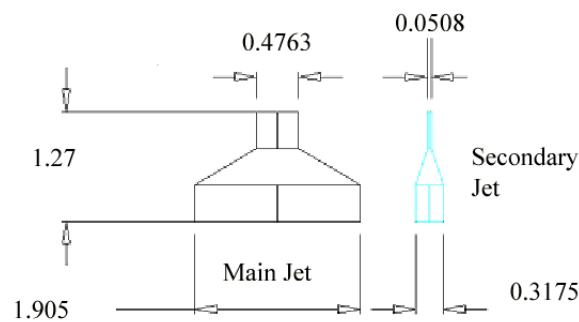


Figure 5.45. Cross-section of the primary (main) and secondary injectors as drilled in the flat plate. All dimensions in centimeter [84].

Pressure orifices were embedded in the surface of the flat plate; however, the pressure field acting on the flat plate was measured and mapped through the use of Pressure Sensitive Paint (PSP) and the pressure orifices were used for calibration and to double check the PSP pressure readings. PSP is an innovative experimental technique that can produce a continuous mapping of an entire pressure field without the need to extrapolate discrete data corresponding to the pressure orifices. The paint covers the surface of the flat plate and is illuminated with a near-UV light source. When a pressure field is applied over the flat plate the paint emits different types of light, depending on the intensity of the force it is locally experiencing; this principle is known as the oxygen quenching effects and it is extensively described by Morris and Donovan [46] and Crites [21]. A CCD camera can take pictures of the patterns produced by the PSP on the surface of the flat plate. The calibration of the PSP is then used in combination with the CCD pictures to deduce the pressure value at each pixel of the image. The final result will be a continuous pressure field over the surface of the flat plate from which the forces and

moments can be calculated. Wallis reported the uncertainty in the forces and moments to be $\pm 11\%$. However, the data acquisition and data reduction of the experiments for the two Mach numbers were performed by two different subcontractors that used different equipment and set up and it is not clear if the uncertainty reported above is valid for the Mach 2.4 or the Mach 4.0 case.

It is important to note that in the Letko case with a simulated secondary injector the ratio of the mass flow of the primary injector to the secondary injector was 10 (Table 5.18). On the other hand in the Virginia Tech cases the ratio was increased to 100 (Table 5.22). The decrease of the size of the secondary injector reflects the philosophy behind the idea of inserting the secondary jets close behind the primary injector; a smaller secondary injector strategically located can create a force magnification much larger than the thrust of the secondary injector alone. Also, the smaller size of the secondary injector would make the jet interaction configuration more efficient and simpler to implement on small vehicles than present-day configurations employing two large injectors of the same size.

5.6.2 Numerical results

The Virginia Tech Mach 2.4 calculations simulate three experiments run at Virginia Tech with a freestream Mach number of 2.4 and a pressure ratio of 14.0. Each experiment featured a different injection configuration as follows (see Figure 5.44 and Table 5.20):

- 1) Only the primary jet activated.
- 2) The primary jet and Group 1 secondary jets.
- 3) The primary jet and Group 1 and Group 2 secondary jets.

The flow conditions for the three test cases are shown in Table 5.21 and the geometric dimensions of the plate are presented in Table 5.22. Note that the ratio of the area of the primary jet to the area of the secondary jet is now 100 instead of 10 as in the case of the Letko case with a simulated secondary injector.

Parameter	
Gas	Air, perfect gas ($\gamma=1.40$)
M_∞	2.40
$P_{\infty, t}$	379.49 kPa
P_∞	25.96 kPa
T_∞	134.8 K
Type of boundary layer	Turbulent (Wilcox $k-\omega$)
Inlet boundary layer (δ_0)	0.9 cm

(a) Free-stream

Parameter	
Gas	Air, perfect gas ($\gamma=1.40$)
M_j	1.0
$P_{j, t}$	354.31 kPa
P_j	187,17 kPa
T_j	234 K
$P_{j, t} / P_\infty$	13.65
Primary Jet mass flow	0.0114 Kg/s *
Primary Jet thrust	3.5 N *
Secondary Jet mass flow	0.00013 Kg/s *
Secondary Jet thrust	0.040 N *

(b) Primary and Secondary Jet. * These values are for a discharge coefficient of 0.75 for both the primary and secondary nozzles.

Table 5.21. Summary of flow parameters for the Virginia Tech Mach 2.40 experiments.

Parameter	
Flat plate entry length, x_0	7.62 cm
Injector diameter, d_j	0.4763 cm
$A_{\text{Primary}}/A_{\text{Secondary}}$	$\cong 100$
Plate entry length, x_0/d_j	16.00

Table 5.22. Flat plate and injector dimensions for the Virginia Tech experiment.

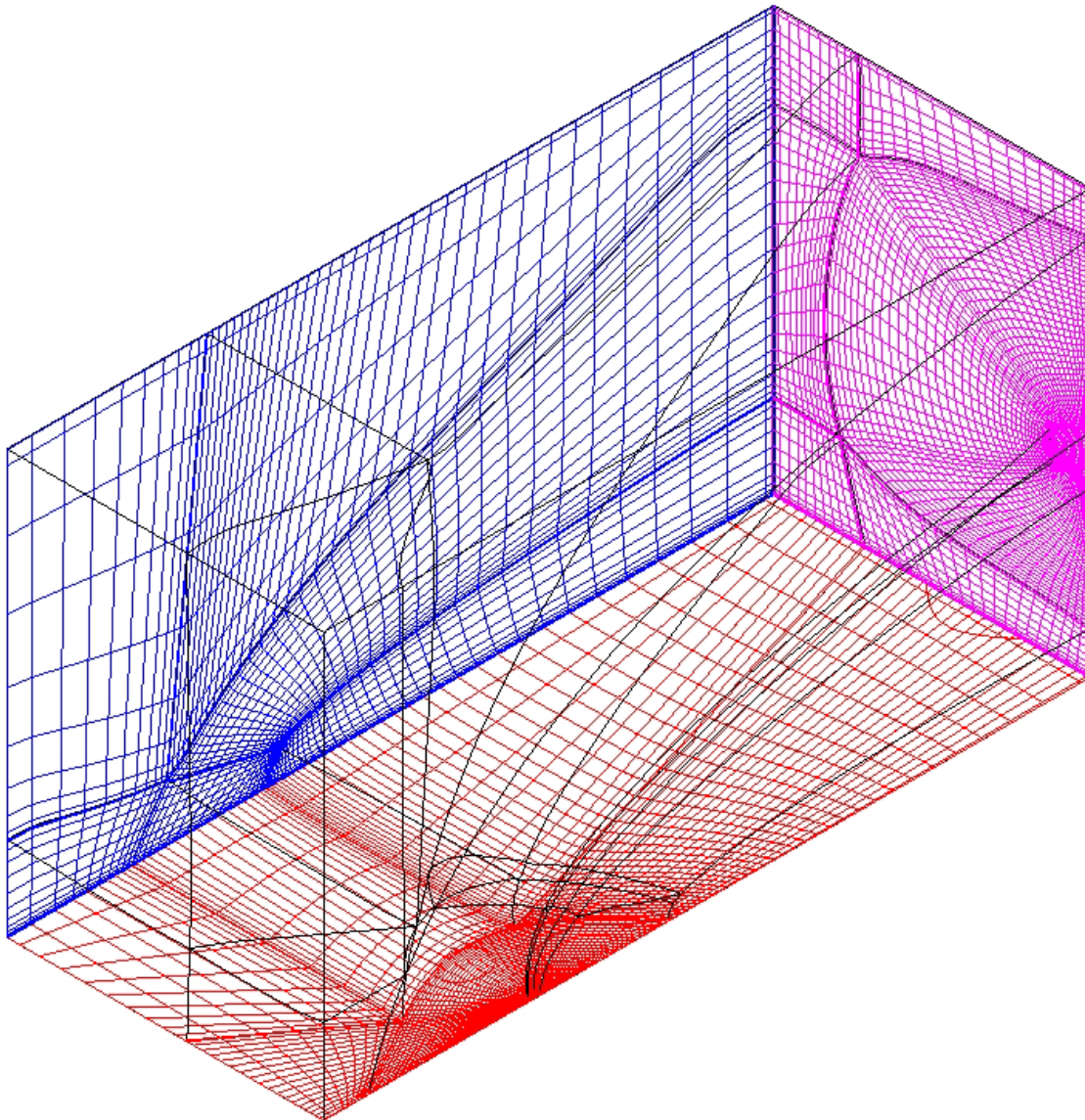
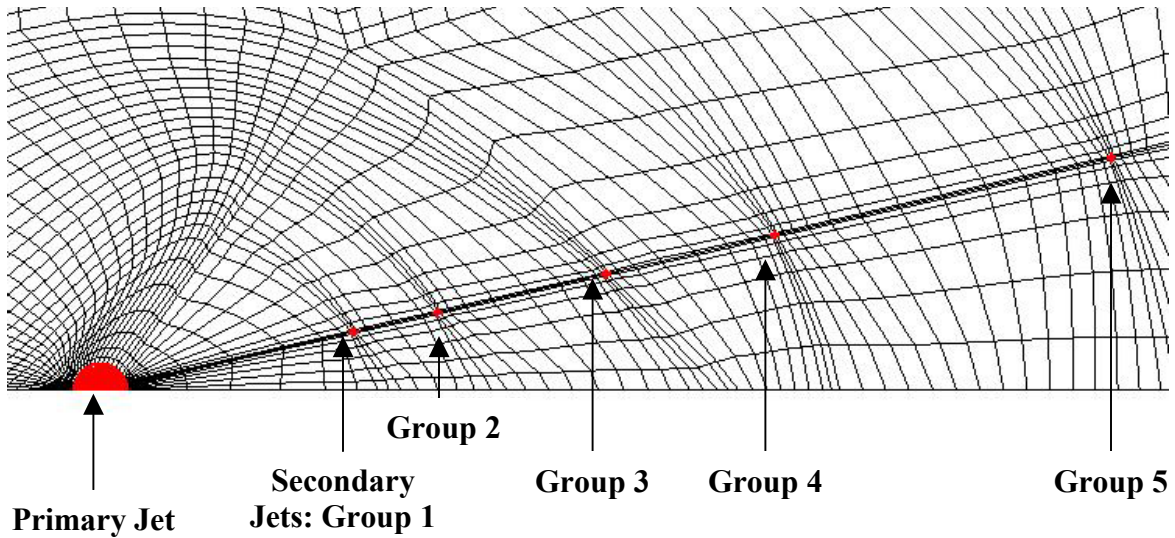
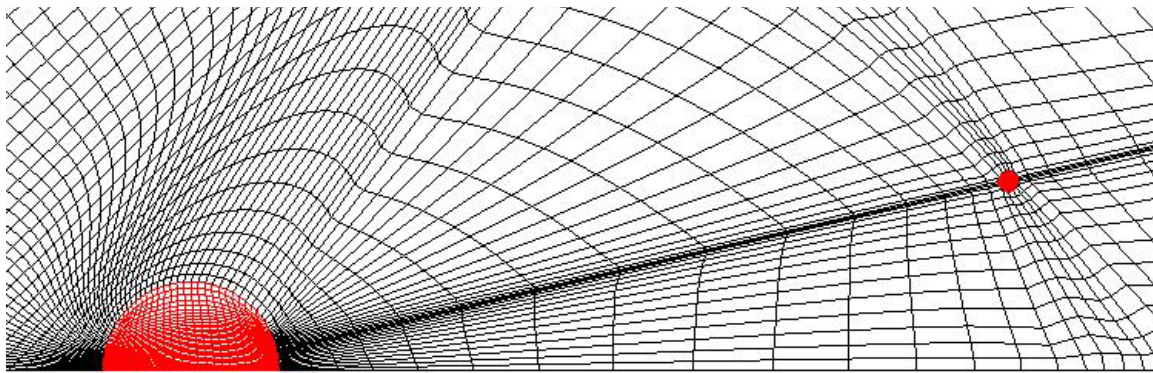


Figure 5.46. Perspective view of the computational grid employed for the Virginia Tech Mach 2.4 cases. It is composed of 12-zone some of which are H-type and others are C-type grid topology. The C-type grids wrap around the primary injector to optimize the

grid refinement in this area. The total number of cells is 1,100,024. Not all grid lines are shown.



a) Plan view of the grid on the surface of the flat plate showing the primary and secondary injectors. Not all grid lines are shown.



b) Detail of the grid on the surface of the flat plate showing the primary jet and the secondary injector of Group 1 jets. Not all grid lines are shown.

Figure 5.47. Plan view of the grid on the surface of the flat plate.

Figure 5.46 shows the grid topology employed in this set of numerical calculations. The overall grid features are the same as for the Letko case. The topology is a mix of H-type and C-type grids that optimize the clustering of the cells around the primary injector (see Chapter 4). However, because of the presence of the secondary injectors, the grid on the surface of the flat plate had to be adapted as shown in Figure 5.47. To modify the grid without modifying the existing grid topology, grid cells were clustered around the radial line along which the secondary injectors lay and along the tangential grid line of the C-grid defining the downstream location of the jets (Figure 5.47 (a)). A difference from the

Letko case with simulated secondary injection is that in the Letko calculations the shape of the secondary injector was roughly rectangular for ease of gridding. In the Virginia Tech cases, care was taken to make sure that the secondary injectors had the same circular shape as those in the experiment (see Figure 5.47 (b)). Note that due to the need to cluster the grid cells in the immediate surroundings of the secondary injectors, some areas of the grid featured relatively large cells spacing.

The effects of the discharge coefficient of the primary and secondary jets were simulated by reducing the cross sectional area of the sonic nozzles by the value of the discharge coefficient. That means that the physical dimensions of the injectors in the numerical simulations are smaller than the dimensions of the real injectors. This assured that the mass flow was the same as that measured in the experiment. No boundary layer was simulated inside the injector so that the jet had a step-profile.

As in the case of previous simulations, the solution was converged on the three grid sequences to check for grid convergence. The discretization errors calculated using the “Mixed 1st and 2nd order extrapolation” procedure for the three Virginia Tech Mach 2.4 cases are shown in Table 5.23. The force and moment coefficients are plotted in Figure 5.48 and Figure 5.49. The discretization error in the normal force was calculated to be 3% for the fine grid sequence of all the three simulations; the error associated with the pitching moment ranges between 4 and 5%. Overall the numerical solution is very close to grid convergence as indicated by the small percentage error in the forces and moments and by the trend of the curves of Figure 5.48 and Figure 5.49 that are almost flat at the point corresponding to the fine grid sequence. Figure 5.48 and Figure 5.49 graphically show also the relatively small predicted effect on the force and moment produced by the secondary injectors.

Case	Richardson Extrapolation		CFD		$\epsilon_{C_{Fy}}$ %	$\epsilon_{C_{Mz}}$ %
	C_{Fy}	C_{Mz}	C_{Fy}	C_{Mz}		
Primary jet	2.35	2.69	2.33	2.65	-3	-4
Primary jet + Group 1 jets	2.43	2.92	2.40	2.88	-3	-5
Primary + Group 1&2 jets	2.49	3.28	2.47	3.23	-3	-4

Table 5.23. Comparison of the solution on the three grid levels with the solution obtained with the “Mixed 1st +2nd Order Extrapolation” for the Virginia Tech case with a freestream Mach number of 2.40. “ ϵ ” is the discretization error in the solution

The percentage increases of the force and moments due to the secondary injectors are given in Table 5.24. The calculated increase in force due to the secondary jets of Group 1 is 3%. When two pairs of the secondary jets were activated, Group 1 and Group 2, the

normal force was increased by double the value obtained with a single jet, i.e. 6%. On the other hand the pitching moment (Table 5.24 (b)) did not show a linear increase as the normal force. The pitching moment coefficient was increased by 9% when only Group 1 was activated and by 22% when Groups 1 & 2 were activated at the same time. The trend in the force and moment is can be explained by the fact that all the secondary injectors produce the same thrust, therefore activating two pairs of secondary injectors instead of one pair doubles the force increase obtained with only one group. However, this explanation hides the fact that the secondary injector experience a different flowfield from each other since Group 1 is very close to the larger primary jet and Group 2 is in the wake of both the primary and Group 1 jets. Differences in the local flowfield mean that each of the secondary jets should produce a different force magnification factor which does not happen here.

Case	Experimental		CFD	
	C_{Fy}	$\delta C_{Fy} \%$	C_{Fy}	$\delta C_{Fy} \%$
Primary	12.05	0	2.33	0
Primary + Group 1	13.32	11	2.40	3
Primary + Group 1&2	14.01	16	2.47	6

(a) Normal Force

Case	Experimental		CFD	
	C_{Mz}	$\delta C_{Mz} \%$	C_{Mz}	$\delta C_{Mz} \%$
Primary	-95.58	0	-2.65	0
Primary + Group 1	-99.67	4	-2.88	9
Primary + Group 1&2	-102.94	8	-3.23	22

(b) Pitching Moment

Table 5.24. Increase in (a) normal force and (b) pitching moment due to the action of the secondary jets without taking into consideration the thrust of the jets. On the right column are the results from the experiment and on the left are the results from the numerical simulations. Virginia Tech cases with a freestream Mach number of 2.40. Note that $\delta C_{()}$ represents the augmentation of the parameter $C_{()}$ with respect to the case with the primary injector only. No jet thrust.

One explanation for this inconsistency in the theoretical prediction is the fact that the pressure ratio of the jets is so small that in spite of the different location of the two secondary jets, the secondary jets of Group 1 do not interact with the flowfield of the primary injector. Therefore, both secondary jets experience approximately the same wake flow produced by the primary injector and, having the same exit conditions, produce the same force magnification factor. The non-linear behavior of the pitching moment can be easily explained by noting that Group 2 is located much further downstream of the injector than Group 1, thus producing the same thrust as the injectors of Group 1 but acting at a larger moment arm. The increase in normal force is consistent with the trend

observed in the Letko case with the simulated secondary injector. In the Letko case, the mass flow of the secondary injector was 10% of the mass flow of the primary injector and the net force augmentation was 10% (see Table 5.19). In the Virginia Tech Mach 2.4 cases, the mass flow through the secondary injector is 1% of the mass flow through the primary injector and the increase in normal force is 3 % with one pair of secondary injectors and 6% with two pairs of secondary injectors, i.e. the force augmentation factor is of the same order of magnitude as the increase in total thrust. Note that the experiment predicted much higher augmentation factors for both the normal force and pitching moment (see Table 5.24). Because the pressure ratio was low, the thrust produced by the primary and secondary injectors was small. So, when the jet thrust is taken into consideration in the calculation of the forces and moments, the results do not change significantly as shown by the values of Table 5.25.

Case	Experimental		CFD	
	C_{Fy}	$\delta C_{Fy} \%$	C_{Fy}	$\delta C_{Fy} \%$
Primary	13.05	0	2.33	0
Primary + Group 1	14.33	10	2.40	3
Primary + Group 1&2	15.04	15	2.47	5

(a) Normal Force

Case	Experimental		CFD	
	C_{Mz}	$\delta C_{Mz} \%$	C_{Mz}	$\delta C_{Mz} \%$
Primary	-95.58	0	-2.65	0
Primary + Group 1	-99.68	4	-2.88	9
Primary + Group 1&2	-102.94	8	-3.23	22

(b) Pitching Moment

Table 5.25. Increase in (a) normal force and (b) pitching moment due to the action of the secondary jets taking into consideration also the thrust of the jets. On the right column are the results from the experiment and on the left are the results from the numerical simulations. Virginia Tech cases with a freestream Mach number of 2.40. Note that $\delta C_{()}$ represents the augmentation of the parameter $C_{()}$ with respect to the case with the primary injector only. No jet thrust.

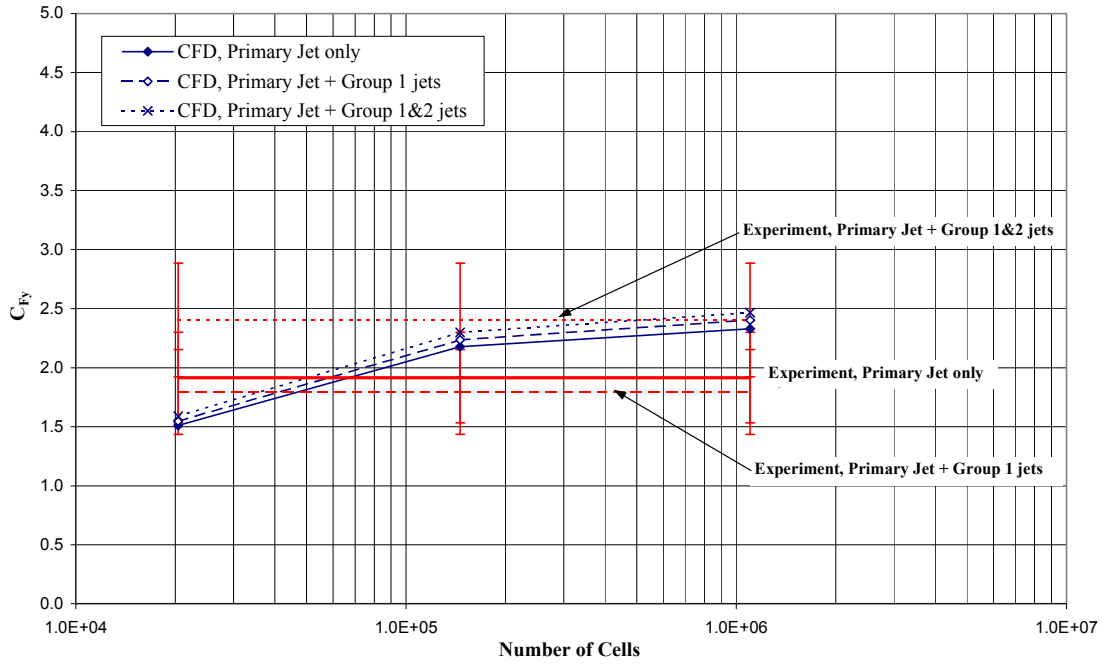


Figure 5.48. Comparison of the normal force coefficient acting on the flat plate for the three Virginia Tech, Mach 2.4, Pr=14 test cases.

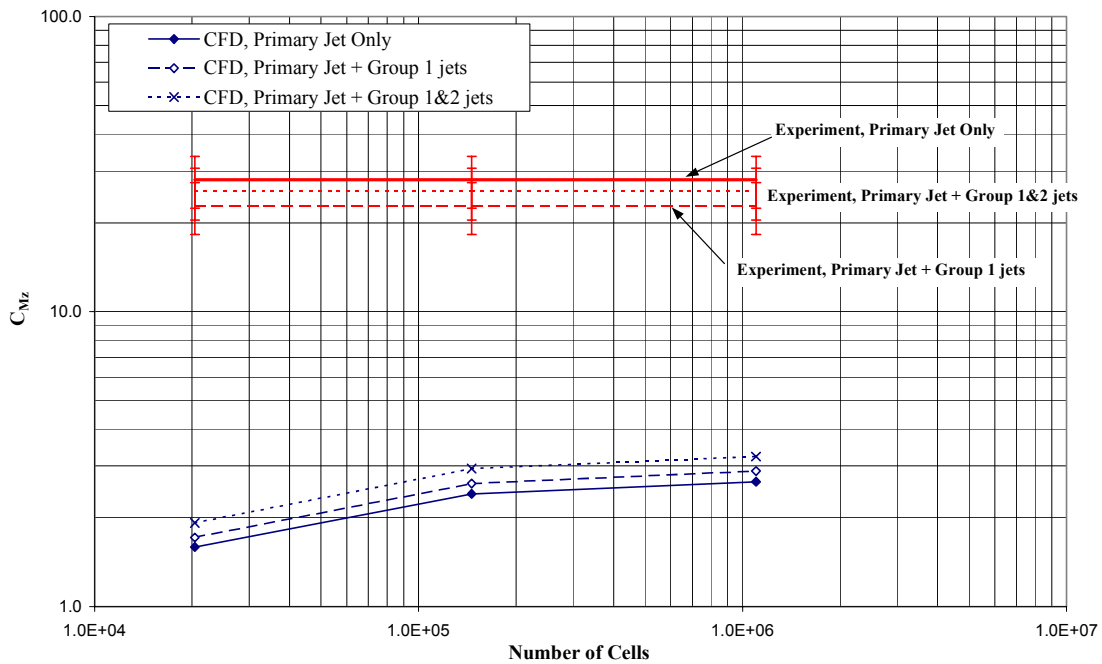


Figure 5.49. Comparison of the pitching moment coefficient acting on the flat plate for the three Virginia Tech, Mach 2.4, Pr=14 test cases.

The small predicted force increase produced by the secondary injectors is reflected in the visual comparison of the Mach contours on the plane of symmetry for the three Virginia Tech Mach 2.4 cases run (Figure 5.50). No clear effect of the secondary injectors is visible in the comparison; the three mappings being extremely similar. It is noteworthy that due to the low pressure ratio (14) of this case, the jet plume is relatively small and it is almost entirely contained within the thickness of the incoming boundary layer. As shown experimentally by Zubkov and Glagolev [99] and numerically by Roger and Chan [60], the effect of a thick boundary layer is to increase the upstream influence of the jet. This effect is achieved because “as boundary layer thickness increases, the thickness of its subsonic portion also increases, so that disturbances caused by the shock wave propagates for large distances upstream” [99]. Therefore, the force augmentation of the jets for the Virginia Tech Mach 2.4 case would have been lower had there not been a relatively thick entry boundary layer.

Differences between the three injection configurations can be noted in the predicted pressure mapping on the flat plate surface shown in Figure 5.52. The influence of the secondary injectors is visible only in the area in the immediate surroundings of the injection location. For the case with only Group 1 jets activated, no major disruption of the flowfield is indicated either far or near the location of the secondary injector. Note in the top section of Figure 5.52 how the “D” pressure line corresponding to a C_p of -0.025 is almost identical for the two cases. A stronger effect on the flowfield is indicated when both the secondary injectors of Groups 1 and 2 are activated (bottom plot of Figure 5.52). The pressure lobe defined by the letter “F”; and corresponding to a C_p of $+0.025$ has decreased in size as a result of the action of Group 2 jets. However, note that in both plots of Figure 5.52, the zero- C_p line hasn’t changed at all as a consequence of switching on the secondary jets. Also, the secondary jets do not produce any effect upstream of the primary injector as highlighted by the size and intensity of the separation region for the three test cases. As seen previously in the Letko case with a simulated secondary injector, the separation region was magnified by the effect of the secondary jet that pushed the barrel shock of the primary jet into a more vertical position thus increasing the blockage effect (see Figure 5.42 and Figure 5.43). However, in the Virginia Tech Mach 2.4 test, the pressure ratio of the jets was not high enough to produce large barrel shocks that impinged one on the other thus creating a strong interaction. On the contrary, each barrel shock, the one produced by the primary injector and the one produced by secondary injectors, acted independently as shown by the small upstream effect produced by the secondary jets. The above impressions drawn from the pressure mappings are confirmed by the C_p plots along the tunnel centerline (Figure 5.51). The predicted effect of the secondary injectors is small in intensity and limited to the region in the immediate surroundings of the secondary jets. No effect of the secondary injectors is visible far ahead of the injection location in the separation region as shown in Figure 5.51 (a). The effect of the secondary injectors on the low-pressure region is to create a localized pressure peak followed by a deeper trough in the pressure distribution. In Figure 5.51 (b) this is highlighted by the red line with crosses that is drawn for the injection case with the secondary jets of Group 1. Note that the pressure peak is located at the same downstream distance as the injection location ($x/d=5.0$). The pressure peak is followed by a dip in the

pressure that is lower than in the case with only the primary jet. The same observations are valid for the injection case with both pairs of secondary injectors (Groups 1 and 2) with the only difference that there are two peaks in the pressure plot corresponding to the two injection locations. The second peak (corresponding to the injection location of Group 2) is lower than the first peak since the secondary jets of Group 2 are further away from the centerline than Group 1. Note that the low-pressure region aft of the two secondary injectors is lower than the other two injection cases and extends further downstream. In the three pressure plots, the effects of the reflected shock impinging on the flat plate are clearly visible as a sharp pressure rise at an x/d of 10.0. It is noteworthy that the location at which the shock impinges on the flat plate is the same for the three injection cases thus confirming that the secondary jets do not have any upstream effect on the primary jet.

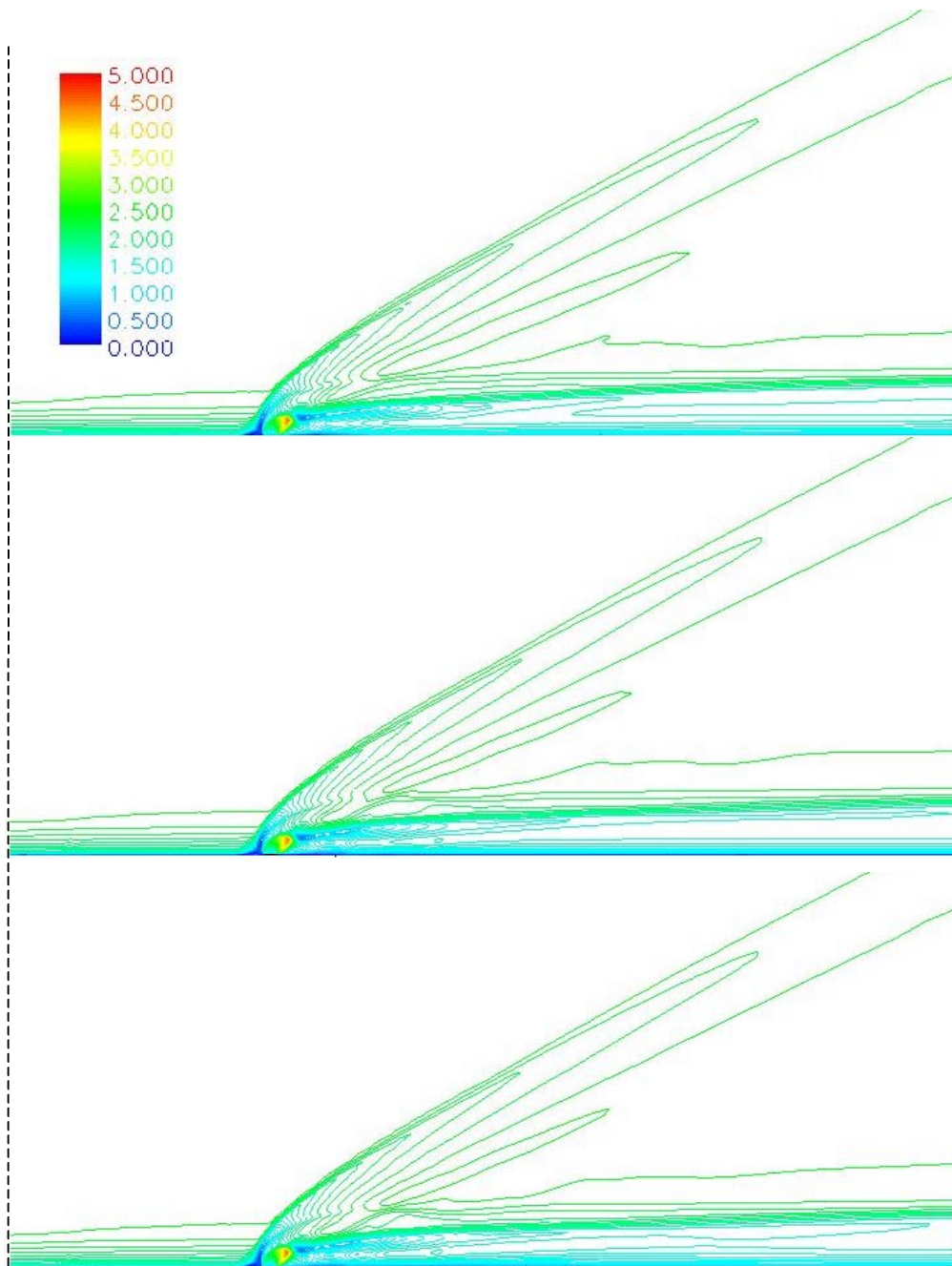
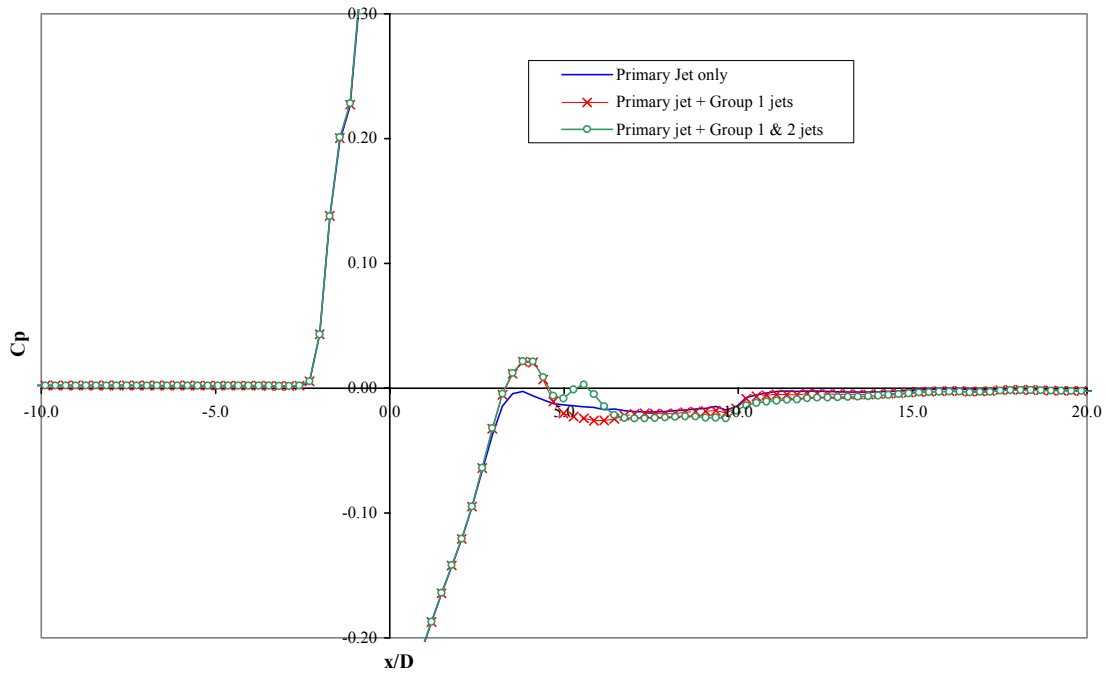
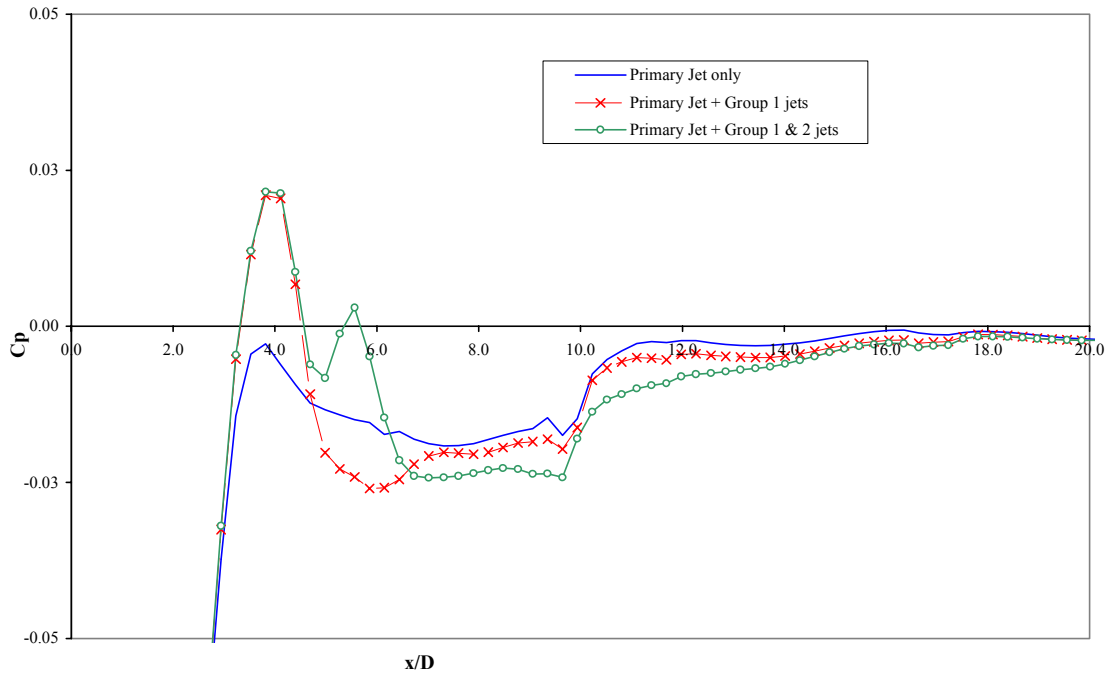


Figure 5.50. Comparison of the CFD Mach contours on the plane of symmetry for the primary jet only case (top), the primary jet plus the secondary jets of Group 1(center) and the primary jet plus the secondary jets of Group 1 and Group 2 case (bottom). Virginia Tech Mach 2.4, $Pr=14$.



(a) over the whole computational domain.



(b) detail of the low-pressure region.

Figure 5.51. Comparison of the CFD C_p plots along the tunnel centerline for the three configurations. (a) Over the whole computational domain. (b) Detail of the low-pressure region where the secondary injectors are located. Virginia Tech Mach 2.4, $Pr=14$.

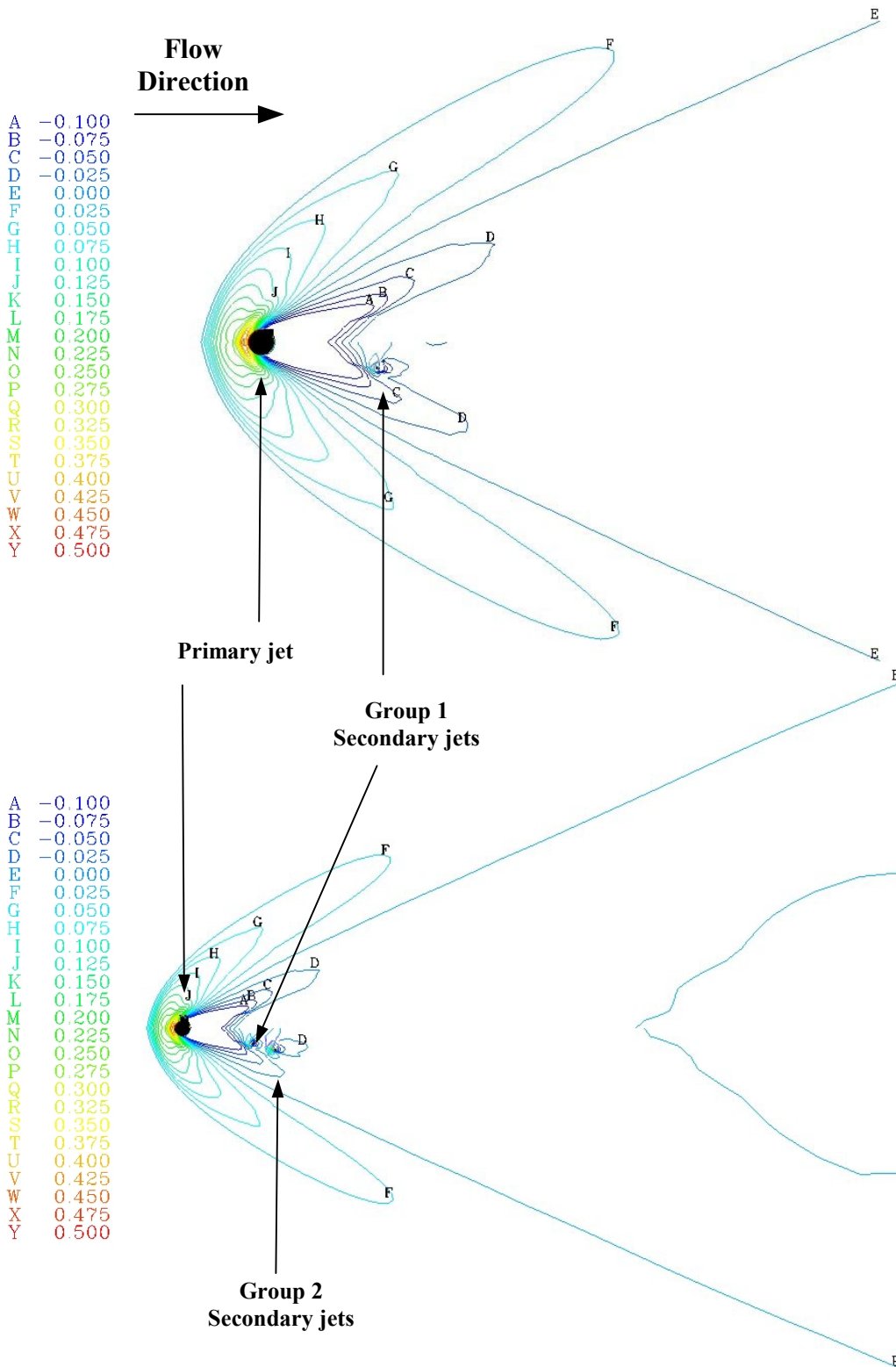


Figure 5.52. Comparison of the CFD C_p mapping for the Primary jet only case (top) and the primary jet plus Group 1 secondary jets case (bottom). Virginia Tech Mach 2.4, $Pr=14$.

5.6.3 Comparison of numerical results with experiment

The numerical calculations were run with the same nominal conditions as the experiments performed in the Virginia Tech supersonic wind tunnel by Wallis [85]. The data collected with the Pressure Sensitive Paint (PSP) during the experiments produced a continuous mapping of the pressure on the surface of the flat plate. However, this technique still presents a high uncertainty level in the exact measurement of pressure data as shown by Figure 5.53. This figure shows a spanwise plot of the static pressure on the surface of the flat plate along three lines that transverse the flat plate ahead of the injector and the separation region. Since these crossplane plots are ahead of the separation, the flowfield is smooth and uniform and the pressure is constant at or close to the freestream values as shown by the numerical data plotted on the left side of Figure 5.53 (remember that the domain of the CFD calculations was only half the physical domain since a symmetry plane exist at $z/d=0.00$). However, the experimental pressure data shows a clear slope in the spanwise direction, with the maximum pressure value reached at the location of minimum z/d . The trend in the experimental data seems to indicate a bias in the PSP data probably due to the fact that the CCD camera was inclined at an angle to the flat plate rather than being perpendicular above it. From similar plots of the spanwise pressure distribution at different x/d locations, an uncertainty range for the pressure readings could be estimated. Using standard error propagation procedures such as those described by Coleman and Steele [19] the minimum experimental uncertainty in the C_p value could be calculated as shown in the C_p plot along the tunnel centerline of Figure 5.54. The comparison of the experimental and numerical C_p plots along the tunnel centerline puts in evidence another possible problem relative to the experimental pressure data. Note in fact how the pressure far downstream of the injector for all the three configurations (Figure 5.54, Figure 5.55, and Figure 5.56) reaches a plateau but it does not recover the value of the freestream static pressure. The recovery of the freestream static pressure far aft of the injector is both predicted by the numerical solution (see the Cubbison, the Letko and the Virginia Tech simulations) and it has been shown to occur in all of the experimental works [22] [42] [70] [5]. This longitudinal bias affects negatively the comparison of the numerical solution with the experiment, but it is not easily reducible to an error estimate due to the presence of the complex jet interaction flowfield and the pressure gradients associated with it. As shown by the pressure plots of Figure 5.54 through Figure 5.56, the calculation of the forces and moments was performed assuming that the pressure ahead of the separation and along the centerline of the tunnel is the correct freestream pressure. As a result of this assumption there is a large area of positive C_p far aft of the Primary injector. The presence of this area of positive C_p has two consequences on the experimental data. The first is that the normal force is over-predicted. The second is that the pitching moment is very negative (i.e. nose-up) due to the large force acting at a large arm.

Another source of discrepancy between the CFD solution and the experiment is the prediction of the separation. The separation location is greatly under-predicted by all the three numerical solution, as is the location of the bow shock. However, the CFD over-

predicts the intensity of the separation compared to the experiment as evidenced by the C_p peaks present in the separation region computed by the CFD. Note that the under-prediction of the separation region is consistent with the results of the previous calculations (Cubbison and Letko) and it is likely mainly attributable to the $k-\omega$ turbulence model [54].

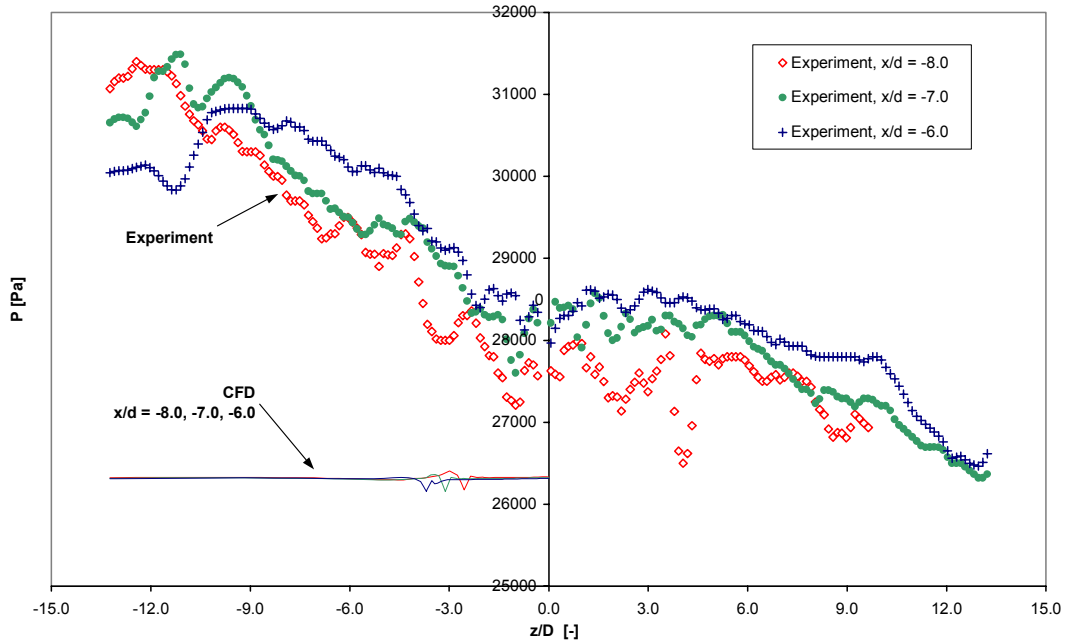


Figure 5.53. Comparison of C_p plots along the tunnel centerline for the experimental and numerical data sets. Virginia Tech, Mach 2.4, $Pr=14$.

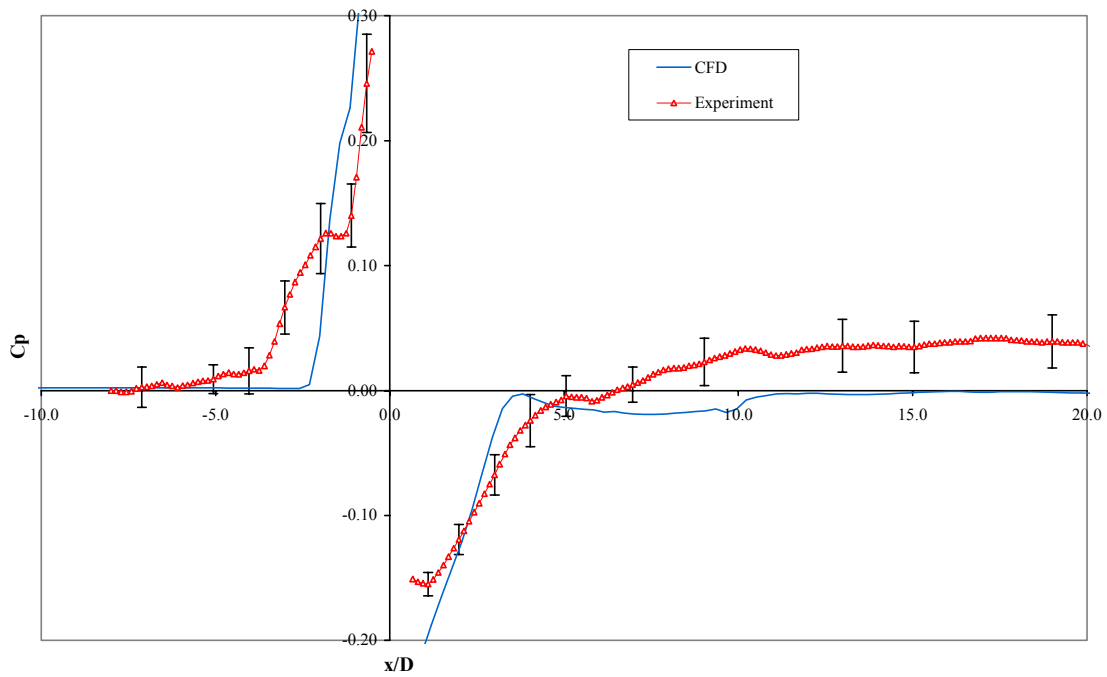


Figure 5.54. Comparison of C_p plots along the tunnel centerline for the experimental and numerical data sets with only the Primary jet. Virginia Tech, Mach 2.4, Pr=14.

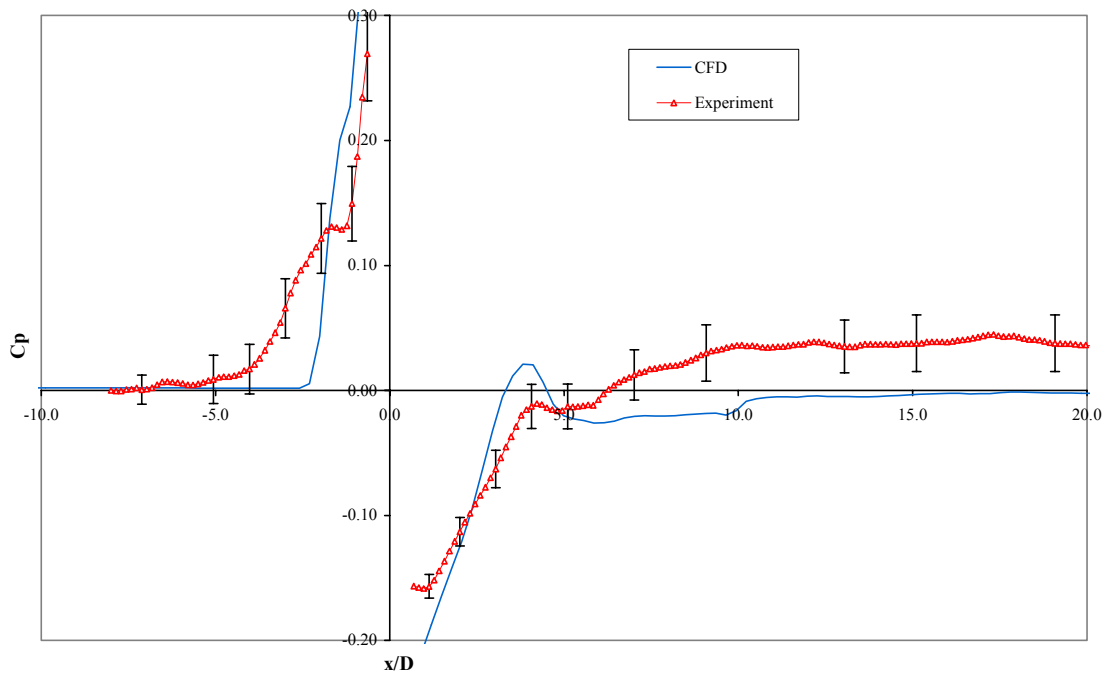


Figure 5.55. Comparison of C_p plots along the tunnel centerline for the experimental and numerical data sets with both Group 1 secondary jet. Virginia Tech, Mach 2.4, Pr=14.

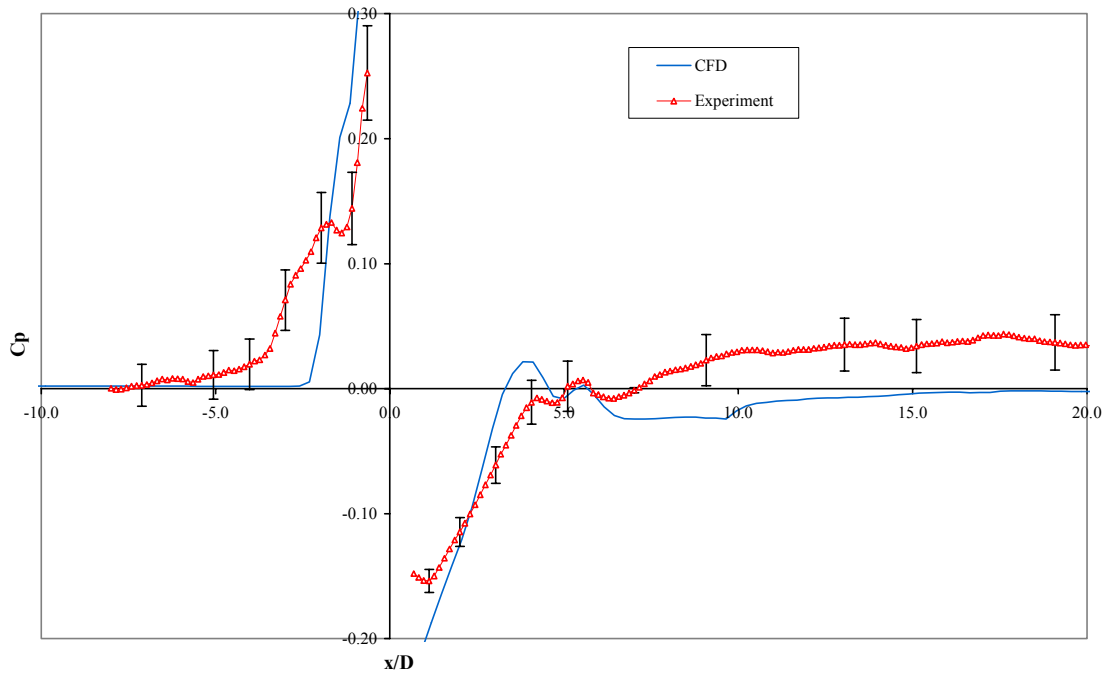


Figure 5.56. Comparison of C_p plots along the tunnel centerline for the experimental and numerical data sets with both Group 1 and Group 2 secondary jets. Virginia Tech, Mach 2.4, $Pr=14$.

The quantitative comparison of the experimental and numerical normal force and pitching moment is not very favorable as shown by the data of Table 5.26. The pitching moment coefficient data especially exhibits large percentage differences. However, the direct comparison of forces and moments is affected by the discrepancy between the actual experimental conditions and the nominal conditions used in the numerical computations. The discrepancy in the flow conditions is evident in the spanwise static pressure plots of Figure 5.53 where the experimental pressure data is higher than the computed pressure. This difference between the experimental flow conditions and those used in the computations is probably due to two main factors. The first factor is the difficulty in accurately controlling the flow conditions in the tunnel. The second and probably the most important factor is the presence of a shock ahead of the separation region as shown by Figure 5.57. This shock is generated by the misalignment of the junction between the tunnel floor and the flat plate mounted flush to the floor. The shock being ahead of the injection location effectively changes the freestream conditions “seen” by the jet interaction flowfield. As a consequence of this inconsistency between the experiment and the numerical calculations, a more indicative and useful quantitative comparison is the analysis of the force augmentation factor produced by the secondary injectors. These values are shown in Table 5.24 as percentage values of the force and

moment results obtained with only the primary jet activated. Again, the numerical solution under-predicts the experimental values. This is probably due to the fact that the CFD fails to predict a stronger separation ahead of the primary injector caused by effects of the secondary jets as seen in the experiments (see the C_p plots of Figure 5.54, Figure 5.55, and Figure 5.56 and the C_p mappings of Figure 5.58, Figure 5.59 and Figure 5.60).

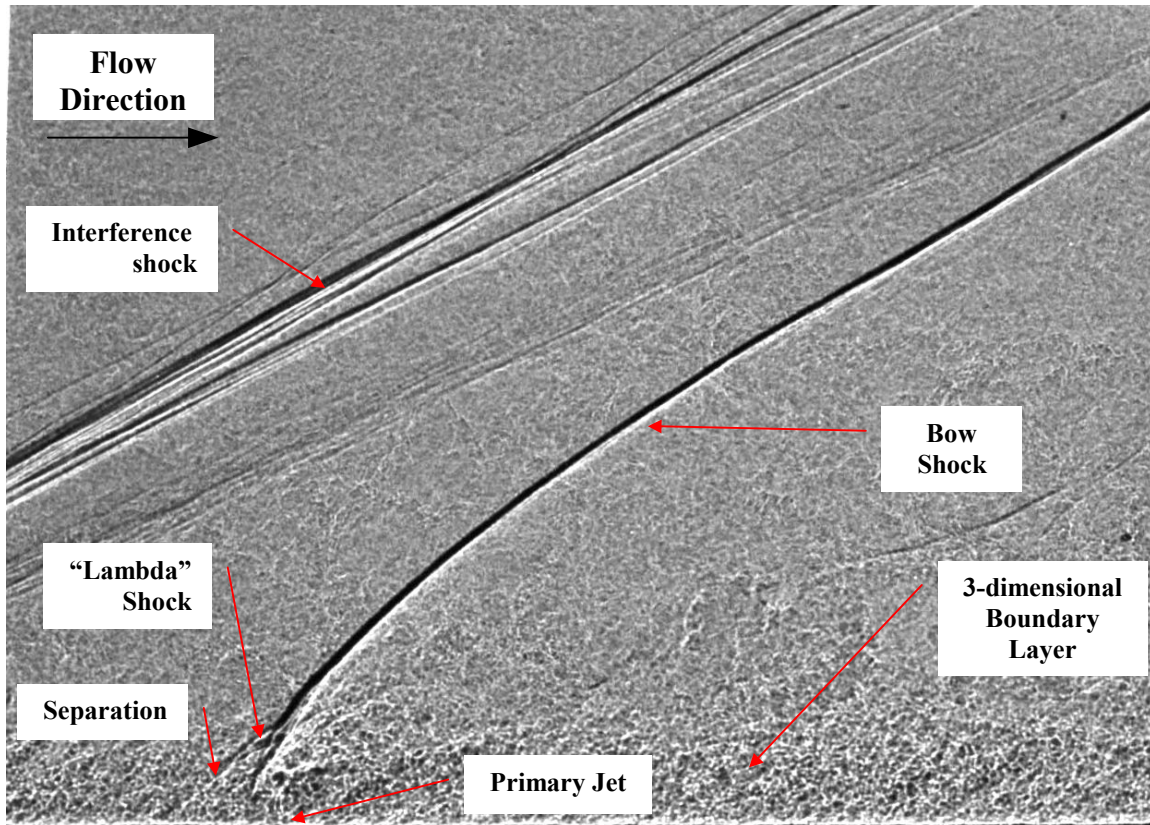


Figure 5.57. Schlieren photograph of the flowfield produced by the case with only the primary jet activated [84]. Virginia Tech, Mach 2.4, $Pr=14$.

The stronger separation ahead of the injector means that the C_p in this area is increased, and the integrated force is augmented while the nose-up pitching moment is decreased. The CFD solution under-estimates especially the augmentation factor of the normal force produced by the secondary jet. Note that the experimental values are more promising from a performance viewpoint than the numerical results since, according to the data of Table 5.24, a pair of secondary jets, each with a mass flow of 1% that of the primary jet produces an 11% increase in normal force. When both pairs of secondary jets are activated (for a combined mass-flow of 2% that of the primary injector) they produce a 16% increase in normal force. These force augmentation factors compare with the 3% and 6% predicted by the CFD. On the other hand, the augmentation values for the pitching moment predicted by the CFD are more favorable than those measured in the experiments. The experimental data shows a more negative pitching moment of 4% and

8% for the case with one and with two pairs of secondary injectors, respectively. The CFD, as discussed before, predicted a decrease in the nose-down pitching moment of 9% and 22%. The CFD solutions correctly predicted the trend in the behavior of the force and moments for all the three injection configurations.

Case	Experimental		CFD		ΔC_{Fy} %	ΔC_{Mz} %
	C_{Fy}	C_{Mz}	C_{Fy}	C_{Mz}		
Primary jet	12.05	-95.58	2.33	-2.65	-81	-103
Primary jet + Group 1 jets	13.32	-99.67	2.40	-2.88	-82	-103
Primary jet + Group 1&2 jets	14.01	-102.94	2.47	-3.23	-82	-103

Table 5.26. Comparison of the experimental to CFD force and for the Virginia Tech case with a freestream Mach number of 2.40.

Figure 5.58 through Figure 5.60 show comparisons of the experimental and numerical pressure coefficient mappings on the surface of the flat plate. Some general comments can be drawn:

- As already noted for the C_p plot along the tunnel centerline, Figure 5.54, the numerical solution consistently under-predicts the extent of the separation region.
- However, the C_p peaks predicted by the CFD in the separation region are higher than those measured in the experiment. This difference could also be due to the lack of definition of the CCD camera, being limited by the number of pixels.
- The zero- C_p line (line “G”) is predicted by the CFD in agreement with previous simulations and with the experimental mappings of Cubbison and Letko. However, the experimental mappings of the Virginia Tech cases do not show a clear zero- C_p line extending further downstream but rather it forms small lobes around the secondary injectors.
- As evidence by the shift in location of the “K” pressure line corresponding to a C_p of 0.133, the experiment measures an upstream effect of the secondary injector. The numerical solution completely fails to capture any upstream effect. Failure to correctly predict the upstream effects of the secondary jets might depend on the turbulence model. Wilcox’s $k-\omega$ model has in fact been shown to inaccurately predict the separation produced by adverse pressure gradients [54].

It appears that the experimental C_p mappings show an overall higher pressure acting on the flat plate. This could be due to the effects of the shock wave produced by the gap between the tunnel floor and the flat plate that were not simulated in any way in the CFD calculations.

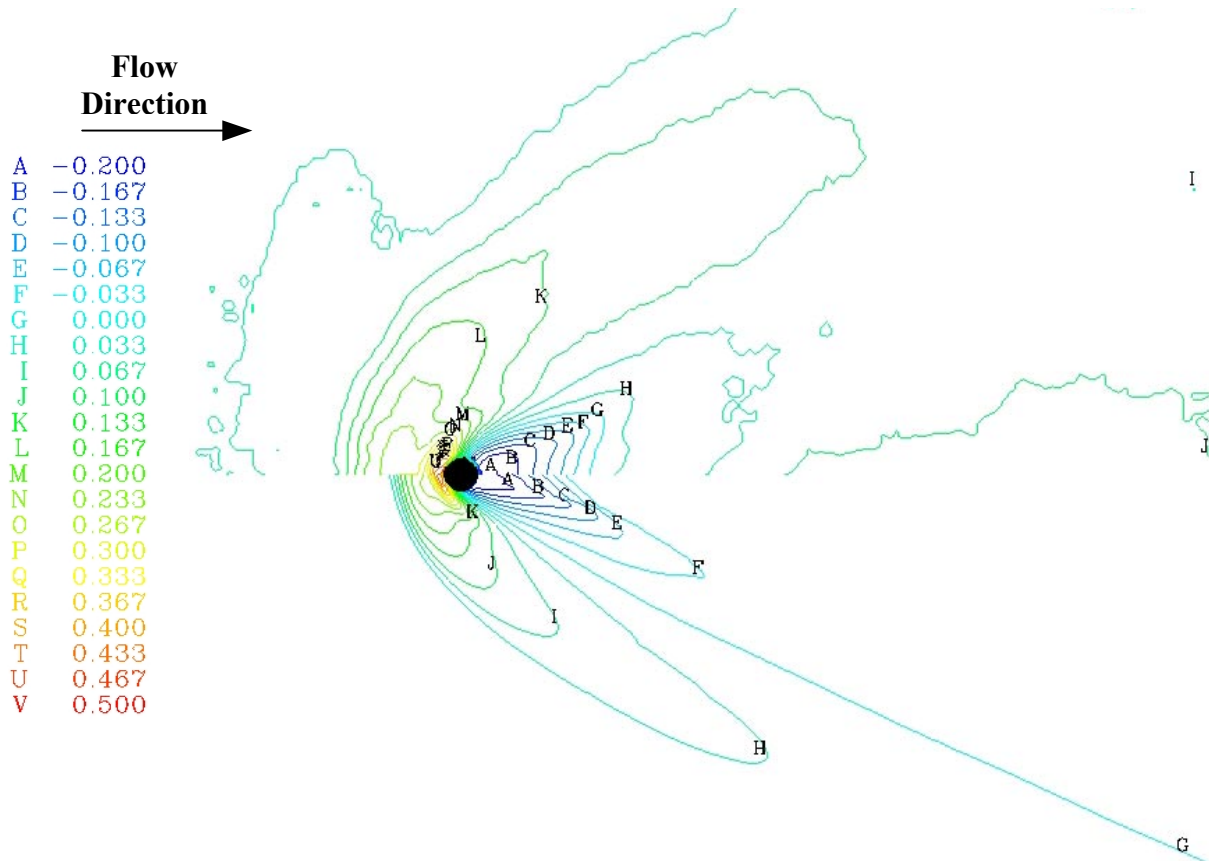


Figure 5.58. Comparison of the experimental (top) and CFD (bottom) C_p mapping for the case with only the Primary injector activated. Virginia Tech Mach 2.4, $Pr=14$.

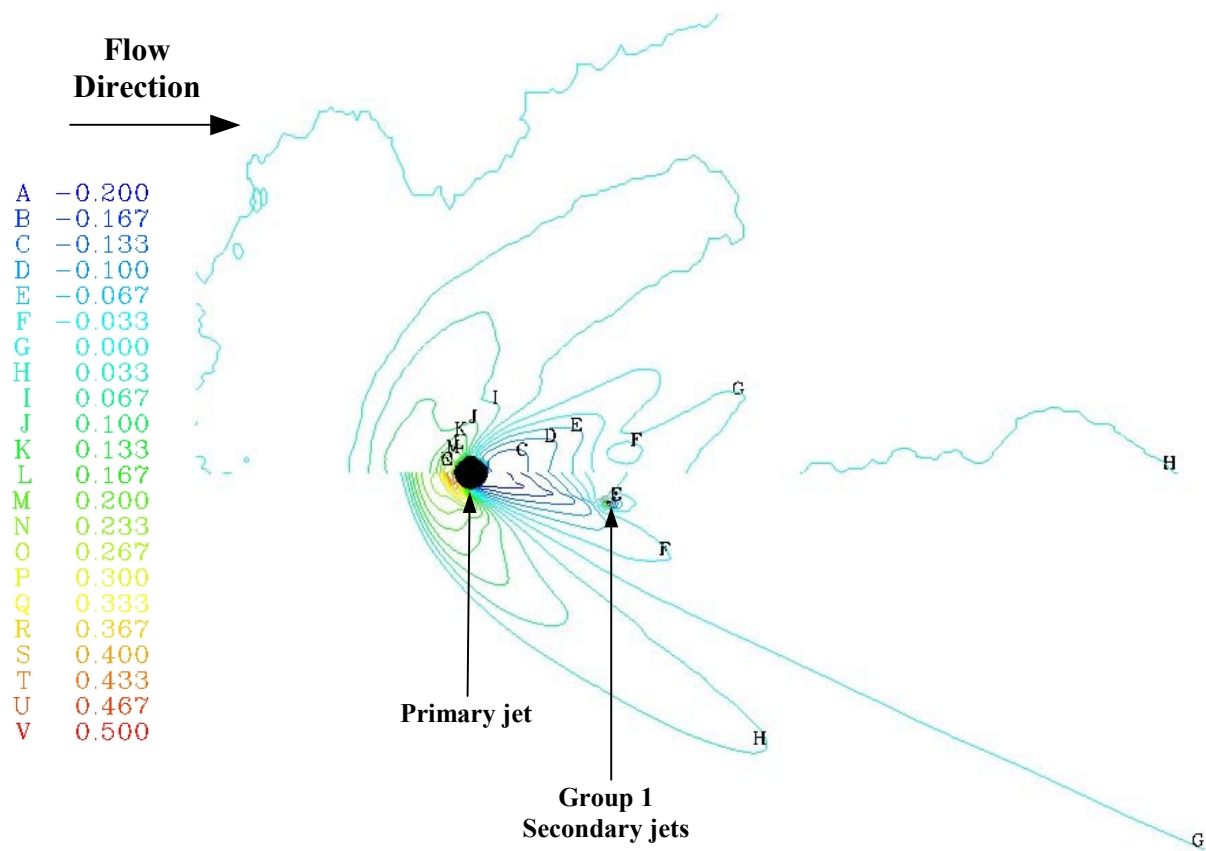


Figure 5.59. Comparison of the experimental (top) and CFD (bottom) C_p mapping for the case with the Primary injector and the secondary injectors of Group 1 activated. Virginia Tech Mach 2.4, $Pr=14$.

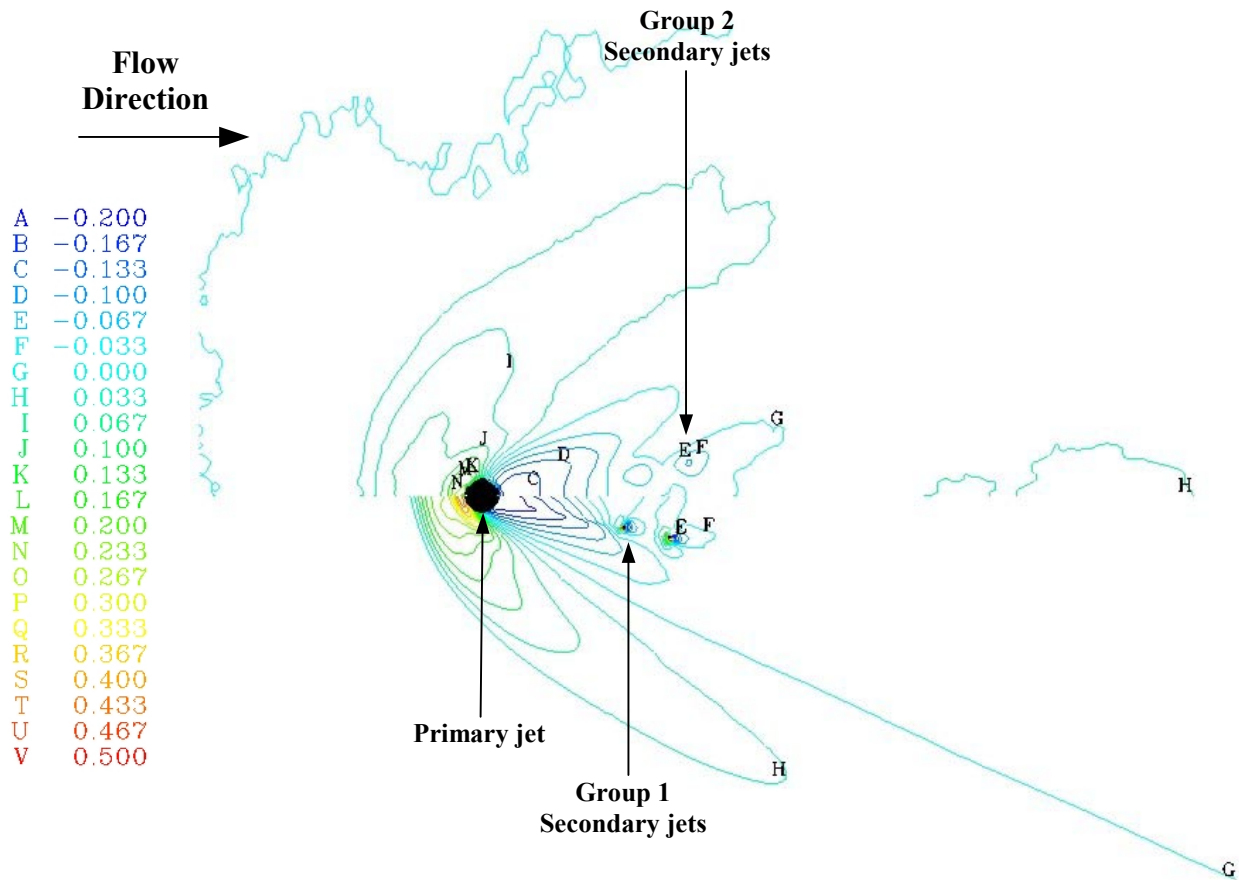


Figure 5.60. Comparison of the experimental (top) and CFD (bottom) C_p mapping for the case with the primary and secondary injectors of Group 1 and Group 2 activated. Virginia Tech, Mach 2.4, $Pr=14$.

5.7 Virginia Tech Mach 4.00, Turbulent (PR 532)

The previous Virginia Tech calculations were a “proof-of-concept” and were run with a relatively low Mach number and pressure ratio (2.4 and 14 respectively). Their scope was to provide an *interim* step between the calculations run with only the primary injector activated (see the Schetz, Cubbison and Letko cases in the previous sections) and the current numerical simulations with multiple jets, high Mach number and with a high pressure ratio. Note that the Virginia Tech Mach 2.4 cases are not very representative of any realistic application since all the jet thrusters applications found in real-life operate at high Mach number and very high pressure ratios. Therefore, the latest set of experiments performed at Virginia Tech were run at with a freestream Mach number of 4.0 and with a pressure ratio of 532, and they are here called the *Virginia Tech Mach 4.0* cases. The full set of conditions is shown in Table 5.28 and Table 5.27. The experimental set up was almost identical to the Virginia Tech Mach 2.4, as has been described in the previous section. The only differences in the experimental-set up between the two cases were:

- The wind tunnel nozzle (changed from the Mach 2.4 to the 4.0).
- The improved plumbing system to handle the much higher pressures necessary to produce the pressure ratio of 532.
- A different CCD camera with better resolution used to photograph the surface of the flat plate covered with Pressure Sensitive Paint (PSP).

The Virginia Tech Mach 4.0 experiments produced a more reliable set of pressure data. The improvement of this set of data with respect to the Virginia Tech Mach 2.4 cases is probably due to two main reasons. The first one is that the imperfections at the junction between the tunnel floor and the flat plate were smoothed. And the second fact is that an improved data acquisition system (primarily the higher-resolution CCD camera) was employed to photograph PSP patterns.

Parameter	
Flat plate entry length, x_0	7.62 cm
Injector diameter, d_j	0.4763 cm
$A_{\text{Primary}}/A_{\text{Secondary}}$	$\cong 100$
Plate entry length, x_0/d_j	16.00

Table 5.27. Flat plate and injector dimensions for the Virginia Tech experiment.

Parameter	
Gas	Air, perfect gas ($\gamma=1.40$)
M_∞	4.025
$P_{\infty, t}$	1,120.58 kPa
P_∞	7.135 kPa
T_∞	70.3 K
Type of boundary layer	Turbulent (Wilcox $k-\omega$)
Inlet boundary layer (δ_0)	1.65 cm

(a) Free-stream

Parameter	
Gas	Air, perfect gas ($\gamma=1.40$)
M_J	1.0
$P_{J, t}$	3,797.62 kPa
P_J	2,006.21 kPa
T_J	261 K
$P_{J, t} / P_\infty$	532
Primary Jet mass flow	0.1159 Kg/s *
Primary Jet thrust	37.53 N *
Secondary Jet mass flow	0.00132 Kg/s *
Secondary Jet thrust	0.4270 N *

(b) Primary and Secondary Jet. * These values are for a discharge coefficient of 0.75 for both the primary and secondary nozzles.

Table 5.28. Summary of flow parameters for the Virginia Tech Mach 4.0 (PR=532) experiments.

The overall grid topology was the same as for the grid used in the Virginia Tech Mach 2.4 case. Both the grid used for the primary jet only case and the grid used for the case with the primary and the secondary injector were composed of 13 zones with mixed H-type and C-type grid topologies (Figure 5.61). However, the grid used for the case with only the primary injector did not have any clustering around the location of the secondary injector, as was the case for the grid used to run the Virginia Tech Mach 2.4 case (see Figure 5.54). Therefore, the grid used for the Virginia Tech Mach 4.0 case with only the primary injector activated was smooth all around the primary injector. The grid used for the case with the primary and secondary injector replaced one of the zones of the previous grid with a modified zone as shown in Figure 5.62. The modified zone served two purposes:

- 1) Simulate the geometry of the secondary injector in the surface of the flat plate.
- 2) Increase the overall refinement of the grid in the region around the secondary injector so that a localized grid-refinement study of the area directly affected by the secondary jet could be performed.

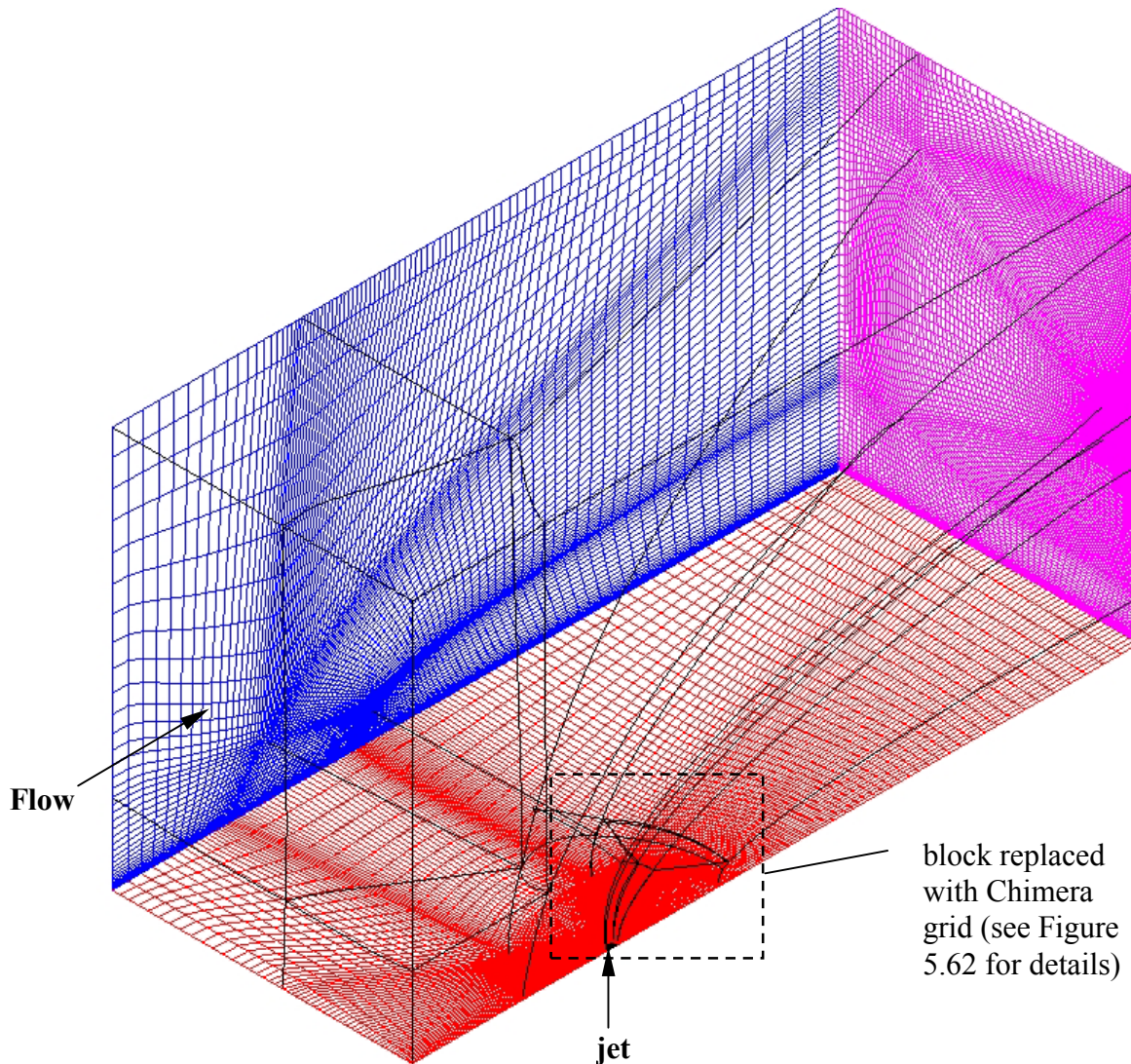
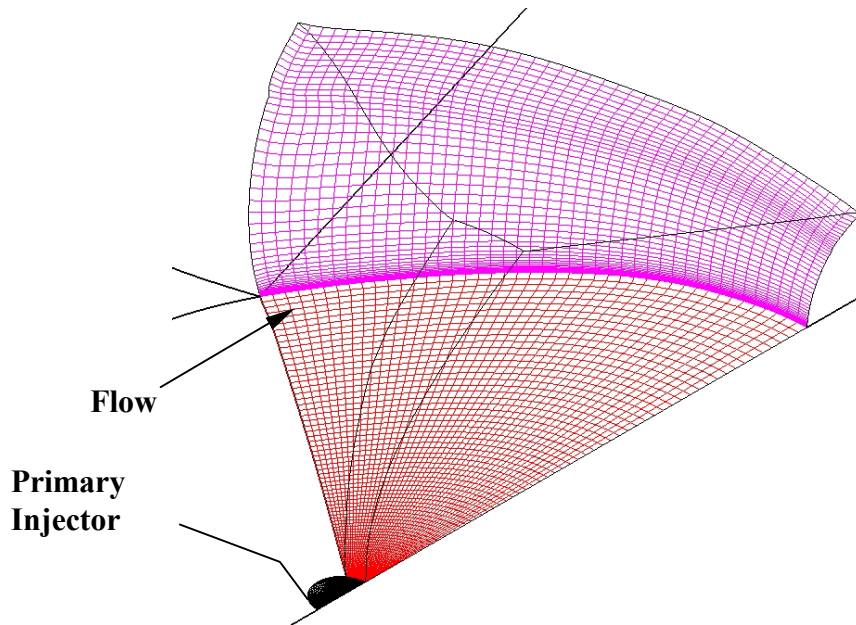
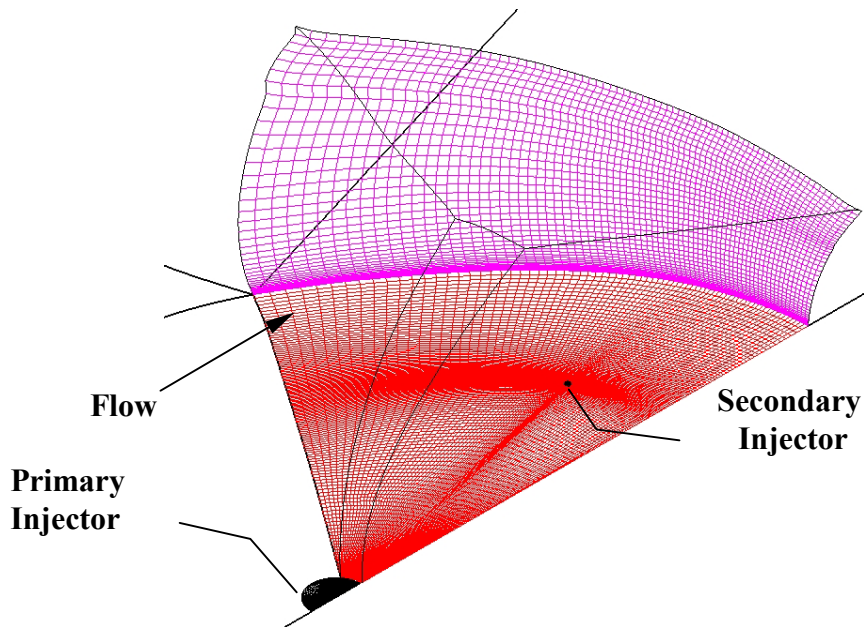


Figure 5.61. Perspective view of the overall grid topology employed for the Virginia Tech Mach 4.0 cases. It is composed of 13-zone some of which are H-type and others are C-type grid topology. The C-type grids wrap around the primary injector to optimize the grid refinement in this area. The total number of cells varied depending on the case: 1,544,098 for the case with only the primary injector activated and 2,073,024 cells for the case with the primary and secondary injectors activated). Not all grid lines are shown. The dashed rectangle shows the location of the block that was replaced with a Chimera grid when the secondary jet was activated. The area inside the rectangle is shown in more detail in Figure 5.62.



(a) Primary Jet only case. The block is made of 179,564 cells and does not have the secondary injector cut in the surface of the flat plate



(b) Primary and secondary jet case. The Chimera grid is made of 814,044 cells and it replaces the block shown above. Note the secondary injector in the surface of the flat plate and the clustering of cells around it.

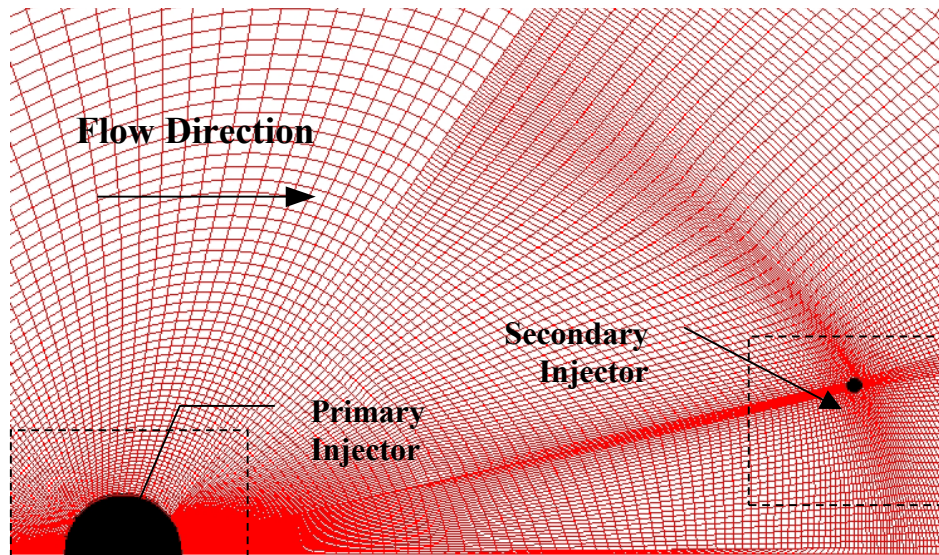
Figure 5.62. Comparison of the regular grid used in the case with only the primary injector and of the Chimera grid used for the case with the primary and secondary injector. Virginia Tech, Mach 4.0, $Pr=532$.

The secondary injector was simulated by contouring the grid lines on the surface of the flat plate and then by clustering cells around it as shown in Figure 5.62 (b) and Figure 5.63 (a). The localized grid refinement study was approached in a different way from the previous grid convergence study performed with the Letko case (see Section 5.5.3). With the Letko case, the grid was refined everywhere in the computational domain so as to generate an additional grid level which had more clustering than the fine grid sequence. The grid convergence study performed on the Letko case showed that the solution was grid converged on the fine grid level at least as far as engineering information is concerned.

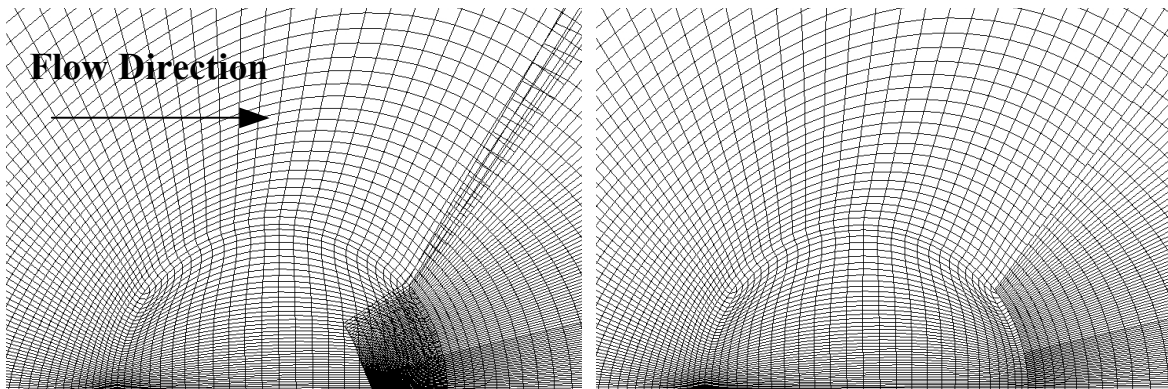
However, that study was performed with only the primary jet activated, and no information was available about the convergence of the solution in the region surrounding a secondary jet. Thus, the Virginia Tech Mach 4.0 case with both the primary and the secondary jets was used to perform a localized grid refinement study in the area around the secondary injector. In order to refine the grid only in the region in the immediate surroundings of the secondary injector without increasing the number of cells in those regions of the computational domain where grid convergence had already been proved, the Chimera method was employed.

In the present study, a Chimera grid was used to substitute a regular block of the original computational domain. The block that was substituted and the Chimera grid that replaced it are shown in Figure 5.62 (a) and (b), respectively. The Chimera grid was considerably finer than the original block (179,564 cells versus 814,044 cells) since, as discussed before, one of the goals of the substitution was to better resolve the flow details in the region around the secondary injector.

The finer Chimera grid allowed very close clustering of the cells around the secondary injector (see Figure 5.63) without negatively affecting the rest of the domain. Since the Chimera grid uses a layer of two interpolation cells to transmit flow information to the neighboring grids, the boundaries of the Chimera grid overlapped the blocks around it as shown by the detail of the primary injector in Figure 5.63 (b). However, the overlapping serves only for the Chimera algorithm, and the physical solution is analyzed only on the non-overlapping section of the two grids as shown in Figure 5.63 (c). The Chimera technology provided an efficient method to refine the grid only in a very localized area without affecting the gridding and the number of cells of the rest of the computational domain. The overall size of the grid with the Chimera block is 2,073,024 cells compared to 1,544,097 of the baseline grid. Note that the half million increase in cell number is concentrated in the region of the secondary jet. To reach such a fine grid level in the region of the secondary jet without using the Chimera method would have required a grid with a minimum overall number of cells of 3.5 million.

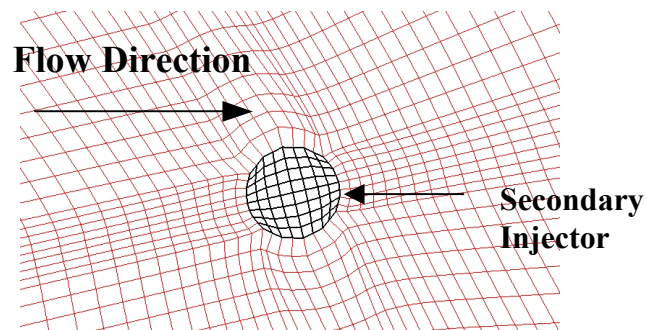


(a) Grid in the region of the primary and secondary injector. Note that the grid surrounding the primary injector is a C-type grid and that the grid section with the secondary injector is a Chimera grid



(b) Gridding of the primary injector with Chimera overlapping shown

(c) Gridding of the primary injector without overlapping



(d) Detail of the gridding of the secondary injector

Figure 5.63. Details of the Chimera grid around the Primary jet and the secondary jet of Group 2. Virginia Tech, Mach 4.0, Pr=532 test cases.

The numerical solution was converged on the three grid sequences for both the case with only the primary injector on and the case with the primary jet and Group 2 jets activated. The normal force and pitching moment obtained from these calculations are shown in Figure 5.64 and Figure 5.65 respectively. From the plots, the solution appears to be grid converged as confirmed by the values in Table 5.29. The discretization error in the normal force is almost zero in both cases. The discretization error in the pitching moment appears to be much higher but these values are misleading. The pitching moment on the fine grid is very close to zero, therefore when results from different grid levels are compared to the fine grid results, the percentage difference appears very high. In addition to this, the diameter of the injector together with the jet thrust are used to non-dimensionalize the moment. Since the diameter is a small value (0.0047 m) the pitching moment coefficient appears to be a large number.

Case	Richardson Extrapolation		CFD		$\epsilon C_{Fy} \%$	$\epsilon C_{Mz} \%$
	C_{Fy}	C_{Mz}	C_{Fy}	C_{Mz}		
Primary jet only	1.16	-0.55	1.16	-0.53	0	-4
Primary jet + Group 1 jets	1.23	-1.34	1.22	-1.06	-1	-21

Table 5.29. Comparison of the solution on the three grid levels with the solution obtained with the “Mixed 1st +2nd Order Extrapolation” for the Virginia Tech case with a freestream Mach number of 4.0. “ ϵ ” is the discretization error in the solution.

The normal force is increased by 4.8% by the effects of the secondary jet.(see Table 5.31). Note that this trend is in agreement with what observed in previous simulations with a secondary injector such as the Letko case and the Virginia Tech Mach 2.4 cases. The moment is made more negative (Table 5.31 (b)) by the secondary jet. This result is very important since it indicates that the secondary jet actually alleviates the nose-down moment created by the primary injector.

The increase in the normal force and the decrease in the nose-down pitching moment can be understood from the pressure coefficient mapping of Figure 5.66. The upper half of the figure shows the results with only the primary injector and the lower part with both injectors activated. The secondary injectors marginally reduce the area of negative C_p behind the primary injector. They also make the separation region extend further upstream than the case with only the primary jet. But, the C_p in the two separation lobes does not reach the high levels seen in the single jet case. This phenomenon is visible in the C_p plot along the tunnel centerline of Figure 5.67. It is noteworthy the complex shape of the zero- C_p line (the “D” line) for the case with only the primary jet (Figure 5.66, top half). In previous cases (Cubbison, Letko, Virginia Tech Mach 2.4) the zero- C_p line appeared to radiate almost linearly from the region of the primary injector towards the downstream location (see Figure 5.52). However, in this case, the zero- C_p line extends

linearly up to a certain downstream location and then it moves back upstream to form a lobe around a region of higher pressure (line “E” in top half of Figure 5.66). Note that when the secondary injectors were activated, the lobe formed by the zero- C_p line around the higher-pressure region was canceled by the effects of the secondary injectors.

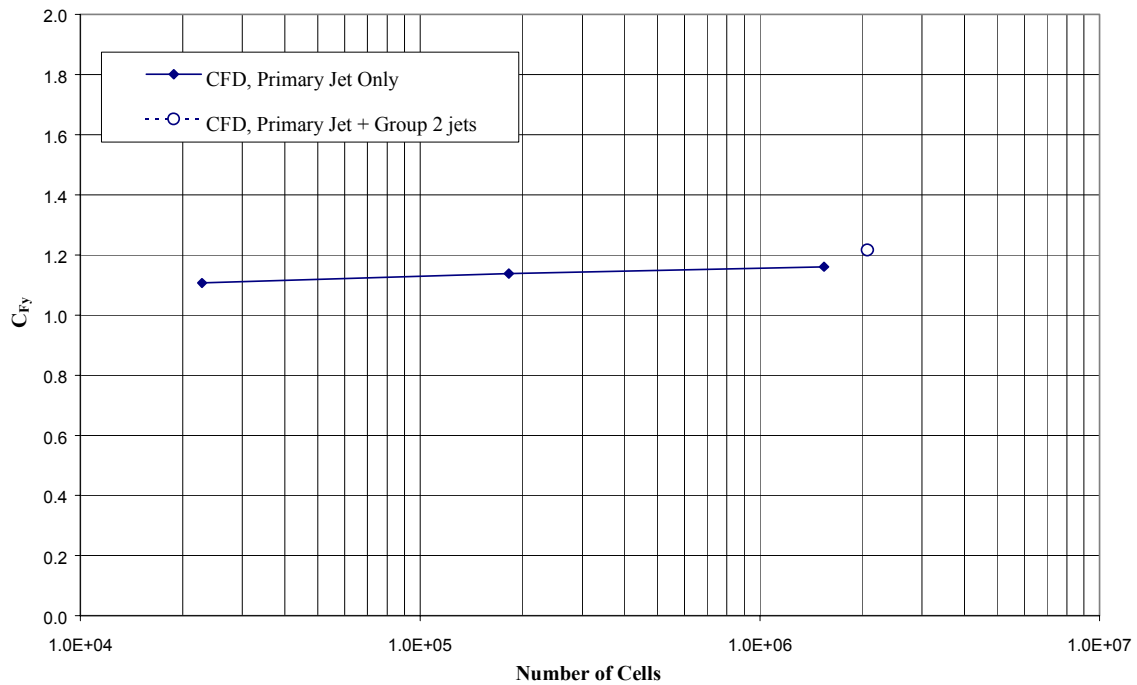


Figure 5.64. Comparison of the normal force, F_y , acting on the flat plate for the two Virginia Tech, Mach 4.0, Pr 532 test cases.

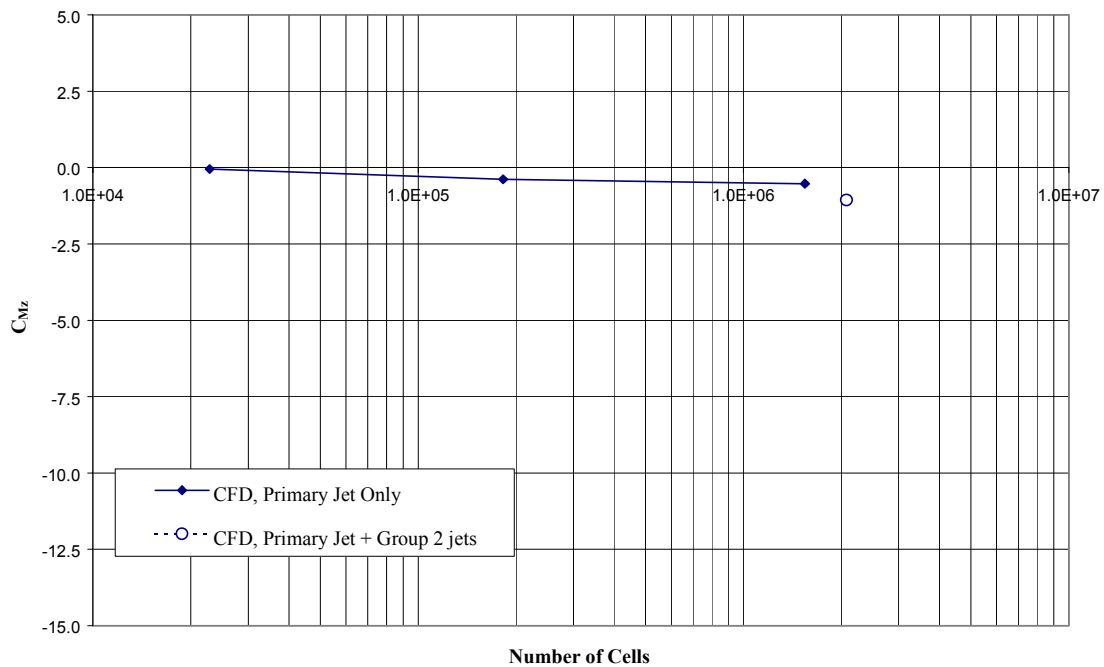


Figure 5.65. Comparison of the pitching moment, M_z , acting on the flat plate for the two Virginia Tech, Mach 4.0, Pr 532 test cases.

The separation region in the case with the secondary jets on appears larger than the case with only the primary injector, even though the peak pressures are lower. The secondary injectors also affect the region aft of the primary injector. Note the steep pressure rise in the middle of the region of negative pressure at a x/d of 5.0. In addition to this, the secondary injector smear and push downstream from x/d of 15.0 to 17.0 the location at which the reflected shock of the Mach disk (see Figure 1.3 for the description of this shock) impinges on the flat plate.

The weakened reflected shock also does not thicken the boundary layer as much as in the case of the primary jet alone, and the region of positive C_p aft of the impingement is shorter. These differences such as the larger separation and the lack of a strong reflected shock for the case with the secondary injectors are confirmed by the mapping of the Mach number contours on the plane of symmetry (Figure 5.68). It is noteworthy the secondary injector impinging on the back side of the barrel shock reduces the size of the barrel shock itself. As a consequence of this, the injectant does not expand to such a large extent as in the primary jet alone case and the Mach disk has virtually disappeared from the top of the barrel shock. Also the wake behind the plume is larger when the secondary injectors are activated, indicating a slower mixing between the injectant and the freestream fluid.

The localized grid convergence study of the mesh around the secondary injectors demonstrated that the fine Chimera grid produced a converged solution. Figure 5.69 shows the comparison of the C_p plot along the axis of the secondary injector for the fine and medium grid sequences. The C_p between the two sequences does not change significantly. Note that the scale of the C_p plot is very small, and it magnifies the differences. It is noteworthy that the C_p distribution follows the same pattern as that produced by the primary injector (Figure 5.67). A gradual pressure increase is created by the separation, and it is followed by a shallow pressure trough. Aft of the trough, there is a steep pressure rise that creates two high-pressure peaks divided by another trough in the C_p . A low-pressure that slowly recovers to the local static pressure region exists aft of the injectors. Note, however, that since all the area represented in Figure 5.69 is immersed in the low pressure region created by the primary injector, the local static pressure is lower than the freestream pressure as indicated by the plateau of negative C_p ahead of the secondary jet.

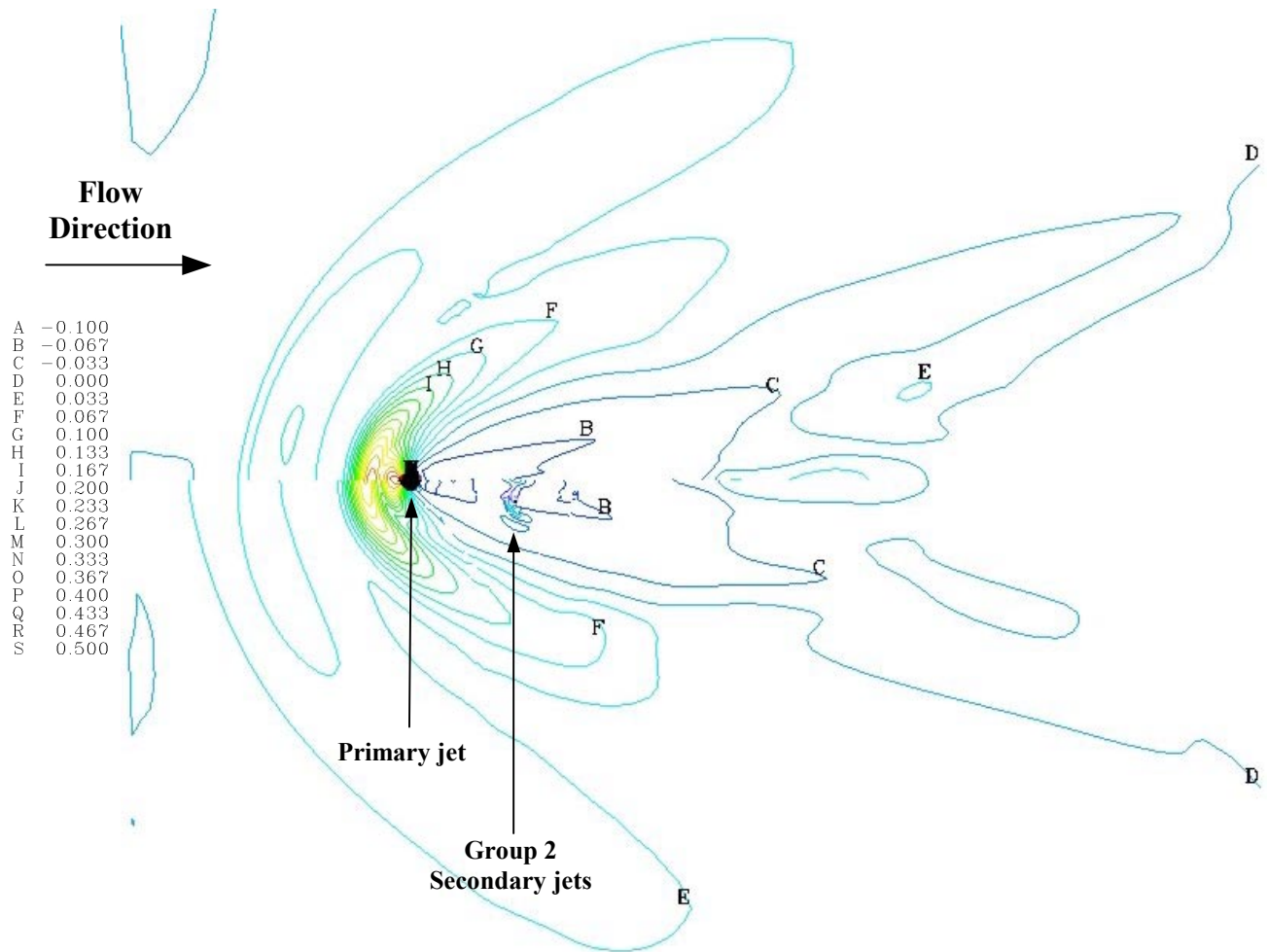


Figure 5.66. Comparison of the CFD C_p mapping for the Primary jet only case (top) and the primary jet plus 1 secondary jet case (bottom). Virginia Tech, Mach 4.0, Pr 532.

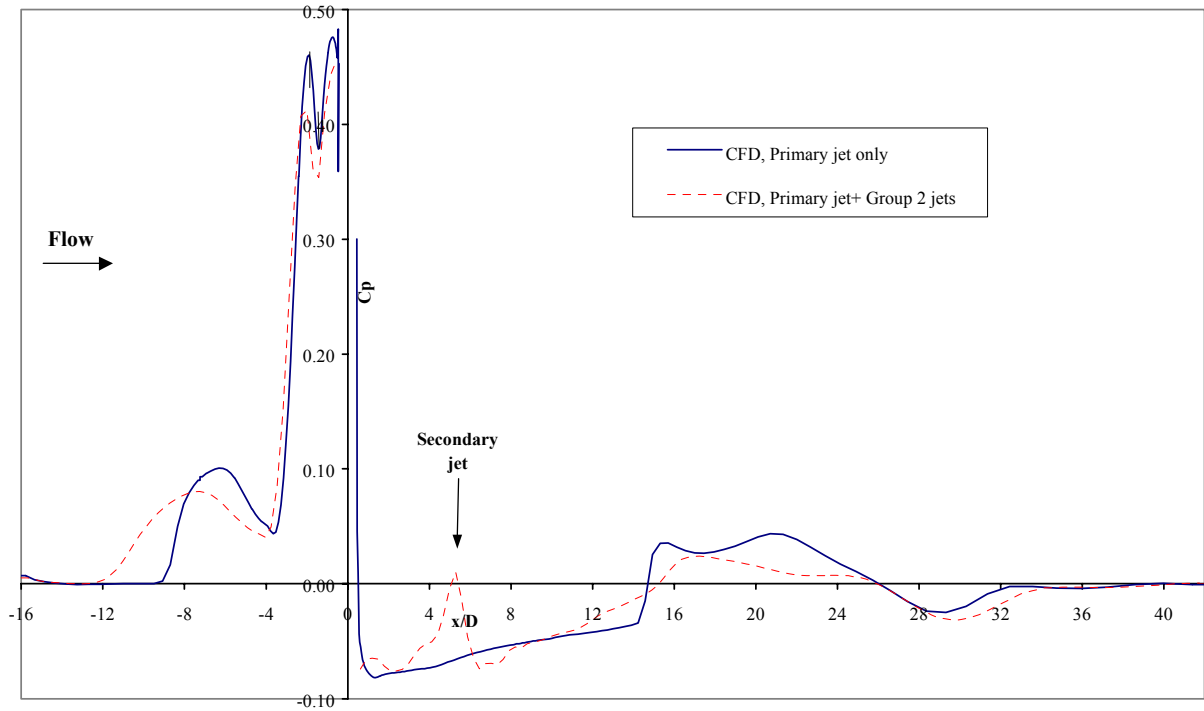


Figure 5.67. Comparison of the C_p plots along the tunnel centerline for the primary jet only case and the Primary + Group 2 jet case. Virginia Tech, Mach 4.0, PR 532.

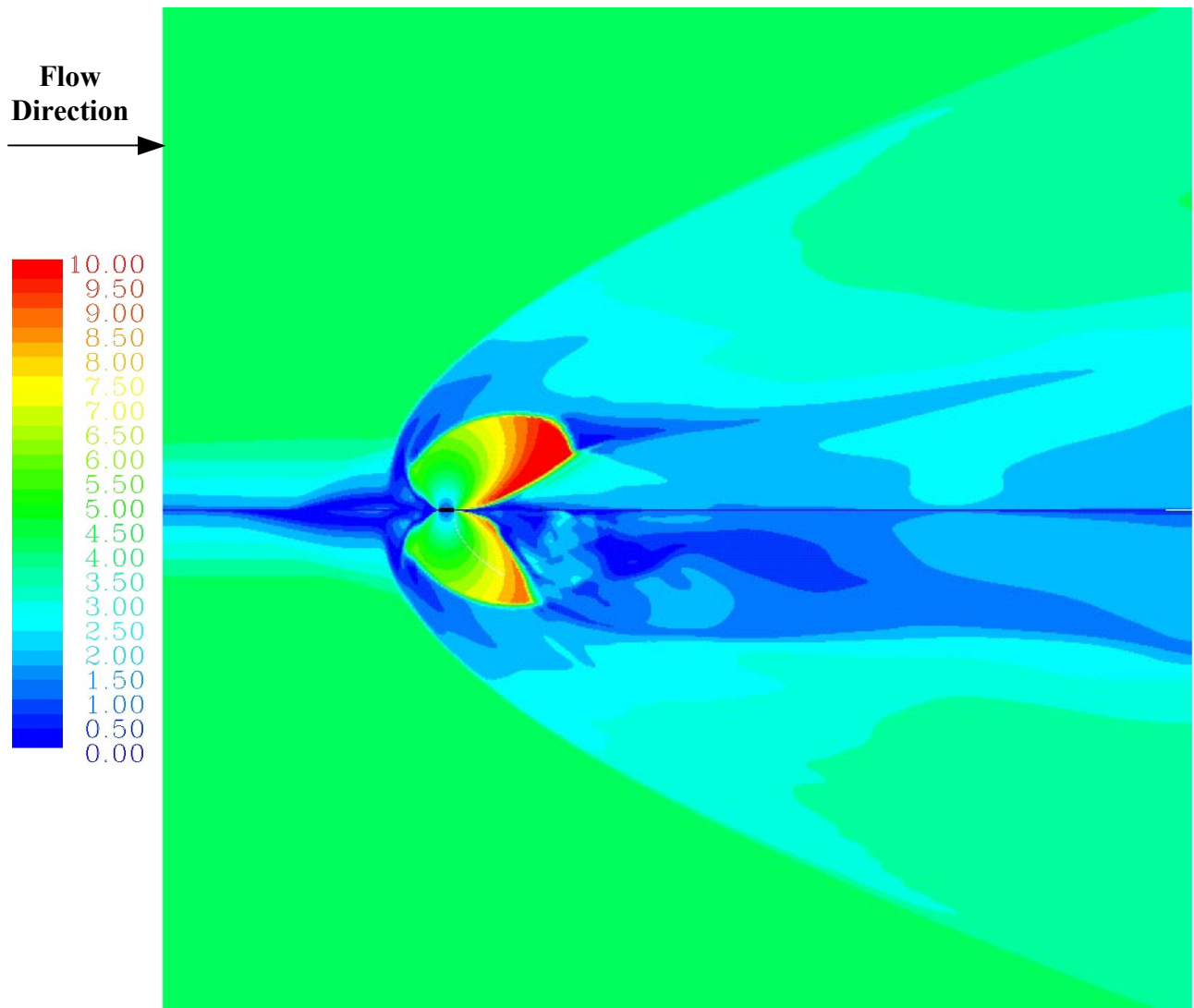


Figure 5.68. Comparison of the CFD Mach contours on the plane of symmetry for the primary jet only case (top) and the primary jet plus 1 secondary jet case (bottom). Virginia Tech, Mach 4.0, Pr=532.

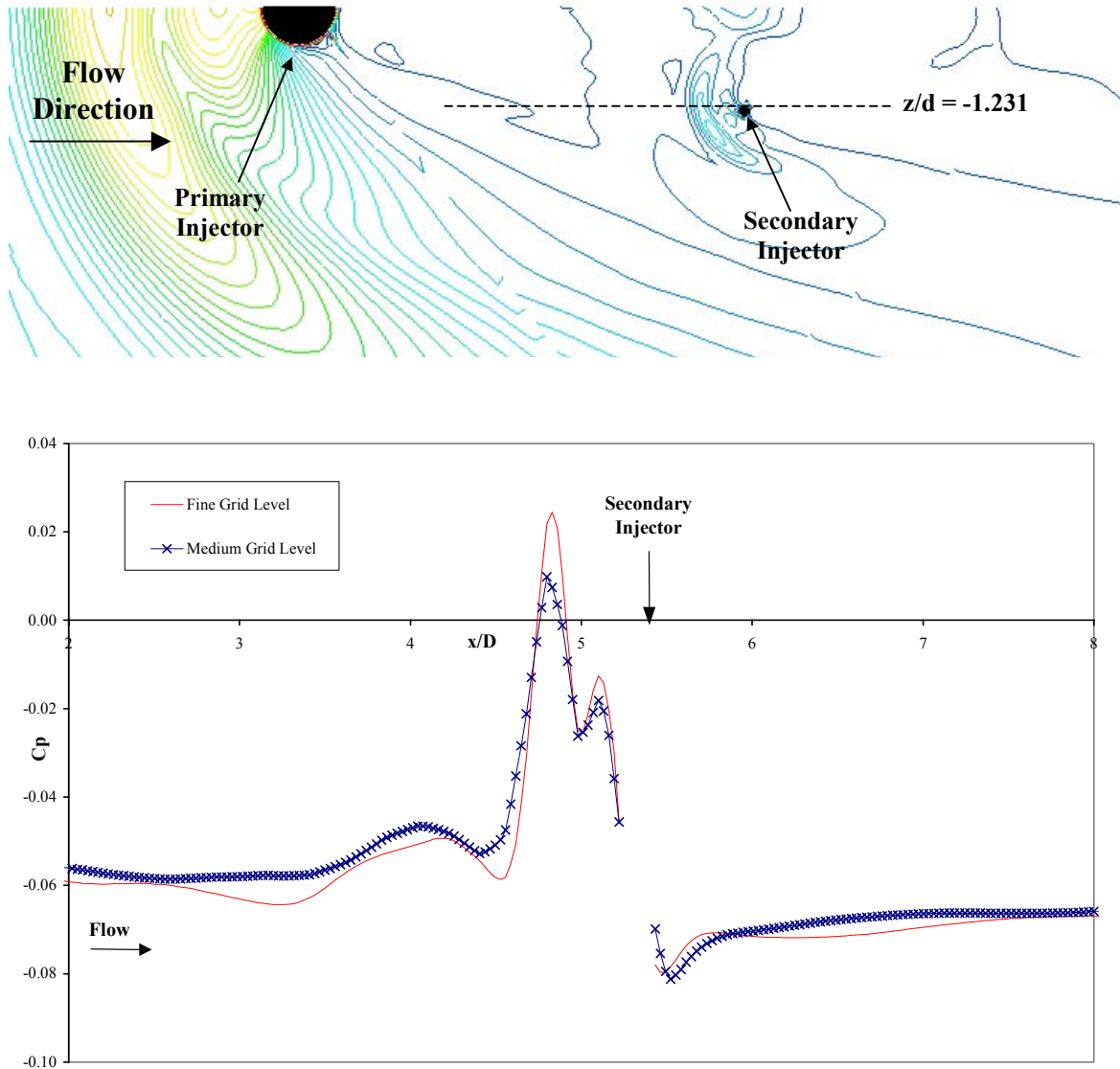


Figure 5.69. Comparison of the pressure coefficient along the same spanwise location as the secondary injector for the medium and fine sequences of the Chimera grid. The top figure shows in detail the line along which the C_p is plotted. Virginia Tech, Mach 4.0, $Pr=532$ with secondary injector.

Comparison of experimental and numerical results

The forces and moments obtained from the numerical solution are compared to the experimental values in Table 5.30 for both the case with the primary jet only and the case with the primary and secondary jets. The CFD solution under-predicted the normal force and the pitching moment in both cases. The difference between the experiment and the computation is 24% and 20 % for the normal force and it increases to 39% and 62% for the pitching moment for the case with the primary jet only and for the case with the secondary jets, respectively. The discrepancy in the forces and moments between the experiment and the CFD solution can be explained by analyzing the pressure mappings and pressure plots of Figure 5.73 through Figure 5.76. Figure 5.73 shows the comparison between the CFD and the experiment for the case with only the primary jet.

Case	Experimental		CFD		$\Delta C_{Fy} \%$	$\Delta C_{Mz} \%$
	C_{Fy}	C_{Mz}	C_{Fy}	C_{Mz}		
Primary jet only	1.53	-0.87	1.16	-0.53	-24	-39
Primary jet + Group 1 jets	1.52	-2.77	1.22	-1.06	-20	-62

Table 5.30. Comparison of the experimental and numerical results for the normal force and pitching moment. Virginia Tech Mach 4.0, PR 532. The limit of integration for these calculations, in meters, are $-0.037 < x < 0.041$ and $-0.07 < z < 0.00$.

The mappings are in good agreement with the isobars having the same shape and the same values. Note, for example, how the zero- C_p line (line “D”) is virtually identical in both sets of results. But, the CFD mapping predicts a higher pressure coefficient in the separation region as shown by the C_p plot of Figure 5.74. From this plot, it is also clear that the experimental data fails to show the two peaks and the trough in the C_p just ahead of the injector. Apart from this discrepancy, the experimental and CFD C_p plots are very similar in the separation region far ahead of the injector and in the region of negative pressure aft of the jet. The experimental C_p mapping shows considerably more noise than the CFD as indicated by the jagged isobars of the top half of the figure. It is not possible to exactly assess whether or not the separation location is properly predicted by the CFD, since the experimental data does not extend upstream far enough. From the C_p plot in Figure 5.74 it seems that the CFD is slightly under-predicting the separation location. It is noteworthy that other numerical works, such as that of Payne, et al. [54], have shown a tendency of the $k-\omega$ turbulence model to under-predict the separation location but to over-predict the C_p peak values in a jet interaction flowfield.

The C_p mapping for the case with the secondary injectors is shown in Figure 5.75. Again, the experiment and the numerical solution are in good agreement as shown by the nearly exact match between the shape and location of the zero- C_p line (line “D”) of Figure 5.75). As for the case with only the primary injector, the CFD predicts two peaks in the C_p just

ahead of the primary injector that do not appear in the experiment. (Figure 5.76). Also the CFD over-predicts the increase in the C_p at a $x/d=5.0$ due to the presence of the secondary injectors (see Figure 5.76). The CFD over-predicts the separation location as shown by the C_p plot of Figure 5.76.

The larger separation region and the higher C_p just ahead of the primary injector as calculated by the CFD explains why the CFD moment is less negative by 62% than the pitching moment from the experiment (Table 5.30). In fact, a force pushing down on the plate at a location ahead of the primary injector produces a positive (nose-down) moment. However, the under-prediction of the normal force from the CFD solution is not so easily explained since both the CFD and the experimental mapping are similar.

The discrepancy in the experimental and CFD results might be attributable to the uncertainty in the measurement of the freestream pressure. Similarly to, but not as much as the Virginia Tech Mach 2.4 case, a relatively large uncertainty affected the freestream pressure. This is shown by the spanwise static pressure plot of Figure 5.71. Note that experimental data was not available for the region in front of the separation. The distribution of Figure 5.71 plots the furthest upstream data that can be extracted from the experiment. The experimental pressure plot shows a peak near the centerline of the flat plate that corresponds to the front section of the separation region. However, far from the centerline, the static pressure should be constant, at the freestream level. Instead there is a slope in the pressure data that indicates a bias in the data acquisition/reduction system. As observed for the Mach 2.4 case (see Section 5.6.3 and Figure 5.53), the probable cause of this spanwise bias is the fact that the CCD camera was inclined at an angle to the flat plate rather than being perpendicular above it. In addition to this, Figure 5.72 shows longitudinal plots of the pressure coefficient far away from the centerline of the tunnel. Note that the experimental pressure distribution in front of the shock (the steep increase in the C_p) is not constant and that the experimental static pressure is higher than that used in the numerical computations. As in the case of the Virginia Tech Mach 2.4 computations, these spanwise plots were used to estimate the experimental uncertainty, computed to be $\pm 15\%$ for the static pressure. The propagation to the pressure coefficient of this error in the static pressure is calculated using standard error propagation procedures (see Coleman and Steele [19]). The uncertainty propagated to the pressure coefficient is then plotted as error bars as shown by the plots of Figure 5.74 and Figure 5.76. Figure 5.71 also put in evidence another issue with the experimental data. The average freestream pressure in the experiment was higher than the one used in the CFD calculations (approximately 10 kPa in the experiment versus 7,135 Pa in the numerical computations). Again, as in the Mach 4.0 case, the higher freestream pressure is attributable to two main factors. The first one is the difficulty of controlling with precision the freestream pressure in the supersonic wind tunnel. The second, and most likely largest contribution, is the presence, in front of the jet interaction flowfield, of a shock generated by the misalignment of the tunnel floor with the flat plate. The combined effect of the sources of errors in the experimental data produced an estimated error of $\pm 18\%$ in the normal force and $\pm 7\%$ in the pitching moment.

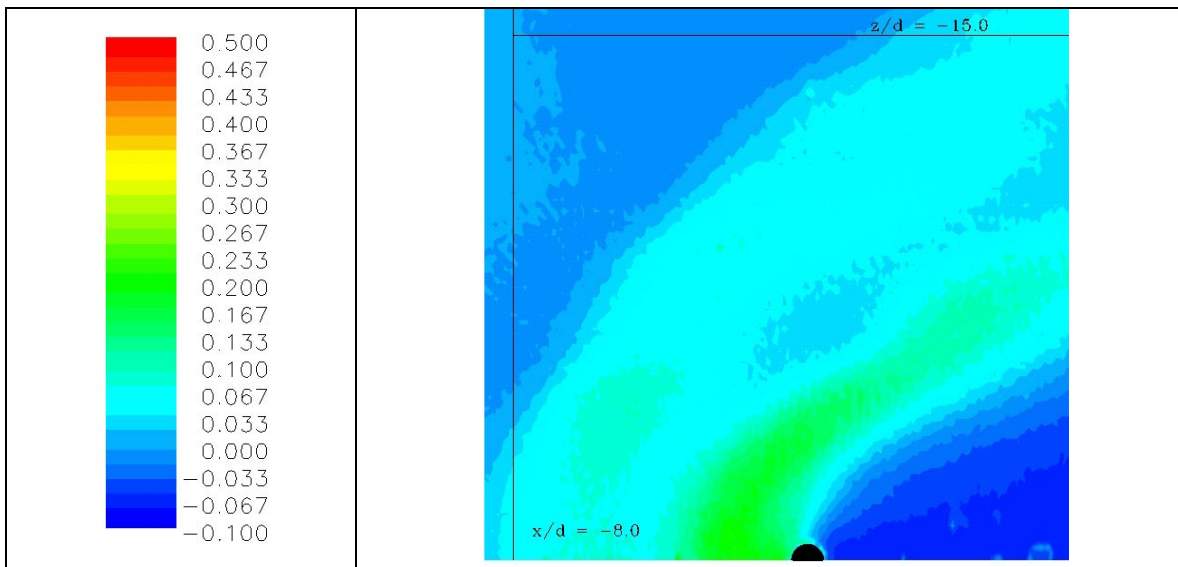


Figure 5.70. Locations of the C_p plots of Figure 5.71 and Figure 5.72 superimposed on the experimental C_p mapping for the case with only the primary jet. Virginia Tech, Mach 4.0, $Pr=532$.

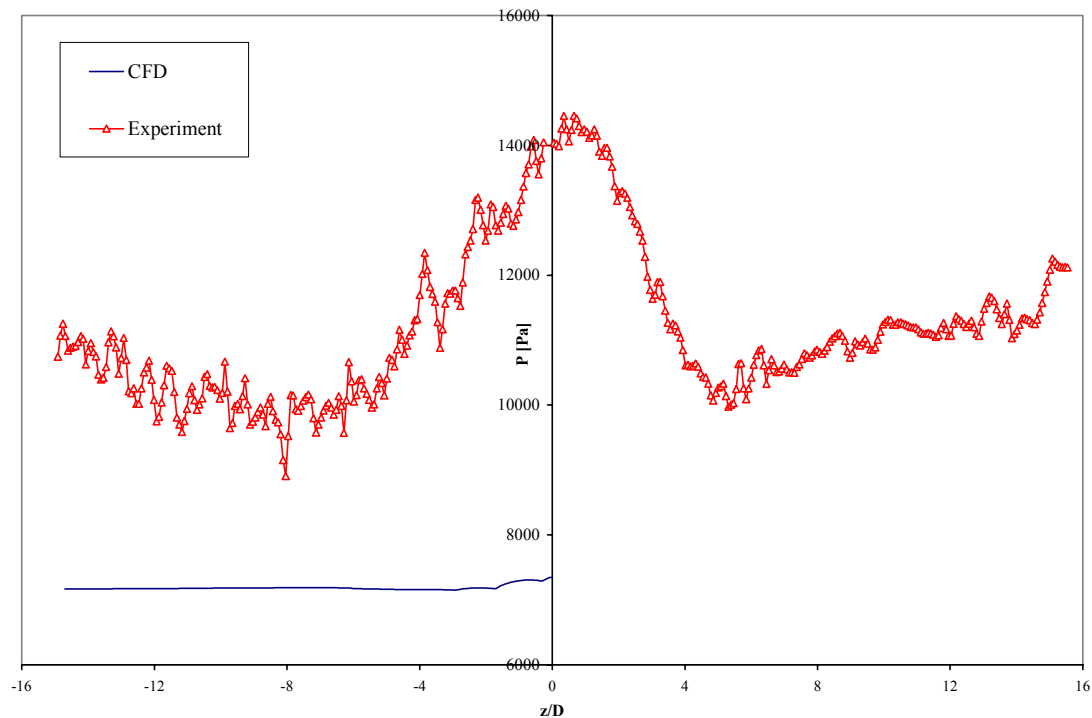


Figure 5.71. Comparison of the experimental and numerical spanwise C_p plots ahead of the separation region at $x/d = -8.0$ for the case with only the primary jet. Virginia Tech, Mach 4.0, $Pr=532$.

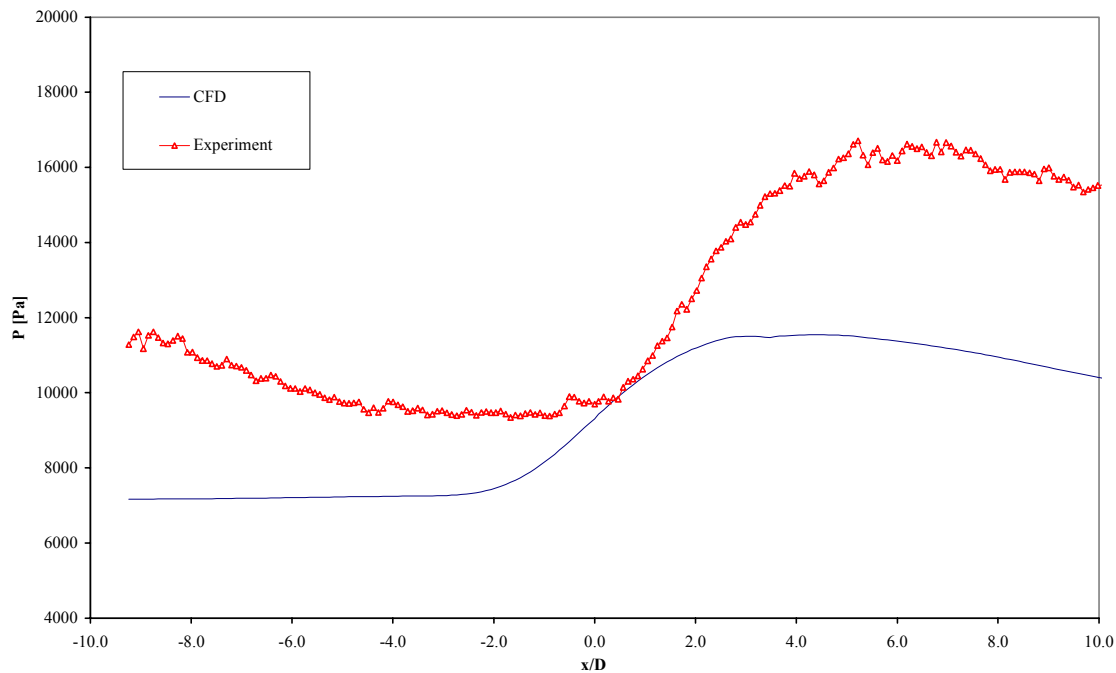


Figure 5.72. Comparison of the experimental and numerical longitudinal C_p plots at $z/d = -15.0$ for the case with only the primary jet. Virginia Tech, Mach 4.0, $Pr=532$.

Due to the discrepancy between the experimental and the numerical freestream conditions it is convenient to compare the force and moment augmentation factor of the secondary jets. The force and moment increase generated by the secondary injectors are shown in Table 5.31 and Table 5.32. Table 5.31 shows the augmentation factors when the contribution of the jets is not considered, i.e. the forces and moments are calculated exclusively from integration of the pressure on the flat plate. The experiment predicts a small decrease of the normal force (-0.9%) due to the secondary injector. This result is in disagreement with previous results and experiments (the Letko case with a simulated secondary injector and the Virginia Tech Mach 2.4 calculations) that predicted an increase in force of the same order of magnitude as the increase in the total jet thrust. On the other hand the numerical result predicts an increase in the normal force which is in agreement with the observations made for the Letko case and the Virginia Tech Mach 2.4 cases. Basically the force augmentation factor is of the same order of magnitude as the increase in total thrust. In fact, one pair of secondary injectors with a combined mass flow which is approximately 2% that of the primary jet, produce a force increase of 4.8% (this is without taking into account the thrust of the jets). The effect on the pitching moment is the same for the experiment and the CFD. In both cases, the pitching moment is made more negative (nose-up), i.e. the nose-down attitude of typical jet interaction configurations is decreased. The experimental data gave a pitching moment increase with respect to the case with only the primary jet of 218% and the numerical solution of 101%

(see Table 5.31 (b)). When the jet thrust is taken into consideration in the calculation, the forces and moments results improve (see Table 5.32). Note that the normal force is almost unchanged in the experiment while it is increased in the CFD solution. The pitching moment shows the same trend as for the calculations without the jet thrust, but the percentage increase is slightly higher due to effects of the secondary injector that is located far downstream of the reference point (Table 5.32 (b)).

Case	Experimental		CFD	
	C_{Fy}	$\delta C_{Fy} \%$	C_{Fy}	$\delta C_{Fy} \%$
Primary jet only	1.53	0.0	1.16	0.0
Primary jet	1.52	-0.9	1.22	4.8

(a) Normal Force

Case	Experimental		CFD	
	C_{Mz}	$\delta C_{Mz} \%$	C_{Mz}	$\delta C_{Mz} \%$
Primary jet only	-0.87	0	-0.53	0
Primary jet	-2.77	218	-1.06	101

(b) Pitching Moment

Table 5.31. Increase in (a) normal force and (b) pitching moment due to the action of the secondary jets without taking into consideration the jet thrust. On the right column are the results from the experiment and on the left are the results from the numerical simulations. Virginia Tech cases with a freestream Mach number of 2.40. Note that $\delta C_{()}$ represents the increase of the parameter $C_{()}$ with respect to the case with the primary injector only.

Case	Experimental		CFD	
	C_{Fy}	$\delta C_{Fy} \%$	C_{Fy}	$\delta C_{Fy} \%$
Primary jet only	2.53	0.0	2.16	0.0
Primary jet	2.53	-0.1	2.23	3.1

(a) Normal Force

Case	Experimental		CFD	
	C_{Mz}	$\delta C_{Mz} \%$	C_{Mz}	$\delta C_{Mz} \%$
Primary jet only	-0.87	0	-0.53	0
Primary jet	-2.78	219	-1.07	103

(b) Pitching Moment

Table 5.32. Increase in (a) normal force and (b) pitching moment due to the action of the secondary jets taking into consideration the contribution of the jet thrust. On the right column are the results from the experiment and on the left are the results from the numerical simulations. Virginia Tech Mach 4.0. Note that $\delta C_{()}$ represents the increase of the parameter $C_{()}$ with respect to the case with the primary injector only.

Figure 5.77 is a shadowgraph of the jet interaction flowfield produced by the primary injector alone. Some of the flowfield characteristics appear clearly in this photograph. However, it is important to note the weak shock ahead of the separation. This shock is the disturbance produced by the junction between the tunnel floor and the flat plate. As mentioned in the discussion of the Virginia Tech Mach 2.4 cases, this shock was not simulated by the CFD and could change the freestream conditions experienced by the jet thus increasing the discrepancy between the experimental data and the numerical solution. Figure 5.78 and Figure 5.79 show the Schlieren photographs for the case with the primary injector only and the case with the primary and secondary injectors, respectively [84]. These photographs were used to draw an outline of the main flow features visible in the experiment such as the barrel shock, the bow shock and the separation-induced shock. Since the Schlieren photographs depict the first spatial derivative of the density, the outline of the flow features drawn from these photographs can be superimposed on the mapping of this parameter on the plane of symmetry produced by the numerical solution. It is important to remember that while the Schlieren picture is a two-dimensional representation of a three-dimensional flow, the CFD solution is a real two-dimensional slice through the flowfield. Therefore, some of the flow features visible in the Schlieren photographs that may appear to lie on the symmetry plane in actuality do not lie on the plane of symmetry but away from it and cannot be compared to the CFD mappings on the symmetry plane. The comparisons of the Schlieren photographs to the numerical solution are shown in Figure 5.80 (Primary jet only) and Figure 5.81 (Primary jet and Secondary jets). In both cases the CFD correctly predicted the location of the separation-induced shock (at least near the location where it impinges on the bow shock), the location and shape of the bow shock and barrel shocks. Note that in the case with the secondary jets the numerical solution correctly predicted the disappearance of the Mach disk from the top of the barrel shock and it

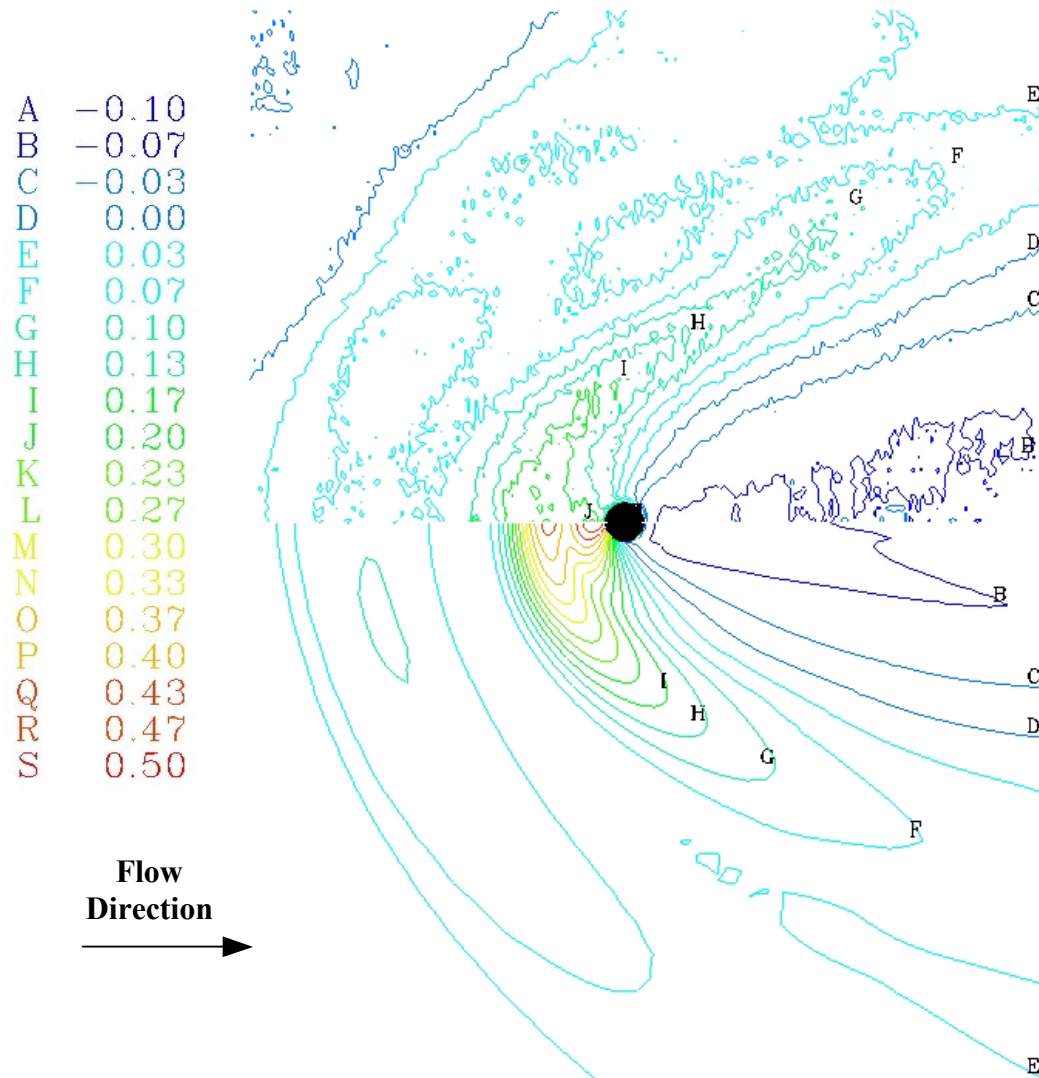


Figure 5.73. Comparison of the experimental (top) and numerical (bottom) C_p mappings on the surface of the flat plate for the case with only the primary jet switched on. Virginia Tech, Mach 4.0, $Pr=532$.

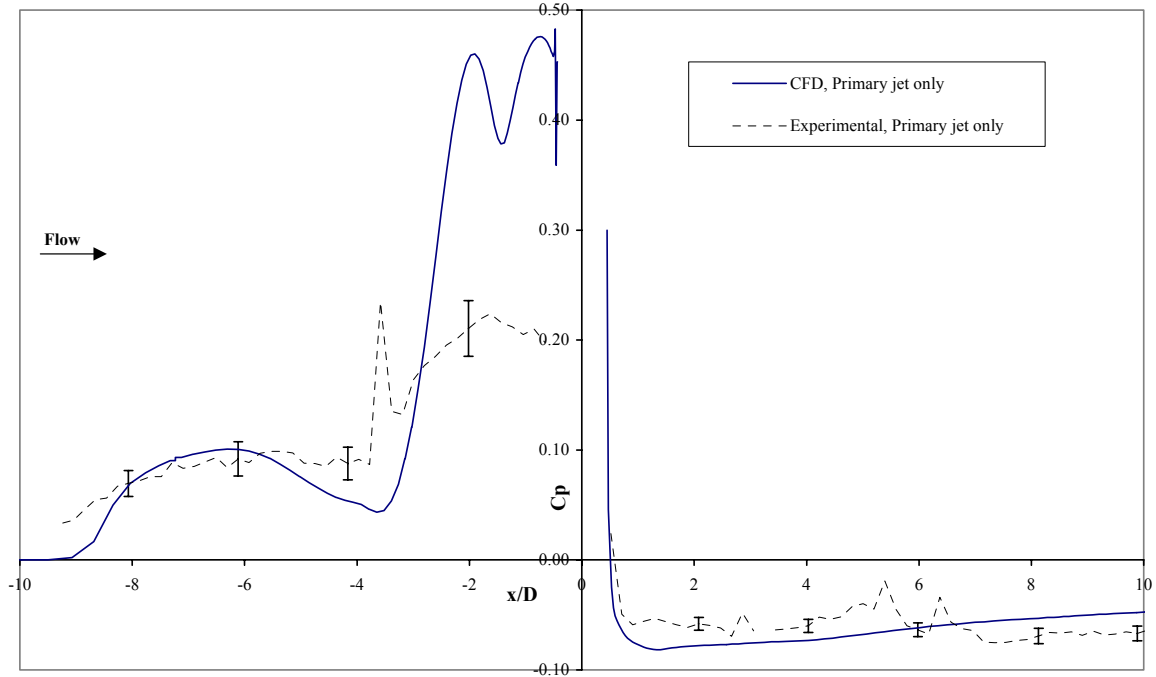


Figure 5.74. Pressure coefficient plots from the numerical solution (solid line) and from the experimental (dashed line with error bars) for the case with only the primary injector. Virginia Tech, Mach 4.0, $Pr=532$.

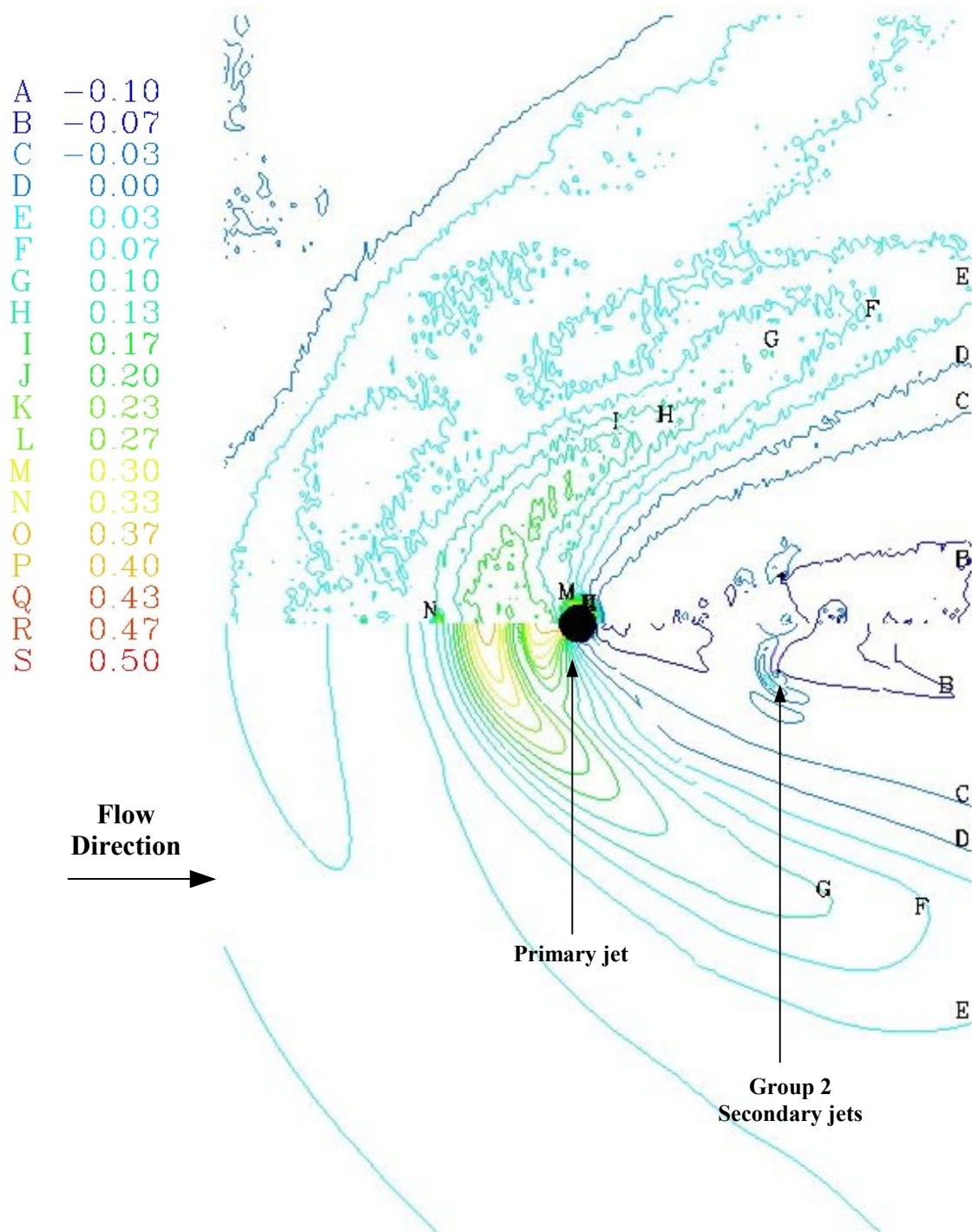


Figure 5.75. Comparison of the experimental (top) and numerical (bottom) C_p mappings on the surface of the flat plate for the case with both the primary and secondary jets activated. Virginia Tech, Mach 4.0, $Pr=532$.

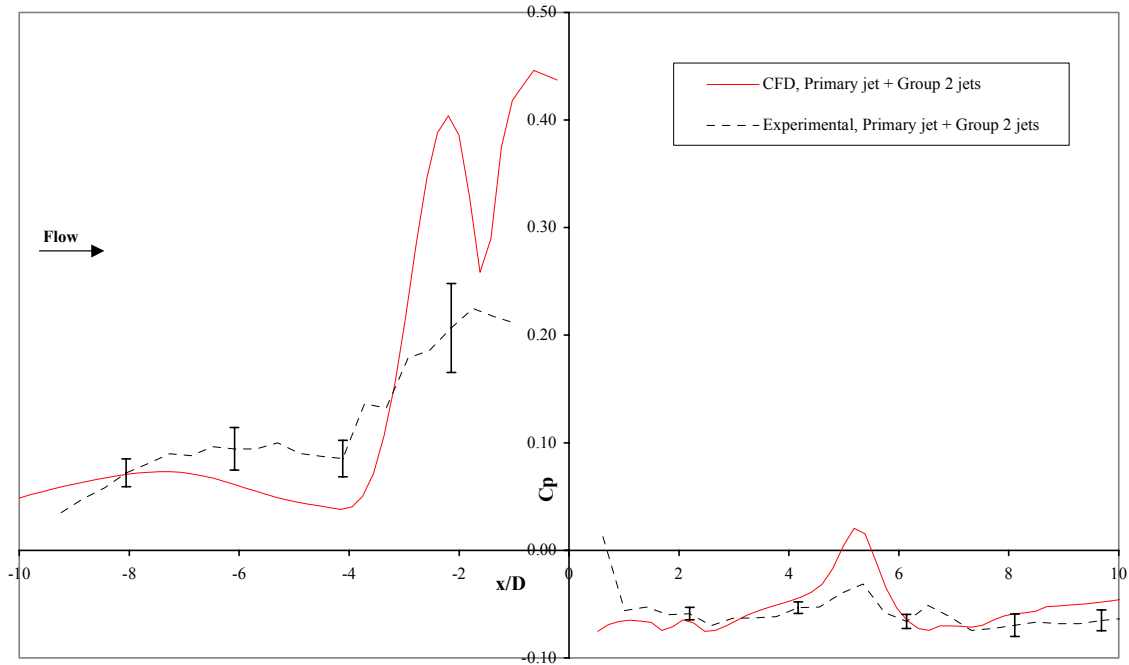


Figure 5.76. Pressure coefficient plots from the numerical solution (solid line) and from the experimental (dashed line with error bars) for the case with the primary and secondary injectors. Virginia Tech, Mach 4.0, $Pr=532$.

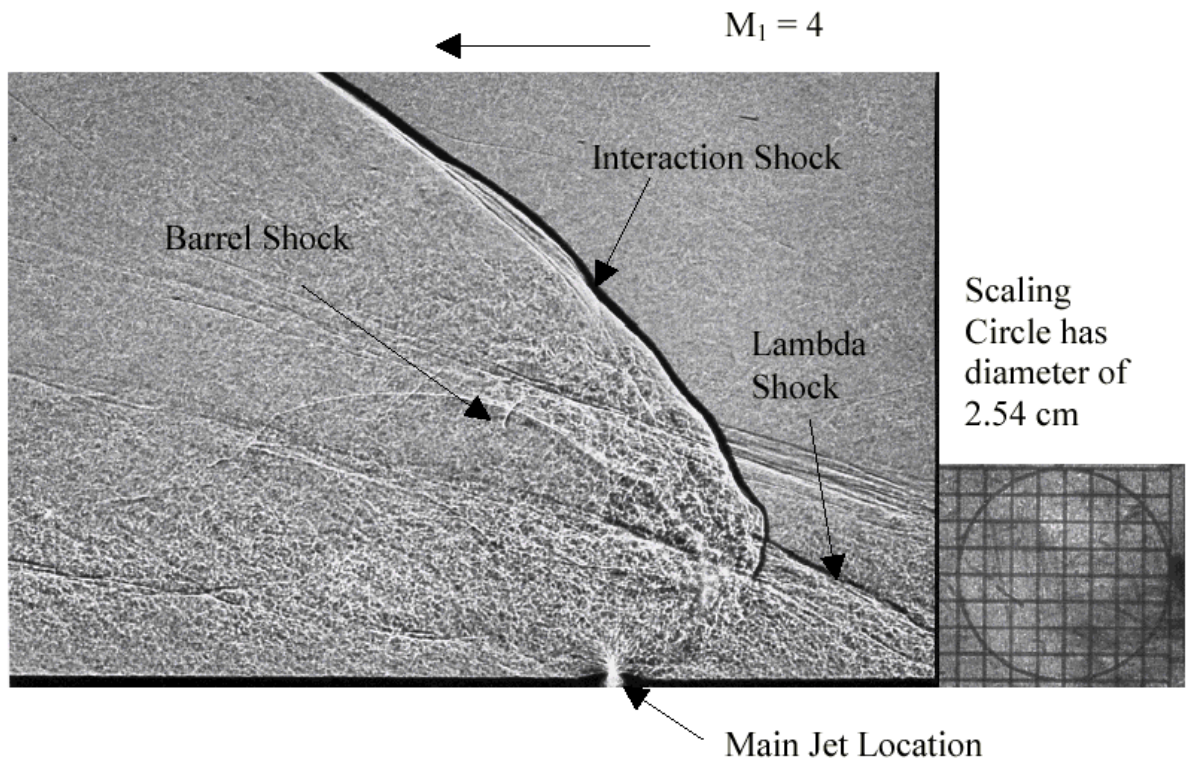


Figure 5.77. Shadowgraph of the flowfield generated by the primary jet only. Virginia Tech, Mach 4.0, $Pr=532$. From Wallis [84].

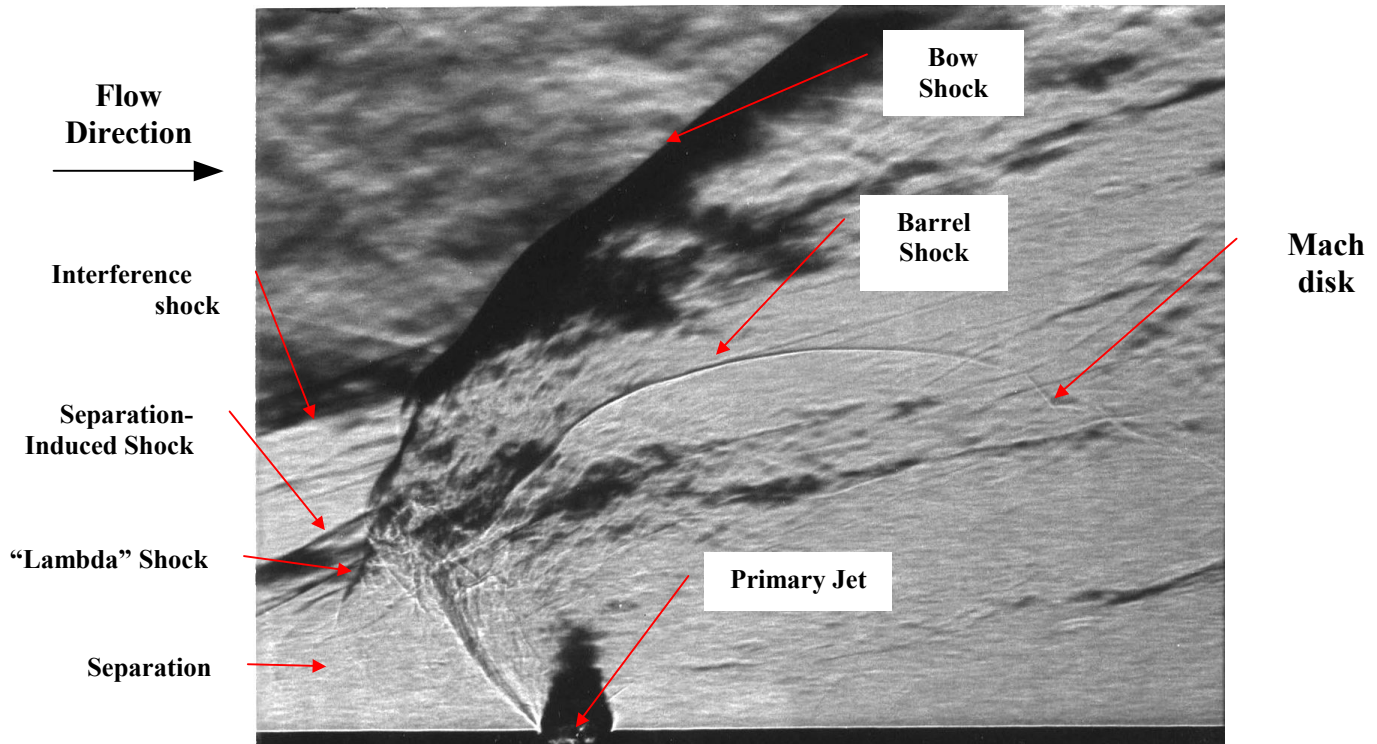


Figure 5.78. Schlieren photograph of the flowfield generated by the primary jet only. Virginia Tech, Mach 4.0, $Pr=532$. From Wallis [84]

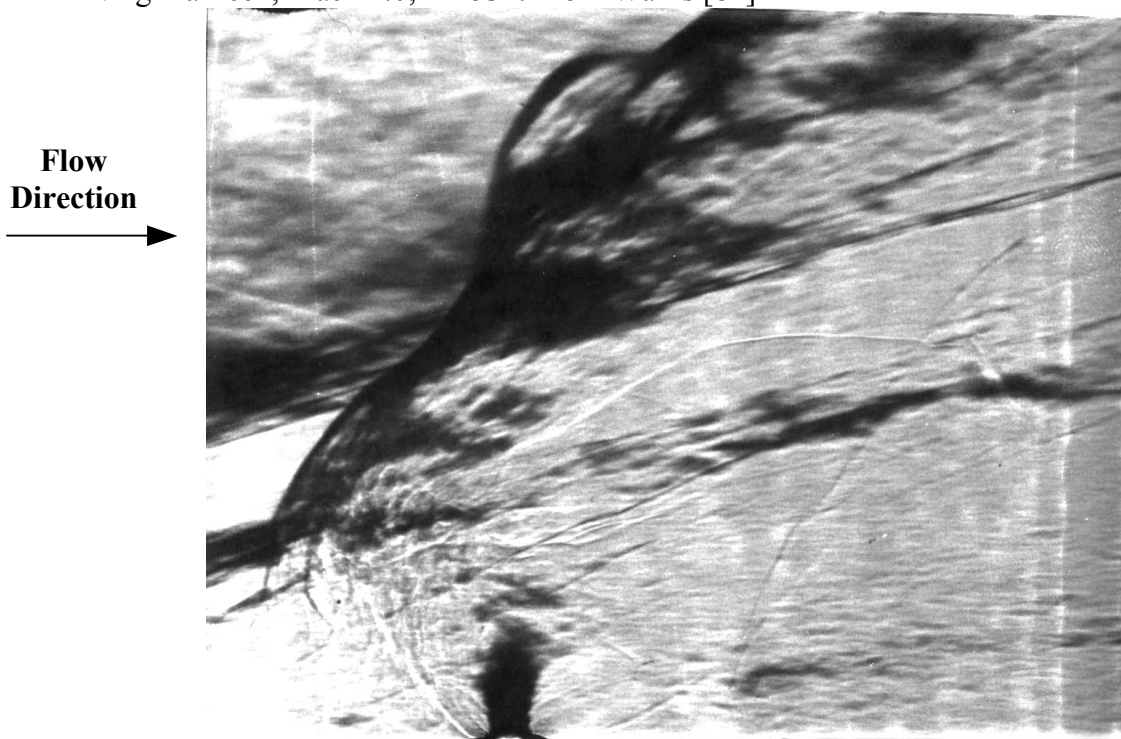


Figure 5.79. Schlieren photograph of the flowfield generated by the primary jet only. Virginia Tech, Mach 4.0, $Pr=532$. From Wallis [84].

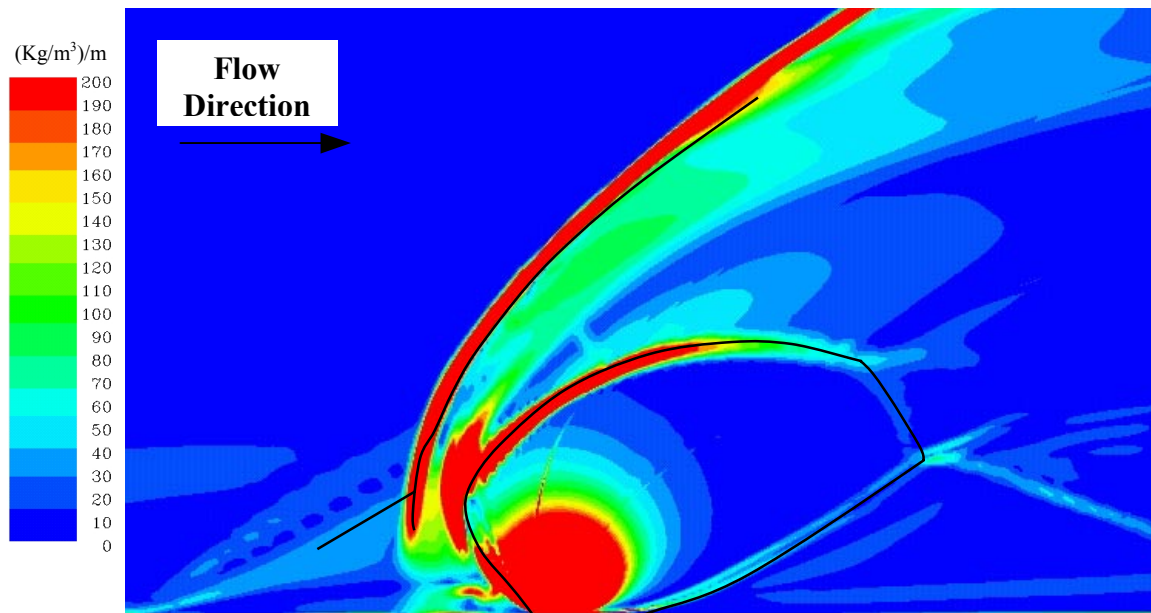


Figure 5.80. Visual comparison of the Schlieren picture with the flowfield features from the CFD solution on the plane of symmetry; the CFD contours represent the spatial derivative of the density. Primary injector only. (see Figure 5.68). Virginia Tech, Mach 4.0, Pr=532.

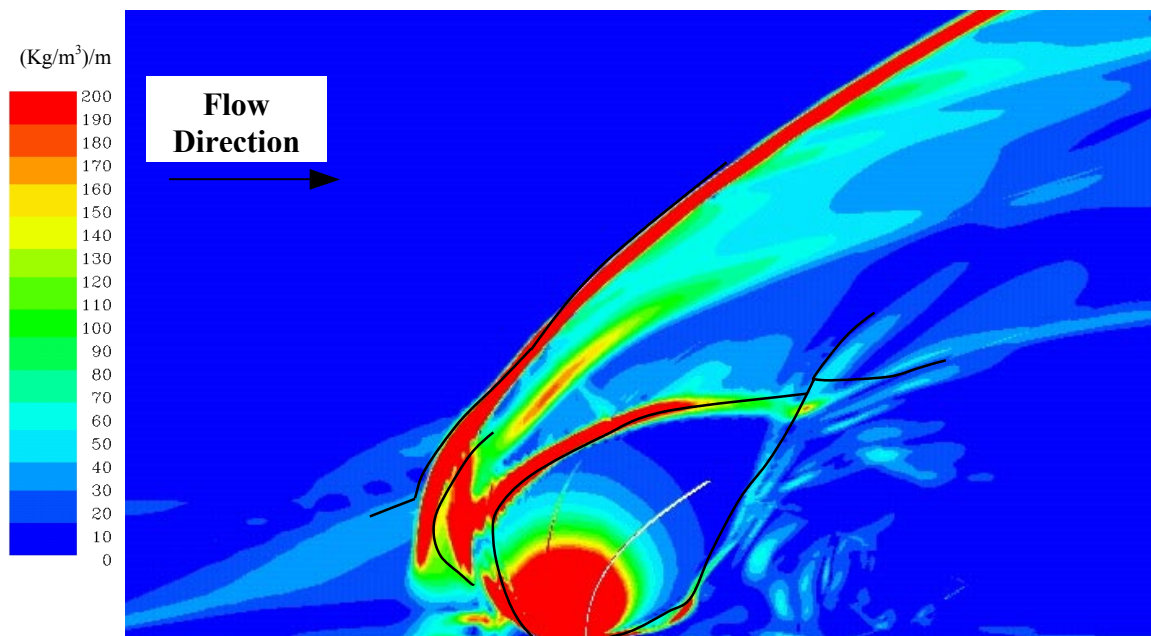


Figure 5.81. Visual comparison of the Schlieren picture with the flowfield from the CFD solution on the plane of symmetry for the case with the primary and secondary injectors. (see Figure 5.68). Virginia Tech, Mach 4.0, Pr=532.

Chapter 6

Analysis of the Jet Interaction Flowfield Using the Numerical Results.

The jet interaction flowfield produced by normal sonic injection into a supersonic crossflow is a very complicated flowfield where strong bow shocks can be found along with separated flows, expansion fans, reflected shocks, a Mach disk, viscous interaction and a complex system of trailing vortices. The analysis presented here is based on the numerical results obtained from the simulation of the Virginia Tech Mach 4.0 case with a jet pressure ratio of 532 and employing Wilcox's $k-\omega$ turbulence model. A general description of the jet interaction flowfield was given in the Introduction and some of its basic characteristics were schematically shown in Figure 1.1, Figure 1.3 and Figure 1.4. These sketches were based on the flowfield descriptions given in many of the experimental and numerical studies presented in the Literature Review section (Chapter 2) and also by the numerical calculations performed in this study.

A detailed view of the jet interaction flowfield is provided by the isometric view of the injection location of the Virginia Tech Mach 4.0 case (Figure 6.3). This snapshot shows the Mach contours mapped on the plane of symmetry, the C_p contours mapped on the surface of the flat plate and the vorticity magnitude contours mapped on the crossplane aft of the barrel shock. The paths of the trailing vortices are highlighted by streamlines that follow the vortex core. Following the flow along its path from right to left, as indicated in the figure by the arrow, the first flow conditions to be encountered are those produced by the undisturbed freestream (Region 1 of Figure 6.2 (a)). A boundary layer profile was used as an inlet boundary condition, since, as discussed in the previous section, the plate was mounted flush to the tunnel wall. The inlet boundary layer is clearly visible at the extreme left of Figure 6.2 (b) where the Mach number on the solid surface of the flat plate is zero, and it gradually increases to the freestream conditions as we move away from the solid wall. The boundary layer is allowed to develop along the flat plate surface until the separation location is reached. Separation (Region 2 in Figure 6.2 (a)) is caused by the shock-boundary layer interaction. The strong pressure gradient caused by the bow shock propagates upstream through the subsonic thickness of the turbulent boundary layer. As noted previously when comparing the Cubbison case with a laminar boundary layer to the Letko case with a turbulent boundary layer, the separation region is much shorter when the boundary layer is turbulent than when it is laminar. This is attributable to two main factors: the velocity profile is such that the thickness of the subsonic portion of the boundary layer is much thicker in a laminar than in a turbulent boundary layer thus allowing disturbances to propagate further upstream. Then, it is well known that turbulent boundary layers stay attached much longer than laminar boundary layers in positive pressure gradient regions [68]. Another difference between the two types of flows is that in a turbulent boundary layer separation the pressure peaks in the separation region are much higher than those in a laminar boundary layer.

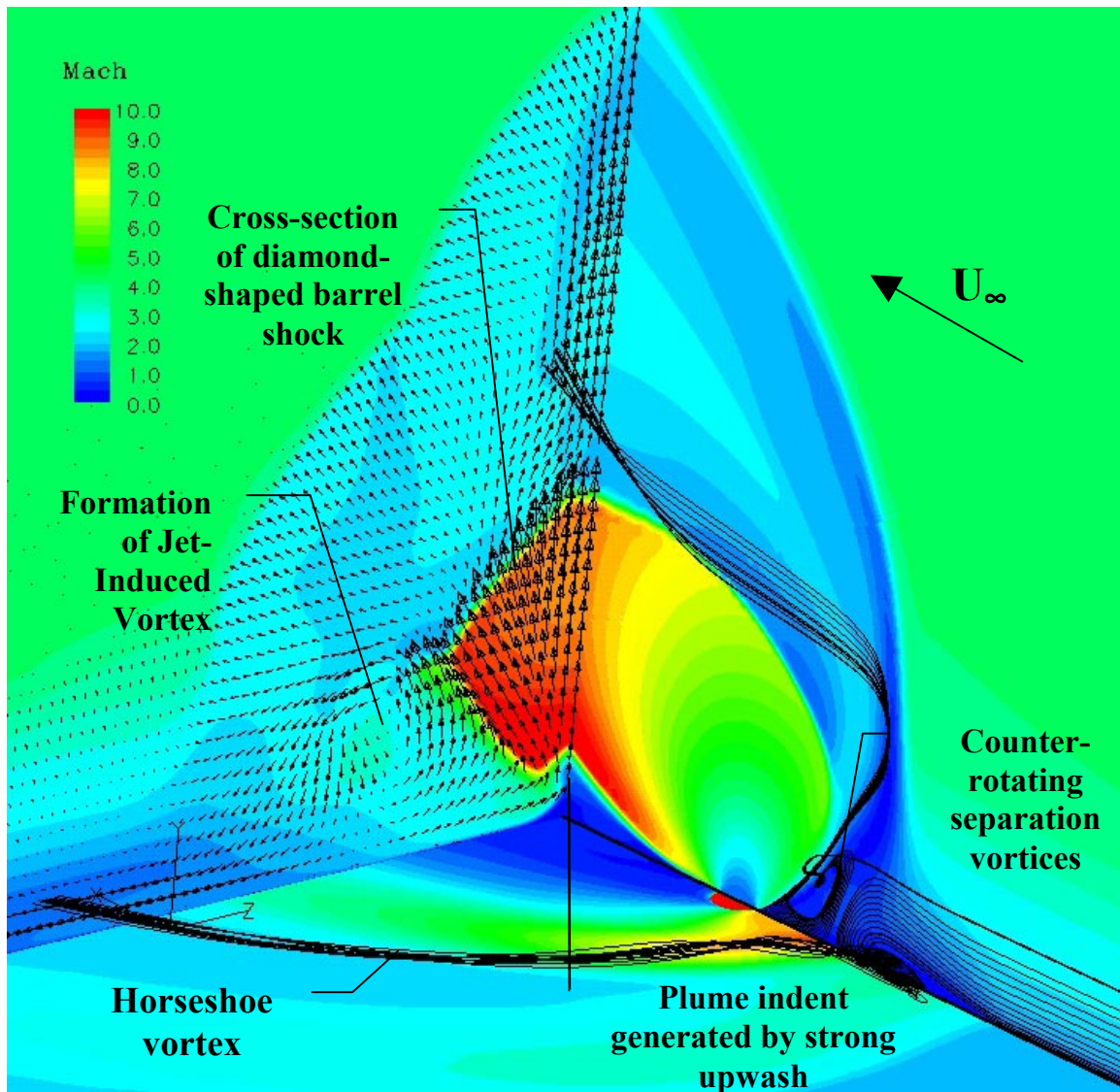
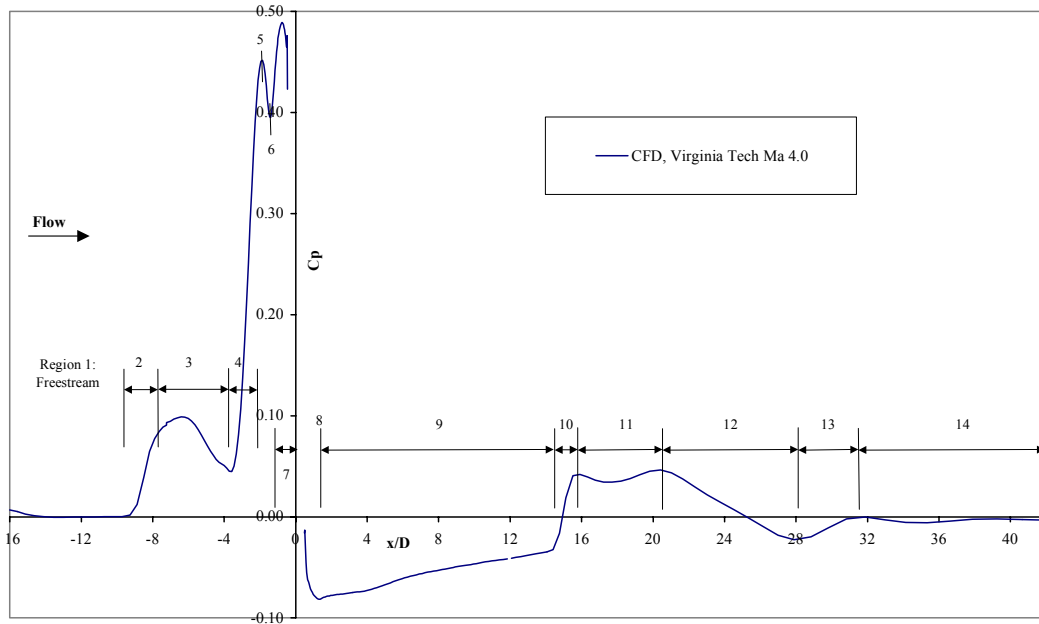
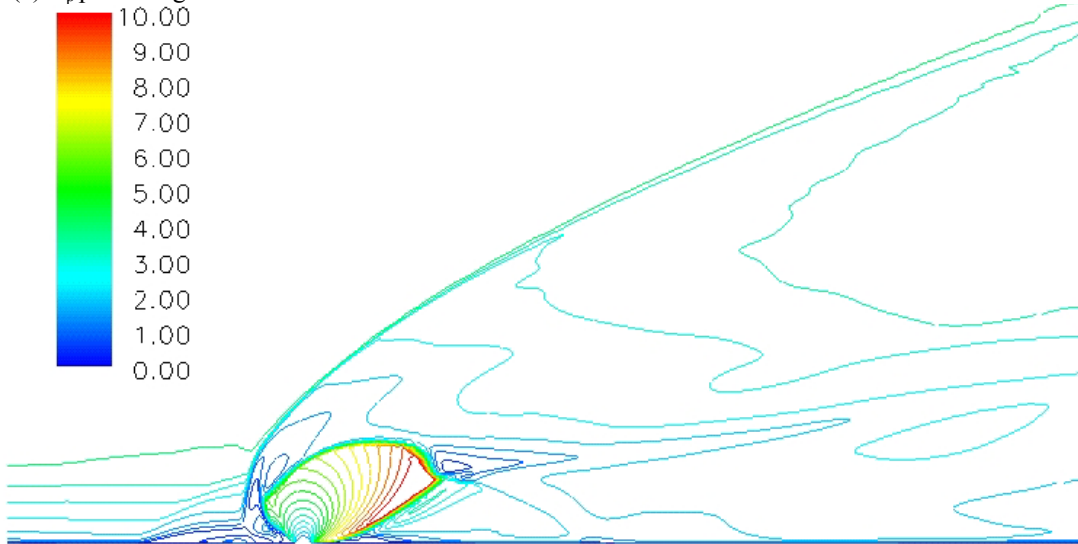


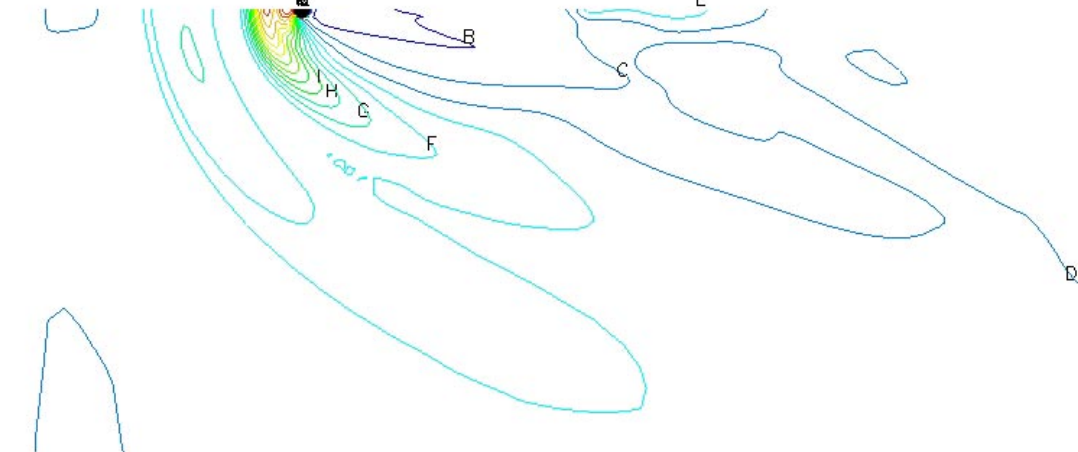
Figure 6.1. Isometric view of the oblique barrel shock with two groups of streamlines highlighting the flow out of the recirculation region ahead of the injector. The contours on the plane of symmetry are Mach number contours, the colors on the flat plate surface are C_p contours and the contours on the crossplane are Mach number contours with velocity vectors (y - z projection) superimposed. Virginia Tech, Mach 4.0, $Pr=532$, Primary jet only.



(a) C_p plot along the tunnel centerline



(b) Mach number contours on the plane of symmetry.



(c) C_p contours on the flat plate surface.

Figure 6.2. Analysis of the jet interaction flowfield produced by the Virginia Tech, Mach 4.0 case with only the primary jet switched on. ($Pr=532$).

Going back to Figure 6.2 (a), the C_p plot along the centerline shows the separation as a region where the pressure increases steeply (Region 2), it plateaus and then decreases slightly (Region 3). The C_p contours of Figure 6.2 (c) show the separation as a well-defined lobe near the plane of symmetry (corresponding to Regions 2 and 3 of Figure 6.2 (a)) that extends downstream and away from the tunnel centerline. The Mach contours of Figure 6.2 (b) also indicate the presence of a separation-induced shock. This shock is not very strong and it impinges further downstream on the bow shock. The boundary between Region 3 and Region 4, where the pressure along the centerline decreases at an x/d of about -4.0 is where the core of the horseshoe vortex forms and is shed sideways away from the symmetry plane as seen in Figure 6.1. The core of the horseshoe vortex appears on the plane of symmetry as one of a pair of counter-rotating vortices clearly visible through the velocity vectors of Figure 6.4 or the streamlines of Figure 6.1. The couple of counter-rotating vortices is divided by an attachment line (Region 5 in Figure 6.2 (a)), indicated as a peak in the C_p plot. On the two sides of the attachment line, the vortices rotate in opposite directions. The rotation of the second vortex is dictated by the shear layer formed at the interface between the barrel shock and the fluid in the separation; the freestream fluid moves in the same direction as the high-momentum expanding injectant it is in contact with. Note the symmetry at least in the trends of the C_p plot along the centerline about Region 5 in Figure 6.2 (a). Both upstream (Region 4) and downstream (Region 6) of Region 5 the pressure drops rapidly and then it recovers to some level in Region 3 and Region 7. The pressure drops corresponds to the acceleration of the fluid moving away from the attachment line and that forms the core of the two counter-rotating vortices. The pressure rise corresponds to the fluid moving away from the attachment line being slowed down and turned around by either the boundary layer fluid ahead of Region 5 or by the barrel shock aft of Region 5.

It is more complicated to trace the path of the second of the two counter-rotating vortices, since the fluid is dispersed in several directions. The primary direction follows the leading edge of the barrel shock away from the solid surface and it is clearly visible in Figure 6.1. As this vortex trails downstream, it keeps moving away from the solid surface and, to a lesser degree, away from the plane of symmetry as it is visible in Figure 6.9 and Figure 6.10 for an $x/d > 8.0$. The rest of the fluid of the second counter-rotating vortex is convected downstream sideways, close to the surface of the flat plate and around the footprint of the barrel shock to form the Surface Trailing Vortex.

As shown by Figure 6.3, the Surface Trailing Vortex in order to be convected around the footprint of the barrel shock moves away from the symmetry plane as the boundary of the barrel shock expands. Once the axis of the injector has been passed at $x/d = 0.0$ and the barrel shock detaches from the surface of the flat plate, the vortex moves back towards the centerline and into the low-pressure region behind the injector. Due to its closeness to the solid surface, the Trailing Vortex entrains large quantities of boundary layer fluid as it trails downstream, as it is evident from Figure 6.7. Chenault and Beran [14] in their numerical analysis of the two-dimensional jet interaction flowfield reported a tertiary vortex in the separation region, rotating counterclockwise and located between the core of the horseshoe vortex and the flat plate. However, in the present study no tertiary vortex was noticed in the separation region. This fact can be due to the fact that a two-dimensional study used extremely refined grids in this region that can capture the

existence of this tertiary vortex. However, it may also be that the tertiary vortex is a characteristic peculiar to only the two-dimensional jet interaction flowfield. In fact, also Chenault, et al. [15] during a three-dimensional numerical simulation of the jet interaction flowfield did not report the existence of this vortex.

Figure 6.2 (b) puts in evidence the “ λ -shaped” shock as it is often referred in the literature. This shock is just ahead of the barrel shock and, especially in shadowgraphs and Schlieren photographs, it appears as the Greek letter “ λ ”. In reality the “ λ -shaped” shock is the merging of the separation-induced shock and the lower part of the bow shock. The Mach number contours along the plane of symmetry show that in evidence that the two shocks actually never merge even though shadowgraphs and Schlieren pictures that “collapse” a three-dimensional flowfield in a two-dimensional plane show them as touching.

The pressure peaks in Regions 6 and 7 of Figure 6.2 (a) are also visible in the pressure mapping of Figure 6.2 (c) as the two small lobes with the highest C_p just in front of the injector. The two lobes merge together as they move away from the centerline and trail downstream to form the footprint of the bow shock on the flat plate surface. The bow shock forms in front of the barrel shock because of the obstruction to the flow created by the latter. A normal shock forms the lower part of the bow shock as shown by Figure 6.3 and in particular by the velocity vectors of Figure 6.4 that, as in the case of a normal shock, do not change direction when crossing the shock. When the bow shock moves away from the plane of symmetry and from the flat plate surface it becomes a curved shock as it bends around the jet plume. This shock pattern is very similar to that generated by a blunt body in a three-dimensional flow. This similitude has been recognized since the early experimental works in jet interaction flowfields and much analytical work has been done to correlate the two flowfields [72] [70] with different degrees of success.

Some of the typical flow structures of the under-expanded jet exhausting in a quiescent medium [45] [95] [96] as seen in Figure 6.5 are visible in the flow snapshot of the jet interaction flowfield shown in Figure 6.6. The main flow feature that the two flowfields have in common is the barrel shock. The barrel shock has the general resemblance of a typical under-expanded jet exhausting in a quiescent medium as shown in Figure 6.5. However, because of the presence of a crossflow in the jet interaction flowfield the back-pressure is not constant around the expanding jet, being much higher on the windward side than on the leeward side of the plume. This non-uniformity of the back-pressure causes the plume to trail downstream and to lose its symmetry. The volume inside the barrel shock is a large expansion fan with its boundaries defined by a recompression shock that merges at the top of the plume into a Mach disk as shown in Figure 6.2 (b) and, more in detail, in Figure 6.6. Because of the mixing with the crossflow and because of the strong bow shock it is difficult to identify the sonic line and the outer shear layer of the jet plume. Furthermore, the windward side of the barrel shock seems to have less resemblance to the under-expanded jet flowfield than the leeward, side, mainly because of the presence of the bow shock. The leeward side of the plume is sheltered from the high pressure gradients of the windward side by the barrel shock itself, therefore more features of the under-expanded jet flowfield can be recognized in this region. However,

the presence of a thick boundary layer and the existence of strong vortical motions coming from the separation region hinders the development of the marked features typical of the under-expanded jet flowfield. For a short distance, the leeward side of the barrel shock is attached to the solid surface of the flat plate. As the barrel shock detaches from the surface (Region 8 of Figure 6.2 (a)) and it leaves a large volume of space to be filled by the mixed freestream and injectant fluids, a large low pressure region is formed (Region 9). The reflected shock extending from the triple point and impinging on the surface at $x/d=15.0$ can be clearly identified in Figure 6.6. The adverse pressure gradient produced by the shock on the surface of the flat plate causes the boundary layer to thicken rapidly across the shock. The location at which the reflected shock impinges on the flat plate is also clearly identifiable in the C_p plot along the tunnel centerline of Figure 6.2 (a) as Region 10.

Past Region 10 of Figure 6.2 (a), the boundary layer grows undisturbed (Region 11) until the Surface Trailing Vortices come in contact with the system of the three Trailing Vortices. The latter lift the Surface Trailing Vortices away from the solid surface (see Figure 6.9 and Figure 6.10 at an x/d of 20.0 and 25.0) thus creating a short region of low pressure (Region 12 of Figure 6.2 (a)). However, the pressure recovers quickly to the freestream value (Region 13) and continues undisturbed downstream (Region 14). The Mach disk at the apex of the barrel shock slows down the supersonic flow inside the plume to a subsonic Mach number. The subsonic stream of fluid forms a slip surface with the supersonic flow around it. Further downstream, the two streams of subsonic and supersonic flows mix together forming a turbulent uniform stream.

The mixing of the various streams of fluid is enhanced by the action of four distinct pairs of counter-rotating trailing vortices (Figure 6.3). The cores of the four vortices are highlighted in Figure 6.7 through the plotting of the vorticity magnitude on a crossplane 15 jet diameters downstream of the injection location. The Surface Trailing Vortex has been discussed earlier, and it was shown that it is generated by the second counter-rotating vortex found in the separation region in front of the injection location. It was also shown that as it trails downstream it entrains large quantities of boundary layer fluid being close to the flat plate surface. Almost all of the fluid contained in this vortex is from the freestream. The Trailing Vortex 1 and Trailing Vortex 3 are a couple of counter-rotating vortices formed as the injectant is compressed through the Mach disk (see Figure 6.9 and Figure 6.10). Most of the fluid contained in these two vortices is injectant fluid, but some freestream fluid is entrained from the shear layer existing at the interface between the barrel shock and the surrounding fluid. Relatively little mixing with the freestream occurs until a location 30 diameters downstream of the injection location. The last vortex shown in Figure 6.7 is Trailing Vortex 2. This vortex forms along the barrel shock axis at the sharp angle formed by the inner reflection line of the barrel shock (Figure 6.8). Figure 6.8 also shows the mechanism that forms the Surface Trailing Vortices. When the barrel shock detaches from the solid surface of the flat plate it leaves a large volume to be filled by the boundary layer fluid. The interaction of the boundary layer fluid being drawn towards the centerline and the shear layer at the interface between the barrel shock and the surrounding gas creates the rotational motion of the vortex that is confined in the small space between the plate surface and the bottom side of the barrel shock. As shown in Figure 6.9 and, in more detail in Figure 6.10 the three upper vortices

(Trailing Vortex 1, Trailing Vortex 2 and Trailing Vortex 3) rotate with respect to each other around a common longitudinal axis (Figure 6.9 and Figure 6.10, $x/d=20.0$). As they trail downstream they merge into a single vortex (Figure 6.10, $x/d=30.0$) that is the main mechanism driving the mixing of the freestream fluid with the injectant. Note that the horseshoe vortex and the Trailing Upper Vortices continue to be convected downstream in their respective locations without merging with other flow structures (Figure 6.9 and Figure 6.10, $x/d=35.0$ and 40.0).

A good insight of the mechanisms that create the pressure field on the flat plate can be obtained by a simulated oil surface flow visualization as shown in Figure 6.12. In this figure the streamlines are drawn just above the surface and highlight the projection of the two-dimensional velocity field just above the surface. It is important to bear in mind that, while this plot is a two-dimensional projection of the streamlines, in reality the flow is three-dimensional and there exist velocity components that are moving particles into (or out of) the direction of the page. The major flow structures such as the bow shock, the separation and the barrel shock are clearly visible as thick lines. The freestream appears undisturbed until the bow shock. Behind the bow shock the freestream takes on a lateral velocity component. In the separation region the fluid is recirculated and flows in the opposite direction as the freestream. From the separation region the horseshoe vortices are shed, as highlighted by the dashed line. The core of these vortices can be easily traced by following the low-pressure lobe on the solid surface. The presence of the barrel shock creates a region of extremely high pressure in front of the injector. Immediately aft of the injector there is a small region where the plume is attached to the solid surface. Once the plume detached from the solid surface a low-pressure region forms and the Surface Trailing Vortices can be found forming in this region. The footprint of the barrel is clearly visible on the surface as well as the attachment lines of the Surface Trailing Vortices. The plume end is clearly visible as well as the disturbance caused by the Mach disk. Further downstream the reflected shock from the Mach disk (see above) impinges on the solid surface. The local increase in pressure along the centerline (see also the C_p plot of Figure 6.2 (a)) causes the Surface Trailing Vortices to move away from the symmetry plane. Once past this location, the Surface Trailing Vortices return to move parallel to the symmetry plane and, apart from some localized low pressure areas, the pressure recovers to the freestream value and the streamlines tend to align themselves with the freestream.

Figure 6.11 shows a top-view of the flowfield for planar planes at different heights above the solid surface. The mappings represent the vorticity magnitude (left half) and the Mach number contours (right half). The first mapping at a y/d of 0.1 shows the same flow features as those described above for Figure 6.12. As we move further away from the solid surface the cross-section of the barrel shock becomes clearly visible. At a y/d of 0.3, there is a large wake of high-vorticity fluid aft of the barrel shock. The vorticity is convected downstream from the shear surface surrounding the barrel. Part of the vorticity is also formed by the detachment of the barrel shock from the solid surface. Note that further downstream the high-vorticity fluid is disrupted by the presence of the reflected shock. The effect of the reflected shock (Figure 6.11, $y/d = 0.3, 0.4$ and 0.6) is to push the high-vorticity fluid away from the plane of symmetry and to mix it with the surrounding freestream fluid. Also, the reflected shock increases the thickness of the boundary layer at

the location where it impinges on the solid surface. This effect is visible in the isolated peak of high-vorticity fluid located downstream of the barrel shock (see Figure 6.11, $y/d = 0.8$ and 1.0). As we move further away from the surface of the flat plate the barrel shock enlarges and it reaches its maximum cross-sectional size around a y/d of 3.0 . Note that the mapping at a y/d of 3.0 shows the formation of the Trailing Vortex 2, its core being denoted by the fluid with a high vorticity intensity that trails laterally on the outside of the barrel shock. In the same picture, it is also shown the formation of the Trailing Vortex 3 at the back end of the shock, where the Mach disk is located. Note that the cross sectional area of the barrel shock shows that the Mach disk is not planar but slightly concave. Moving further away from the solid surface, the barrel shock decreases in size until it disappears (Figure 6.11, $y/d = 6.0$) and only the upper section of the bow shock is visible. As expected and as visible in the mappings on the plane of symmetry (Figure 6.6), the bow shock curves in the same direction as the freestream as it moves away from the flat plate (Figure 6.11, compare snapshots at $y/d = 7.0$ and 15.0).

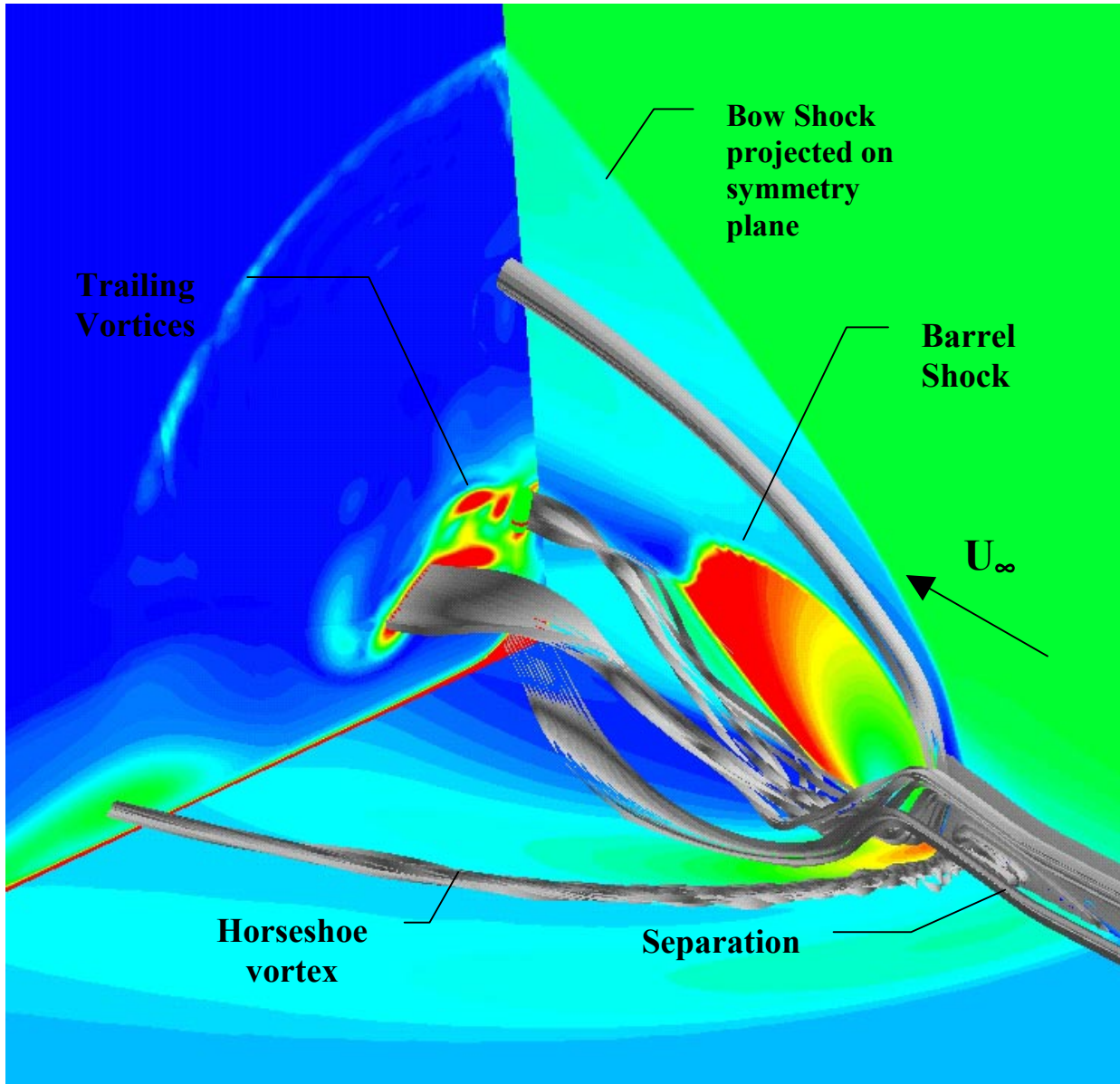


Figure 6.3. Isometric view of the oblique barrel shock with the groups of streamlines identifying the main rotational motion. The contours on the plane of symmetry are Mach number contours, the contours on the flat plate surface are C_p contours and the contours on the crossplane are vorticity magnitude contours. Virginia Tech, Mach 4.0, $Pr=532$, Primary jet only.

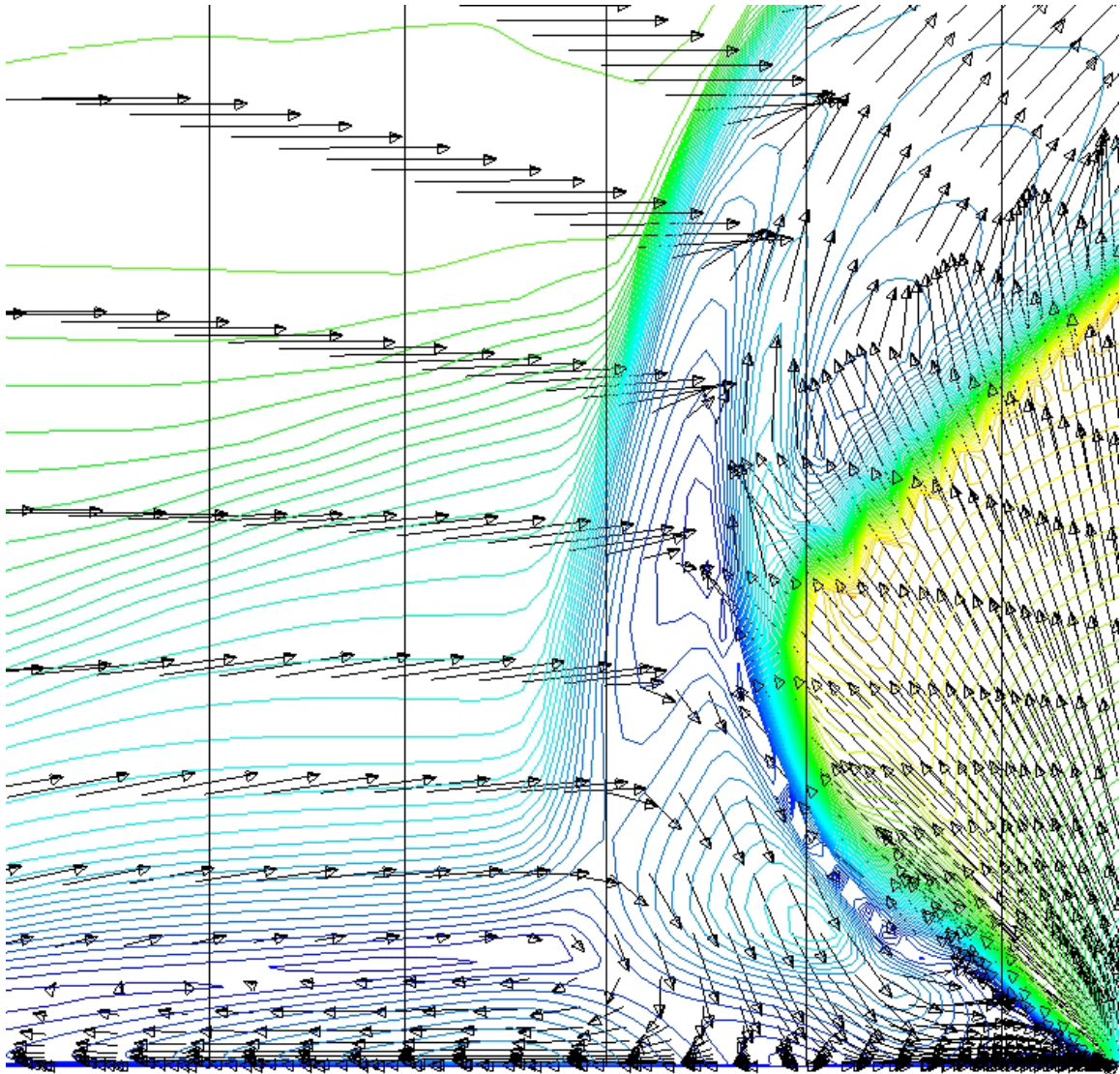


Figure 6.4. Velocity vectors and Mach number contours on the plane of symmetry in the separation region just ahead of the injector. Virginia Tech, Mach 4.0, $Pr=532$, Primary jet only.

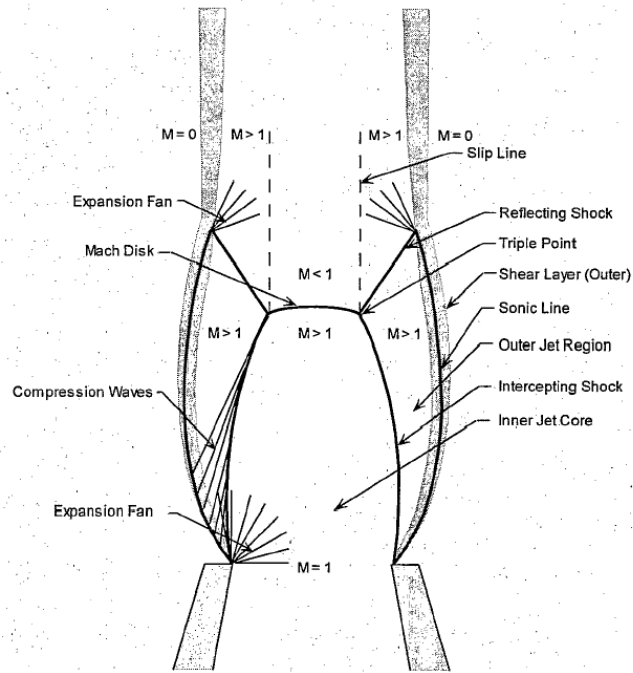


Figure 6.5. Schematic of the flowfield generated by an under-expanded sonic jet exhausting in a quiescent medium [95].

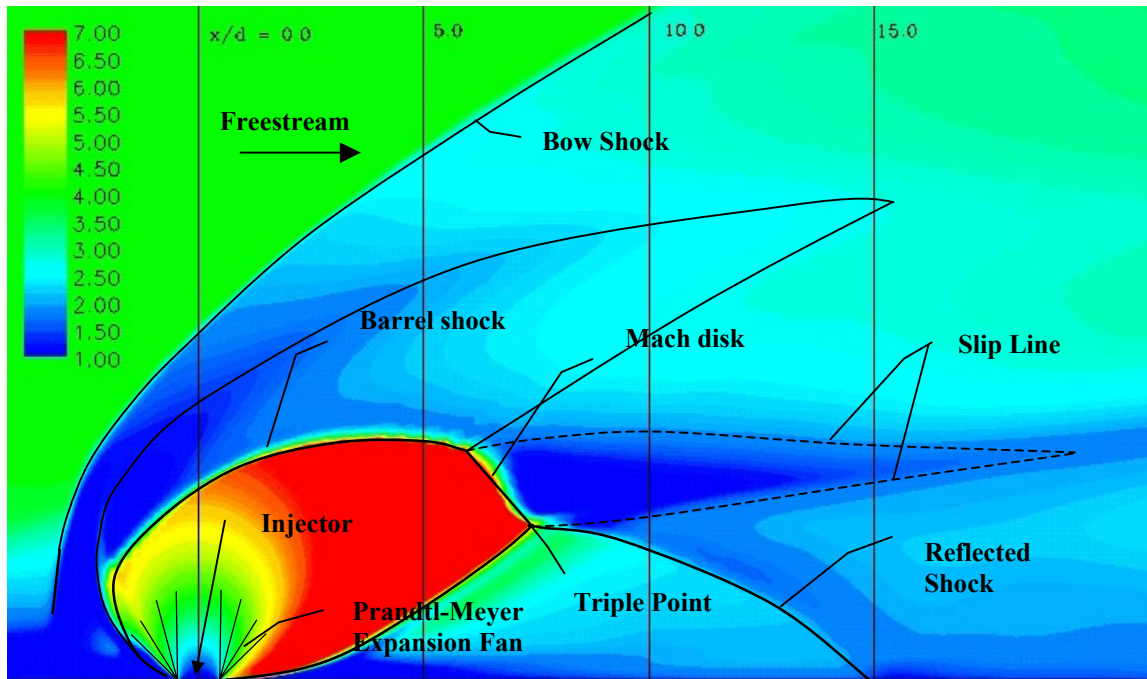


Figure 6.6. Crossplane mappings of vorticity magnitude (left) and Mach number (right) with velocity vectors superimposed at a location of $x/d=15.00$ downstream of the injector. Virginia Tech, Mach 4.0, $Pr=532$. ($y/d: 0-10.0$, $z/d: 0-5.0$).

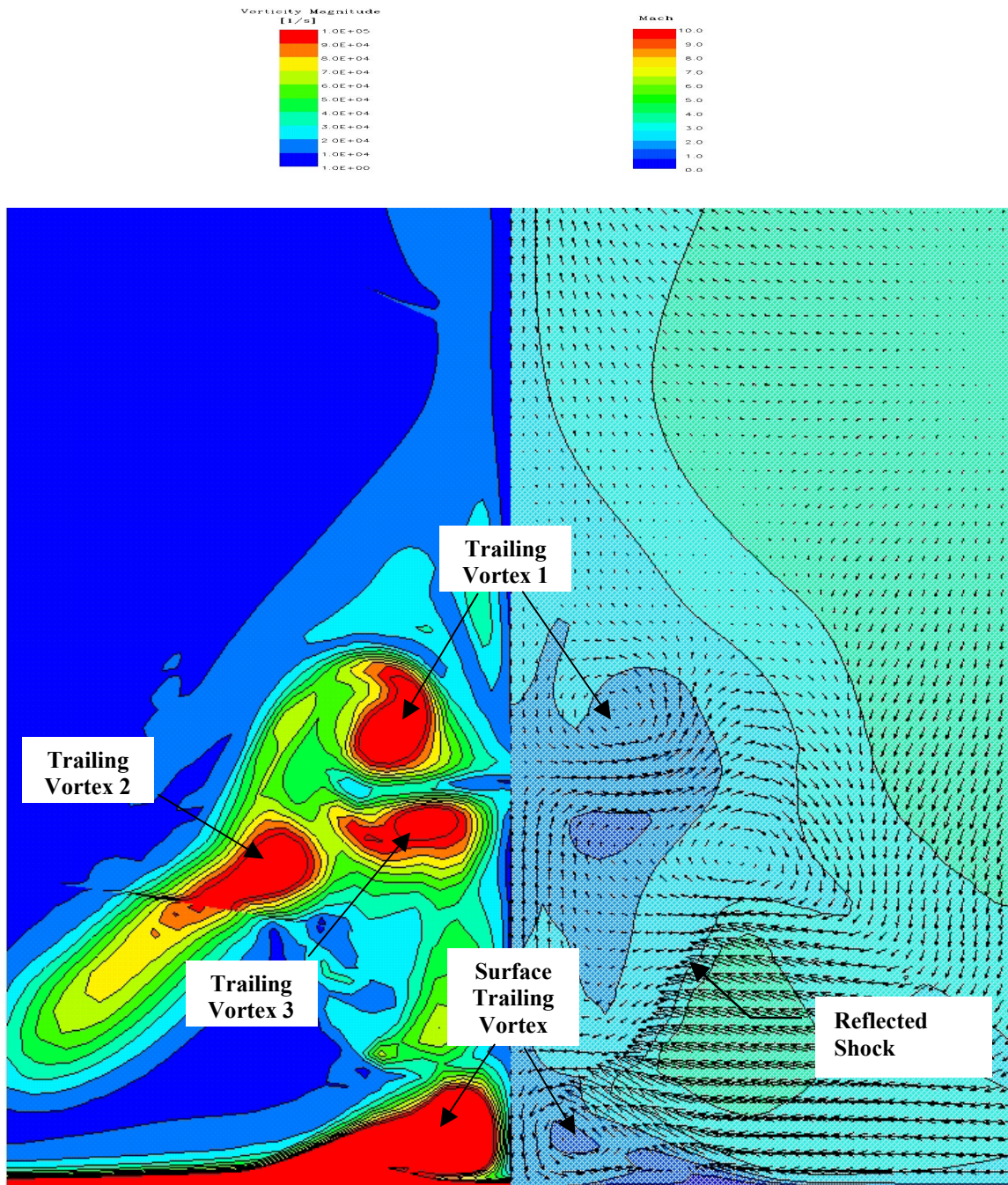


Figure 6.7. Crossplane mappings of vorticity magnitude (left) and Mach number (right) with velocity vectors superimposed at a location of $x/d=15.00$ downstream of the injector. Virginia Tech, Mach 4.0, $Pr=532$. (y/d : 0-10.0, z/d : 0-5.0).

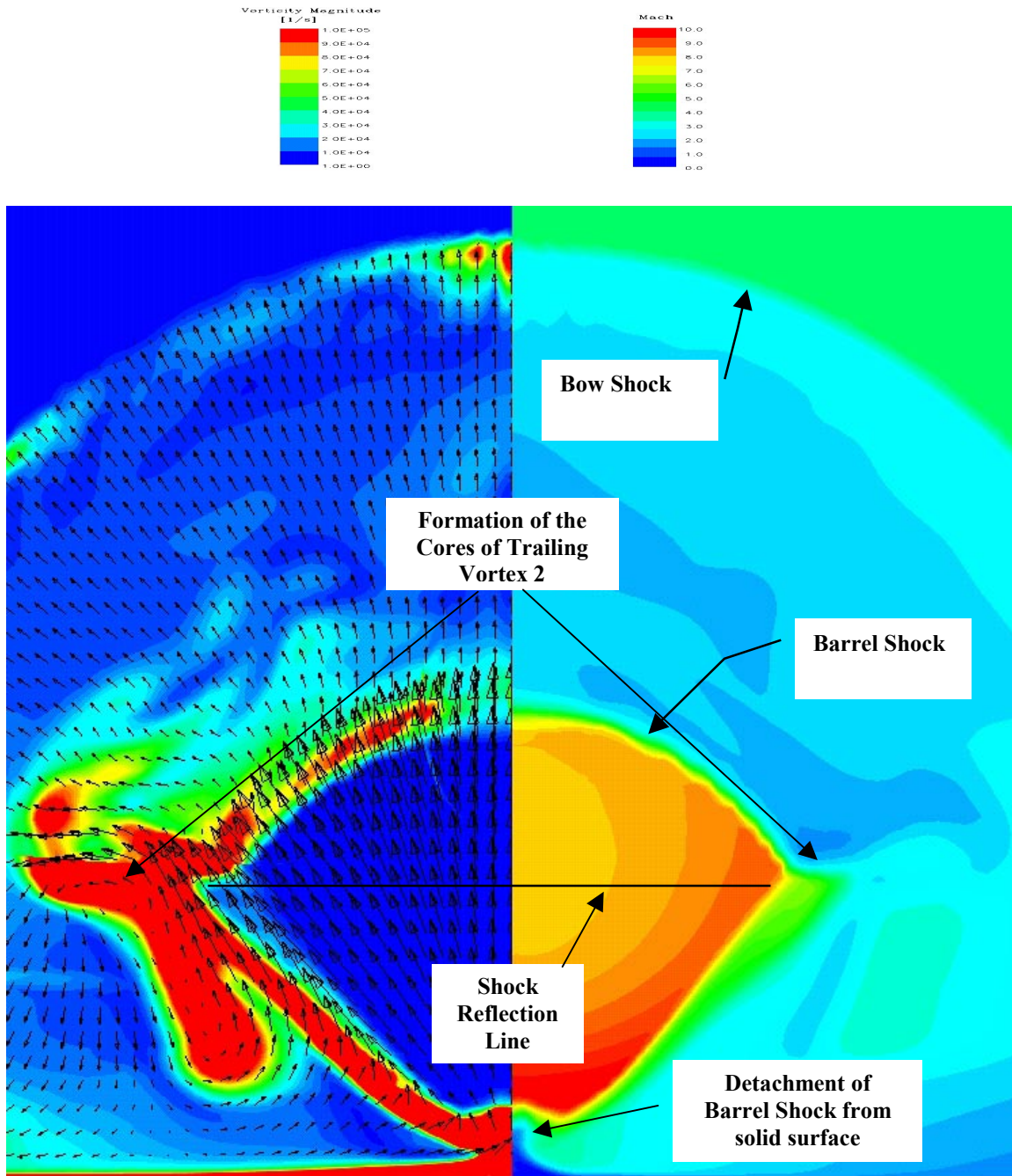


Figure 6.8. Crossplane mappings of vorticity magnitude (left) with projected velocity vectors and Mach number (right) with velocity vectors superimposed at a location of $x/d=3.5$ downstream of the injector. Virginia Tech, Mach 4.0, $Pr=532$.

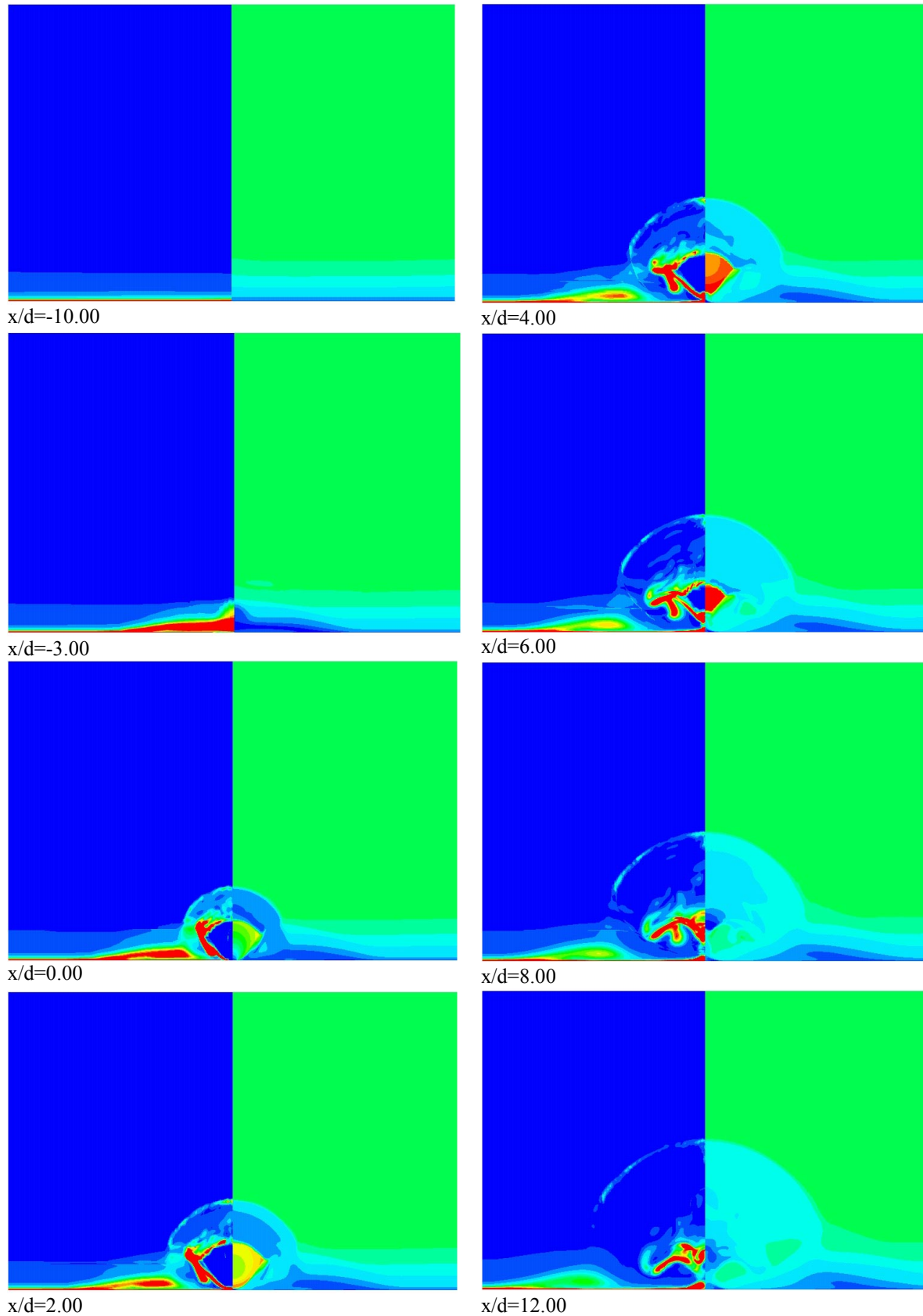


Figure 6.9. Crossplane mappings of vorticity magnitude (left) and Mach number (right) at different x/D . Virginia Tech, Mach 4.0, $Pr=532$. (y/d : 0-32.0, z/d : 0-24.0).

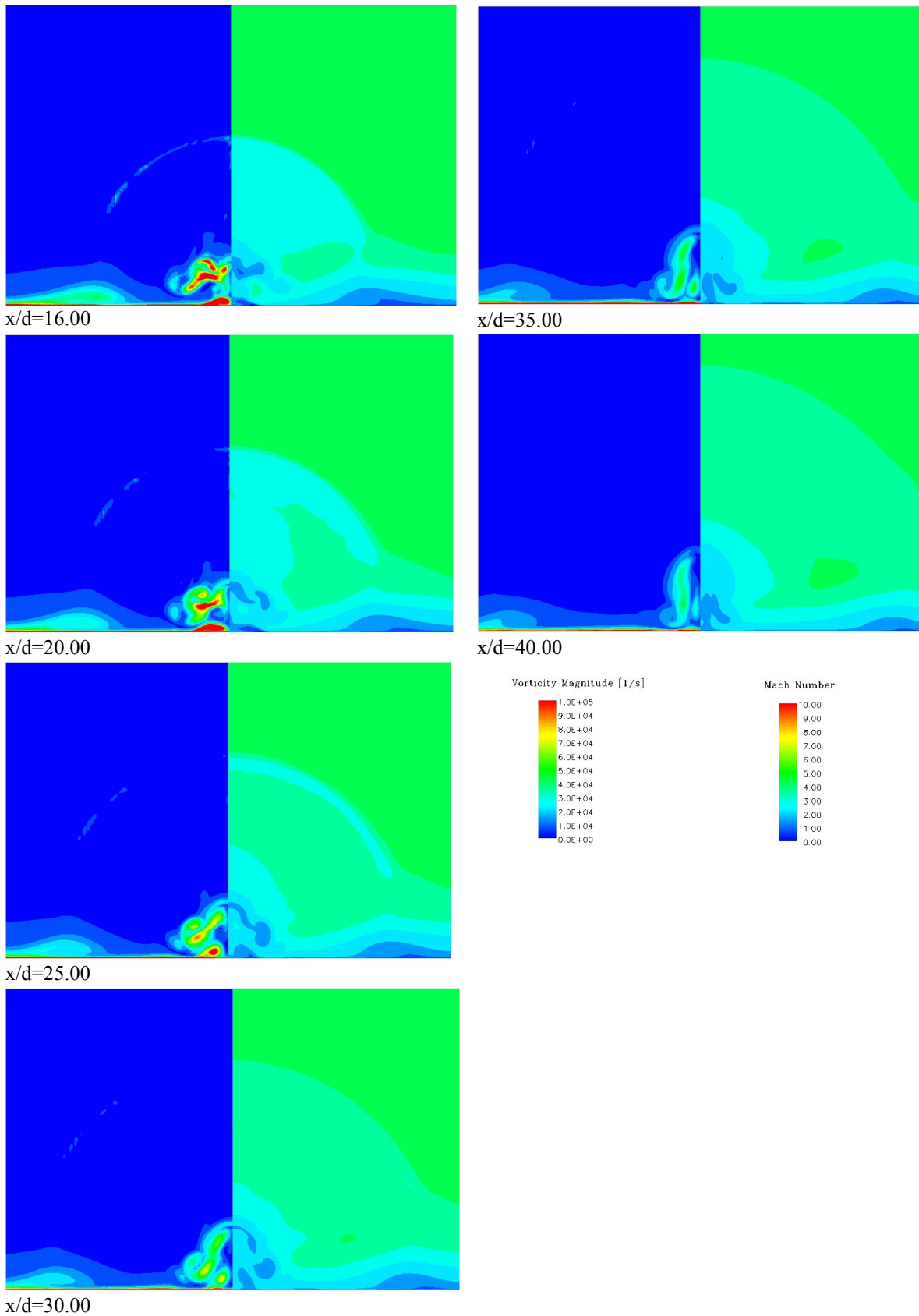


Figure 6.9 (Continued).

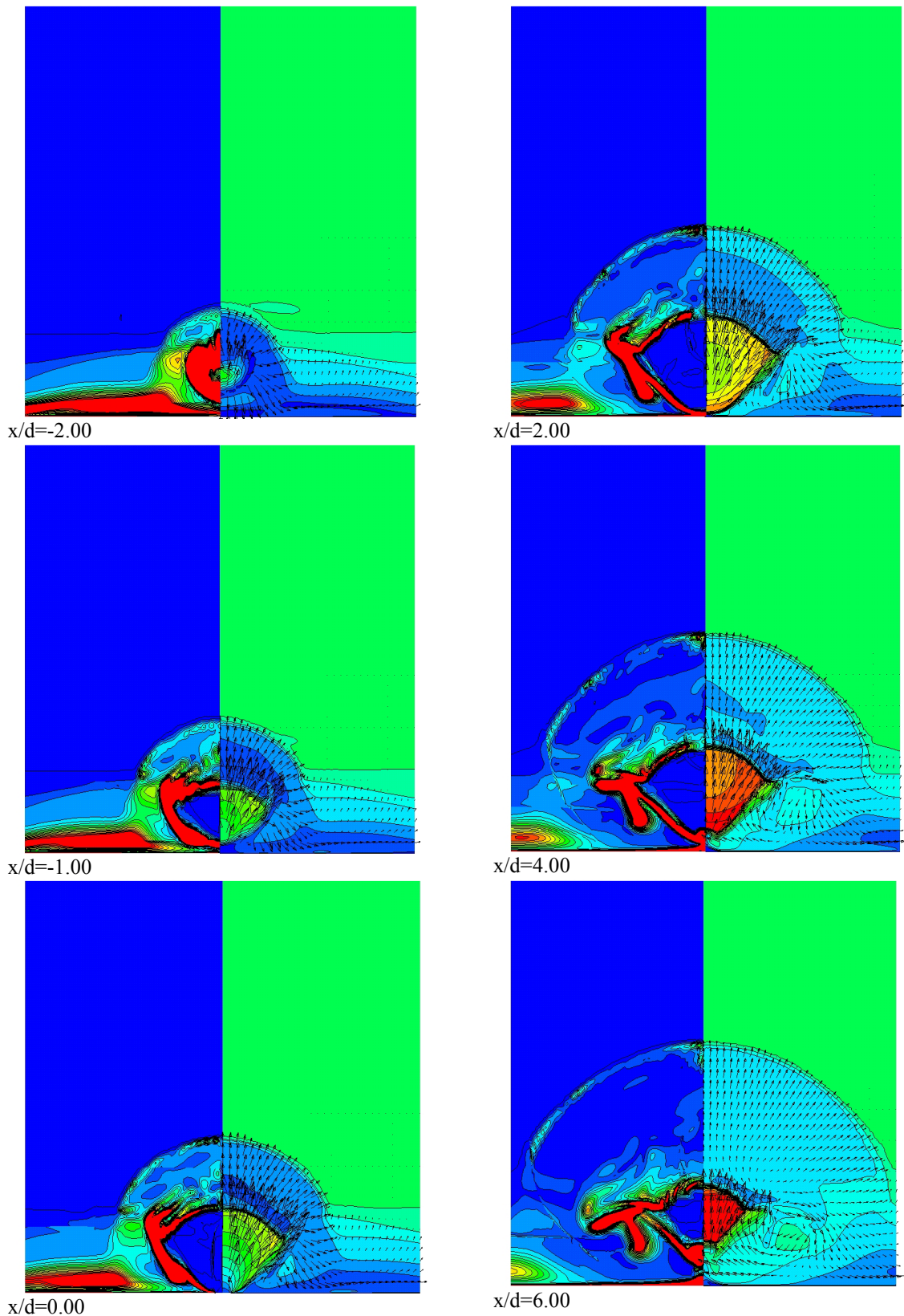


Figure 6.10. Blown-up crossplane mappings of vorticity magnitude (left) and Mach number (right) with velocity vectors superimposed at different x/D . Virginia Tech, Mach 4.0, $Pr=532$. (y/d : 0-21.0, z/d : 0-10.0).

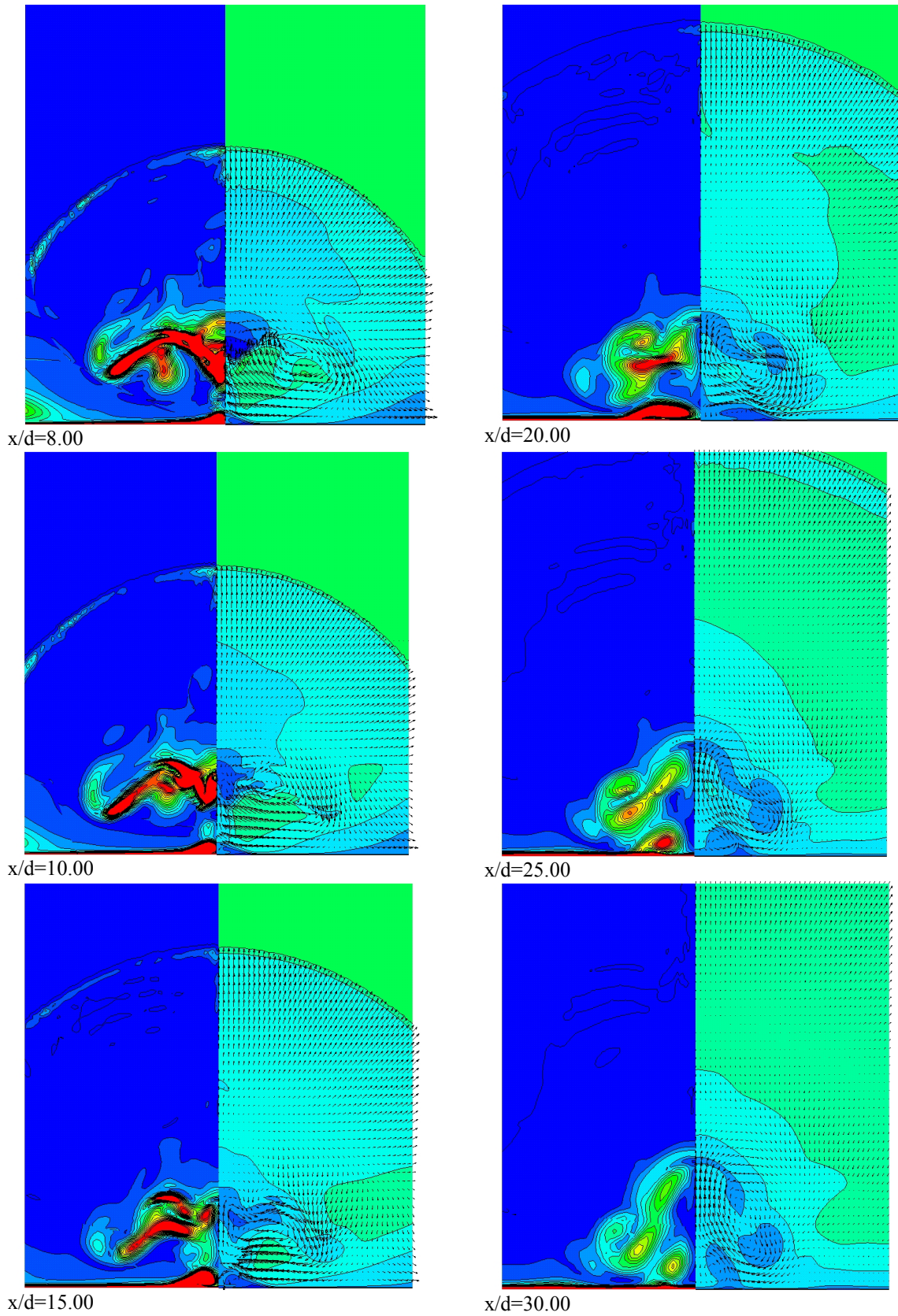


Figure 6.10 (Continued).

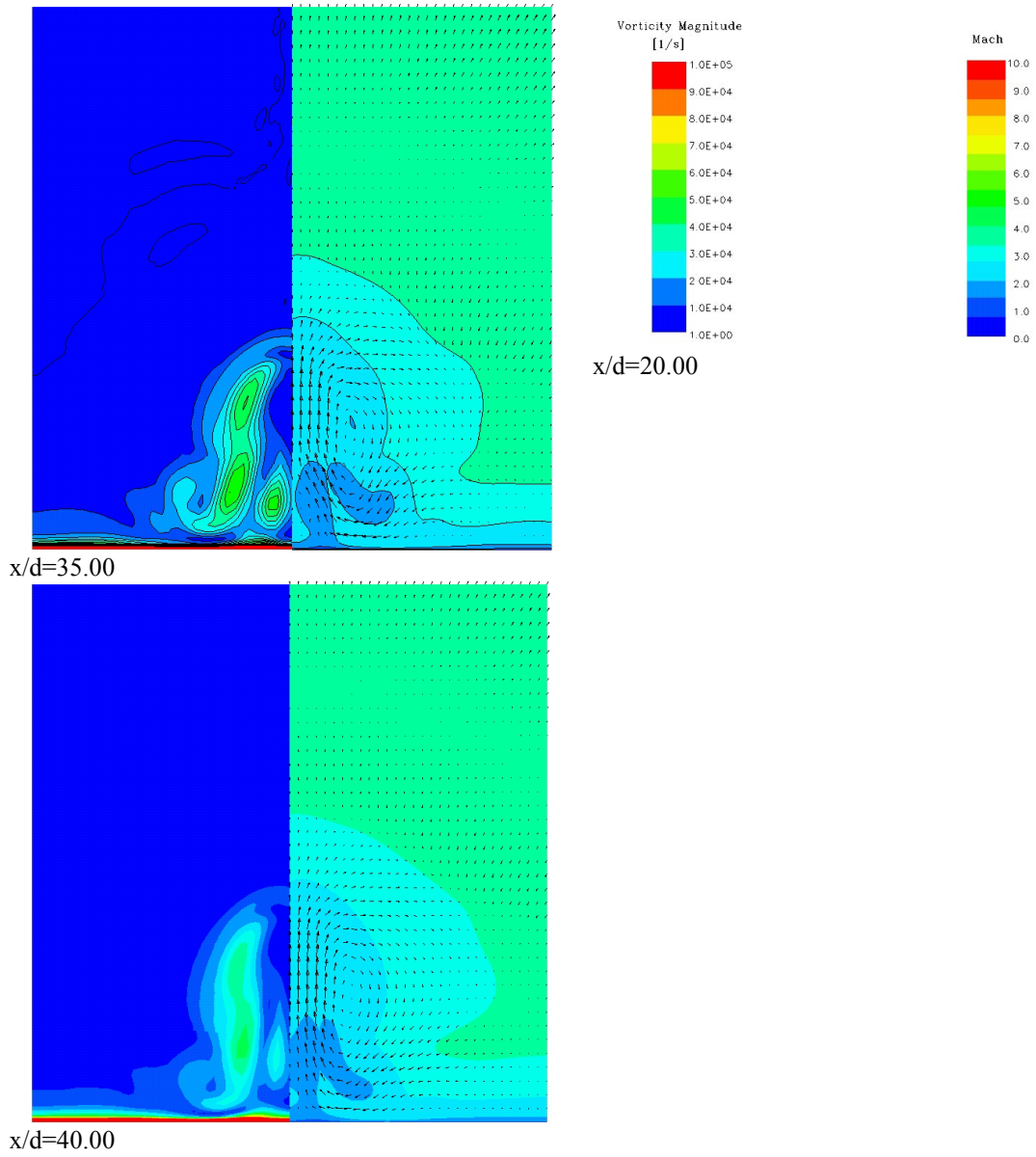


Figure 6.10 (Continued).

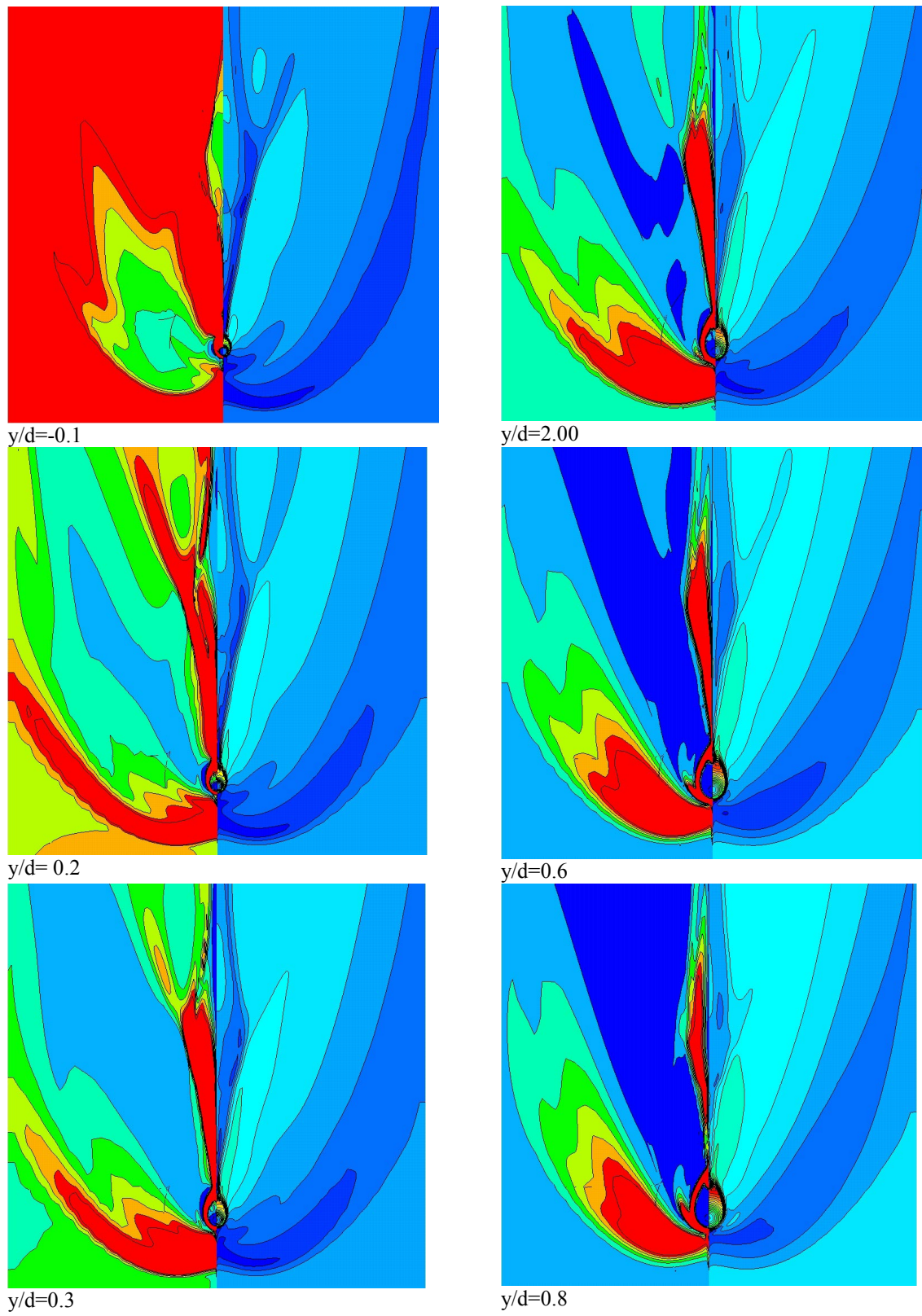
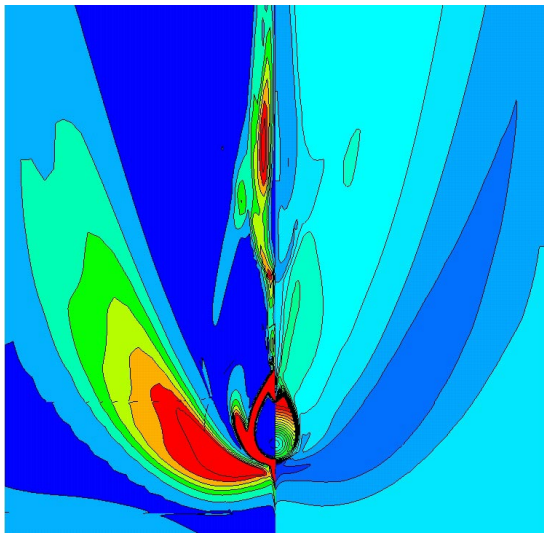
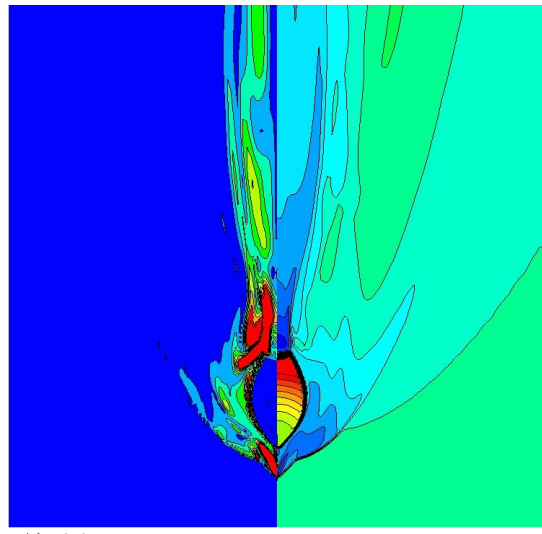


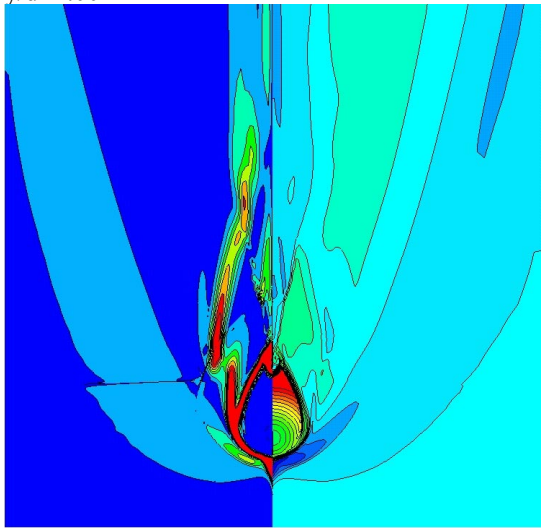
Figure 6.11. Planar mappings of vorticity magnitude (left) and Mach number (right) at different heights over the flat plate surface (y/D). Virginia Tech, Mach 4.0, $Pr=532$. (x/d : $-8 \rightarrow 39.0$, z/d : $0 \rightarrow 24.0$).



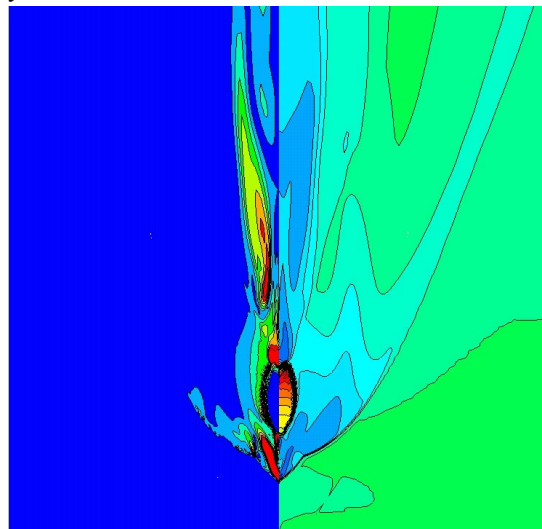
$y/d=1.00$



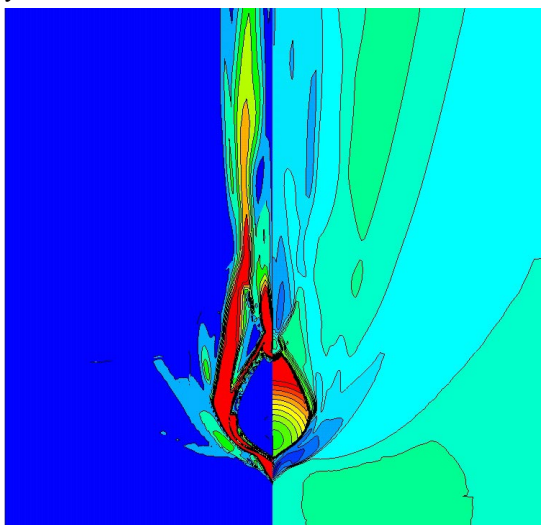
$y/d=4.0$



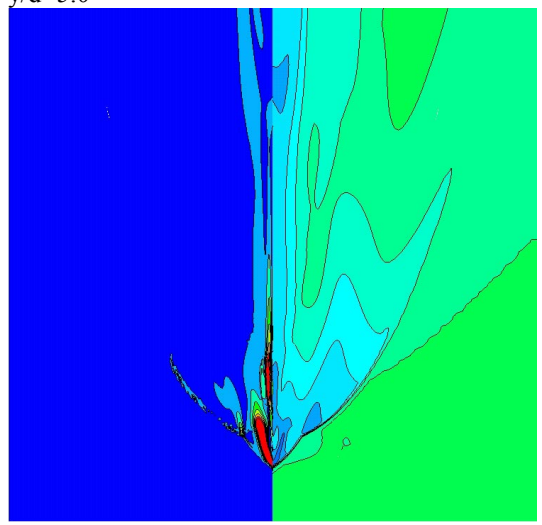
$y/d=2.0$



$y/d=5.0$

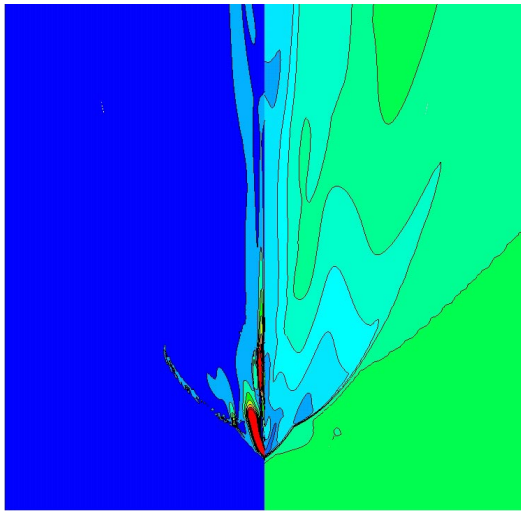


$y/d=3.0$

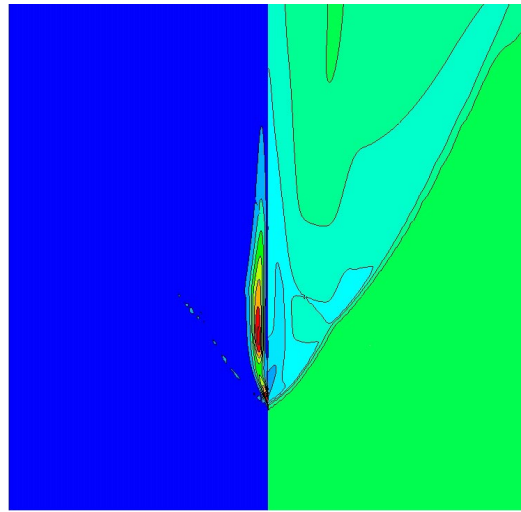


$y/d=6.0$

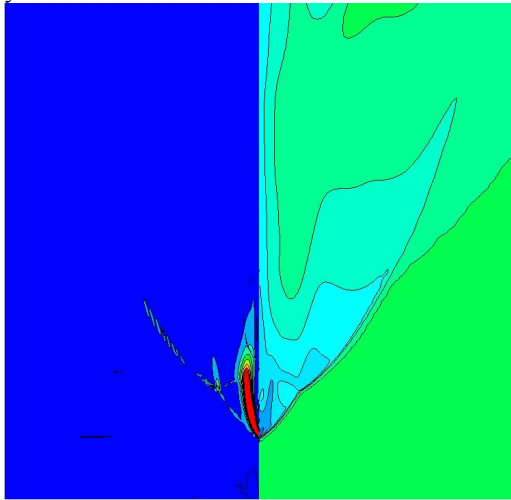
Figure 6.11. (Continued).



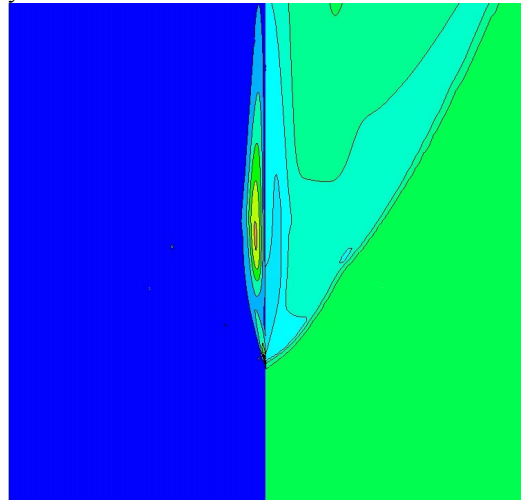
y/d=7.0



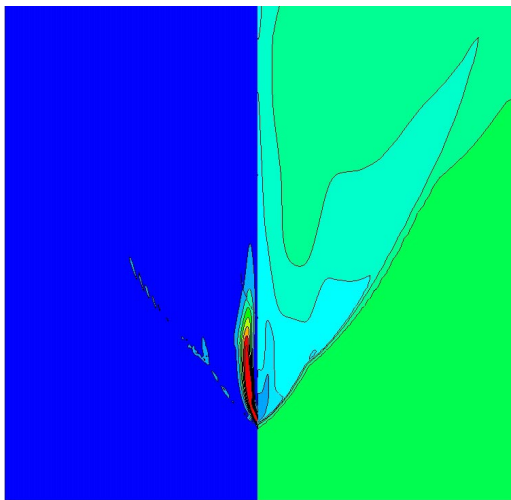
y/d=12.5



y/d=8.0



y/d=15.0



y/d=10.0

Figure 6.11. (Continued).

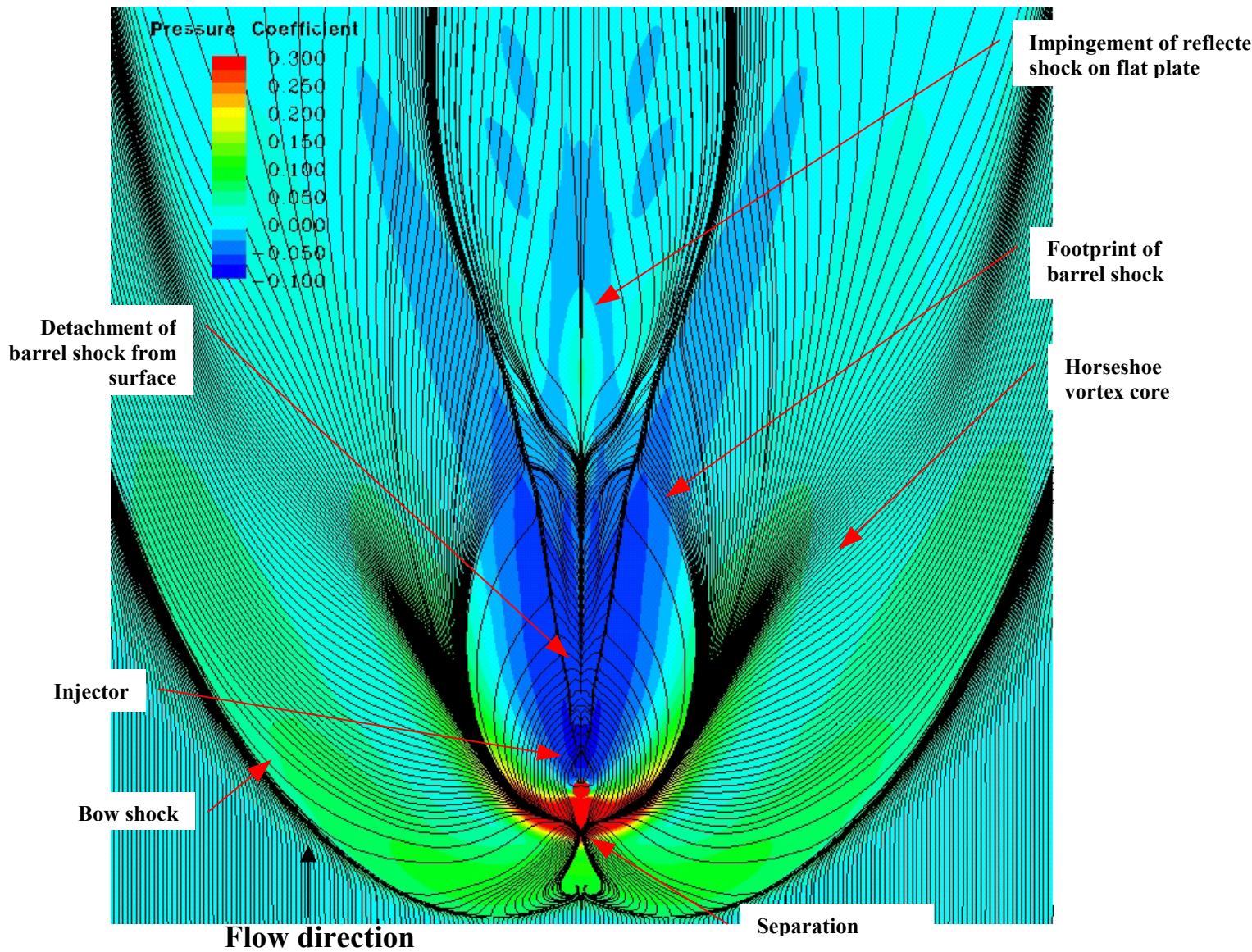


Figure 6.12. Streamlines above the flat plate simulating oil surface flow visualization with pressure coefficient mapping superimposed. Virginia Tech, Mach 4.0, $Pr=532$. ($x/d: -7 \rightarrow 40.0$, $z/d: 0 \rightarrow 24.0$).

Chapter 7

Summary and Conclusions

Numerical simulations of a three-dimensional, jet interaction flowfield produced by several configurations of sonic circular injectors exhausting normal into a supersonic crossflow were presented. The numerical calculations solved the compressible Reynolds Averaged Navier-Stokes equations (RANS) using the General Aerodynamic Simulation Program (GASP), a commercial CFD code developed by AeroSoft Inc. Both laminar and turbulent calculations were performed employing the perfect gas assumption. The CFD study is a numerical assessment of a proposed idea to improve present-day jet thruster configurations used on hypersonic vehicles. The new suggested configuration consists of inserting a pair of smaller secondary injectors behind the primary jet. The secondary injector, when properly located, can alleviate the problems generated by the region of low pressure that forms behind the single primary injector. This low-pressure region is undesirable in jet thruster configurations for two main reasons. First and most important, it creates a strong nose-down pitching moment that must be compensated for by inserting another injector far aft of the center of gravity of the vehicle. The second problem is the reduction in the net lateral force produced by the thruster. In fact, the low-pressure region on the surface of the vehicle acts as a suction and it works against the thrust of the jet. Small secondary injectors, by impinging on the barrel shock produced by the primary injector and by decreasing the low-pressure region behind the primary injector can eliminate the need of using a second large injector far aft of the center of gravity of the vehicle to counter-balance the nose-down pitching moment. The numerical studies were also aimed at providing support to the preliminary experimental studies of the innovative jet interaction configuration that were performed in the supersonic wind tunnel at Virginia Tech. The integration of the numerical effort with the experiments proved to be essential to thoroughly study the complex jet interaction flowfield. Finally, the numerical simulation results can be interrogated to provide many details about the fluid physics of the complex flow.

7.1 Summary of the relevant accomplishments

The numerical study was carried out in a systematic way, starting with the simulation and analysis of relatively simple jet interaction cases, building knowledge and experience in this type of calculations and then moving on to the simulation of a more complex jet interaction case. In the preliminary stages of this study, jet interaction flowfields on a flat plate with laminar boundary layers were simulated. The first laminar case simulated a test from Schetz, et al. [65] performed in 1967 with a freestream Mach number of 2.10, pressure ratio of 60 and sonic injection. A comparison of the numerical solution to the shadowgraph of the flowfield showed good agreement in the shape and position of the shock and of the jet plume. No pressure data was available from the original paper and

therefore the comparison between the CFD solution and the experiment was limited to the visual comparison of the flow features. Important experience was acquired about the meshing process for this type of problem and how to optimize the cell clustering and the grid topology to improve the quality of the solution. The second laminar case was a simulation of an experiment run in 1961 by Cubbison [22] with a freestream Mach number of 2.92, a pressure ratio of 677 and sonic injection. Pressure mappings on the flat plate and shadowgraphs of the plume were available for this experiment. The CFD solution over-predicted the normal force by 21% and the pitching moment by 18%. But, the large uncertainty associated with the experimental data makes the comparison of the forces and moments not very indicative. More significant was the favorable comparison of the pressure mappings on the surface of the flat plate and of the pressure coefficient plots along the tunnel centerline. The CFD solution seemed to properly predict the separation location, the high-pressure lobes of the bow shock and the low-pressure region behind the injector. These positive results were confirmed by the visual comparison of the flow features visible in the Schlieren photograph with the CFD solution.

The overall positive results obtained from the laminar calculations prompted the research to focus on the simulation of the more complex case of injection on a flat plate with a turbulent boundary layer. The first simulation of a jet interaction problem with a turbulent boundary layer using Wilcox's $k-\omega$ turbulence model was that of an experiment run in 1965 by Letko [42], with freestream Mach number of 4.5, a pressure ratio of 680 and sonic injection. The comparison of the experimental and computed pressure mapping on the flat plate showed that the CFD was correctly predicting the shape of the pressure patterns, but the pressure levels were somewhat higher than the experimental levels thus producing higher forces and moments. This discrepancy was found to be mainly attributable to the lack of information about the jet mass flow and to the assumption of a discharge coefficient of 1.00. Simulations of the flow in the sonic nozzle showed that a discharge coefficient of 0.78 was a more realistic estimate than the initial estimate of 1.00. The flowfield calculations with the corrected discharge coefficient showed an improved agreement with the experiment, especially taking into consideration the uncertainty in the experimental values. The computed normal force differed by 25% from the experimental force value and the pitching moment by 45%. The comparisons of the pressure coefficient mappings were somewhat more favorable, and the numerical solution was able to correctly predict the shape and intensity of the low-pressure region. Grid convergence was shown for the single jet case by converging the solution on four grid sequences and comparing the flow features and integrated quantities to the finest grid level. The discretization error for the finest grid level, calculated using a modified Richardson's extrapolation was 0% for the normal force and 2% for the pitching moment. The Letko simulation was also used as a preliminary test case to study the effects of inserting a pair of secondary injectors aft of the primary jet. Computations were run on a medium-sequence grid to simulate such a configuration and to check the trends in the forces and moments. The preliminary results showed that a secondary injector with a mass flow of 10% of the primary injector increased the normal force by 9% and decreased the nose-down moment by 24%.

Both the laminar and turbulent calculations were simulations of past experiments and highlighted the need for more accurate experimental results if these were to be used to confirm the numerical predictions. The Virginia Tech cases [84][85] were conceived in part because of this need for more reliable experimental data. Two sets of experimental data with different freestream Mach numbers and different jet pressure ratios were available. The first set, a proof-of-concept for the configuration, had a freestream Mach number of 2.4 and a pressure ratio of 14. The second set of experiments was run at a freestream Mach number of 4.0 and a pressure ratio of 532. In both sets of experiments Pressure Sensitive Paint (PSP) was used to map the pressure field on the surface of the flat plate. Also, accurate data was available about the discharge coefficient of the nozzle (0.78). The numerical calculations simulated the turbulence effects using Wilcox's $k-\omega$ model. The grids used in these calculations were an evolution of the computational grids used in the previous calculations, and they optimize the cell distribution in the region around the injectors where the highest pressure gradients are to be found. The grids used in the calculations of the two sets of experiments are slightly different. The grid used in the Mach 2.4 cases (1,100,024 cells) simulates the secondary injectors by imposing the jet conditions at selected cells on the surface of the flat plate. Three computations with a Mach number of 2.4 were converged: primary jet only, primary jet and one pair of secondary jets and primary jet and two pairs of secondary jets. The three calculations were run using exactly the same grid and changing only the boundary conditions at the appropriate cells designed to simulate the secondary injectors.

The comparison of the experiment with the CFD forces and moments for the Virginia Tech Mach 2.4 cases did not show good agreement. The difference for the three converged cases was on the order of 85% for the normal force and 97% for the pitching moment. However, a bias was found in the experimental pressure field. This bias negatively affected the direct comparison of the forces and moments. In addition to the bias in the data, Schlieren photographs of the flowfield showed that a weak shock was present in the tunnel flow ahead of the jet interaction flowfield. This shock was found to be produced by the junction between the tunnel floor and the flat plate mounted flush to it. The shock effectively altered the freestream conditions "seen" by the jet. Due to this discrepancy between the freestream condition of the experiment and of those used in the CFD calculations, a more valuable comparison was found to be the analysis of the force augmentation factors generated by the secondary jets. The experiment predicted an augmentation factor of 11% with one pair of secondary jets and 16% with two pairs of secondary jets for the normal force and of 4% and 8% for the pitching moment, respectively. The percentage refers to the increase in the force or moment with respect to the case with only the primary injector. The CFD under-predicted the augmentation factors of the normal force (3% and 6%) but gave better estimates for those of the pitching moment (9% and 22%). The pressure coefficient plots indicated that as seen in the turbulent calculation of the Letko experiment, the CFD under-predicted the extent of the separation region. Furthermore, while the experiment showed that the effects of the secondary injectors propagated upstream and increased the strength of the separation region, no upstream effect was predicted by the numerical solution. The under-prediction of the effects of the secondary jets and the absence of any upstream effect highlighted

one possible problem affecting the calculations with the secondary injector: lack of adequate grid refinement in the region where the secondary jets are located. It was hypothesized that in spite of overall good grid convergence, the grid around the secondary injector might not be able to capture some relevant flow physics created by the interaction of the primary with the secondary jets. Therefore, a finer grid was developed for the simulations of the Virginia Tech Mach 4.0 cases. The new baseline grid had 1,544,098 cells for the case with only the primary injector. For the case with the one pair of secondary injectors, a fine Chimera grid that simulates the secondary injector replaced one of the computational blocks of the baseline grid. Therefore, the grid used to simulate the case with only the primary injector has fewer cells (1,544,098) than the one used to simulate the secondary injector case (2,073,024). The Chimera grid had a two-fold use. The first was to simulate the secondary injector without changing the cell distribution in the baseline grid. The second was to provide a very fine mesh in the region surrounding the secondary injector so as to make possible a localized grid-convergence study. As in the Mach 2.4 case, the Mach 4.0 experimental results were affected by high uncertainty mainly due to the weak shock created by the junction of the tunnel floor with the flat plate and, to a lesser degree, by a bias in the PSP data. The comparison between the experiment and the numerical solution showed better agreement than the one obtained in the previous case. The CFD under-predicted the normal force by 24% for case with only the primary jet and by 20% for the case with one group of secondary jets. The pitching moment was under-predicted by 39% and 62%, respectively. Again, the comparison of the augmentation factors is more relevant than the direct comparison of the forces and moment due to the slightly different freestream conditions of the numerical computations. The experimental augmentation factors were measured to be -1% (i.e. a decrease) for the normal force and a pitching moment more negative than the case with the primary jet alone by 218%. The CFD predicted an increase in the normal force of 4.8% and a decrease in the nose down attitude of 101%. The CFD and the experiment disagreed in the prediction of the trend of the normal force. On the other hand, both the CFD and the experiment predicted a decrease in the nose-down pitching moment caused by the secondary jets. The CFD also correctly predicted the separation region for the case with only the primary injector. This time the numerical solution showed an upstream effect of the secondary injector that caused the separation region to extend further upstream. However, the experiment did not show such a strong upstream effect as that predicted by the numerical solution. The prediction by the CFD of the upstream effect of the secondary jets and the overestimation of the separation region suggest two major findings. The first one is that a fine grid in the region where the secondary injector interacts with the barrel shock of the primary injector is essential to correctly predict the upstream effects of secondary jets. Second, the non-conservative property of the Chimera zonal boundaries might negatively affect the accuracy of the numerical solution. In particular the presence of strong shocks across the Chimera boundary is detrimental to the reliability of the numerical results. In spite of this problem, the visual comparison of Schlieren photographs to the numerical solutions showed a high level of agreement. The CFD properly predicted the location and inclination of the separation-induced shock, of the bow shock, the barrel shock, the Mach disk and the reflected shocks that trail downstream of the jet plume.

The jet interaction flowfield generated by a single jet was studied further in detail to better understand the mechanisms that sustain the formation of the low-pressure region aft of the injector. This analysis concluded that the detachment of the barrel shock from the solid surface of the flat plate associated with the vortical motion originating in the separation region are the main phenomena creating the low-pressure region.

7.2 Conclusions

The numerical study showed that it is possible to improve present-day jet thruster configurations by using smaller secondary injectors that interact with the primary jet. The study showed that the main improvement that this configuration produces is a considerable reduction in the nose-down pitching moment typical of jet interaction flows. However, it is important to optimize the design of the injection configuration so as to maximize the effect of the secondary injectors. In the present configuration a pair of secondary jet with approximately 2% the mass flow of the primary jet produced an increase in the normal force of 5% and a decrease in the nose-down pitching moment of 101%. It is believed that these values can be improved by locating the secondary jets at a more convenient location.

The investigation further showed that a combined effort of numerical studies and experiments could efficiently and effectively lead to the understanding of complex fluid-dynamics phenomena. Such a coordinated approach is most desirable in the development and design stages of new technologies because of its time- and cost-saving advantages over an exclusively experimental approach.

From the point of view of the numerical techniques it was shown that Reynolds Averaged Navier Stokes equations in conjunction with a first-order two-equation turbulence model such as Wilcox's $k-\omega$ can reproduce the main physics of a highly complex phenomenon such as the multiple jet interaction flowfield. The $k-\omega$ turbulence model proved to be reliable and robust and the results it provided for this type of flowfield were accurate enough from an engineering standpoint to make informed decisions about the configuration layout. However, in spite of the overall good performance the $k-\omega$ turbulence model failed to correctly predict the flow in the regions of strong adverse pressure gradients. Comparisons with experimental results showed that the separation region was often under-predicted, highlighting the need to employ second-order turbulence models that, according to other numerical studies [15], may improve the accuracy of the computations. In addition to the above it might be useful to study the unsteady behavior of the flowfield by running time-dependent simulations. In general, the steady-state RANS equations were found accurate enough to provide correct physical mean-flow solutions from an engineering standpoint.

A large effort was dedicated to the development of an efficient computational grid that could capture the flow-physics with the least amount of cells. The grid was adapted to the physics of the flow using a combination of H- and C-type grids. Also, Chimera or overset grids were employed in the simulation of the secondary injectors to improve the efficiency of the calculation. Grid generation proved to be the most expensive task in terms of man-hours. A solution to decrease the grid generation effort would be the use of a simpler H-type grid that reaches the desired mesh –refinement level by simply increasing the number of cells. However, with today's technology and computational resources, such an approach is not a realistic one at least for routine engineering applications. This is mainly because of the large grid size that would be needed by an H-type grid (probably around 6 million cells for a three-dimensional multiple jet interaction calculation) to properly describe the flowfield.

Grid convergence was shown to be achieved for the case of single injection by conducting a thorough convergence study. The discretization error was calculated through a modified Richardson extrapolation to be as low as 0%. Grid convergence was also shown to be achieved in the flowfield around the secondary injector through a localized grid convergence study that made use of the Chimera grid. The normal force for the case with only the primary jet was predicted with an acceptable level of accuracy from the engineering standpoint by all the grid sequences. The discretization errors in the normal force was computed to be -5%, -2% and 0% for the coarse, medium and fine grid sequences, respectively.

7.3 Recommendations for future work

The recommendations focus on two aspects of the present study. The first one is the assessment of the performance and the improvement of the proposed jet interaction configuration. The second one is the improvement of the modeling through the use of the Reynolds averaged Navier-Stokes equations of complex flowfields.

The experiments run in the Virginia Tech supersonic wind tunnel were preliminary tests to assess the validity of the proposed jet interaction configuration. Due to the simplicity of the test set up and to the innovative nature of the Pressure Sensitive Paint (PSP) technique the experiments were affected by some problems. The experimental data suffered from a high degree of uncertainty. The Pressure Sensitive Paint (PSP) proved to be very useful to describe the pressure field and to perform qualitative comparisons with the numerical solution. However, the calculation of the forces and moments from integration of the PSP pressure field produced a high uncertainty level. Furthermore the flow disturbances caused by imperfections in the junction between the tunnel flow and the flat plate effectively altered the freestream condition experienced by the jet. To obviate these two problems it is suggested that a new set of experiments is run. A flat plate with a sharp leading edge and mounted on a three-axis balance would solve both of the aforementioned problems. Schlieren pictures and PSP could be used to provide visual comparisons of the experimental and computational flowfields. An increased number of

pressure orifices in the flat plate could provide reliable discrete pressure data as well as a mean to calibrate the PSP at different locations over the plate. It would be useful to obtain skin friction measurements on the flat plate so as to have more types of experimental data to compare the numerical solutions with.

The current locations of the secondary injectors on the flat plate used in the experiments were chosen intuitively according to the position of the zero- C_p line in the Cubbison experiment. In order to optimize the location of the secondary injector with respect to the primary jet it would be necessary to perform a sensitivity study. A preliminary attempt to use sensitivity analysis with sliding boundary conditions applied to a two dimensional jet interaction flowfield was performed by Borggard, Cliff and Godfrey [10]. However, the study was performed in two dimensions, the injector was subsonic and it was not exhaustive. Therefore, there is the need for a thorough sensitivity study that could be run as a complement to a parametric study.

The turbulent calculations showed that in most cases Wilcox's $k-\omega$ turbulence model failed to accurately predict separation. In light of the results of numerical studies performed by other researchers with similar flows it is recommended that a second-order turbulence model be applied to the solution of the jet interaction flowfield. This calculation could take advantage of the soon-to-be released implementation of the Reynolds Stress turbulence model in GASP version 4.0. The existing converged fine-grid solutions with Wilcox's $k-\omega$ model could be restarted using the Reynolds Stress model. The new calculations would accomplish two main objectives. The first one would be to compare the experimental results to more reliable numerical solutions. The second objective would be an assessment of the capacity of Wilcox's $k-\omega$ model to properly model complex flowfields such as jet interaction.

The use of the Chimera grid greatly facilitated the task of inserting a secondary injector inside a computational domain without the need to modify the existing grid. Also it made it possible to refine the region in the immediate surroundings of the secondary injector without affecting the rest of the grid. However, the non-conservative Chimera zonal boundaries are a probable cause of inaccuracy in the numerical solution. It is suggested the implementation of a Chimera scheme with conservative zonal boundaries be undertaken. A Chimera grid with conservative zonal boundaries would allow the refinement of the computational grid in zones where the highest pressure gradients are found without the need to modify the grid topology and to increase drastically the total number of cells.

The perfect gas assumption was proven to be reasonable for the scope of this study. However, it would be advisable to perform a numerical study of the jet interaction flowfield employing a model for air that takes into account low-pressure, low-temperatures real gas effects.

Chapter 8

Bibliography

- [1] “*Computational and experimental assessment of jets in crossflow*”, AGARD Conference Proceedings, No. 534, Winchester, United Kingdom, April 1993. 1.
- [2] M. B. Abbot, D. R. Basco, “*Computational Fluid Dynamics. An Introduction for Engineers.*”, Longman Scientific & Technical, co-published in the US with John Wiley & sons, Inc. New York, 1989. ISBN 0-582-01365-8.
- [3] J. D. Anderson, Jr., “*Modern Compressible flow with historical perspective*”, 2nd Edition, McGraw-Hill Inc., New York, 1990, ISBN-0-07-001673-9.
- [4] J. D. Anderson, Jr., “*Hypersonic and high-temperature gas dynamics*”, McGraw-Hill Inc., New York, 1989, ISBN-0-07-001671-2.
- [5] S. Aso, S. Okuyama, “*Experimental study on mixing phenomena in supersonic flows with slot injection*”, AIAA Paper 91-0016, January 1991.
- [6] S. Aso, S. Okuyama, Y. Ando, T. Fujimori, “*Two-dimensional and three-dimensional mixing flow fields in supersonic flow induced by injected secondary flows through traverse slot and circular nozzle*”, AIAA Paper 93-0489, January 1993.
- [7] S. Aso, Tannou, S. Maekava, S. Okuyama, Y. Ando, Y. Yamane, “*A study on mixing phenomena in three dimensional supersonic flow with circular injection*”, AIAA Paper 94-0707, January 1994.
- [8] B. S. Baldwin, H. Lomax, “*Thin layer approximation and algebraic model for separated turbulent flows*”, AIAA Paper 78-257, July 1979.
- [9] J. A. Benek, J. L. Steger, F. C. Dougherty, “*A Flexible Grid Embedding Technique with Application to the Euler Equations*”, AIAA Paper 83-1944, 1983
- [10] J. T. Borggaard, E. M. Cliff, A. G. Godfrey, “*Sensitivity Analysis with Sliding Boundary Conditions*”, AIAA Paper 2002-0100, January 2002.
- [11] J. L. Brown, “*Turbulence model validation for hypersonic flows*”, AIAA paper 2002-3308, June 2002.
- [12] W. M. Chan, R. J. Gomez III, S. E. Rogers, P. G. Buning, “*Best Practices in Overset Grid Generation*”, AIAA Paper 2002-3191, June 2002.
- [13] I. Celik, O. Karatekin, “*Numerical Experiments on Application of Richardson Extrapolation with Non-Uniform Grids*”, ASME Journal of Fluids Engineering, Vol. 119, pp584-590, September 1997.

- [14] C. F. Chenault, P. S. Beran, “ κ - ϵ and Reynolds stress turbulence model comparisons for two-dimensional injection flows”, AIAA Journal, Vol. 36, No. 8, August 1998.
- [15] Clarence F. Chenault, P. S. Beran, R. D. Bowersox, “Numerical investigation of supersonic injection using a Reynolds-stress turbulence model”, AIAA Journal, Vol. 37, No. 10, pp. 1257-1269, October 1999.
- [16] C. F. Chenault, “Analysis of turbulence models as applied to two- and three-dimensional injection flows”, Ph.D. Dissertation, Department of Aeronautics and Astronautics, U.S. Air Force Institute of Technology, AFIT/DS/ENY/98M-01, Wright-Patterson Air Force Base, OH, March 1998.
- [17] S. W. Clark, S. C. Chan, “Numerical investigation of a transverse jet for supersonic aerodynamic control”, AIAA Paper 92-0639, January 1992.
- [18] T. J. Coakley, “Turbulence modeling methods for the compressible Navier-Stokes equations”, AIAA Paper 83-1693, 1983.
- [19] H. W. Coleman and W. G. Steele, “Experimentation and Uncertainty Analysis for Engineers”, John Wiley & Sons, Inc. New York, 1989.
- [20] R. Courant, K. O. Friedrichs, H. Lewis, “Über die Partiellen Differenzgleichungen der Mathematischen Physik”, Mathematische Annalen, Vol. 100, pp. 32-74, 1928. Translated into English as “On the Partial Differential Equations of Mathematical Physics”, IBM Journal of Research and Development, Vol. 11, pp. 215-234, 1967.
- [21] R. C. Crites, “Pressure Sensitive Paint Technique”, Von Karman Institute for Fluid dynamics, Lecture Series 1993-05, Measurement Techniques, April 19-23, 1993.
- [22] R.B. Cubbison, B.H. Anderson, J.J. Ward, “Surface Pressure Distributions with a sonic jet normal to adjacent flat surfaces at Mach 2.92 to 6.4”, NASA Technical Note D-580, 1961.
- [23] Fred L. Daum, “Air Condensation in a Hypersonic Wind tunnel”, AIAA Journal, Vol.1 No. 5, May 1963.
- [24] J. P. Drummond, “Numerical investigation of the perpendicular injector flow field in a hydrogen fueled scramjet”, AIAA Paper 79-1482, July 1979.
- [25] W. M. Eppard, W. D. McGrory, M. P. Applebau, “The Effects of Water-Vapor Condensation and Surface Catalysis on COIL Performance”, AIAA Paper No. 2002-2132, 2002.
- [26] E. J. Fuller, R. W. Walters, “Navier-Stokes Calculations for 3D gaseous fuel injection with data comparisons”, AIAA Paper 91-5072, December 1991.
- [27] GASP 3.2 User Manual, AeroSoft, 1997, ISBN 0-9652780-0-x.
- [28] GASP 4.0 Online User Manual, AeroSoft, 2001, www.aerosft.com/Gasp/Manual/download.php3.

- [29] P. Gerlinger, J. Algermissen, D. Bruggemann, “*Simulation of turbulent slot injection of different gases into a supersonic air stream*”, AIAA Paper 94-2247, June 1994.
- [30] A. I. Glagolev, A.I. Zubkov, Yu A. Panov, “*Supersonic flow past a gas jet obstacle emerging from a plate*”, Fluid Mechanics, Soviet Research, Vol. 2, No.3, 1967, pp. 97-102, Scripta Publishing Co. 1979. Originally published in Nauk Trudy Insti. Mekh. Mosk. Gosud. Univ.
- [31] A.I. Glagolev, A.I. Zubkov, Yu A. Panov, “*Interaction between a supersonic flow and gas issuing from a hole in a plate*”, Fluid Mechanics, Soviet Research, Vol. 3, No. 2, 1968, pp99-103, Scripta Publishing Co. 1979. Originally published in Nauk Trudy Insti. Mekh. Mosk. Gosud. Univ.
- [32] GRIDGEN Version 13.3 user manual, Pointwise, Inc., PO Box 210698, Bedford, TX 76095. 1999.
- [33] B. Grossman, “*Fundamental concepts of gas dynamics*”, Version 3.09, January 2000, Class Notes of the High-Speed Aerodynamics Class taught during the Summer II session, July-August 2000, in the Department of Aerospace and Ocean Engineering. Virginia Tech, Blacksburg, VA 24061.
- [34] Philip-Hill, Carl Peterson, “*Mechanics and thermodynamics of propulsion*”, 2nd Edition, Addison-Wesley Publishing Company Inc., 1992, ISBN 0-201-14659-2.
- [35] S. Hosder, B. Grossman, R. T. Haftka, H. Mason, L. T Watson, “*Observations on CFD simulation uncertainties*”, AIAA Paper No. 2002-5531, June 2002.
- [36] T. Hsieh, “*Analysis of the Scaling Effects for missile Configuration with Lateral Thruster*”, AIAA Paper No. 99-0810, January 1999.
- [37] P. A. Hunter, “*An investigation of the performance of various reaction control devices*”, NASA MEMO 2-11-59L, March 1959.
- [38] G. Jeanfavre, C. Benoit, M. C. Le Pape, “*Improvement of the robustness of the Chimera method*”, AIAA Paper 2002-3290, June 2002.
- [39] K. Karamcheti, “*Principles of ideal-fluid aerodynamics*”, Krieger Publishing Company Inc., Krieger Drive, Malabar, Florida 32950, Chapter 2, p. 131, 1966, ISBN 0-89874-113-0.
- [40] K. D. Kennedy, B. J. Walker, C. D Mikkelsen, “*Comparisons of CFD calculations and measurements for a sonic jet in a supersonic crossflow*”, AIAA Paper 2000-3313, July 2000.
- [41] B. Launder, G. Reece, W. Rodi, “*Progress in the development of a Reynolds-stress Turbulence closure*”, Journal of Fluid Mechanics, pp. 537-566, Vol. 68, January 1975.
- [42] W. Letko, “*Loads induced on a flat plate at a Mach number of 4.5 with a sonic or supersonic jet exhausting normal to the surface*”, NASA Technical note D-1935, 1963.

- [43] W. Matusa, M. Satoh, H. Yamada, "*Effects of Water Vapor Condensation on the Performance of supersonic Flow Chemical Oxygen-Iodine Laser*", 1995.
- [44] G. J. McCann, D.W. Bowersox, "*Experimental investigation of supersonic gaseous injection into a supersonic free-stream*", AIAA Paper 96-0197, June 1996.
- [45] J. McDaniel, C. Glass, D. Staack,, C. Miller, "*Experimental and computational comparison of an under-expanded jet flowfield*", AIAA Paper No. 2002-0305, January 2002.
- [46] M. Morris, J. Donovan, "*Application of Pressure and Temperature Sensitive Paints to High Speed Flows*", AIAA Paper 94-2231, June 1994.
- [47] J. Morrison "*A Compressible Navier-Stokes solver with Two-Equation and Reynolds Stress turbulence closure models*", NASA CR-4440, May 1992.
- [48] J. Morrison, T. Gatski, T. Sommer, H. Zang, R. So, "*Evaluation of a near-wall turbulent closure model in predicting compressible ramp flows*", "Near-wall turbulent flows", pp. 239-250, edited by R. So, C. Speziale, B. Launder, Elsevier, New York, 1993.
- [49] A. Nedungadi, and M. J. Lewis, "*Computational Study of three-dimensional Shock-Vortex interaction*", AIAA Journal of Aircraft, Volume 34, No. 12, December 1996.
- [50] A. Nedungadi, and J. Lewis, "*A Numerical Study of Fuel Mixing Enhancement Using Oblique Shock/Vortex Interactions*", AIAA Paper No. 96-2920, February 1997.
- [51] R. Neel, R.W. Walters, R.L. Simpson, "*Computations of Steady and Unsteady Low-Speed turbulent separated flows*", 35th AIAA Aerospace Sciences Meeting and Exhibit, 6-9 January 1997, Reno, NV. AIAA Paper 97-0653
- [52] "*Near-wall turbulent flows: proceedings of the International Conference on Near-Wall Turbulent Flows*", 15-17 March 1993, Tempe, AZ. Edited by Ronald M.C. So.
- [53] D. Papamoschou, D. G. Hubbard, M. Lin, "*Observations of supersonic transverse jets*", AIAA Paper 91-1723, 1991.
- [54] J. L. Payne, C. J. Roy, S. J. Beresh, "*A comparison of turbulence models for a supersonic jet in transonic cross flow*", 39th AIAA Aerospace Science Meeting and Exhibit, 8-11 January 2001, Reno, NV.
- [55] K.M. Peery, S.T. Imlay, "Blunt-body flow simulations", AIAA paper 88-2904, 1988.
- [56] J. R. Pietrzyk, D. G. Bogard, M. E. Crawford, "*Hydrodynamic measurements of jets in crossflow for gas turbine film cooling applications*", Journal of Tubomachinery, Vol. 111, 1989.
- [57] D. Rizzetta, "*Numerical simulation of slot injection into a turbulent supersonic stream*", AIAA Paper 92-0827, January 1992.

- [58] P. J. Roache, "*Verification and validation in computational science and engineering*", Hermosa Publisher, Albuquerque, New Mexico, 1998.
- [59] P. J. Roache, "*Quantification of uncertainty in computational fluid dynamics*", Annual Review of Fluid Mechanics, Vol. 29, pp. 123-160, 1997.
- [60] R. P. Roger and S. C. Chan, "*Parameters affecting penetration of a single jet into a supersonic crossflow: A CFD Study - II*", AIAA Paper No. 98-0425, January 1998.
- [61] C. J. Roy; M. A. McWerhter-Payne, W. L. Oberkampf, "*Verification and validation for laminar hypersonic flowfields*", AIAA Paper No. 2000-2550, June 2000.
- [62] C. J. Roy; "*Grid convergence error analysis for mixed-order numerical schemes*", AIAA Paper No. 2001-2006, June 2001.
- [63] J. Santiago, J. Dutton, "*Crossflow vortices of a jet injected into a supersonic crossflow*", AIAA Journal, Volume 35, Number 5, Pg. 915-917, May 1997.
- [64] J. Santiago, "*An experimental study of the velocity field of a transverse jet injected into a supersonic crossflow*", Ph.D. thesis, Department of Mechanical and Industrial Engineering, University of Illinois at Urbana-Champaign, IL, August 1995.
- [65] J. A. Schetz, P. F. Hawkins, Harry Lehman, "*Structure of Highly Under-expanded Transverse Jets in a Supersonic Stream*", AIAA Journal, Volume 5, Number 5, Pg. 882-884, May 1967.
- [66] J. A. Schetz, F. S. Billig, "*Penetration of a fluid jets into a supersonic stream*", Journal of Spacecraft and Rockets, Volume 3, Pg. 1658-1665, 1966.
- [67] J. A. Schetz, S. Cox-Stouffer, R. Fuller, "*Integrated CFD and experimental studies of complex injectors in supersonic flows*", AIAA Paper 98-2780, June 1998.
- [68] J. A. Schetz, "*Boundary layer analysis*", Prentice Hall, Englewood Cliffs, New Jersey 07632, Chapter 7, p. 240, 1993, ISBN 0-13-086885-X.
- [69] J. S. Shang, D.L. McMaster, N. Scaggs, M. Buck, "*Interaction of Jet in Hypersonic Cross Stream*", AIAA Journal, Vol. 27, No. 3, pp. 323, March 1989. Body of Rev
- [70] F. W. Spaid, E. E. Zukoski, R. Rosen, "*A study of secondary injection of gases into a supersonic flow*", NACA Technical Report No. 32-834, Jet Propulsion Laboratory, California Institute of Technology, Pasadena, CA, August 1966.
- [71] H. G. Stever, K. C. Rathbun, "*Theoretical and Experimental Investigation of Condensation of air in Hypersonic Wind Tunnels*", NACA Technical Note 2559, November 1951.
- [72] W. T. Strike, C. J. Schueler, "*Investigation of interference effects produced by lateral jets on surfaces in a supersonic stream*", AIAA Paper 63-184, June 1963.
- [73] J. C. Tannehill, Dale A. Anderson, Richard H. Pletcher, "*Computational Fluid Mechanics and Heat Transfer*", 2nd Ed., Taylor&Francis, 1101 Vermont Avenue, NW, Suite 200, Washington DC 20005-3521, 1997, ISBN 1-56032-046-x.

- [74] W. Thomson, Lord Kelvin, "*On the Equilibrium of Vapor at a Curved Surface of Liquid*", Proceeding of the Royal Society (Edinburgh), Vol. 7, no. 80, 1870.
- [75] H. Schlichting, "*Boundary Layer Theory*", 6th Edition, translated by J. Kestin, McGraw-Hill Inc., New York, 1968.
- [76] T. I-P. Shih, "*Overset Grids: Fundamentals and Practical Issues*", AIAA Paper 2002-3259, June 2002.
- [77] J. L. Steger, E. C. Dougherty, J. A. Benek, "*A Chimera Grid Scheme*", ASME Mini-Symposium on Advances in Grid Generation, Houston, Texas, June 1982.
- [78] D. S. Thompson, "*Numerical solution of a two-dimensional jet in a supersonic crossflow using an upwind relaxation scheme*", AIAA Paper 89-1869, June 1989.
- [79] W. M. VanLerberghe, J.C. Dutton, R. P. Lucht, L. S. Yuen, "*Penetration and mixing studies of a sonic transverse jet injected into a Mach 1.6 crossflow*", AIAA Paper 94-2246, June 1994.
- [80] M. Vinokur, "*On one-dimensional stretching functions for finite difference calculations*", Journal of Computational Physics, Vol. 50, No. 3, pp.215-234, 1983.
- [81] W. G. Vincenti, C. H. Kruger, Jr., "*Introduction to gas dynamics*", John Wiley and Sons, Inc., New York, 1965.
- [82] P. W. Vinson, J. L. Amick, H. P. Liepman, "*Interaction effects produced by jet exhausting laterally near base of ogive-cylinder model in supersonic main stream*", NASA MEMO 12-5-58W, February 1959.
- [83] D. M. Voitenko, A. I. Zubkov, Yu A. Panov, "*Existence of supersonic Zones in three-dimensional Separation Flows*", Fluid Mechanics, Soviet Research, Vol. 2, No.1, 1967, pp. 20-24, Scripta Publishing Co. 1979. Originally published in Nauk Trudy Insti. Mekh. Mosk. Gosud. Univ.
- [84] S. Wallis, "*Innovative transverse jet interaction arrangements in supersonic crossflow*", Master Thesis, Department of Aerospace and Ocean Engineering, Virginia Tech, December 2001.
- [85] S. Wallis, J. A. Schetz, "*Experimental studies of jet interaction with a main jet and an array of smaller jets*", AIAA paper 2002-3148, June 2002.
- [86] R. E. Walker, Stone A. R., Shandor, M., "*Secondary gas injection in a conical rocket nozzle. I. Effect of Orifice diameter and molecular weight of injectant*", AIAA Journal, Vol. 1, pp. 334-338, 1963.
- [87] C. R. Wang, "*Application of a turbulence model for jet and crossflow interaction*", AIAA Paper 2000-2655, June 2000.
- [88] Z. J. Wang, N. Hariharan, R. Chen, "*Recent Developments on the Conservation Property of Chimera*", AIAA Paper, June 1997.
- [89] E. H. Weidner, J. P. Drummond, "*Numerical study of a staged fuel injection for supersonic combustion*", AIAA Journal, Vol. 20, No. 10, October 1981. (AIAA Paper 81-1468R).

- [90] J. F. Wendt (editor), "*Computational Fluid Dynamics. An Introduction.*", with contributions by J. D. Anderson, G. Degrez, E. Dick, a Von Karman Institute book, Springer-Verlag, Berlin, Heidelberg, New York, 1991. ISBN 3-540-53460-
- [91] D. C. Wilcox, "*Turbulence Modeling for CFD*", 2nd Ed, DCW Industries, INC. 5354 Palm Drive, La Cañada, CA 91011, 1998.
- [92] D. C. Wilcox, "*Reassessment of the scale determining equation for advanced turbulence models*", AIAA Journal, Vol. 26, No. 11, pp. 248-251, 1988.
- [93] D. C. Wilcox, "*Comparison of Two-Equation turbulence models for boundary layers with pressure gradient*", AIAA Journal, Vol. 38, No. 8, pg. 1414-1421, 1993.
- [94] S. Williams, R. Hartfield, Jr., "*An analytical investigation of angled injection into a compressible flow*", AIAA Paper 96-3142, July 1996.
- [95] M. A. Woodmansee, J. C. Dutton, "*Experimental measurements of pressure, temperature, and density in an under-expanded sonic jet flowfield*", AIAA Paper No. 99-3600, June 1999.
- [96] M. A. Woodmansee, J. P. Kuenher, R. P. Lucht, J. C. Dutton, "*Pressure, temperature, and density measurements using high-resolution N₂ CARS*", AIAA Paper No. 98-3456, 1998.
- [97] H. Zhang, R. So, M. Zhu, "*A near-wall second-order turbulence model for wall-bounded flows*", "Ninth Symposium on Turbulent Shear Flows", Chapter 8, Springer-Verlag, New York, 1993.
- [98] H. Zhang, R. So, T. Gatski, C. Speziale, "*A near-wall second-order closure for compressible turbulent flows*", "Near-wall turbulent flows", pp. 209-218, edited by R. So, C. Speziale, B. Launder, Elsevier, New York, 1993.
- [99] A.I. Zubkov, A.I. Glagolev, "*The effect of boundary layer thickness and transverse curvature of the surface on the geometry and forces acting in the separation zone produced by injection of a jet into a supersonic flow over that surface*", Fluid Mechanics, Soviet Research, Vol. 8, No.1, January-February 1979, ISSN0096-0764/79/0010-0069\$07.50/0, Scripta Publishing Co. 1979. Originally published in Nauk Trudy Insti. Mekh. Mosk. Gosud. Univ., No. 44, 43-50.
- [100] E. E. Zukoski, F. W. Spaid, "*Secondary Injection of gases into a supersonic flow*", AIAA Journal, Vol. 2, No. 10, pp. 1689-1696, October 1964.

Appendix A. General form of Conservation laws

The reader is reminded that the present discussion as well as all the rest of the present work is valid only for non-relativistic physical systems, i.e. those systems in which the Newtonian laws are assumed to appropriately approximate the physical phenomena.

In Chapter 3.2 the Navier-Stokes equations were presented in conservation form. However, the Navier-Stokes equations are valid only within the assumption that the fluid under consideration is a continuum. For continuum it is meant a system of particle for which, on a macroscopic scale, meaningful statistical averages of the motion of the particles can be taken [34]. This implies that the number of particles in an infinitesimal volume is very high. For air at standard room conditions and for the macroscopic phenomena fluid dynamics deal with the continuum assumption is certainly true since one cubic millimeter of air contains roughly 2×10^{16} molecules [34]. The extremely large number of particles in such a small volume makes so that any statistical average of the motion of the particles is a valid and meaningful average. The continuum assumption breaks down when the mean path of a molecule is of the same order of magnitude of the characteristic length of the flow. In this case it is appropriate to talk about rarefied flow or, in the case in which the free-path is larger than the characteristic length, of free-molecular flows. An indication of whether or not the continuum assumption is valid can be supplied by the similarity parameter called Knudsen number, Kn. The Knudsen number is defined as the ratio of the particle mean path, λ , to the flow characteristic length, L . Usually it is assumed that the continuum assumption holds for Knudsen numbers less than 0.2. Above this value the flow is considered rarefied and, for a Knudsen number greater than 1.00, free-molecular flow exist (for a more extensive discussion see Anderson [4]). For rarefied or free-molecular flows the continuum assumption is not valid anymore and it is necessary to use the kinetic energy approach in which the dynamics of the collision of the particles as well as the intermolecular forces are mathematically modeled. However, the conservation laws (mass, momentum and energy) in their most universal form do not need the continuum assumption and therefore are valid also for rarefied flows. The conservation laws in their most general form and for general linear coordinates are presented here in conservation form.

Conservation of mass:

$$\frac{\partial \rho}{\partial t} + \nabla \cdot (\rho \mathbf{V}) \quad (5.32)$$

Conservation of momentum:

$$\frac{\partial (\rho \mathbf{V})}{\partial t} + \nabla \cdot (\rho \mathbf{V} \mathbf{V}) = F_{ij} \quad (5.33)$$

where the tensor on the right hand side of the equation, F_{ij} , represents the total force acting on the infinitesimal mass. Usually the total force is composed by body forces (also known as volume forces) and surface forces. Using this convention the total force can be decomposed as:

$$F_{ij} = \rho f_i + \nabla \cdot \Pi_{ij} \quad (5.34)$$

The first term on the right-hand side of Equation , f_i , represent the body forces (sometimes also called volume forces). Body forces act at a distance and on the entire mass of the system. Examples of body forces are gravity and electromagnetic forces. Usually in fluid dynamics only gravity force is the relevant body force. Therefore the force vector f_i can be replaced by the gravity vector, g_i . The second term on the right hand side of Equation , Π_{ij} , is a tensor representing the surface forces. Surface forces are created by external stresses acting on the surface boundary of the infinitesimal mass. All the stresses are represented by the components of the stress tensor, Π_{ij} , and can be further divided into normal stresses (the stress components along the diagonal of the stress tensor that also include the inviscid component of the stress, pressure) and shear stresses (the off-diagonal stress components of the stress tensor). It is at this point, with the selection of an approximate mathematical model to describe the shear stresses that the conservation laws lose their generality. For a large range of fluids, it can be stated that the stress at a point is linearly dependent on the rates of strain of the fluid. With this observation it is possible to derive a general deformation law that relates the stress tensor to the strain tensor and, in turn, the shear stain tensor to the pressure and rate of change of the velocity components (for a derivation see Schetz J. A. Schetz, “*Boundary layer analysis*”, Prentice Hall, Englewood Cliffs, New Jersey 07632, Chapter 7, p. 240, 1993, ISBN 0-13-086885-X. or Schlichting [75]). Then the shear stress tensor can be expressed as:

$$\Pi_{ij} = -p\delta_{ij} + \mu \left(\frac{\partial u_i}{\partial x_j} + \frac{\partial u_j}{\partial x_i} \right) + \delta_{ij}\mu' \frac{\partial u_k}{\partial x_k} \quad (5.35)$$

where δ_{ij} is the Kronecker delta, μ is the first coefficient of viscosity (laminar viscosity), μ' is the second coefficient of viscosity. The two viscosity coefficients are related to each other through the coefficient of bulk viscosity, κ , through:

$$\kappa = \frac{2}{3}\mu + \mu' \quad (5.36)$$

However, the coefficient of bulk viscosity is considered to be negligible (Stoke’s hypothesis) except for the study of shock structures or in the study of acoustic waves. With this assumption the two viscosity coefficients are related by:

$$\mu' = -\frac{2}{3}\mu \quad (5.37)$$

Also, as mentioned above, it is convenient in fluid dynamics to distinguish the inviscid component from the viscous or shear component since the latter is negligible in special cases and can be dropped from the conservation equations thus leading to the inviscid study of the flow. Following the common fluid dynamics convention the stress tensor can then be sub-divided as:

$$\Pi_{ij} = -p\delta_{ij} + \tau_{ij} \quad (5.38)$$

where the first term, a scalar, is simply the pressure or inviscid component and the second term, a tensor, is the viscous stress tensor given by:

$$\tau_{ij} = \mu \left[\left(\frac{\partial u_i}{\partial x_j} + \frac{\partial u_j}{\partial x_i} \right) - \frac{2}{3} \delta_{ij} \frac{\partial u_k}{\partial x_k} \right] \quad (5.39)$$

Substitution of Equation (5.38) and Equation (5.39) into Equation (5.33) produces the proper Navier-Stokes equations, i.e. the equation of conservation of momentum for a single-species, Newtonian fluid and the start point for the discussion presented in [33]. Note that the result of the above substitution, after some simple re-arrangement of the terms is the same as Equation (3.2), here repeated for completeness:

$$\frac{\partial \rho u_i}{\partial t} + \frac{\partial}{\partial x_i} (\rho u_i u_i + p \delta_{ij}) = \frac{\partial}{\partial x_i} (\tau_{ij}) + \rho f_i \quad (5.40)$$

The conservation of energy is

$$\frac{\partial \rho e_o}{\partial t} + \frac{\partial}{\partial x_i} (\rho e_o u_i + p u_i + \rho e_o u_i) = \frac{\partial}{\partial x_i} (\tau_{ij} u_j) - \frac{\partial q_i}{\partial x_i} + \rho (u_j f_j) + \rho \dot{q} \quad (5.41)$$

where

$$e_o = C_v T + \frac{1}{2} u_i u_i \quad (5.42)$$

Appendix B. Full set of numerical results on all the grid sequences for the Virginia Tech cases.

Sequence	Number of Cells	Richardson Extrapolation		CFD		$\epsilon_{C_{Fy}}$ %	$\epsilon_{C_{Mz}}$ %
		C_{Fy}	C_{Mz}	C_{Fy}	C_{Mz}		
3	20,410	2.354	2.687	1.51	1.59	108	122
2	145,798			2.18	2.41	23	31
1	1,100,024			2.33	2.65	3	4

(a) Primary jet only

Sequence	Number of Cells	Richardson Extrapolation		CFD		$\epsilon_{C_{Fy}}$ %	$\epsilon_{C_{Mz}}$ %
		C_{Fy}	C_{Mz}	C_{Fy}	C_{Mz}		
3	20,410	2.430	2.924	1.55	1.71	103	109
2	145,798			2.24	2.61	15	8
1	1,100,024			2.40	2.88	3	5

(b) Primary jet + group 1 secondary jets.

Sequence	Number of Cells	Richardson Extrapolation		CFD		$\epsilon_{C_{Fy}}$ %	$\epsilon_{C_{Mz}}$ %
		C_{Fy}	C_{Mz}	C_{Fy}	C_{Mz}		
3	20,410	2.494	3.276	1.59	1.92	98	85
2	145,798			2.30	2.94	7	28
1	1,100,024			2.47	3.23	3	4

(c) Primary jet + group 1&2.

Table B.1. Comparison of the solution on the three grid levels with the solution obtained with the “Mixed 1st +2nd Order Extrapolation” for the Virginia Tech case with a freestream Mach number of 2.40. “ ϵ ” is the discretization error in the solution.

Sequence	Number of Cells	Richardson Extrapolation		CFD		$\epsilon C_{Fy} \%$	$\epsilon C_{Mz} \%$
		C_{Fy}	C_{Mz}	C_{Fy}	C_{Mz}		
3	22,824	1.04	-7.12	0.99	-0.70	-5	-90
2	182,584			1.02	-4.92	-2	-31
1	1,544,097			1.04	-6.84	0	-4

(a) Primary jet only

Sequence	Number of Cells	Richardson Extrapolation		CFD		$\epsilon C_{Fy} \%$	$\epsilon C_{Mz} \%$
		C_{Fy}	C_{Mz}	C_{Fy}	C_{Mz}		
3	32,391	1.03	-4.84	0.94	2.46	-9	-151
2	259,128			0.94	2.46	-9	-151
1	2,073,024			1.02	-3.83	-1	-21

(b) Primary jet + group 2 secondary jets.

Table B.2. Comparison of the solution on the three grid levels with the solution obtained with the “Mixed 1st +2nd Order Extrapolation” for the Virginia Tech case with a freestream Mach number of 4.0. “ ϵ ” is the discretization error in the solution.

Appendix C. Reynolds Stress turbulence Model.

All the turbulent calculations presented in this study employed Wilcox's $k-\omega$ turbulence model [91]. However, the use of a second-order model such as the Reynolds Stress turbulence model might have produced a better agreement between the experimental results and the numerical solution because of its capability of automatically accounting for convection and diffusion of the Reynolds stress tensor and the effects of flow history. Also a parallel comparison of the numerical results obtained with the $\kappa-\omega$ turbulence model to those obtained with the RS turbulence model would have highlighted the deficiencies of first-order turbulence models. Chenault, et al. [14] showed that in two-dimensional flows the Reynolds stress turbulence model produced marginally better results than the $k-\epsilon$ model. However, for the three-dimensional study of a jet interaction case Chenault, et al. [15] and Chenault [16] showed that the RS turbulence model produced consistent and accurate predictions of the flow whereas the $\kappa-\epsilon$ turbulence model failed to produce consistent results. In the present study an attempt was made to run a numerical simulation of the Virginia Tech Mach 4.0 employing the Reynolds Stress turbulence model. Since GASP Version 4.1 does not have any second-order turbulence model implemented as yet another numerical code was selected to run this calculation. The code chosen for the RS calculations was the Integrated Algorithm for Arbitrary Configurations (ISAAC), a numerical code developed by J. Morrison at NASA Langley. However, due to time restrictions and to computational limits of the ORIGIN machines only very simple two-dimensional cases were run and the idea of running on the fine grid level (1.5M cells) the Virginia Tech Mach 4.0 case had to be abandoned. Note that a Reynolds Stress turbulence model requires the simultaneous solution of a minimum of 12 governing equations if the working fluid is composed of only one species: the five Navier-Stokes equations, six transport equations for the Reynolds Stress tensor, τ_{ij} , and one equation for the dissipation rate. Following is a brief description of the Zhang, So, Gatski, Speziale (ZSGS) [98] Reynolds Stress turbulence model suggested by Chenault as being reliable and accurate for jet interaction flowfields [14] [15] [16]. The same model was used in the trial calculations run with the RS turbulence model in this study. At the end of the section the code ISAAC is briefly described; ISAAC is a potential tool for future further investigation of the jet interaction flowfield using second-order turbulence models.

Reynolds Stress Turbulence Model

Second-order turbulence models are assumed to capture more of the true physical nature of a flow-field because they directly compute the Reynolds Stress (RS) tensor. In order to obtain a useful expression for the RS tensor, moments of the Navier-Stokes (NS) equations are taken, i.e. the NS equations are multiplied by a fluctuating property and the product is time-averaged. The final goal is to obtain a differential equation for the RS tensor. Following Wilcox (pp. 17-19, Ref. [91]) through the above procedure and reporting the final result in the form presented by Zhang et al. [52], the final form of the RS transport equation is:

$$\frac{\partial}{\partial t}(\bar{\rho}\tau_{ij}) + \frac{\partial}{\partial x_k}(\bar{\rho}\tilde{u}_k\tau_{ij}) = \bar{\rho}\tilde{P}_{ij} + \bar{\rho}\Pi_{ij} - \bar{\rho}\varepsilon_{ij} + \frac{\partial}{\partial x_k}(\bar{\rho}D_{ijk}^v) + \frac{\partial}{\partial x_k}(\bar{\rho}\tilde{D}_{ijk}^t) \quad (5.43)$$

where:

$$\bar{\rho}\tilde{P}_{ij} = \bar{\rho}\tau_{ik}\frac{\partial\tilde{u}_j}{\partial x_k} - \bar{\rho}\tau_{jk}\frac{\partial\tilde{u}_i}{\partial x_k} \quad (5.44)$$

is the exact production term, Π_{ij} is the modeled pressure-strain term, D_{ijk}^v is the molecular diffusion, and D_{ijk}^t is the turbulent diffusion. ISAAC offers several RS models. The RS model used in this study was the Zhang, So, Gatski, Speziale (ZSGS) [98]. The choice fell on this model because it was specifically developed for supersonic flows, can be integrated to the wall without the use of wall functions, and its reliability has been extensively proven for flat plates [98], flat plates with injection [15], compression ramps [48] and flows around axi-symmetric bodies [47]. The terms in the RS transport equation as modeled in the ZSGS RS turbulence model are:

$$D_{ijk}^v = \overline{\sigma'_{ik}u'_j} + \overline{\sigma'_{jk}u'_i} \cong \bar{\mu} \left(\frac{\partial\tau_{ij}}{\partial x_k} + \frac{\partial\tau_{jk}}{\partial x_i} + \frac{\partial\tau_{ik}}{\partial x_j} \right) \quad (5.45)$$

$$D_{ijk}^t = -\bar{\rho}\overline{u_i''u_j''u_k''} \cong \bar{\rho}C_s \frac{K}{\varepsilon} \left(\frac{\partial\tau_{ij}}{\partial x_k} + \frac{\partial\tau_{jk}}{\partial x_i} + \frac{\partial\tau_{ik}}{\partial x_j} \right) \quad (5.46)$$

$$\varepsilon_{ij} = \left(\overline{\sigma'_{ik}\frac{\partial u'_j}{\partial x_k}} + \overline{\sigma'_{jk}\frac{\partial u'_i}{\partial x_k}} \right) \cong \frac{2}{3}\varepsilon\delta_{ij} + \frac{\varepsilon_{ij}^{wall}}{\bar{\rho}} \quad (5.47)$$

$$\Pi_{ij} = \left(\overline{p'\frac{\partial u'_i}{\partial x_j}} + \overline{p'\frac{\partial u'_j}{\partial x_i}} \right) - \frac{\partial}{\partial x_k} \left(\overline{p'u'_i\delta_{jk}} + \overline{p'u'_j\delta_{ik}} \right) \quad (5.48)$$

where the two parts of the velocity-pressure gradient correlation tensor, Π_{ij} , are also known separately as the pressure strain rate and the pressure diffusion. Zhang, et al. proposed a model for Π_{ij} where:

$$\Pi_{ij} \cong \phi_{ij,1} + \phi_{ij,2} + \phi_{ij}^R + \phi_{ij}^{wall} \quad (5.49)$$

the first two terms being the high-Reynolds number model of Launder, et al. [41], the third term the pressure echo term proposed by Zhang, et al. and the final term the near-wall correction formulated by Zhang, et al. [97].

The six RS transport equations are coupled with a transport equation for the isotropic dissipation rate. The model of this transport equation, again as proposed by Zhang, et al. [98], is:

$$\frac{\partial}{\partial t}(\bar{\rho}\varepsilon) + \frac{\partial}{\partial x_k}(\bar{\rho}\tilde{u}_k\varepsilon) = \frac{\partial D_\varepsilon^v}{\partial x_k} + \frac{\partial D_\varepsilon^t}{\partial x_k} + P_\varepsilon - D_\varepsilon + \Psi + \xi \quad (5.50)$$

The terms in the above transport equation as modeled in the ZSGS RS turbulence model are:

$$D_\varepsilon^v = \bar{\mu} \frac{\partial \varepsilon}{\partial x_k} \quad (5.51)$$

$$D_\varepsilon^t = C_\varepsilon \bar{\rho} \left(\frac{K}{\varepsilon} \right) \tau_{ij} \frac{\partial \varepsilon}{\partial x_k} \quad (5.52)$$

$$P_\varepsilon = C_{\varepsilon 1} \bar{\rho} \left(\frac{\varepsilon}{K} \right) \frac{P_{ii}}{2} \quad (5.53)$$

$$D_\varepsilon = C_{\varepsilon 2} \bar{\rho} \left(\frac{\varepsilon^2}{K} \right) \quad (5.54)$$

$$\Psi = C_{\varepsilon 1} f_{\omega 2} P_{ii} \left(\frac{\varepsilon}{2K} \right) \quad (5.55)$$

$$\xi = f_{w 2} \bar{\rho} \left(-\frac{2\varepsilon \bar{\varepsilon}}{K} + 1.5 \frac{\bar{\varepsilon}^2}{K} \right) \quad (5.56)$$

$$\tilde{\varepsilon} = \varepsilon - 2\bar{v} \left(\sqrt{\frac{\partial K}{\partial x_j}} \right)^2 \quad (5.57)$$

$$\bar{\varepsilon} = \varepsilon - 2\bar{v} \left(\frac{K}{x_j^2} \right) \quad (5.58)$$

The damping function f_{w2} is given as:

$$f_{w2} = \exp \left[- \left(\frac{\text{Re}_T}{40} \right)^2 \right] \quad (5.59)$$

and the closure constants are:

$$C_\varepsilon = 0.1 \quad C_{\varepsilon 1} = 1.5 \quad C_{\varepsilon 2} = 1.83 \quad \sigma = 1.5 \quad (5.60)$$

Closure for the energy equation is achieved by modeling the turbulent heat flux as:

$$C_p \rho \overline{u_k'' T''} = - \left(\frac{C_p \mu_T}{\text{Pr}_T} \right) \frac{\partial \tilde{T}}{\partial x_k} \quad (5.61)$$

where Pr_T , the turbulent Prandtl number is set to 0.9, and the turbulent eddy viscosity is defined as:

$$\mu_T = \bar{\rho} C_\mu f_\mu \left(\frac{K^2}{\varepsilon} \right) \quad (5.62)$$

where $C_\mu = 0.096$ and the damping function is given as:

$$f_\mu = \left(1 + \frac{3.45}{\sqrt{\text{Re}_T}} \right) \tanh \left(\frac{y^+}{115} \right) \quad (5.63)$$

where:

$$y^+ = \left(\frac{y u_\tau}{\bar{v}} \right) \quad u_\tau = \sqrt{\frac{\tau_{wall}}{\bar{\rho}_{wall}}} \quad (5.64)$$

and τ_{wall} is the shear stress at the wall.